UNIVERSITY OF LEEDS

Solid-State Nanopores for the Detection and Characterization of Engineered Nanomaterials

Samuel Confederat

Submitted in accordance with the requirements for the degree of

Doctor of Philosophy (PhD)

The University of Leeds
Faculty of Engineering and Physical Sciences
School of Electronic and Electrical Engineering
Bragg Centre for Materials Research

June 2023

Abstract

The field of nanotechnology has pushed a remarkable transition towards exploring and harnessing unique properties and functionalities presented by engineered nanomaterials. An extensive investigation of their physicochemical properties is of paramount importance to gain insight into their structural–functional relationships.

Recent developments in nanoscale characterization techniques, such as the use of solid-state nanopores have enabled single-molecule measurements, offering unprecedented insights into investigating nanomaterials on individual basis. The ability of nanopores to provide label-free and rapid detection and characterization of nanomaterials in solution based on their ionic current readout makes this technique a great candidate. However, its use in nanomaterials characterization is still limited by the need to tailor the nanopore aperture size to the size of the analyte, impeding the analysis of heterogenous samples due to low signal-to-noise-ratio readouts and low throughput.

In this thesis, a polymer electrolyte nanopore-based approach for enhanced detection of engineered nanomaterial is demonstrated. The heterogenous nature of nanomaterials, including size, shape, assembly state, and functionalization layer is explored by means of ionic current recordings with solid-state nanopores based on pulled glass nanopipettes. Firstly, the analysis of DNA supramolecular assemblies in their native state is demonstrated in a rapid and high-throughput manner, employing the polymer electrolyte system. Furthermore, the fingerprinting and quantification of the assembly yield in different folding mixtures based on nanopore discriminants is showed with a fixed tailored pore size. Secondly, the polymer electrolyte nanopore system enabled the analysis of a range of functional nanomaterials, particularly targeting the analysis of metallic nanospheres, nanorods, plasmonic nanostars, and protein-based spherical nucleic acids. Overall, this thesis demonstrates the potential of solid-state nanopores as a versatile tool for interrogating different characteristics of engineered nanomaterials. These findings can contribute to complementing the toolbox of nanomaterials characterization and support innovation in nanomaterials development for many applications.

Acknowledgements

Firstly, I would like to express my gratitude to Dr. Paolo Actis and Prof. Christoph Wälti for their guidance and great support throughout my PhD journey. A few sentences are not enough to sum up how grateful I am for my team. Paolo thank you for writing me that email back in February 2019 about this PhD in Leeds and for being such a great supervisor from day one. Thank you for keeping me always on the radar, even when my itchy feet were wondering in the far corners of the world. Thank you for making this PhD journey fun for me, dosed with travelling, and of course plenty of research trouble to keep me entertained, and most importantly for believing in me and giving me the freedom to explore. Christoph thank you for your wonderful calmness and wisdom, and bringing sanity to my work, and most importantly for having my back. I appreciate all your advice received during this period. Also, I will always cherish our lab Christmas fondue dinners. Thank you for looking after all of us (like a true Captain). For sure I would call you if I get lost somewhere on a raft drifting in the open seas (not inconceivable).

I would also like thank to Dr. Virginia Pensabene and Prof. Helen Picton for the opportunity to work on a very stimulating and interdisciplinary project. I am grateful for the different perspectives of biomedical research that I learnt from working together with you. Also, I would like to thank Andreia for helping me on this project.

I am thankful to all my collaborators throughout this PhD project. I would like to thank Dr. Pietro Strobbia and Dr. Devleena Samanta for their support with exciting novel nanomaterials. Thank you Dr. Federico Thei and Elements SRL for our nanopore collaborations and the visit at your site in Cesena. Thank you Ilaria Sandei for the amazing DNA origami we made in the lab and sharing weekends pipetting for hours staple mixtures. Thank you NanoComposix for the wonderful uniform nanoparticles samples used for my nanopore measurements.

I am also very grateful to our SENTINEL ITN. It was a true pleasure to be part of this network with such wonderful people and great scientists. I will always cherish our wonderful training weeks in different parts of Europe. Special thanks to Manuel and Max

for our secondments spent together and all the fun outside the lab, such as getting lost in the Bermuda Triangle of Bochum. I would also like to thank Sarah King for being such an amazing manager for our ITN and for putting up with all my puzzling travel plans.

I can say that this PhD thesis is a product of crossing boundaries outside lab, outside countries, outside the norms what research is sometimes believed to be. I endorse the spirit of research movement and multidisciplinary collaborations. I have always considered science something that unites us, regardless of gender, nationality, language, distance, or political situation. Science shows how much we can learn from one another and that we can find progress together.

Special thanks to Ryanair, EasyJet, KLM, Delta airlines and many airports across the world for the frequent possibility to work on my PhD project whilst travelling. I cannot forget all the aircrafts (B737, B787, A320, A330, E190) that I spent hours flying and analysing data, writing thesis chapters and manuscripts.

I would like to extend my thanks to the Bioelectronics lab members. For me Bioelectronics lab always felt like home. Special thanks to Fabio, Dimitrios, Chalmers, and Elena, you were my family in Leeds. A very big thank you to my PhD partners in crime – Fabio and Dimitrios. We started this PhD journey together and I am very grateful for having you guys by my side through thick and thin. Looking back, I think we had it all (pandemic, lockdowns, labs move), but also so many wonderful moments together and many reasons to laugh, be excited, and celebrate achievements together. Moreover, I am thankful to Elena for not stealing my job, and also for being forced to learn about aircrafts during our lunch breaks. Chalmers, thank you for making our nanopore work so much better with PEG (the answer to everything), but also for the many fun moments outside the lab and inviting us over for dinners and games.

I am also very grateful for all the fun activities that I was able to enjoy at the University of Leeds. I would like to thank my fencing club at Leeds University and in particular my M1 and M2 teams for sharing exciting moments fencing against other universities in

competitions. I would also like to extend my appreciation to the Swing Society and the many wonderful people I got to know there.

I would like to thank my friends outside the lab as well. I am grateful to all my lovey friends from EEE and MNP for all the fun moments spent together. Special thanks to my friend Simone for being there for me from the beginning of my PhD, undoubtedly the best chef in Leeds. I would like to thank Mo for all the fun trips and for inevitably saying yes to all my ridiculous travel plans. I would like to express my massive appreciation to Africa for being there for me and for giving me such great support throughout this journey and all the wonderful moments shared together and putting up with my sense of humour. Though, it still hurts greatly bring crossed out from the squash hit-list (no chance for vindication).

Lastly, I would like to thank my family for their endless support, for believing in me, and for their unconditional love. A young boy from Romania had big dreams that one day he will do science and explore the world. Many years spent far away from home, and yet you were always there for me. May this achievement be a symbol for all your sacrifices and love.

This PhD journey has been a transformative period in my life and I am grateful to look back and proudly say that:

'I Did It My Way'

Intellectual Property and Publications Statement

The candidate confirms that the work of this thesis is his own, except where work which has been adapted for jointly authored publication has been included. Where relevant, the contribution of other authors to the work submitted has been indicated. The candidate confirms that the appropriate reference to the work of others mentioned in this thesis has been made.

- **Chapter 1** contains content that was adapted for the following co-authored publication:

"The New Era of High-Throughput Nanoelectrochemistry", Xiangdong Xu, Dimitrios Valavanis, Paolo Ciocci, Samuel Confederat, Fabio Marcuccio, Jean-François Lemineur, Paolo Actis, Frédéric Kanoufi, and Patrick R. Unwin, Analytical Chemistry 2023, 95, 1, 319–356. Xiangdong Xu, Dimitrios Valavanis, Paolo Ciocci, Samuel Confederat, Fabio Marcuccio contributed equality to this work.

- **Chapter 3** contains content that was adapted for the following first author publication:

"Nanopore fingerprinting of supramolecular DNA nanostructures", Samuel Confederat, Ilaria Sandei, Gayathri Mohanan, Christoph Wälti, Paolo Actis, Biophysical Journal 2022, Volume 121, Issue 24, Pages 4882-4891.

- **Chapter 4** contains content that was adapted for first author submission:

“Nanopore Sensors for Enhanced Detection of Nanoparticles", Samuel Confederat, Seungheon Lee, Der Vang, Dimitrios Soulias, Fabio Marcuccio, Timotheus I. Peace, Martin Andrew Edwards, Pietro Strobbia, Devleena Samanta, Christoph Wälti, Paolo Actis. bioRxiv.2023.2003.2031.534385.

Contents

List of Figures

List of Tables

Abbreviations

AFM	**Atomic Force Microscopy**
CDB	**Controlled Dielectric Breakdown**
DLS	**Dynamic Light Scattering**
DNA	**Deoxyribonucleic Acid**
dsDNA	**duble-stranded Deoxyribonucleic Acid**
ECS	**Equivalent Charge Surplus**
EDL	**Electric Double Layer**
EDTA	**Ethylenediaminetetraacetic Acid**
EOF	**Electroosmotic Force**
EPF	**Electrophoretic Force**
ICR	**Ion Current Rectification**
kbp	**kilo-base pair**
mRNA	**messenger Ribonucleic Acid**
PBS	**Phosphate-buffered Saline**
PCR	**Polymerase Chain Reaction**
PEG	**Polyethylene Glycol**
RNA	**Ribonucleic Acid**
SEM	**Scanning Electron Microscopy**
SERS	**Surface-enhanced Raman Spectroscopy**
SNA	**Spherical Nucleic Acid**
SNR	**Signal-to-Noise Ratio**
ssDNA	**single-stranded Deoxyribonucleic Acid**
TEM	**Transmission Electron Microscopy**

Chapter 1: Introduction

1.1. Overview

In this chapter a detailed description of the general topic of the thesis is given. It is then followed by a discussion on characterization methods of emerging nanomaterials and their applications. A description of characterization of nanomaterials with single-entity resolution is provided, highlighting the opportunities and challenges of such methods. The main discussion is centered on solid-state nanopores as a single-entity tool for the characterization of nanomaterials, highlighting recent creative developments. The chapter is concluded with a perspective on the current challenges in analyzing nanomaterials and heterogenous mixtures with solid-state nanopores, linking up with the main objectives of this thesis.

1.2. Emerging functional nanomaterials

Harnessing the power of materials has played a pivotal role in shaping our society. From early times, materials have driven progress in many different shapes, from utilization of basic tools, to buildings, transport, and clothing, to mention a few. Over the years we

have learn a great deal how to exploit materials and building blocks to improve our daily lives, but also to push innovation in different sectors. The recent shift towards nanotechnology has opened a vast potential, spanning from electronics, to medicine, and energy. Here the spotlight is on design and synthesis of innovative nanomaterials. Nevertheless, characterization of materials at the nanoscale still remains a major endeavor, requiring sensitive and high-throughput methods for their analysis. Characterizing nanomaterials is crucial for achieving their full potential and understanding their unique properties at the nanoscale. Here, the accurate characterization of such nanoscale materials can support optimal performance, safety, and meeting established regulations and standards. For example, in medicine, characterization of nanomaterials can support new boost in the development of effective drug delivery constructs, modernizing treatment paradigms. In electronics, this can translate in progressing towards enhanced efficiency of devices. Meanwhile, in energy, well characterized nanomaterials can play an important role in high-performance renewable technologies.

Recent advancements in the field of nanotechnology has brought a major shift in the way materials are designed, synthesized, and utilized. Traditionally, materials were engineered at the macroscopic scale, with a focus on the bulk properties and their applications. However, the field of nanotechnology has pushed a remarkable transition towards exploring and harnessing the unique properties and functionalities exhibited by materials and the nanoscale (1). One critical aspects of the shift from macro to nanomaterials is the ability to have precise control over the size, shape, and composition of the engineered nanostructures (2). This unprecedented level of control stimulated the engineering of nanomaterials for a wide range of applications. One example in this sense is the size-dependent optical properties, such of quantum dots, with implications in fabrication of displays and lighting, and biomedical imaging (3). Another aspect of exploiting nanoscale materials is the increase in surface area, allowing enhanced interactions with the local environment in a highly responsive and sensitive manner. The investigation of anisotropic nanoparticles is another niche that has stimulated great developments in optics, catalysis, and biomedical research (4). Furthermore, nanoscale engineering of DNA and protein-based hybrid nanomaterials has enabled numerous strategies for drug delivery systems and biosensors (5,6). Some of the upcoming classes

of functional nanomaterials are being described in the following subsections, with a main emphasis on anisotropic nanoparticles and nucleic acid-based engineered nanomaterials.

1.2.1. Anisotropic nanoparticles

A recent class of nanomaterials that is becoming widely utilized in numerous applications is anisotropic nanoparticles (7). Figure 1.1 exemplifies some of the most commonly used anisotropic nanoparticles, with applications in bio-imaging in the visible to near-infrared region (Figure 1.1A), surface-enhanced Raman spectroscopy (Figure 1.1B), and surface-enhanced catalysis (Figure 1.1C) (4). Anisotropic nanoparticles refer to nanoscale particles that possess different properties or shapes in different directions (7). The intriguing properties of anisotropic nanoparticles stem from the precise control of their orientation and spatial arrangement. Various techniques can be employed to synthesize anisotropic nanoparticles, including seed-mediated growth, template-assisted synthesis, or supramolecular assembly (7). Common shapes of anisotropic nanoparticles include rods, stars, triangles, among others (4). An appealing feature of anisotropic nanoparticles is their shape-dependent plasmonic resonances, supporting plasmon band in the near-infrared (NIR) region (8). This is attractive due to the low absorption of tissues in this region, opening up possibilities for bioimaging and photothermal therapy (9). Apart from this, anisotropic nanoparticles such as gold branched nanostars have been reported as suitable sensing probes due to the presence of hotspots that can significantly enhance the Raman scattering signal of nearby molecules, supporting amplified Raman signals (10). With regard to the surface-enhanced catalysis, anisotropic particles that present facets with high density of active sites often display enhanced catalytic activity. Examples, such as palladium nanocubes or platinum nanowires, have demonstrated enhanced catalytic activity in reactions, including fuel cells and hydrogenation (11).

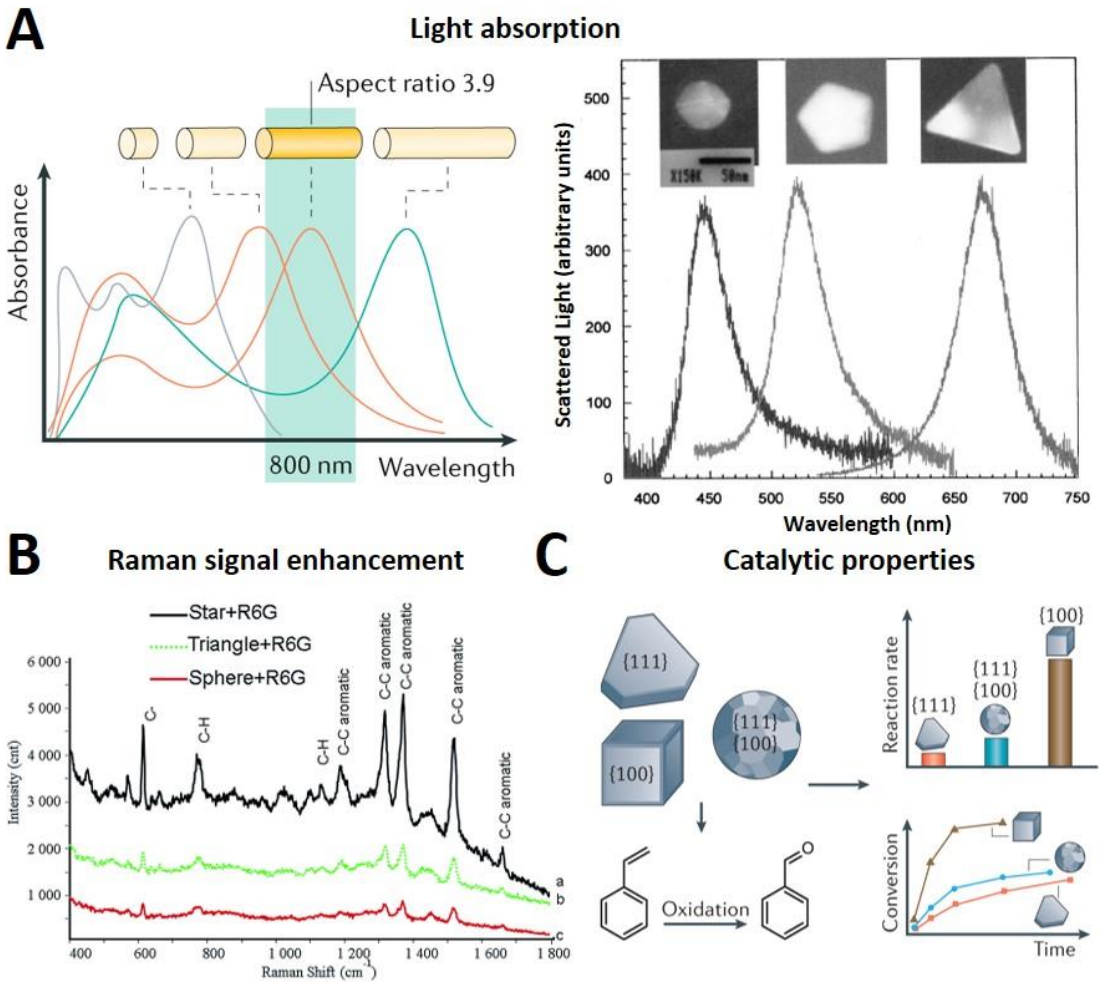

Figure 1.1: Representative examples of engineered nanoparticles with anisotropic shapes tuned for specific applications. **(A)** Shape-dependent plasmonic resonance tuning by adjustment of the aspect ratio of gold nanorods, and silver nanoparticles of different shapes: spherical, pentagon, and triangle nanoparticles (50 nm scale bar) that can lead to plasmonic resonance bands at different wavelengths. Adapted from ref. (4) and ref. (12). **(B)** Surface Enhanced Raman Scattering (SERS) by gold nanoparticles using Rhodamine 6G (R6G) probe molecule. The SERS effect for the R6G systematically increases with increase in the local curvature of the gold nanoparticles, as a result of higher number and strength of the local field hotspots. Adapted from ref. (13) (C) Example of catalytic properties influenced by nanoparticle shape through control of the crystallographic facets. Silver nanocubes show higher activity for styrene oxidation in colloidal solution than near-spherical nanoparticles and nanoplates, due to their more-reactive planes. Adapted from ref. (4).

1.2.2. Nucleic acid-based nanomaterials

With the continuous developments in nanotechnology, nucleic acids have received a great attention not only as carriers of genetic information, but also as adaptable functional material. The field of DNA structural nanotechnology, pioneered by Seeman (14), has become an established research field following the principle of creating precise and ordered nanostructures based on the Watson-Crick base pairing. The exceptional

level of sequence programmability has led to the engineering of different kinds of structural and functional materials based on DNA (15). Furthermore, the concept of the DNA origami folding technique introduced by Rothemund (16) has been stimulating the generation of new programmable nanomaterials. The DNA origami technique relies on the self-assembly properties of DNA, involving the use of a long single-stranded DNA (ssDNA) scaffold and a mixture of hundreds of short ssDNA strands designed to bind specific region of the scaffold (16). The hybridization of the staples based on the Watson-Crick base-pairing drives the folding of the scaffold in well-defined nanostructures (16), as depicted in Figure 1.2A-B. This DNA folding concept has sparked a variety of constructs with implications in drug delivery, biosensing, and templating (17). The DNA origami approach brings the possibility of engineering nanoscale objects with different shapes and sizes with nanometer precision. A great promise of these DNA-based constructs has been the development of drug delivery nanocarriers (18). Apart from the biocompatibility and biodegradability aspects, another attractive feature of these DNA nanostructures is the ease of functionalization with various molecules. This led to the development of various drug delivery constructs where the molecules of interest are embedded in the DNA nanostructure. One example in this sense is the work carried out by Zhang *et al.*, where self-assembled DNA origami nanostructures were utilized to perform *in vivo* delivery of the anticancer drug doxorubicin by noncovalent intercalation of the drug molecules into the DNA nanostructures, (18), as shown in Figure 1.2C.

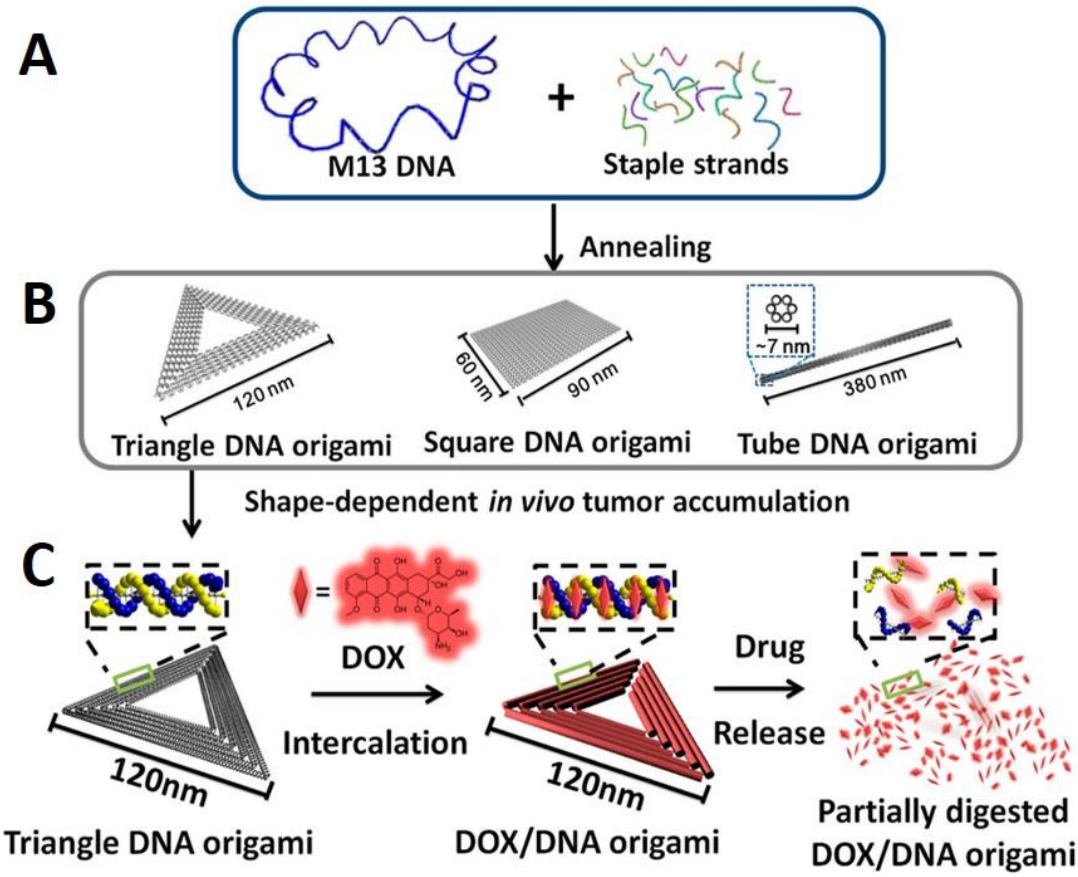

Figure 1.2: DNA origami folding of nanostructures. **(A)** Schematic depicting the DNA origami folding process. A long single-stranded DNA scaffold (M13mp 18 phage genomic DNA) is folded by addition of mixture of hundreds of short complementary rationally designed staple strands to different regions of the scaffold strand, causing the scaffold to fold into well-defined structures in one-step annealing process: triangle, square, and tube origami shapes **(B)**. Example of triangular-shaped DNA origami drug carrier, depicting the loading of doxorubicin (DOX) anti-tumour drug through intercalation **(C)**. Adapted from ref. (18).

Apart from 2D structures, different 3D designs have been proposed as well, showing increased stability in serum and encapsulation efficiency (19-21). In this sense, Liu *et al.* proposed in their work a tetrahedral nanostructure (Figure 1.3A), by folding DNA origami sheets into a hollow 3D structure facilitated by the hybridization of DNA strands placed at the edges of the 2D sheets (20). A particularly attractive feature explored by the authors for this 3D DNA construct is the controlled conformational change in response to adhesion to epithelial cell molecules (EpCAM), a molecular biomarker expressed in circulating tumor cells. Moreover, incorporation of fluorophores or other imaging agents into these constructs can facilitate their tracking.

Given the fact that the DNA origami folding is limited in size by the length of the DNA scaffold utilized, hierarchical self-assembly strategies employing pre-folded DNA

building blocks have been suggested for supramolecular assemblies and periodic arrays (22,23). Here, the building strategy revolves around the DNA specificity, by incorporating ssDNA to the edge of one structure unit and its complementary ss DNA to another structure unit that allows bridging the two in a predictable and repeatable manner. Wang *et al.* demonstrated in their study the programming of supramolecular assemblies from pre-folded building blocks, showing the ability to form dimer and hexametric superstructures (Figure 1.3B) (23). The use of such building approaches at the nanoscale can increase the DNA design space and maximize the potential of DNA-based constructs for engineering intricate functional nanomaterials.

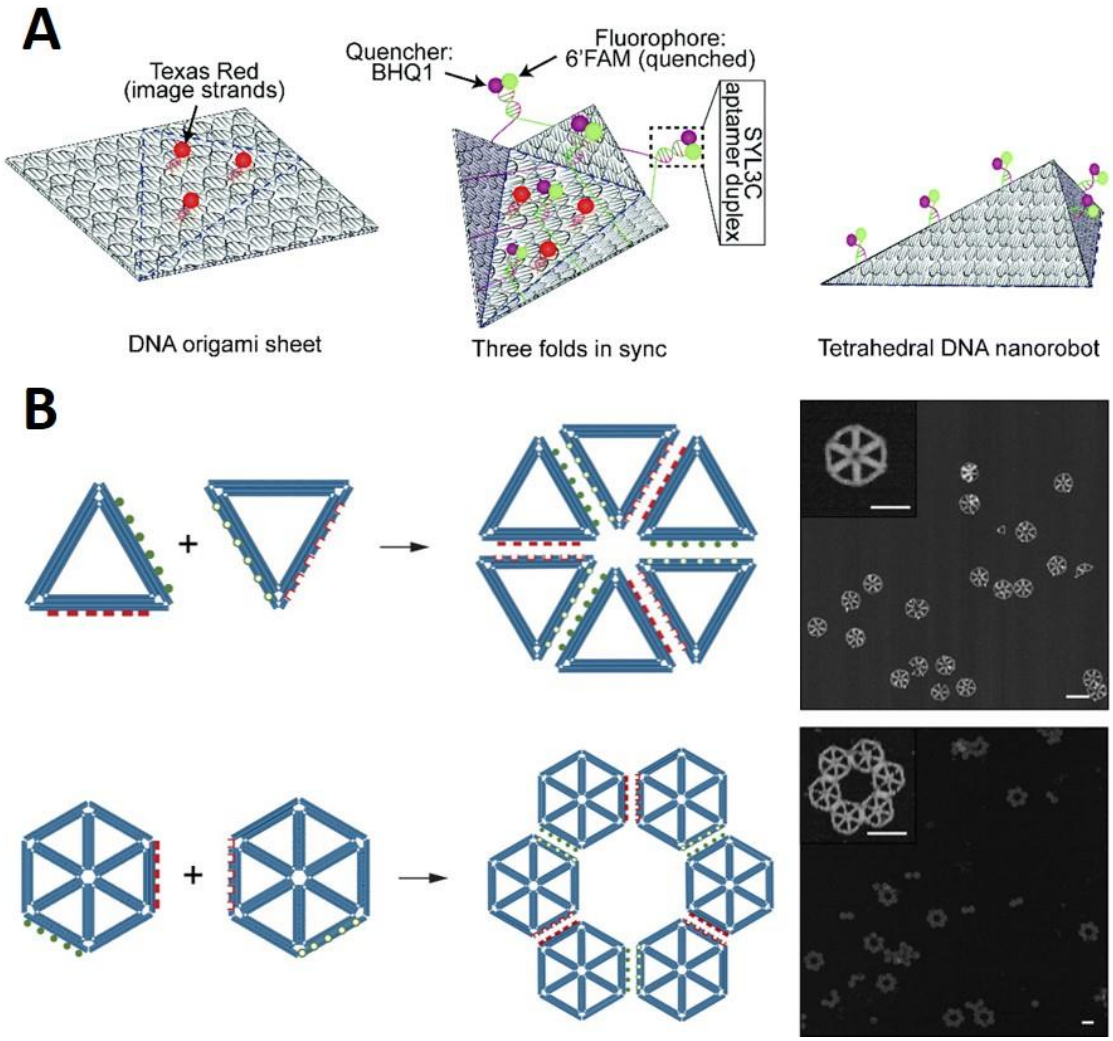

Figure 1.3: Supramolecular DNA origami assemblies. **(A)** Schematic design of the folding of tetrahedral DNA 3D nanostructure and its conformational change. An aptamer duplex is used for recognition and trigger a conformation change by the EpCAm biomarker. The confirmation transition is monitored by separation of the adjacent DNA-conjugated fluorophore and quencher assembled on the DNA origami sheets. Adapted from ref. (20). **(B)** Supramolecular assemblies formed by triangle and hexagonal DNA origami building blocks, together with the AFM imaging (100 nm scale bars). Adapted from ref. (23).

1.2.3. Hybrid nanomaterials

The growing demand for new innovative materials has stimulated the utilization of two or more nanomaterials in a hybrid configuration to amplify desired features, creating materials with enhanced properties and functionalities. These hybrid nanomaterials can be created by joining different components at the nanoscale, ranging from colloids, DNA origami constructs, proteins, lipids, among others, to obtain synergetic effects that improve their multifunctionality, compared to their use on individual basis. As a result, materials with improved performances (thermal/mechanical stability, electron conductivity, spatial arrangement, light emission, permeability, etc.) can be created by tuning their composition and morphology.

One emerging trend in hybrid materials is building plasmonic superstructures that are simple to integrate on solid substrates. The combination of DNA origami folded nanostructures with metallic nanoparticles has been proposed for multiple applications where the precise nanometer arrangement of the DNA origami structure and the tuned optical properties of noble metal nanoparticles when these organic and inorganic components are paired. An example in this direction is the work carried by Zhan *et al.* on the integration of gold bowtie nanostructures on DNA origami sheets for single-molecule SERS measurements (Figure 1.4A) (24). Capture strands were utilized to attach the gold nanostructures on two rectangular DNA origami sheets linked together. Here, the gold nanostructures were functionalized with thiolated ssDNA, complementary to the capture strands present on the origami constructs. A similar approach was also reported by Tanwar *et al.* where gold star-shaped nanoparticles with tunable gaps were assembled on the DNA origami dimerized tiles and a Raman reporter molecule positioned in between the nanostars gap (25). DNA origami has the special advantage that it allows for spatial control over the conformations of the plasmonic nanostructures in response to environmental signals.

Another emerging class of hybrid nanomaterials has been introduced by the Chad Mirkin group, termed protein spherical nucleic acids (ProSNAs) (26). This class of hybrid nanomaterials consists of a protein core with a chemically modified dense shell of oligonucleotides (Figure 1.4B). The strategy proposed in their studies allows independent variation of the protein core and the nucleic acid shell to target different functionality (26). A major advantage brought by these hybrid constructs is the

increased stability of the proteins from degradation, and increased cellular uptake due to their functionalization, making them suitable probes for intra-cellular measurements (27). Furthermore, the enhanced cellular uptake of ProSNAs facilitates intracellular delivery of functional proteins for therapeutics, overcoming cellular entry and degradation of cell-impermeable proteins (28).

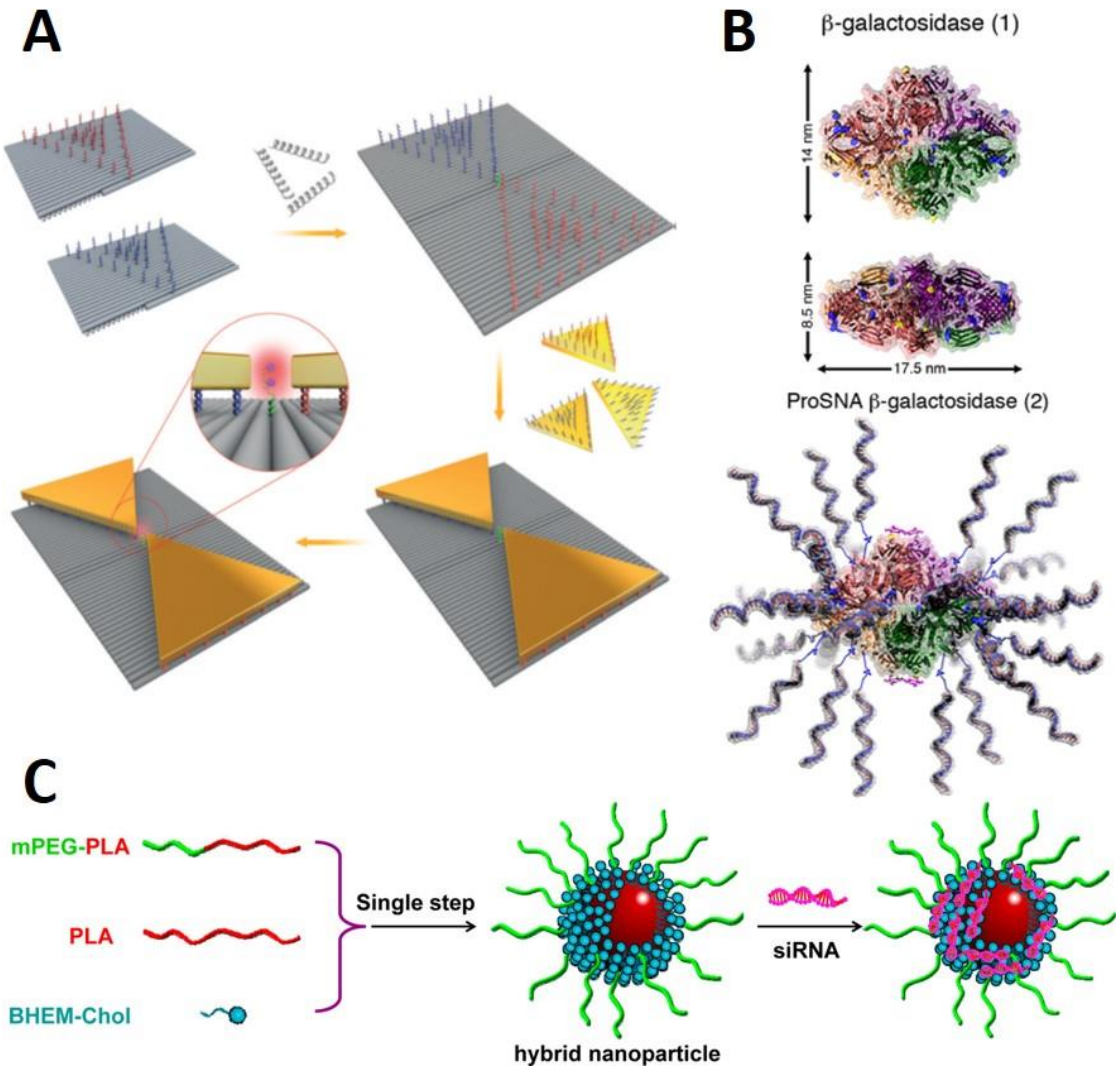

Figure 1.4: Emerging classes of hybrid nanomaterials. **(A)** Schematic of plasmonic bowtie nanostructures assembled on DNA origami dimer construct and a Raman probe positioned at the gap of the gold nanostructures. Adapted with permission from ref. (24). **(B)** Protein spherical nuclei acids (ProSNAs) based on β-galactosidase protein core with a shell of oligonucleotides conjugated on the surface of the protein. Adapted from ref. (28). **(C)** Schematic representation of a lipid-polymer nanoparticle with siRNA molecules bound. The hybrid nanoparticle consists of a PLA core, a hydrophilic PEH shell, and cationic lipid monolayer (BHEM-Chol). Adapted from ref. (29).

Lastly, another class of hybrid nanomaterials which have demonstrated great potential in nanomedicine is the use of RNA therapeutic molecules and lipid-based nanoparticles (Figure 1.4C) (29), as demonstrated by Yan *et. al*. (29). This combination results in a powerful platform that can enable various RNA molecules to be efficiently packed and delivered to targeted cells and tissues. RNA-based therapeutics, such as messenger RNA (mRNA), small interfering RNA (siRNA), and micro RNA (miRNA) have shown great potential in diseases treatment, vaccine development, and modulating gene expression (30). The efficient use of these RNA molecules has been limited by their instability, degradation, and poor cellular uptake (30). However, in combination with lipid-nanoparticles, their encapsulation, stability, and efficient cell delivery to target cells can be dramatically improved (31). Furthermore, lipid-based nanoparticles can be designed to obtain controlled release of the embedded RNA molecules, supporting prolonged therapeutic effects. With ongoing advancements in nanotechnology, these nanomaterials systems hold great promise in opening new avenues for precision medicine, standing as a versatile and effective platform for developing novel therapeutics (31).

Whereas, the engineering of nanomaterials has showed tremendous progress and continuous expansion in terms of nanoscale precision and new applications, some of the current challenges revolve around their scalability and characterization. Of particular importance here is the development of analytical tools that can provide sensitive, comprehensive, and high-throughput analysis of engineered nanomaterials. This aspect is discussed in the following subsections, with a particular emphasis on the single-entity analysis.

1.3. Characterization of engineered nanomaterials

For the efficient use of engineered nanomaterials, it is important to fully characterize their nanoscale properties and behavior under various conditions, relevant to the application in question. Understanding their properties through reliable characterization can improve their design and performance. For instance, the widespread use of engineered nanomaterials and their commercialization requires extensive characterization in terms of their quality and batch-to-batch reproducibility,

which currently still poses challenges for their translation from laboratories into real-world applications (32). From an analytical standpoint, discrimination of variations at the nanoscale is a challenging endeavor itself. Therefore, techniques that support simultaneous and integrated information in a high-throughput manner with regard to the makeup and behavior of nanomaterials are highly demanded. This section describes some of the most relevant features investigated for synthesized nanomaterials and current techniques employed in their analysis, emphasizing their practical strengths and limitations and their distinction as ensemble and single-entity techniques.

1.3.1. Physicochemical properties of engineered nanomaterials

As mentioned above, a great endeavor when it comes to engineered nanomaterials is analyzing their physicochemical properties and correlating them to their functions and behaviour. Nanoscale objects are typically dispersed into discrete entities with particular characteristics. Key chemical and physical parameters for nanomaterials typically include: size, shape, composition, surface charge, and concentration, amongst others (33). In engineered nanoparticles, size and shape influence their diffusion properties, fluid drag, optical characteristics, and cellular uptake (34,35). One key aspect often interrogated in nanomedicine is the relationship between size/shape and the toxicity of nanoparticles, as well as internalization and degradation properties (36). Whereas, in nanoparticle synthesis, size distribution can inform on the quality of the suspension.

Surface charge is another key parameter. As a fundamental component for controlling the aggregation state, the electrostatic repulsion between nanoparticles favors stability of colloidal suspensions (37). Particularly, when suspended in an electrolyte solution, the screening of the nanoparticles can increase the aggregation state of a suspension (38). A defined measure of the surface charge and the colloidal stability for nanoparticle is represented by the zeta potential (ζ) (39). Factors that can affect the zeta potential of nanoparticles in a solution, include ionic strength, pH, and adsorption of charged/uncharged species (38). In addition to regulating a colloidal suspension's stability and tendency to aggregate, the surface charge also exerts an influence on the interaction of the particle with the environment (40).

1.3.2. Ensemble and single-entity characterization techniques

A large spectrum of techniques can be applied for the characterization of nanomaterials, based on different modalities, such as: optical spectroscopy, light scattering, electron microscopy, chromatography, electrophoresis, *etc*. (41). In this subsection, some of the most commonly utilized techniques are mentioned. Here, two distinct approaches can be made, namely ensemble techniques and single-entity measurement techniques (Figure 1.5). Whereas, a single molecule detector concept is depicted in the middle panel of Figure 1.5, it is important to note that analysis of a single-molecule generally entails a dynamic system (rather than a single-molecule snapshot) and therefore the sampling and time-dependent effect, as well as surrounding medium playing a role in the analysis process.

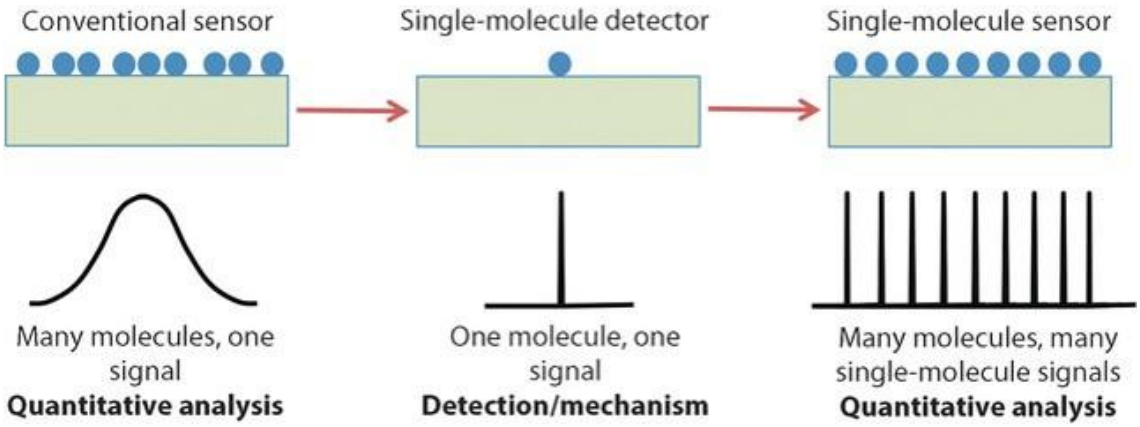

Figure 1.5: Concept of ensemble-based and single-molecule measurement. Adapted from ref. (42).

Ensemble measurement techniques refer to measurement approaches where a large population of nanomaterials is measured simultaneously, providing averaged information of the same quantity. These approaches benefit from relatively fast measurements (within several minutes), accelerating the measurement output and facilitating the screening for desirable properties in different samples. Apart from this, ensemble technique can provide statistical data on the average properties of the nanomaterials populations evaluated. Two such techniques that are often employed in routine analysis of nanomaterials are UV-Vis spectroscopy and dynamic light scattering (DLS). These techniques have a great contribution in analysis of synthesized batches, allowing the user to extract important information, such as size distribution, stability in

different conditions, and concentration (33). UV-Vis spectroscopy, based on the principle of measuring the ultraviolet and visible light absorption by a sample, is commonly used to evaluate nanomaterials characteristics such as: size, concentration, aggregates formation, and in some cases surface functionalization as well (43). DLS is an ensemble-based technique that measures the scattered light intensity fluctuations of particles in a sample to determine the size distribution (44). By observing variation in the scatter light as a result of the Brownian motion of particles in solution, DLS extracts information about their hydrodynamic size and diffusion properties (44). This measurement technique is a great choice for routine analysis of monodisperse samples, in various solvents, providing quick and non-invasive measurements (45). However, given the dependence on scattering light intensity on particle size, the larger components present in solution can cause bias in size estimation (45). This poses limitations for the analysis of heterogenous samples, for accurately estimating the size of non-spherical nanomaterials, due to the spherical model assumed in the analysis (45). Another category of techniques involves the measurements at the individual particle level, hereby referred as single-entity techniques. Opposite to traditional ensemble-based methods where the mean response is obtained, single-entity measurements can capture subtle variations in the sample on the basis of their individual assessment, supporting detection of heterogeneity within a population of nanomaterials (42). Furthermore, from the analytical perspective, the ability to inspect nanomaterials at the single-entity level allows a direct count of the analytes, eliminating potential concentration constrains and the need for calibrations (42). One technique that has gained popularity for providing high-resolution single-particle measurements at the nanoscale is the use of transmission electron microscopy (TEM). During TEM measurement, a beam of electrons is focused and transmitted through the specimen investigated to create an image (33). Here, the interactions between the electrons and the specimen provide information regarding the size and morphology of analyte on individual basis (33). Hence, TEM can provide size and shape information of heterogenous nanomaterial samples. A significant trade-off generally acknowledged in utilizing TEM is the requirement of performing measurements in dry under high vacuum conditions (46). To circumvent this, TEM approaches such as cryo-TEM and liquid cell TEM (LCTEM) can favour characterization of nanomaterials in their hydrated or liquid

state. This allow the user to explore in situ characterization of aqueous dispersions, such as characterizing nanoparticles dispersion in biological media or probing dynamic processes such as nucleation and growth under various aqueous conditions, as previously reported by Brydson and co-workers (47-49). While these approach are still evolving, limitations are posed by the use of specialized equipment and the effect of electron beam on the samples (46). Another method that can be explored for such measurements is the use of atomic force microscopy (AFM) which supports measurements in solution and under physiological conditions. AFM operates by scanning a shaper probe (cantilever) over the surface of sample disperse on a substrate, measuring the forces between the probe and sample surface to generate a topographic image with high-resolution (41). AFM can be employed for examining nanomaterials characteristics, such as size, morphology, surface roughness, and mechanical properties. Although, both AFM and TEM are powerful techniques that can provide detailed information at the nanoscale level, they are limited in terms of their measurement throughput and sample immobilization (50). This comes at the cost of longer measurement time to cover different areas imaged/scanned and potential artefacts due sample sedimentation on the substrate used. Another technique that has been proposed for single-entity measurements of nanomaterials is based on solid-state nanopores (51). This approach relies on the passage of individual analytes through a nanoscale aperture, allowing for the detection of changes in ionic current, which can then be used to infer about the physicochemical properties, such as size, charge, shape, and analyte concentration (51). The main advantages brought by this approach is the ability to provide rapid and non-destructive measurements of nanomaterials in solution, without the need for extensive sample preparation or the use of high sample concentrations (52). Furthermore, different strategies can be applied to sustain large number of analytes measured and maximize the analysis throughput with low-volume requirements. The unique ability to monitor the passage of analytes at the single level, makes nanopores a technique with an untapped potential in detection and characterization of a wide range of nanoscale analytes.

1.4. Solid-state nanopores

The development of solid-state nanopore technology in the last decades has enabled numerous applications in single-entity research (53,54). This section provides an overview of the general sensing principle in nanopores, highlighting different nanopore configurations and recent developments in performing quantitative analysis and enhanced detection modalities using nanopore systems.

1.4.1. Nanopore working principle

The general nanopore readout relies on resistive pulse sensing where the nanopore links two compartments filled with an electrolyte solution with electrodes immersed in each compartment (Figure 1.6A) (55). Electrolytes used in the two compartments of the nanopore setup are typically monovalent salt (*e.g.,* KCl, NaCl, LiCl). Upon the application of a potential bias across the pore through the pair the electrodes placed on each side, a constant ionic current is measured, defined as the open pore current. After the introduction of analytes into the electrolyte compartment, they are translocated through the nanopore causing a temporary modulation in the measured ionic current. The characteristic of the current perturbations such as current magnitude, duration, and frequency (Figure 1.6B), lead to information about the physico-chemical properties of the analyte (*i.e.*, size, charge, shape, concentration) and its interactions with the nanopore (51,55,56). Due to the nanoscale dimensions of the pore which are closely matching the size of the analyte, the nanopore-based readout involves counting molecules at the individual level. This sensing approach enabled, *inter alia*, the single-molecule analysis of RNA (57), DNA nanostructures (58-60), proteins (61,62), ribosomes (63), and virus particles (64,65). Furthermore, nanopores have been employed in the analysis of inorganic colloids and nanoparticles (66-68).

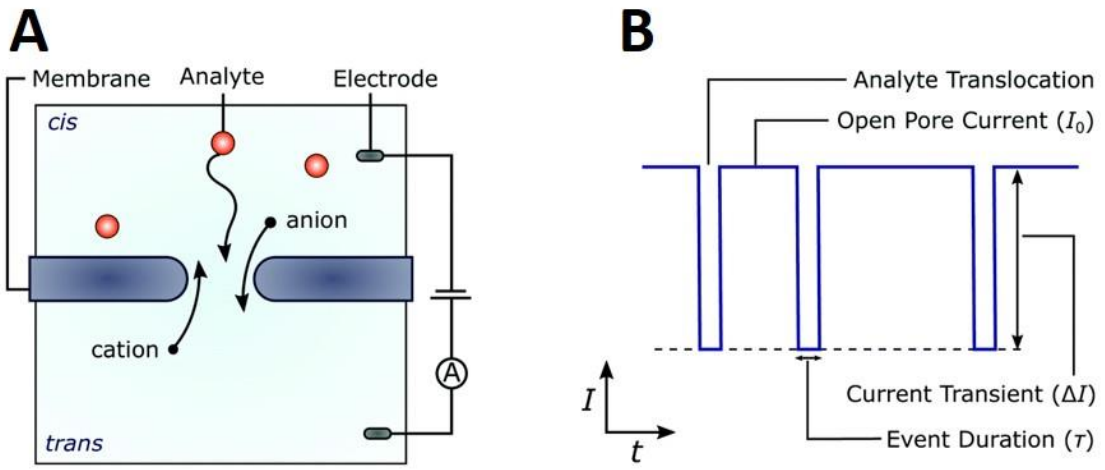

Figure 1.6: Nanopore working principle. **(A)** Schematic depicting the working principle of conventional nanopore sensing. A nanoscale size pore separates two reservoirs filled with electrolyte buffer and a electrodes placed on each side. By applying a constant voltage bias across the pore, the analyte translocate through the pore resulting in a change in the open current, in form of translocation pulse with a characteristics amplitude and duration dependent on the analyte **(B)**. Adapted from ref. (69).

1.4.2. Nanopore configurations and fabrication

Nanopores can be categorized into three main groups, based on in the nature of the materials they are made of, *i.e.,* biological, solid-state, and hybrid nanopores (70). Initially, the most exploited nanopores were the biological nanopores. Biological nanopores refer to a class of nanopore that comprise pore-forming proteins inserted into planar lipid or synthetic membranes (71). One widely used example here is α-hemolysin (αHL) nanopores, with a pore diameter of 1.4 nm (72), initially used in nanopore sequencing experiments. This was followed other variants (i.e. MspA) and other engineered and modified biological pores, such as improving accuracy and speed of improved nanopore sequencing performance. The small dimensions of these pores and their reproducible nature have played a major role in pushing the field of nuclei acid sequencing, as demonstrated by the commercialization of nanopore sequencing devices from Oxford Nanopore Technologies Ltd (73). Nevertheless, the intrinsic small dimensions of such pores limit their use to a narrow range of analytes, particularly restricted to the analysis of nucleic acid and small molecules. Considering their limited applicability for the broader use of engineered nanomaterials, this class of nanopores is not further discussed here.

Solid-state nanopores have gained recent popularity in comparison with biological nanopores, due do their advantages in terms of stability, control of pore size, surface functionalization, and compatibility/integration with other techniques (microfluidic or optical techniques) (51). Subjected to the choice of material and fabrication approach, the geometry and architecture of solid-state nanopores vary from one another. To date, the most popular choices in terms of configuration is the use of planar thin membranes (SiN_x, SiO_2, graphene) (51). Nanofabrication approaches commonly applied for these nanopore, involve the use of focused electron/ion beam sculpting techniques and controlled dielectric breakdown (CDB) (51).The most applied method for creating pores with diameters in the low nanometre regime relies on electron/ion beam milling in a free-standing thin membrane (Figure 1.7A) (51). Adjustments of the beam spot size, duration, and position on the thin membrane allows for precise control of the pore size and shape (74). While this fabrication approach provides tuning the pore to very small dimensions, it involves the use of expensive instrumentation that requires experienced user and time-consuming process to yield a larger number of pores. Another emerging fabrication approach recently proposed is the use of CDB (Figure 1.7B) (75). To form a nanopore, the membrane is subjected to a strong electric field in an electrolyte solution which favours structural defects caused by the tunnelling leakage current occurring, resulting in a dielectric breakdown of the thin membrane (75). An attractive aspect in this case is the direct fabrication of nanopores in microfluidic devices, as this fabrication is done in solution using an electrolyte solution, which can greatly reduce the fabrication and assembly steps involved in the production process (76). However, in this process pore size are generally limited to a maximum of approximately 20 nm, due to the increased likelihood of multiple pore formations or pores with irregular shapes (77).

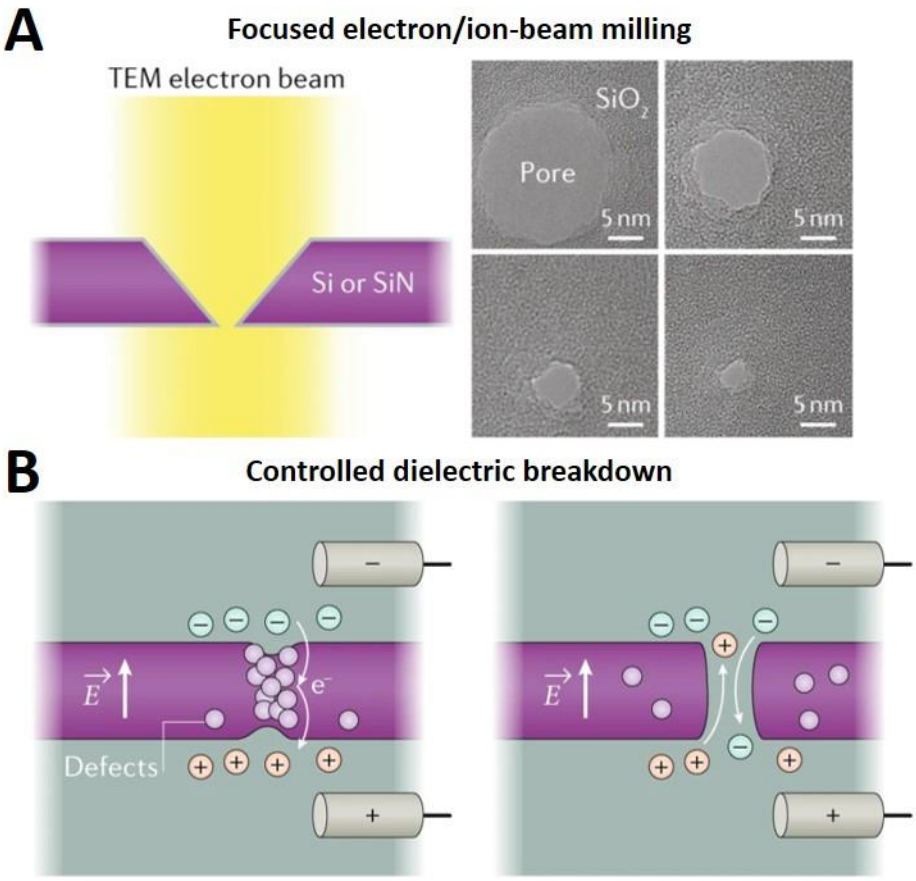

Figure 1.7: Schematic representation of thin membrane solid-state nanopore fabrication methods. **(A)** Focused electron/ion-beam milling displaying a sequence of TEM images showing nanopore formation in silicon dioxide membrane (right panel) using an electron beam (left panel). **(B)** Nanopore fabrication by means of controlled dielectric breakdown. The membrane is exposed to an electric field where structural defects are produced due to tunnelling leakage current, favouring the formation of nanopore through the membrane. Adapted from ref. (51).

Another fabrication approach yielding solid-state nanopores with conical geometry is the laser-assisted pulling of quartz capillaries (Figure 1.8) (78,79). This simple and fast approach for fabricating nanopores with tuneable pore sizes relies on the use of a benchtop laser-puller instrument. The fabrication processes involves heating of a glass or quartz capillary and applying a pulling force from each end of the capillary, resulting in two nanopipettes with similar pore sizes (78). The pore size tuning generally comes down to adjusting the heating and pulling parameters of the laser-puller and the dimensions of the capillary used (78). While this fabrication is somewhat limiting for fabrication of sub- 10 nm pore, it allows the user to easily tune the pore size in a wider range and obtain pores fabricated in cost-effective and rapid manner without multiple steps. Furthermore, the 3D geometry of the nanopipettes can prove advantageous in

different applications and integration in confined volumes or manipulation in the x, y, z dimensions (80).

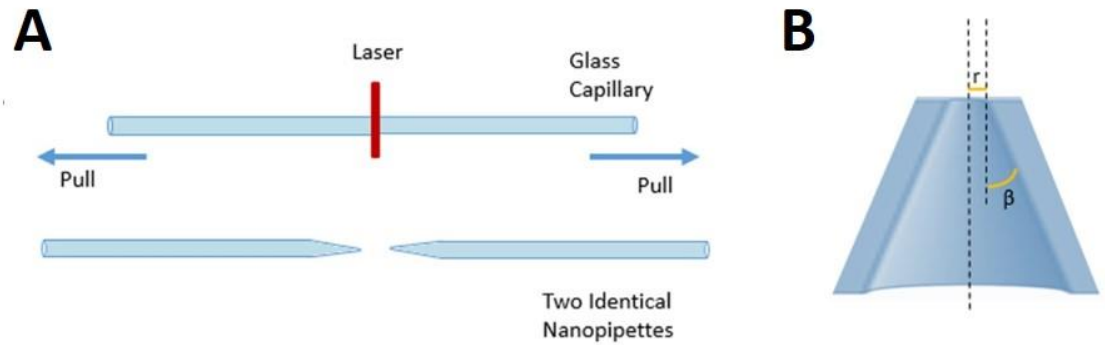

Figure 1.8: Laser-pulled nanopores. **(A)** Schematic representation of nanopore fabrication by means of laser-pulling a glass capillary. A capillary is mounted and subjected to heating by means of a laser, followed by a hard pull step from the two ends of the capillary, resulting in a pair of nanopipettes with similar pore size. **(B)** Representative geometry of the nanopipette, indicating the pore radius (r) and the cone half-angle (β). Adapted from ref. (81).

Lastly, a third recognised class of nanopores is represented by the so-called hybrid nanopores (Figure 1.9), combining the features of solid-state and biological nanopores. This nanopore configuration usually involves the combination of solid-state nanopores with larger orifice (SiN_x membrane or glass nanopipette), acting as support for docking a biological component with a constricted aperture, such as using protein pore (82) or DNA origami nanostructures (83).

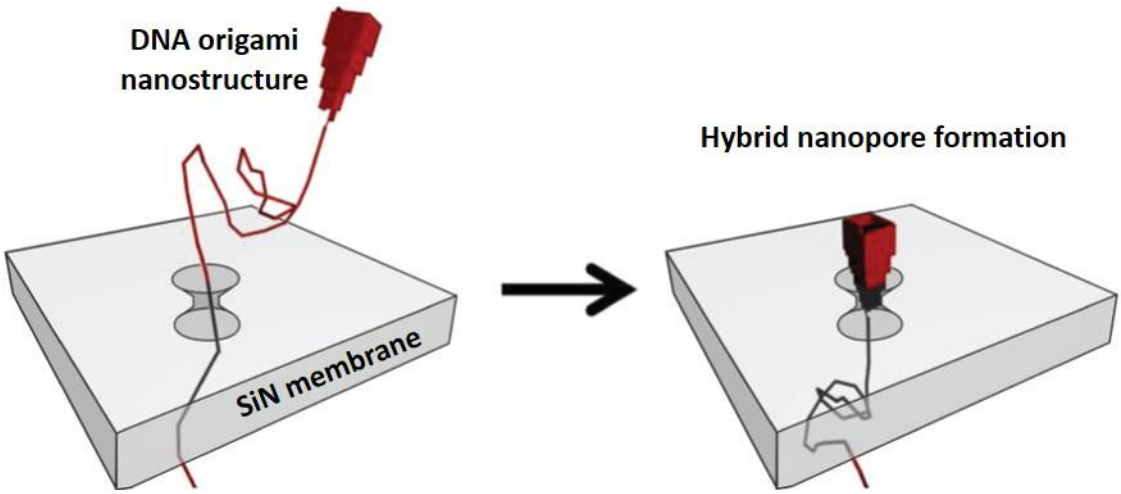

Figure 1.9: Example of hybrid nanopores**.** Schematic representation hybrid nanopore comprising of silicon nitride membrane and a 3D DNA origami nanostructure with a double-stranded overhang that is docked inside the orifice of the SiN_x larger pore. Adapted from ref. (83).

1.4.3. Properties and considerations in nanopore sensing

Nanopore sensing relies on the recorded current signal to provide information about the characteristics of the analytes investigated. Upon the application of an electrical bias across the pore, ions flow through the pore, altering the ionic current. This operating principle is similar to the traditional Coulter Counter technique (84). The nanoscale dimensions of the fabricated pore allows measurements at the single-molecule level (52). The ionic conductance of the nanopore can be described including the bulk conductivity (the electrolyte solution used), the counterions shielding the surface charge of the pore, and the pore geometry (85). Considering a negatively charged pore with a cylinder geometry, the pore conductance (G) can be expressed by Equation 1.1:

$$G = \frac{\pi}{4}\frac{4d^2}{L}\left((\mu_K + \mu_{Cl})n_{KCl}e + \mu_K\frac{4\sigma}{d_{pore}}\right)(Eq.\,1.1)$$

where d_{pore} is the diameter of the pore, L_{pore} represents the length of the pore, μ_{K} and μ_{Cl} are the electrophoretic mobilities of potassium and chloride ions, n_{KCl} is the concentration of potassium and chloride ions, e is the elementary charge, σ is the surface charge density in the nanopore (85).

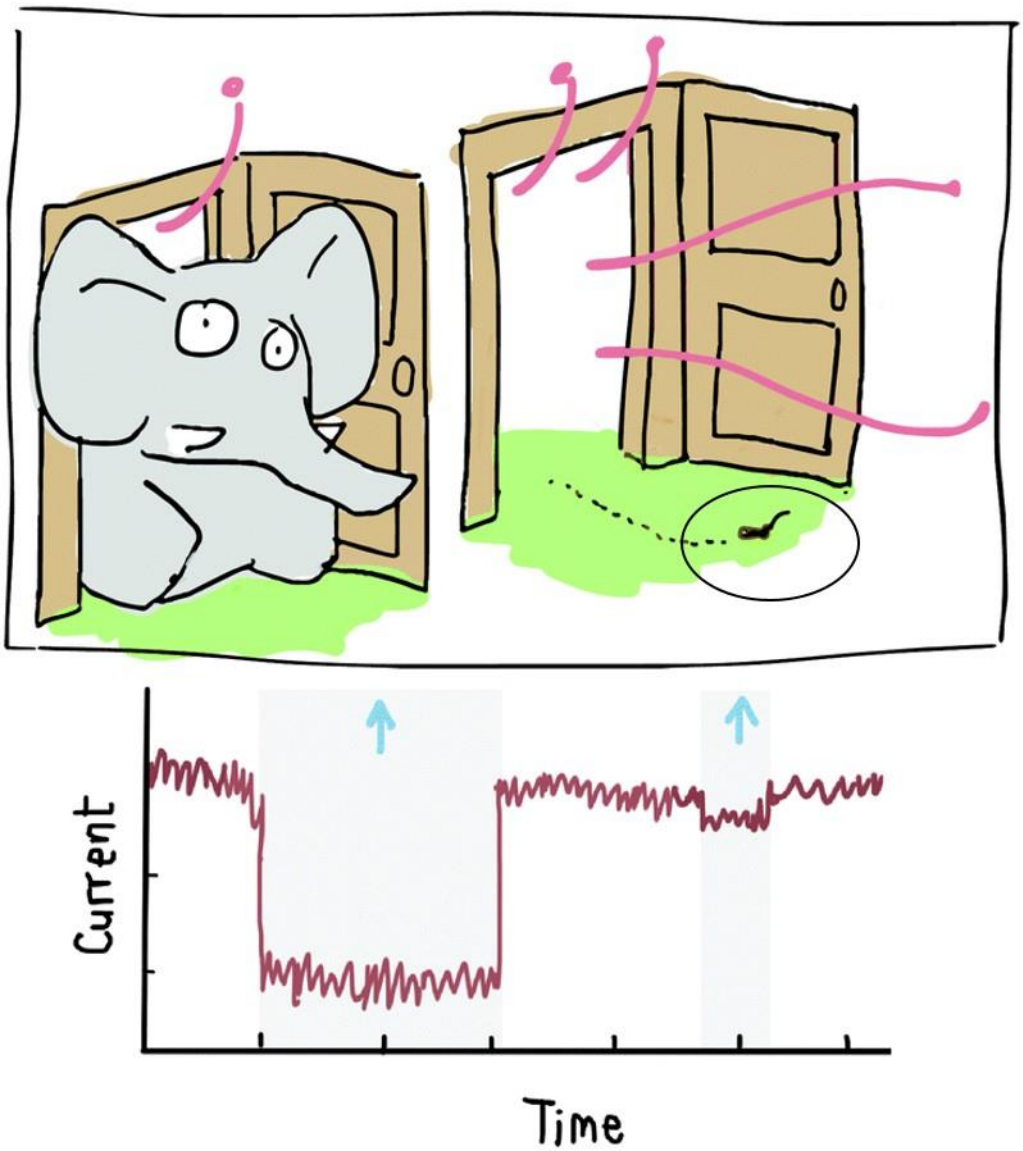

Figure 1.10: Ion current blockage. Schematic representation of ion current blockade in nanopore sensing, using the analogy of an elephant *versus* an ant moving through a door. Adapted from ref. (86).

In a typical nanopore setup, analytes are driven electrophoretically (or in some cases electroosmotically) through the narrow constriction of the pore that separates the two reservoirs filled with electrolyte solution. The translocation of an individual analyte causes a characteristics temporal change in the recorded ionic current. Translating this in terms of signal-to-noise ratio (SNR), a large change in the ionic current is ideal in resolving the translocation signal from the current baseline. When the pore size is close to the dimensions of the translocating analyte, a pronounced change in the ionic current is obtained. Opposite to this, if the pore is large relative to the dimensions of the analyte, the current will be little impacted by the translocating analyte. A good analogy for this

principle is displayed in Figure 1.10. Pushing an elephant through a door will greatly reduce the air flow through the door, whereas an ant moving through the door barely causes any change.

One important parameter in nanopore analysis is the amplitude of the peak current associated with a translocation event. The peak current amplitude is generally accepted to be related to the occupied volume of the analyte, physically hindering the ionic current flow in the sensing region of the pore, also referred as volume exclusion effect (87). This peak current amplitude is often defined as ΔI, with typical values in range of tens or hundreds of pA. This nanopore parameter has been the most utilized in assessing the size/geometry of various analyzed by nanopores. Recent studies have pointed deviations from the general resistive-pulse sensing (85,88). Depending and ionic strength of the electrolyte solution and the surface charge of the pore, the ΔI can observed as a resistive (current reducing, $\Delta I < 0$) pulse or conductive (current enhancement, $\Delta I > 0$) pulse during a translocation event, with conductive events reported in low ionic strength conditions (below 300 mM KCl) (85,88). Furthermore, it has been suggested that the current enhancement effect can also be rationalized by introducing highly charged analytes in low ionic strength electrolyte solution, which causes a temporary increase in the ion flux during the translocation through the pore (89).

Whilst electrophoretic force (EPF) is generally regarded as the dominant force in most of the nanopore experiments, the negatively charged surfaces of solid-state nanopores also generate an electroosmotic flow (EOF) (90), and ion current rectification (ICR) (91). Charged pore surfaces in contact with the electrolyte solution built up an electrical double layer (EDL) made up of counterions (92). Under an electric field, EOF arises due to the interaction between the electric field induced by the applied voltage and movement of ions within the EDL, generating a corresponding flow of the surrounding liquid (92). Depending on the charge of the analyte and the polarity of the nanopore wall, EOF acts on translocating analyte inside the nanopore, either complementing the EPF or pointing in the opposite direction (90). As for the ICR effect, this is described by an asymmetric ion distribution that results in non-linear current-voltage response, due to preferential current flow in the direction of one polarity, typically observed in pores with asymmetric geometry (i.e., conical pores) (91).

Another parameter frequently investigated in nanopore analysis is the duration of the translocation event (dwell time), reflecting the duration of time the analyte resides in the sensing region of the nanopore. Dwell time is defined as the time between the initial change in the ionic current and its recovery to the baseline. The dwell time distribution can be used to extract information regarding the charge, mobility, and shape, or interaction of the analyte with the pore (86). In several reports, an inverse relationship between the dwell time and the applied electrical bias has been experimentally demonstrated (93,94). Frequently, this is used as diagnostic for electrophoretically driven transport, recording translocation events at several applied voltages. Here, an important factor is also played by the length of the pore with longer pore lengths sustaining an increased interaction between the analyte and the pore. Tuning of the pore geometry and translocation conditions (applied voltage, ionic strength, *etc.*) are important factors that can affect the event duration and resolving the events within the temporal bandwidth of the instrument (86).

Another characteristic explored during the single-molecule nanopore analysis is the capture rate (event rate). This parameter refers to the rate at which translocation events are detected, usually defined as events per unit of time (e.*g.,* s^{-1} or min^{-1}). It has been previously suggested that during the translocation process the analyte in the solution follows two main stages: (a) transport from the bulk solution to the capture volume in the vicinity of the pore by Brownian motion; and (b) the analyte enters the capture volume near the aperture generated by the electric field, overcoming an entropic barrier (95). The particle flux (*J*) describes (Equation 1.2) the frequency at which the analyte enters the capture volume (hemispherical for a cylinder pore) (95):

$$J = \frac{\pi d^2 \mu}{4L} V_{bias}\, c \quad (Eq.1.2)$$

where V_{bias} represents the applied voltage and c is the concentration of the analyte in the bulk, L represents the length of the pore.

In order to perform statistical analysis, is important to record a larger number of translocation events. Recording a large data set involves long recording times, which is consequently dependent on the analyte capture rate. While measurements in considerably more concentrated samples can lead to a high capture rate and the recording of many events in a short amount of time, a fine tuning is required. High

analyte concentration can cause crowding and clogging of the nanopore sensing region. On the other side, very low concentration translates in long recording times to gather sufficient number of translocation events.

As highlighted in this section, recording translocation events with high SNR and high capture rate within the temporal bandwidth of the instrument require tuning/modification of the nanopore and the translocation conditions, such as ionic strength, applied voltage, concentration where possible. Different strategies to obtain enhanced detection with solid-state nanopore systems are described in the following subsection with an emphasis on sensitivity, selectivity, and measurement throughput.

1.4.4. Strategies for enhanced detection with solid-state nanopores

There are several aspects of nanopore analysis that can expand its applicability in the context of detection at the single-particle level, including: sensitivity, selectivity, multiplexing, stability, and throughput. In the recent years, several nanopore strategies have been proposed that overall contributed to the enhanced performance of solid-state nanopores for various applications.

Chemical surface modifications

Surface coatings of solid-state nanopore can bring numerous practical advantages for performing long and stable nanopore recordings with reduced non-specific interactions and/or clogging that can hinder the translocation of large number of molecules, a particular challenge acknowledged in the case of protein analysis (96). One practical approach reported in this case, is the use of nanopores coated with surfactants. Hu *et al.* reported the use of Tween 20 coating for preventing adsorption of proteins to silicon nitride pores (97). Another effective chemical modification was described by Yusko *et al.* where silicon nitride nanopores underwent a lipid-bilayer coating (Figure 1.11A) by exposure to a solution of small unilamellar liposomes (98). This approach enabled them to control the size of the nanopore (reducing the pore diameter) and slowing down the translocation of the targeted proteins and obtain single-molecule measurement of amyloid beta oligomers and fibrils. Furthermore, the lipid bilayer was further tuned by incorporating lipid-anchored ligand or receptor molecule for selective capture of proteins. Apart from this, a more recent strategy for boosting the sensitive discrimination of proteins was proposed by Schmid *et al.*, where a nanopore electroosmotic trap (NEOtrap) was formed by immobilizing a spherical DNA origami

nanostructure onto a passivated silicon nitride pore (Figure 1.11B) (99). Here, the DNA origami nanostructure seals off the pore, stimulating the electroosmotic trapping of nanoparticles irrespective of charge and sustaining long-duration measurements (several hours). By reversing the applied voltage, a different protein can be trapped and measured in the nanocavity.

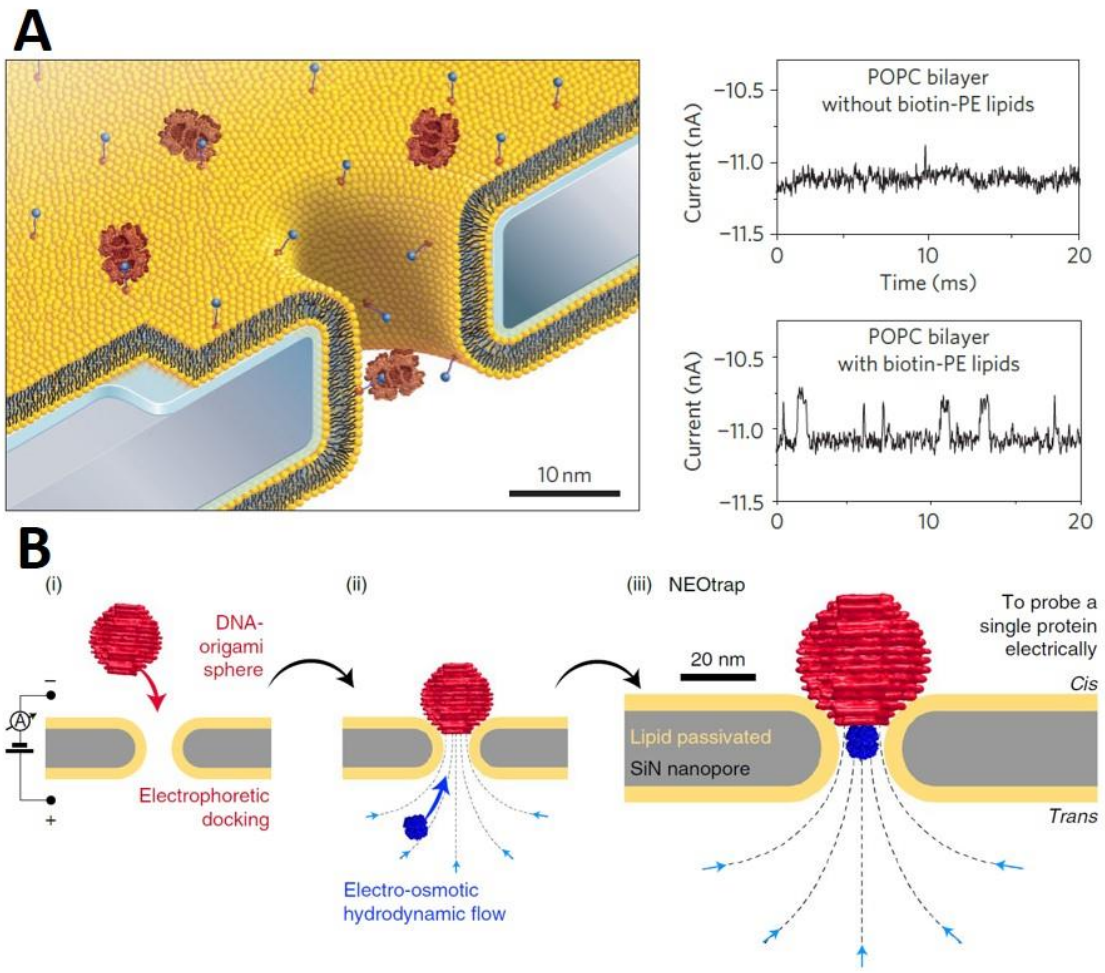

Figure 1.11: Example of functionalized solid-state nanopores. **(A)** Schematic of lipid coated (yellow layer) solid-state nanopore with streptavidin proteins (red) bound to lipid-anchored biotin-PE ligands (blue). Representative ionic current traces denoting the enhanced detection and selective capture of the protein in the presence of the biotinylated lipids coated on the nanopore. Adapted with permission from ref. (98). **(B)** Schematic displaying the steps involved in the formation of NEOtrap: (i) electrophoretic docking of spherical DNA origami nanostructure onto the passivated silicon nitride nanopore; the induced hydrodynamic flow (ii) favour the trapping of proteins in the nanopore by means of electroosmosis (ii). Adapted from ref. (99).

Multi-pore configurations

The development of multi-pore configuration is as viable strategy to increase the throughput of nanopore-based sensors, by recording one sample or additional samples in parallel. Capitalizing on the new developments in nanofabrication, arrayed nanopore configuration can be designed. Wen *et al.* proposed in their work a 30-100 nanopores array in a suspended silicon nitride membrane which was used for the detection of nanoparticles (Figure 1.12A) (65). While these high-end fabrication approaches are attractive in terms of precision, they pose challenges for large-scale production. An alternative strategy with potential for high yield and simple fabrication is the use of nanoimprint lithography with a Si microneedle stamp, as demonstrated by Choi *et al.* (100). Here, sub-10 nm nanopores were fabricated in a freestanding polymer membrane in a single-step process. A different strategy in increasing the high-throughput in nanopore measurement relies on the multibarreled glass nanopipettes that can be independently controlled (Figure 1.12B) (101,102), allowing for simultaneous detection, as well as trapping and dynamic manipulation, of individual molecules.

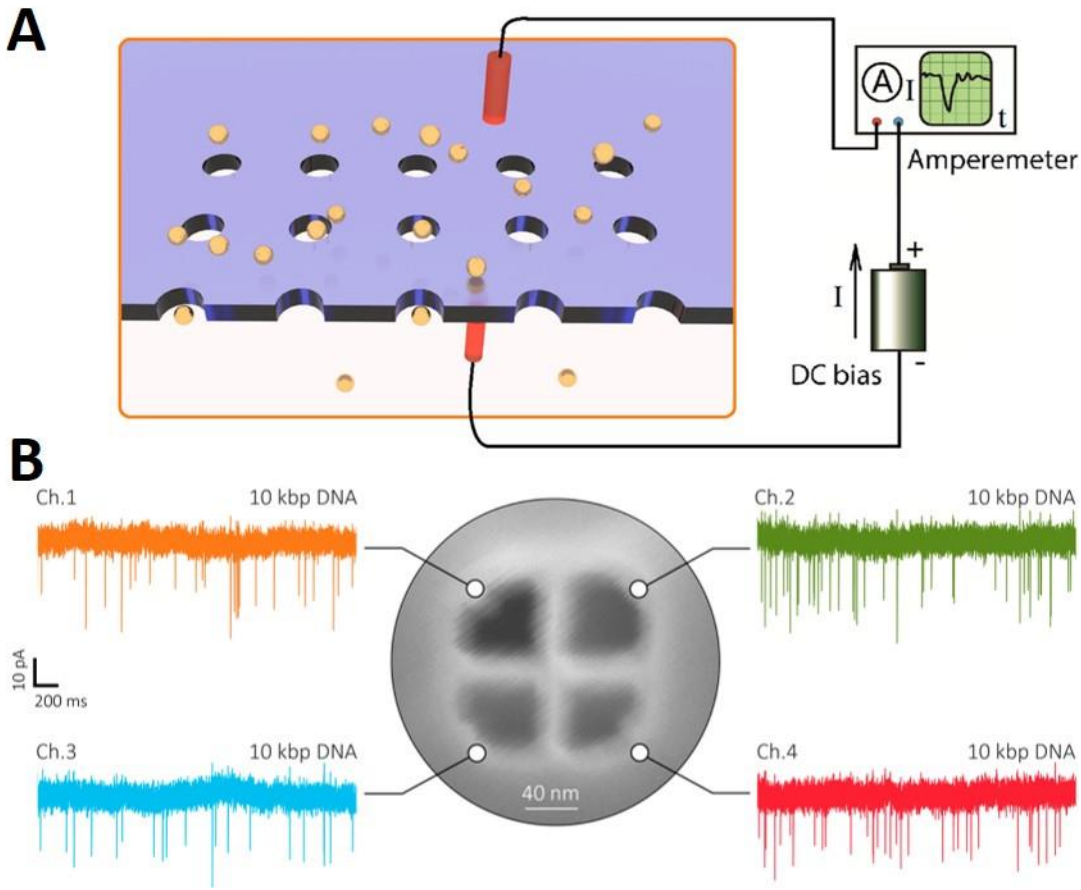

Figure 1.12: Example of multi-pore configurations. **(A)** Schematic of solid-state nanopore array setup for addressing the translocation of nanoparticles through multiple nanopores. Adapted with permission from ref. (103). **(B)** SEM image of quad-barrel nanopipete depicting ionic current traces from each barrel used for the translocation of 10 kbp DNA molecules from inside the barrel into the bath. Adapted from ref. (102).

Molecular probes

To address shortcomings in the detection of small molecules with solid-state nanopores that are either present in low concentrations or require very small pore diameters, the use of molecular probes has been proposed. This detection approach can sustain sensitive and selective detection without the need of amplification or additional sample preparation. Edel and co-workers proposed a highly sensitive and selective strategy for binding biological targets using gold nanoparticles molecular probes (104). Their approach consisted of functionalized gold nanoparticles with either dsDNA or antibodies that allow the binding of clinically relevant biomarkers (procalcitonin and short microRNA sequences), forming dimer nanoparticle complexes upon the binding. Rather than directly observing the molecule of interest, the detection was carried out indirectly by measuring the translocation of the dimeric nanoparticles with the captured target.

The sensing strategy relied on differentiating the monomer (one peak signature) and dimeric state (double-peak signature) recorded with the nanopore platform, as shown in Figure 1.13A. The same group have also proposed the use of supercharged unstructured polypeptides (SUPs) as molecular carriers for nanopore detection of proteins. The SUPs molecular probes favored the differentiation of individual proteins with different sizes and shapes by slowing down their translocation as a result of the electrostatic interactions of the molecular probe with the surface of the nanopore. The protein discrimination was based on the identification of subpeaks features, characteristic of the individual proteins bound (105).

DNA-based molecular probes that facilitate multiplexed detection by means of solid-state nanopores have been reported by Keyser and co-workers (106,107). A recent example is the use of DNA dumbbell nanoswitches for multiplexed nucleic acid detection and bacterial identification, with simultaneous detection using barcoded carriers (106). As shown in Figure 1.13B, a DNA carrier combined with multiple dumbbell switches that undergo a topology change from open to close upon hybridization of target strands. In terms of the nanopore readout this translated in observing a nanopore current signal transition from two small peaks signal in open state to a large single peak signal in the close state.

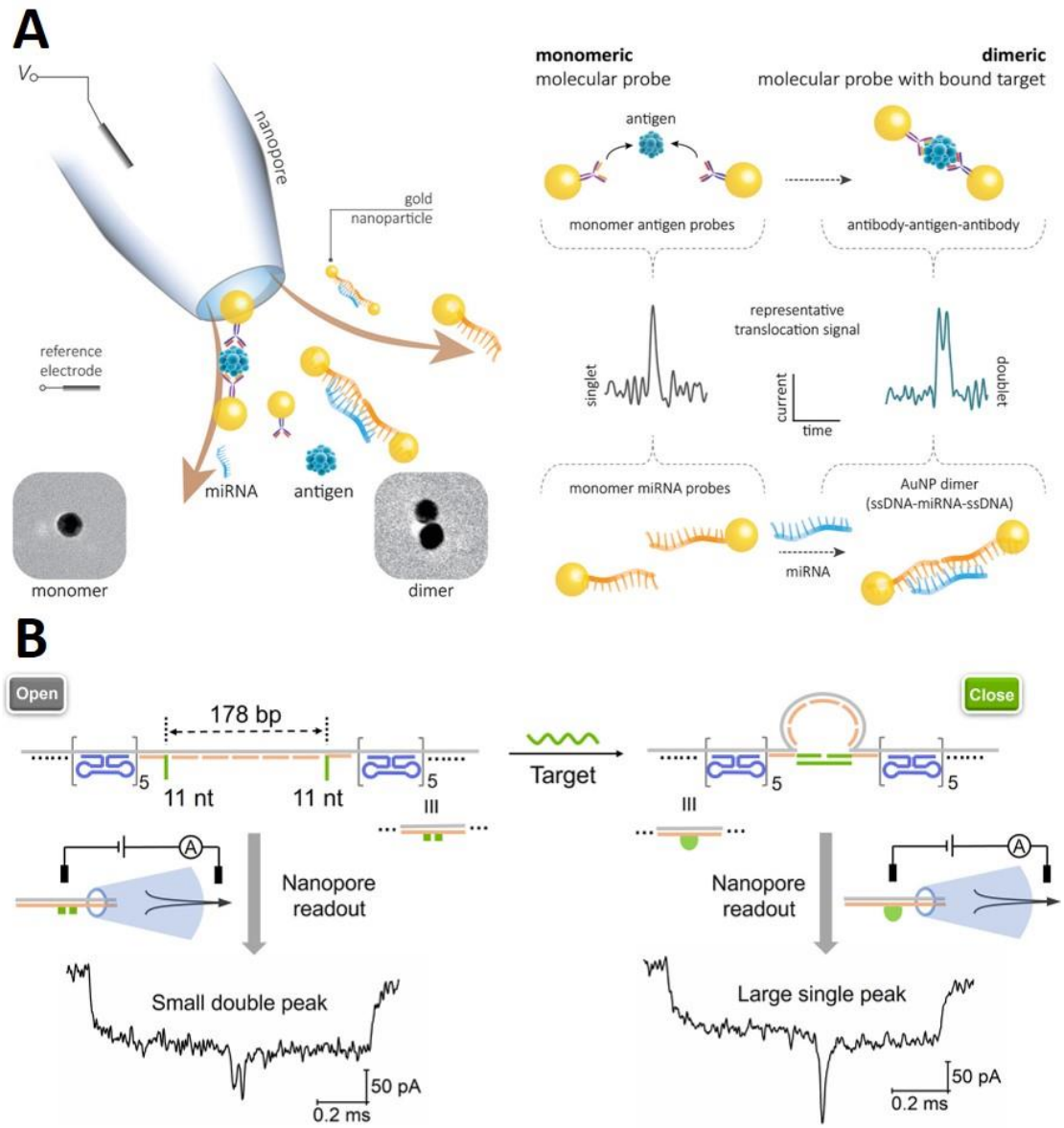

Figure 1.13: Example of nanopore sensing utilizing molecular probes. **(A)** Schematic showing the concept of the dimer-forming gold nanoparticle probes. Upon the capture of the biomarker of interest by the functionalized nanoparticles, a nanopore readout discrimination based on the presence of singlet or duplet translocation signal can be observed for the monomeric and dimeric state. Adapted with permission from ref. (108). **(B)** Schematic DNA carrier with probes (green) and two groups of dumbbells (blue) that undergo a topological change from open state to close state upon the hybridization of a DNA target strand. The characteristic nanopore readout changes from a small double peak current signal when is the open state to a large single peak signal when is switched to the close position. Adapted from ref. (106).

Polymer electrolyte nanopore

Another strategy for obtaining enhanced detection of analytes with solid-state nanopores reported by our group relies on the utilization of a polymer electrolyte external solution to enhance the translocation signal of analytes (57). This strategy

brings the advantage of a very simplistic and easy-to-implement approach where the polyethylene glycol (PEG) molecular agent is added to the electrolyte solution where the nanopore (in this case nanopipette) is immersed. Previous work on the use of such polymer electrolyte nanopore systems has shown a dramatic increase in the current signals recorded (57,109). Importantly, this nanopore adaptation does not require any intermediate steps and is compatible with a range of electrolyte solutions and ionic strengths, supporting the sensing of multiple biomolecules and nanoparticles. As reported in a mechanistic study on the use of such platform for the enhanced detection of DNA molecules, PEG is assumed to bind the cations (K^+) present in the external bath and therefore cause an imbalance in the mobility of the ions which results in ion depletion in the region of the pore (110). Thanks to this PEG-induced effect, the translocation of different charged biomolecules resulted in obtaining high-amplitude conductive peaks, maximizing the SNR of nanopore readout with the same pore (57,109). Figure 1.14 illustrates the effect of the polymer electrolyte external bath in driving the enhancement of the translocation signal, compared with the no-PEG conditions. Moreover, it has been suggested that polymer electrolyte interface also plays a role in contributing to the conductive signal enhancement, introducing additional ions in the pore region when an analyte is translocating through (110).

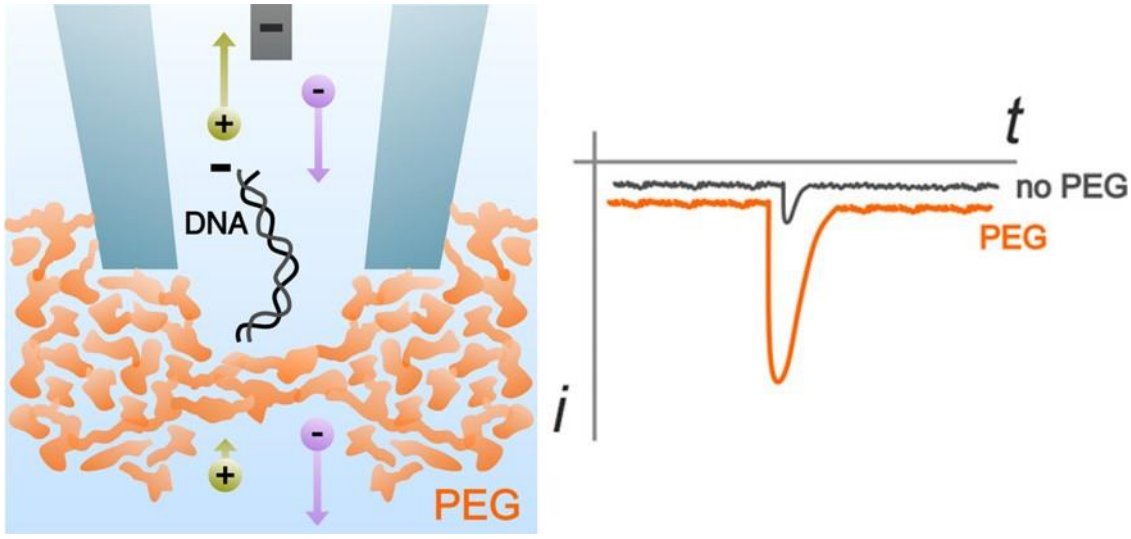

Figure 1.14: Polymer electrolyte nanopore. **(A)** Schematic and representative translocation signals obtained for dsDNA translocating from inside the nanopipette into the external electrolyte solution with and without the addition of PEG. Adapted from ref. (110).

1.4.5. Applications and challenges in nanopore analysis of nanomaterials

The ability to detect particles on individual basis with nanoscale tailored pores brings many advantages in characterizing new emerging functional nanomaterials in a rapid and label-free manner. As described above, different nanopore sensing modalities and strategies for increasing ionic current SNR and temporal resolution for various molecules makes this technique a potential toolbox that can complement the existing techniques commonly applied in the characterization of the nanomaterials. Nanopore parameters such as peak current amplitude and dwell time can contribute to the characterization of individual analytes and correlate these with important characteristics of engineered nanomaterials (*i.e.*, size, shape, charge). The ability to record larger numbers of events associated to the translocation of unlabeled individual particles in solution, yields distributions of the nanopore current parameters and can be further used for statistical and quantitative analysis.

Whereas nanopore sensing has been expanded to a wide range of molecules or in some cases used as a biosensor platform, particularly DNA-based and protein-based molecular structures, little research has been carried out on nanopore analysis of heterogeneous mixtures. Often synthesized mixtures, whether they are DNA-based nanostructures, colloidal suspensions, or hybrid nanomaterials, are known to have a heterogenous character. This could translate in nanoscale variations related to their size, shape, confirmation, or charge. Such aspects of newly engineered nanomaterials challenge the wider use of nanopores for their comprehensive characterization. Particular limitations are posed by the requirement to tune the pore size to the dimensions of the analyte investigated in order to maximize the readout signal. Secondly, the requirement of using high ionic strength electrolyte solution can hinder the investigation of nanomaterials that are less stable, particularly in the cases of synthesized colloidal suspensions. Lastly, improving the stability during nanopore recordings can prove beneficial in the analysis of low concentration samples that are limited by the nature of the synthesis process or have an intrinsic low yield. The configuration of the nanopores comes with a great benefit of accommodating volumes down to few microliters. Nevertheless, it is desired to yield a large number of events in the case of low concentration samples, which comes at the cost of long recordings and therefore the stability aspect is key in such measurement.

Taking into account these practical considerations, the potential of nanopore-based characterization of a large spectrum of engineered nanomaterials with real-life applications can be explored.

1.5. Thesis aim and objectives

The overall aims of the research project were to explore the analysis of engineered functional nanomaterials by means of solid-state nanopores. Nanopore measurements stand as a toolbox with an untapped potential in the label-free and rapid detection and characterization of a variety of nanomaterials. The experiments described here aimed at providing a comprehensive analysis of different functional nanomaterials and explore their heterogenous (size, shape, assembly yield) character with the use polymer electrolyte nanopore-based system at the single-entity level. In this regard, a first focus was on the analysis of DNA supramolecular assemblies and devising a methodology for fingerprinting their assembly state, as well as developing quantitative analysis of their yields in the folding mixtures. Secondly, the PhD project aimed to expand the applicability of the nanopore-based systems and adapt the translocation conditions in order to probe the analysis of relevant hard and soft, uniform and anisotropic nanoparticle mixtures with a high-degree of discrimination based on their nanoscale variations.

Chapter 1 discusses the overall background in the context of the research described in this thesis. A broad overview of the different classes of emerging nanomaterials is given and the importance in elucidating their physicochemical properties. Then, characterization methods for discriminating nanoscale variations are described, putting an emphasis on the potential of use of solid-state nanopores as toolbox for characterizing such nanomaterials. A major focus is put on the concept of nanopore analysis, configurations, and recent strategies that support enhanced detection of various analytes. Challenges of nanopore analysis in the context of engineered nanomaterials are also detailed. Lastly, the aims of thesis are described, followed by a brief overview of the content of each chapter of the thesis. Content from this chapter is published in a recent review in Analytical Chemistry Journal as shared first author (111).

Chapter 2 details the materials and methods used to conduct the experiments described in the thesis. A major focus is put on describing the setup and translocation conditions utilized in the nanopore-based measurements, as well as the fabrication and characterization of the solid-state nanopores.

Chapter 3 describes the detection of supramolecular DNA nanostructures with different assembly degree. A rapid and label-free approach is proposed for fingerprinting higher-order assemblies of DNA origami nanostructures with single-entity resolution, enabled by nanopore recordings. A comparison with the gold standard methods for characterization of DNA folded mixtures (AFM and gel electrophoresis) is given in the context of yield quantification of each folded DNA nanostructure. Work from this chapter is published in Biophysical Journal (60).

Chapter 4 explores the use of a polymer electrolyte nanopore-based approach for the analysis of different classes of functional nanoparticles with distinct chemical composition, capping agents and physical properties. A strong focus is put on tackling the analysis of heterogenous mixtures and discriminating soft nanoparticles based on their functionalization layers. Work from this chapter is published in BioRxiv (112) and submitted to for journal publication.

Chapter 5 summarizes the main conclusions of the thesis and discusses future research directions.

Chapter 2: Materials and methods

2.1. Overview

In this chapter, an overview of the materials and methods used to conduct the research described in this PhD thesis is given. First, a detailed explanation of the nanopipette fabrication and characterization is given. Next, a description of the nanopipette measurement setup is provided, together with the data analysis methods applied in this research. Lastly, an overview of the sample preparation applied throughout the different nanopipette experiments is described. In addition to this general description, each results chapter consists of its own materials and methods section describing in detail the experimental conditions used, ranging from sample preparation to measurement conditions.

2.2. Nanopipette fabrication

The fabrication of nanopipettes starts from a quartz capillary pulled into a pair of sharp nanopipette tips by means of a benchtop laser-puller (Sutter Instruments P2000)(113), as depicted Figure 2.1. One aspect of paramount importance is the nanopore size of the tip of the nanopipette to maximise the signal-to-noise ratio for the detection of various analytes. This requires tailoring of the pore size to closely match that of the analyte under investigation. The fabrication started with a quartz capillary (*i.e.* 1.0 mm outer diameter x 0.5 mm inner diameter) that was pulled into a needle-shape nanopipette by means of CO_2 laser-based puller. In short, a focused laser beam melts the quartz capillary, followed by pulling forces from opposite sides of the capillary, resulting in a

pair of two nanopipettes with nominally the same pore size (Figure 2.1A). Several parameters of the laser-pulling process require optimization to obtain reproducible pore sizes. Each laser-puller is different and dependent on the environmental conditions (*i.e.* room temperature, humidity) where it is operated. There are five parameters that needs to be adjusted in order to achieve the desired pore size: HEAT, FILAMENT, VELOCITY, DELAY, and PULL. From these parameters, the greatest influence is provided by the HEAT and PULL parameters. For instance, applying increased HEAT and PULL values leads to smaller pores, and vice-versa. Table 2.1 displays an example of optimized pulling program for pulling nanopipettes in the 100 nm regime using quartz capillaries. In order to maintain a reproducible response of the laser-pulling process, a two-line program was applied. The first line program mainly defines the shape and length of the nanopipette's taper. Whereas the second line program defines the size of the pore at the tip of the nanopipette.

Table 2.1: Example of optimized parameters for laser-pulling nanopipettes.

HEAT	FIL	VEL	DEL	PULL
750	4	30	150	80
650	3	40	135	150

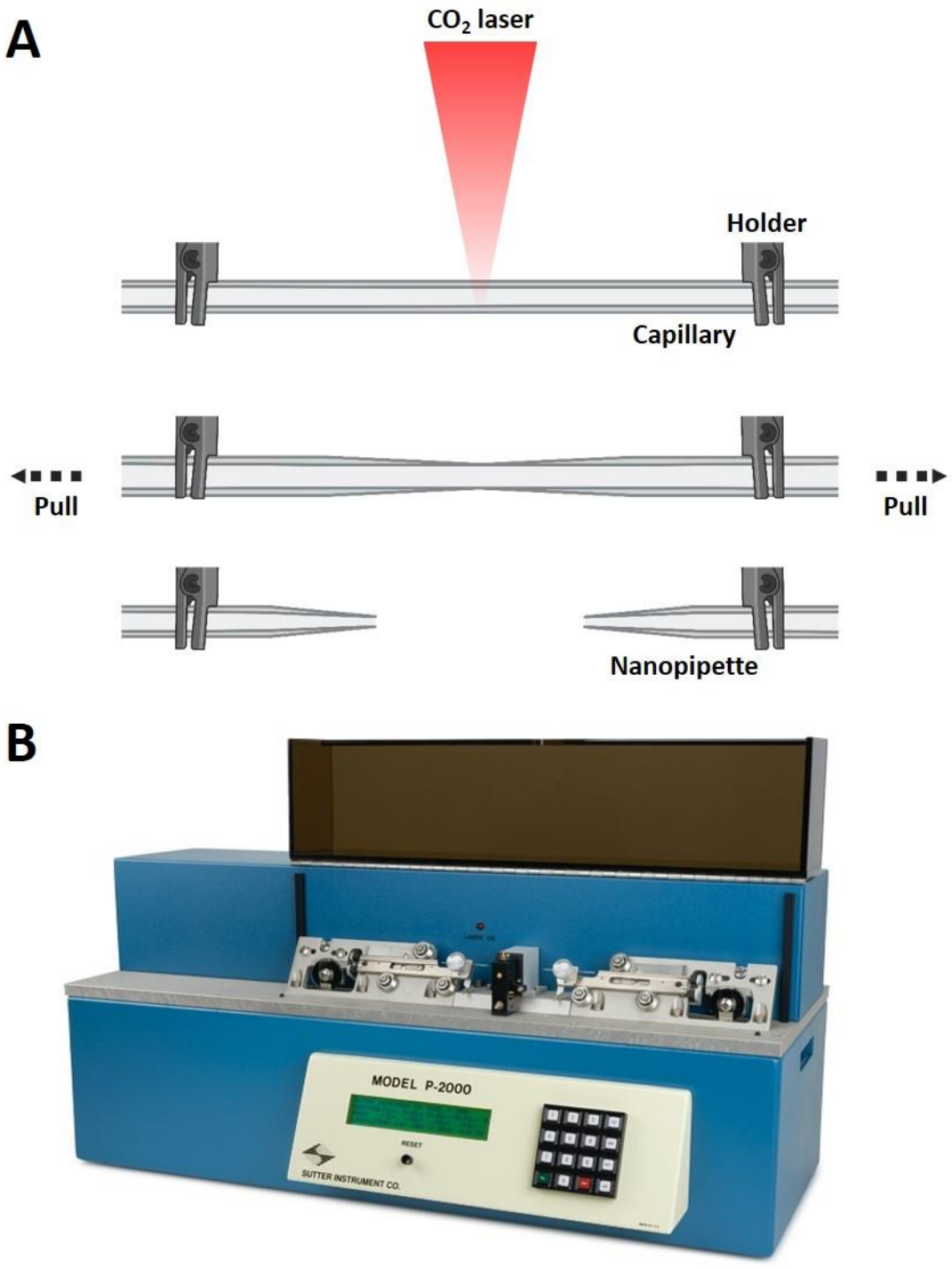

Figure 2.1: Laser-pulling process. **(A)** Schematic representation of the laser-pulling process, where a quartz capillary is subjected to laser-heating using a CO_2 laser, followed by a hard-pull step to produce a pair of nanopipettes with similar pore size. **(B)** Picture of P-2000 (Sutter Instruments) benchtop laser-puller (113).

To further facilitate the fabrication of nanopipettes with different pore sizes, the choice of the starting capillary diameter can be adjusted. Two examples of capillaries utilized in this research are shown in the Table 2.2. For pore size ranges above 100 nm, quartz

capillaries with diameter dimensions of 1.2 mm outer diameter x 0.9 mm inner diameter were used. Alternatively, for pore sizes bellow 100 nm, quartz capillaries with dimensions of 1.0 mm outer diameter x 0.5 mm inner diameter were used. Apart from the capillary diameter, the thickness of the glass (outer diameter – inner diameter) plays a role in the pore size tuning.

Table 2.2: Example of quartz capillary dimensions used for nanopipette fabrication

Capillary	Outer diameter (mmm)	Inner diameter (mm)	Barrel
Quartz	1.0	0.5	Single
Quartz	1.2	0.9	Single

2.3. Nanopipete characterization

Once a consistent laser-pulling program was optimized, the resulting nanopipettes need to be characterized to assess the nanopore diameter. In this research, two approaches for characterizing nanopipettes were used: direct morphological characterization utilizing Scanning Electron Microscopy (SEM) and indirect pore size estimation based on electrical resistance measurements. Figure 2.2 shows representative SEM images of a nanopipette fabricated by laser-pulling. Such a morphological characterization technique can allow both pore size and taper length estimation of the nanopipette. SEM is common technique applied for the morphological characterization of nanopipettes with pore sizes in the nanometre regime (78), whereas Transmission Electron Microscopy (TEM) can be employed to inspect in fine detail various geometrical aspects of the tip region, such as: taper length, cone-angle, wall thickness of the pore (114). Even though SEM is a commonly used method for pore size estimation of nanopipettes, it is a time-consuming process, and it is limited by the electron beam exposure. Due to the charging effect of the quartz capillary, SEM imaging of nanopipettes with relatively small pore sizes (< 50 nm) can prove challenging. An alternative solution is coating the nanopipette tip with a thin layer of a conductive material, such as sputtering gold or iridium.

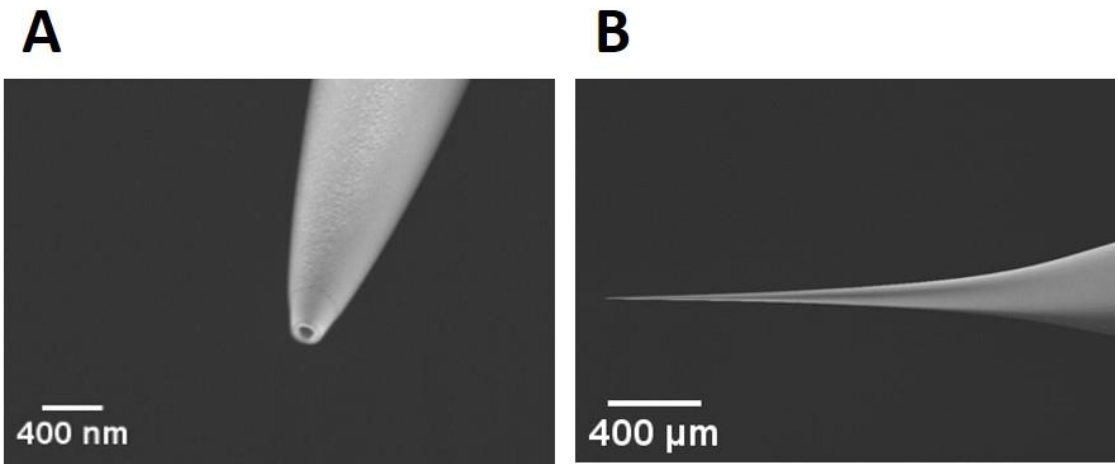

Figure 2.2: SEM characterization of laser-pulled nanopipetttes with a pore size diameter of approximately 60 nm. **(A)** SEM micrograph of the nanopipette pore size. **(B)** SEM micrograph of the nanopipette taper.

A second approach implemented for the pore size estimation of laser-pulled nanopipettes is the electrical resistance determination from the current trace obtained using Ohm's law. Generally, a linear response is expected for the IV curve recorded over a range of voltages using a patch-clamp amplifier. In Figure 2.3, a characteristic IV curve recorded between +500 mV and – 500 mV in 100 mM KCl is shown for a pore size diameter of approximately 60 nm. However, it is worth mentioning that the conductance can be influenced by several parameters, such as the electrolyte concentration and wall surface charge which can induce an ion current rectification effect. As opposed to the morphological characterization, this electrical approach is simple and favours a quick estimate of the pore size and check that the nanopipette is stable for measurements and the tip is not blocked/damaged.

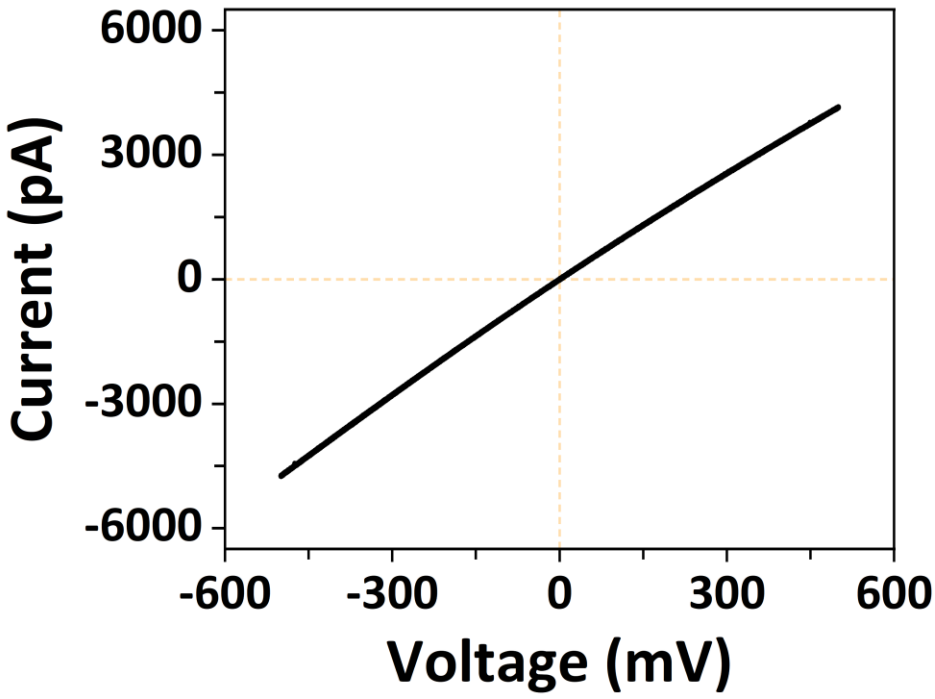

Figure 2.3: Representative current-voltage (IV) curve of laser-pulled nanopipette with a nominal pore size diameter of approximately 60 nm. A pore resistance of 85 ± 10 MΩ was measured (N=7 nanopipettes from different pulls)., corresponding to a pore diameter size variation of less than ~5 nm.

2.4. Electrochemical setup

The nanopore setup utilized for translocation experiments is described in Figure 2.4. The translocation experiments were carried out by filling the nanopipette with the translocation buffer containing the analyte of interest. An Ag/AgCl wire was inserted in the nanopipette barrel and acted as the working electrode, while a second Ag/AgCl wire was immersed in the bath and acted as the counter and reference electrodes. The analyte is driven from inside the nanopipette into the outer bath upon the application of a potential bias. The electrodes are connected to a MultiClamp 700B patch-clamp amplifier (Molecular Devices) and DigiData 1550B digitizer (Molecular Devices) to record the ionic current.

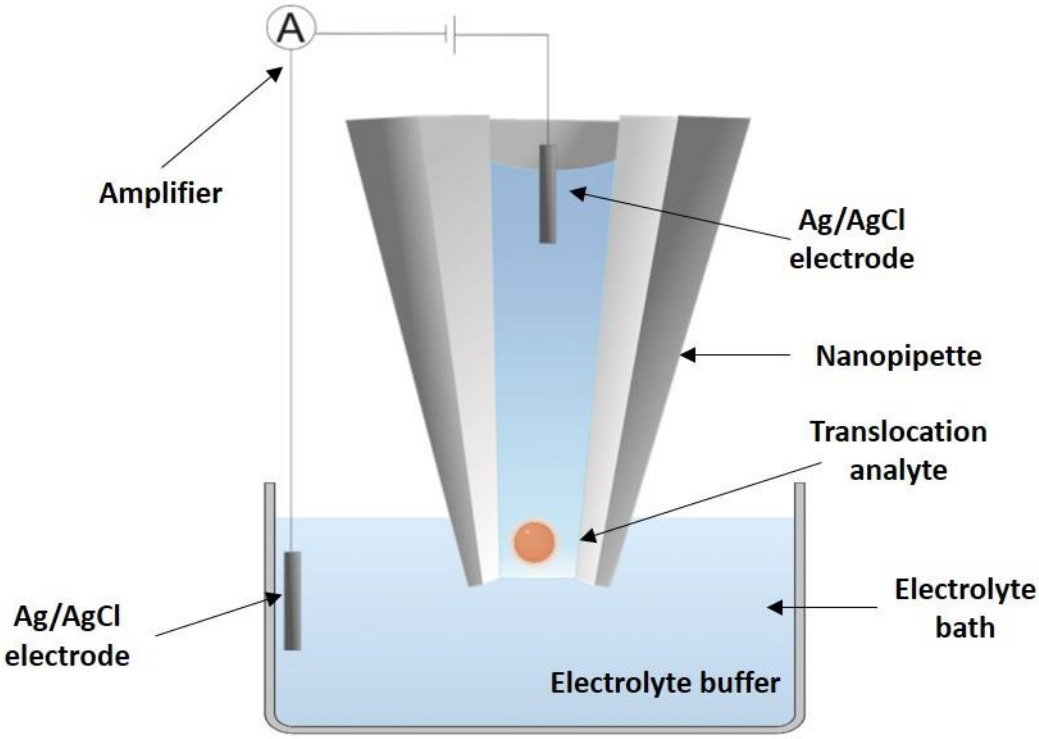

Figure 2.4: Schematic representation of the general setup utilized for the nanopore translocation measurements. The analyte of interest is added inside to the nanopipette and a pair of Ag/AgCl electrodes are placed in the barrel and outside in the electrolyte bath. Upon the application of potential bias, the analyte can be driven from inside the nanopipette into the outer bath.

Figure 2.5 displays the corresponding ionic current traces recorded in the absence of an analyte (Figure 2.5A) and when nanoparticles are translocated from inside the nanopipette into the outer bath (Figure 2.5B). The translocation events result in perturbations of the ionic current baseline, where each current spike is associated with the translocation of one analyte.

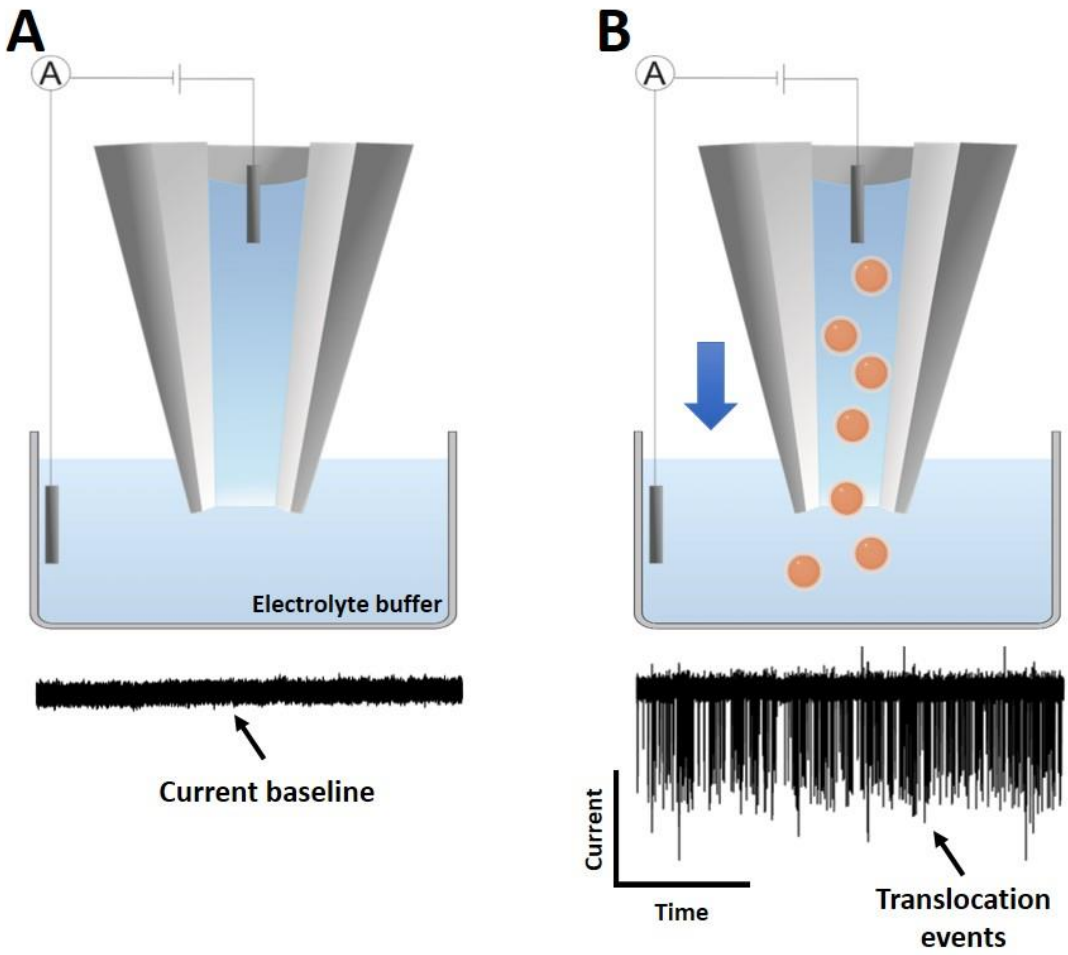

Figure 2.5: Ionic current measurement nanopipettes. **(A)** Ionic current trace recorded when no analyte was added to the nanopipette. The ionic current through the nanopore is carried by anions and cations in the electrolyte buffer. **(B)** Representative ionic current trace showing translocation events upon the translocation of nanoparticles from inside the pipette into the outer bath.

2.4.1. Electrolyte solution

The translocation buffers used in the nanopore measurements were 100 mM KCl or 50 mM KCl (unless stated otherwise) prepared in Tris-EDTA (10 mM Tris, 1mM EDTA, pH 8.0). A pH of 8.0 was chosen to maximize the negative charge of the molecules translocated in these buffer conditions. The solutions were prepared using ultrapure water and the solutions were further filtered using 0.1 µm filter (Milipore) to remove any potential contaminants. A similar electrolyte solution was used inside the nanopipette and in the outer bath. A particular difference was the addition of Poly-ethylene glycol agent (PEG 35k) to the outer bath, as described in each specific section.

2.5. Electrodes preparation

Non-polarizable Ag/AgCl electrodes were used in the electrochemical setup for the nanopore measurements. The choice of utilizing Ag/AgCl electrodes stems from fast charge transfer properties from the electrode to the solution and their ease of fabrication. Together with the electrolyte solution, the Ag/AgCl electrodes drive the transport of ions across the nanopore. By applying a constant voltage, a potential difference takes places between the electrodes. Equations 2.1. and 2.2 depict the redox reactions taking place, stimulating the flow of cations (K^+) and anions (Cl^-) in opposite directions. KCl is a suitable choice of electrolyte due to the similar diffusion coefficients of the K^+ and Cl^- ions (115). Redox reaction taking place at the electrodes used in nanopore measurements. The AgCl is being reduced which leads to the formation of Cl^- (cathode). Whereas, Ag is being oxidized to form AgCl (anode).

$$AgCl_{(s)} + e^- \rightarrow Ag_{(s)} + Cl^- \textit{ (Eq. 2.1)}$$

$$Ag_{(s)} + Cl^- \rightarrow AgCl_{(s)} + e^- \textit{ (Eq. 2.2)}$$

The Ag/AgCl electrodes were freshly prepared before each nanopore measurement by chlorination of 0.25 mm silver wire (Goodfellow Cambridge Ltd). Following this, the electrodes were rinsed and sonicated in MiliQ water at room temperature.

2.5.1. Faraday Cage

For all experiments the nanopore setup was placed inside a Faraday cage to reduce noise and thus to enable the detection and analysis of low current levels (pA). To further minimise potential vibrational interferences, the Faraday cage was placed on a custom-made anti-vibration platform, as shown in Figure 2.6.

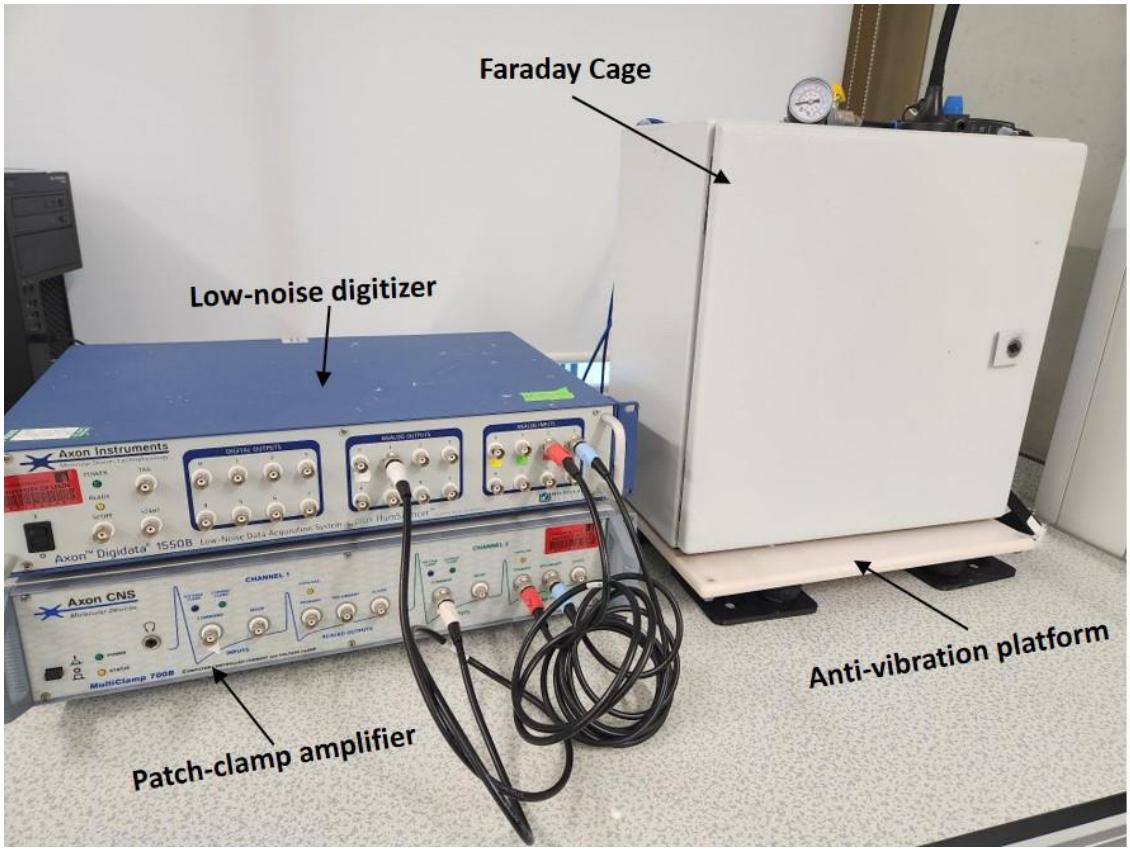

Figure 2.6: Image of the nanopore setup. A patch-clamp amplifier is used to apply a voltage and measure ionic current in a two-electrode configuration through a single nanopore which is integrated inside a Faraday cage to minimize interferences and external noise. A low-noise digitizer is used to convert the analog signals into discrete digital data that can be visualized, processed, and analyzed.

2.5.2. Nanapore data acquisition and analysis

Analysis of the current traces recorded with the nanopore setup was carried out using the Transalyzer MATLAB script, developed by Plesa *et al.* (116). A general workflow scheme of the data process is described in Figure 2.7. The data analysis starts with the recorded current trace in raw format (abf). In the first step, the local baseline and rms noise level (σ) is determined. In order to extract events, a thresholding algorithm is applied to extract the translocation events. Here, the events are identified if they are above the threshold limit set (Figure 2.8), which is defined by the multiplication of the rms noise level (σ) with a set a peak detection factor. The peak detection factor is selected in such a way that the largest number of events is selected, whilst minimizing the detection of noise spikes from the baseline.

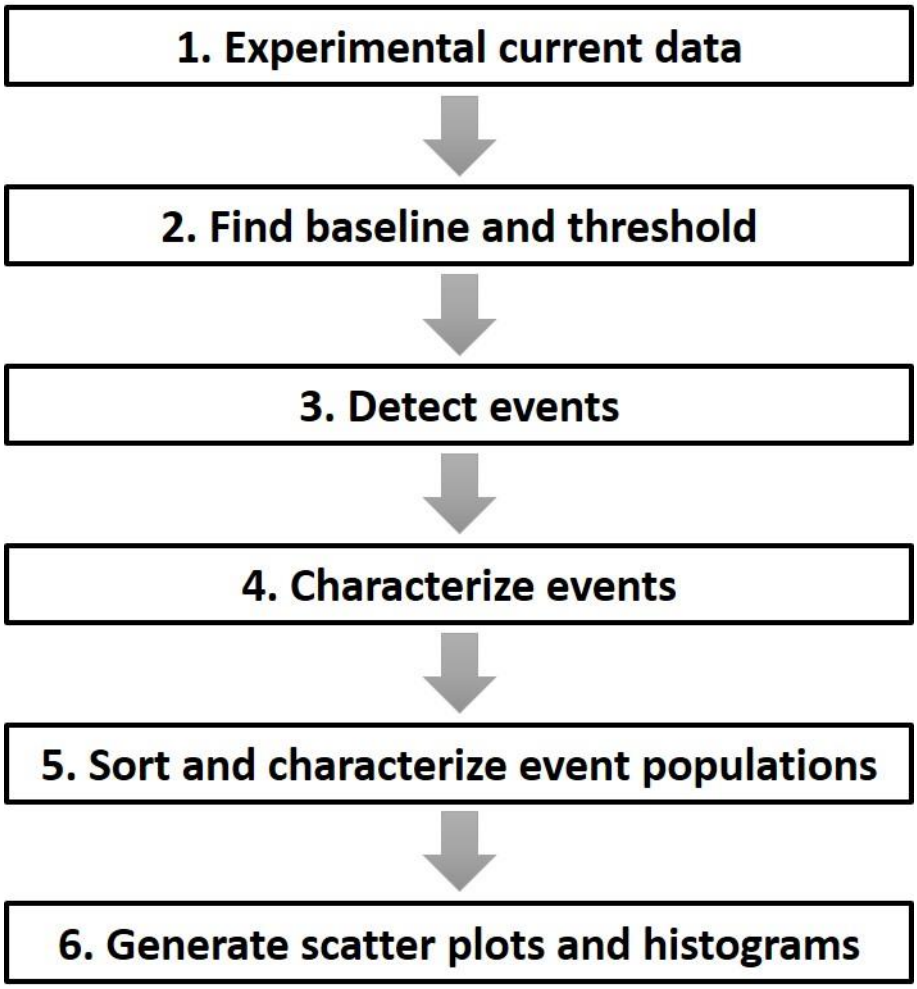

Figure 2.7: Workflow typically employed in the data analysis of the nanopore current traces.

As shown in Figure 2.8A-B, a 7σ threshold was applied and only events above this threshold were considered in the analysis. The 7σ refers to a threshold that is seven standard deviations away from the mean distribution of the baseline. When this threshold factor is applied for peak detection, it implies that a peak must be significantly higher than the average value of the baseline current, in order to be considered as a valid peak. 7σ is associated with values very far from the mean, beyond ranges that are typically coved by a confidence interval, with p-values that are very close to zero. This threshold value was chosen to increase the likelihood of identifying only the most pronounced peaks associated with a true translocation event, while disregarding small fluctuations in the ion current cause by noise.

This event detection step is followed by characterization of the translocation events according to their features, such as peak amplitude, dwell time, and equivalent charge deficit (Figure 2.8C). The event features are detected on an individual basis. This step is

then proceeded by sorting and characterizing the event populations. Lastly, relevant clustering and statistics can be generated by generating scatter and histogram plots (Figure 2.8D-F). The obtained events were further analysed and plotted using Origin 2019b.

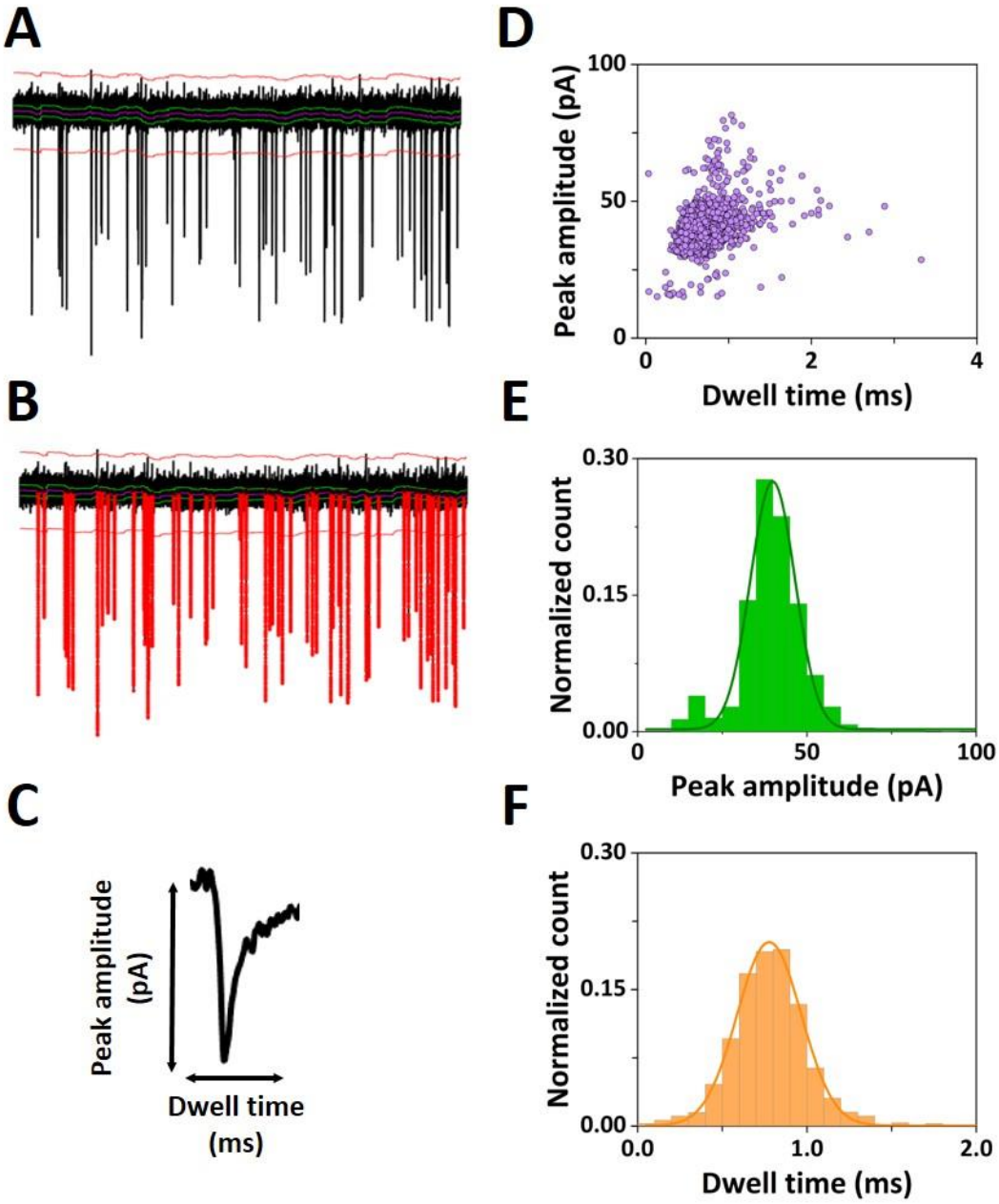

Figure 2.8: Examples of nanopore translocation data analysis. **(A)** Representative ion current trace with the 7σ threshold indicated by the red line. **(B)** Same trace as in panel A with the perturbations in the ion current identified as translocation events. **(C)** Representative event with the translocation peak characteristics. **(D)** Scatter plot with peak amplitude versus the dwell time. **(E)** Histogram of the peak amplitude distribution. **(F)** Histogram of the dwell time distribution. The solid lines represent Gaussian fits to the data.

Chapter 3: Nanopore fingerprinting of supramolecular DNA nanostructures

3.1. Overview

In this chapter, the detection and characterization of supramolecular DNA nanostructures is described. A solid-state nanopore employing a poly-ethylene glycol enriched electrolyte was utilized to deliver real-time, non-destructive, and label-free fingerprinting of higher-order assemblies of DNA origami nanostructures with single entity resolution. An introduction to the DNA origami concept and its applications is first presented. Then, current methods used in characterizing and assessing the yield of folded DNA nanostructures are described.

The results section emphasizes the nanopore-based detection of folded DNA nanostructures and the quantification of the assembly yield of four different assembly designs from the ion current signals recorded. Furthermore, the assembly yield is compared with standard techniques, such as gel electrophoresis and AFM. Lastly, the chapter is concluded by offering a perspective of proposed nanopore approach for DNA

nanostructures assessment and discuss how this approach can further complement the current methods utilized in the analysis of supramolecular DNA assemblies. The work described in this chapter was adapted for publication in the Biophysical Journal (60).

3.2. Aim and challenges

Solid-state nanopores have enabled the single molecule detection of a range of analytes in a rapid and label-free manner. However, they often lack the ability to provide quantitative information of heterogeneous mixtures where nanostructures of different sizes are present, which often is the case in the analysis of folded supramolecular DNA nanostructures. Here, we demonstrate a single-molecule and high-throughput approach for the analysis of higher-order DNA origami assemblies with a polymer electrolyte nanopore. This nanopore approach enabled the characterisation of DNA origami nanostructures at statistically relevant numbers in real-time and at single-molecule resolution while being non-destructive and label-free, and without the requirement of lengthy sample preparations or use of expensive reagents. The quantification of the assembly yield of DNA origami nanostructures was demonstrated based on their equivalent charge surplus computed from the ion current signals recorded.

3.3. Introduction

The use of DNA as a building block for the engineering of nanoscale materials is one of the corner stones of DNA nanotechnology (117). In particular, the invention of the DNA origami approach, which exploits Watson-Crick base-pairing between a single-stranded DNA scaffold and multiple short staple-strands to fold the scaffold into a specific predefined geometry (118), allowed the folding of nanostructures with large surface area while simultaneously enabling spatially controlled assemblies and site-specific chemical functionalisation (17). These unique characteristics have enabled the assembly of nanostructures and patterns with controlled geometry and function, either by directly folding the scaffold (119,120), or via higher-order assembly of pre-formed DNA tiles (22,23,121), which found applications in biosensing (59,63,122-124), drug delivery (125,126), and as tools for studying biological processes (127,128), *inter alia*.

Fuelled by these rapid developments in engineering and fabricating complex DNA nanostructures, there is an increasing demand for their characterisation, including the assessment of assembly yields. Traditionally, the characterisation and assessment of yield of DNA constructs has relied on methods such atomic force microscopy (AFM), which relies on multiple scans of the folded structures and counting molecules from each scan, and agarose gel electrophoresis, which relies on measuring the intensity of the separated bands associated with each DNA nanostructure (129). A rapid, label-free, and single-molecule approach would complement these techniques and would provide a valuable addition to the existing tools.

In recent years, nanopores have been established as a powerful tool for the characterisation of DNA nanostructures with single molecule resolution. Nanopore sensing is based on the measurement of transient perturbations of the ion current through a nanopore caused by the translocation of an analyte (51,130). The characteristics of these perturbations, such as the amplitude and duration, provide information about the physico-chemical properties of the translocating molecule, including size, charge, and shape (55,131). Nanopore sensing has also been successfully applied for the detection of colloidal nanoparticles (66,132) and biological nanoparticles including virus particles (133), ribonucleic particles (63), protein aggregates (134), and DNA nanostructures (83,88,135,136). Our group has previously demonstrated the analysis of 2D DNA origami (137) and single molecule biosensing (59) using nanopores and has recently shown the marked enhancement of single molecule detection within a crowded nanopore (109). Other groups used DNA-based nanoswitches for sensing applications using nanopores (138), and a similar approach has been used for miniaturised molecular data storage (139).

Here, the single molecule detection of supramolecular DNA assemblies by solid-state nanopore analysis is reported. It is demonstrated that the perturbations in the ion current caused by the translocation of a DNA origami nanostructure can fingerprint different states of higher-order assemblies, ranging from an individual monomer building block to multimer assemblies. The quantification of the assembly yields of a range of higher-order assemblies of DNA nanostructures with single-entity resolution is obtained and benchmarked against agarose gel electrophoresis and AFM imaging.

3.4. Materials & methods

3.4.1. DNA nanostructures

The design of the four DNA nanostructures used here follows the design published by Tikhomirov *et al*. (22,140) and was carried out using the CaDNAno 2.3 software (141). All four nanostructures were folded from the single-stranded ssDNA M13mp18 (7249 bp) following the standard procedure for DNA origami fabrication (4). For the higher-order assemblies, the individual tiles were first folded individually using three main kinds of staples: bridge staples, interior staples, which constitute the main body of the tile, and a specific set of edge staples, which allow for a specific interaction between the structures. While the same set of bridge staples and interior staples is shared by all DNA nanostructures, each one of them has a different set of edge staples. The edge staples can be "giving" (featuring a two-nucleotide extension), "receiving" (with a two-nucleotide truncation) or inert (characterised by two hairpins, forming a loop conformation, and preventing the further higher-order assembly of DNA origami along that side). Each structure can have eight giving/receiving staples or five inert staples. For the assembly, we followed published protocols (22,140) where the edges of each tile can be labelled as north, south, east, and west. Each set of interactive edge staples is complementary to just one other specific set of edge staples (north giving edges are complementary to west receiving edges, west giving edges to south receiving edges, east giving edges to north receiving edges, and south giving edges to east receiving ones), allowing for a targeted assembly and avoiding spurious interactions. Furthermore, the addition of the negation strands, which are complementary to the edge staples, inactivate the excess edge staples so that the monomers can be used in higher-order assemblies (22,140). To fold the structures, the individual monomer structures having complementary edge sequences were mixed together in equal concentrations and volumes, in order to increase the yield of the assembly (141). Specifications on the sequences and the interactions between the pre-assembled monomers for all the higher-order structures used in this work are provided in the data repository (142).

3.4.2. DNA nanostructures folding

The single-stranded M13mp18 DNA scaffold 7249 bp was purchased from New England Biolabs (NEB, UK) at an initial concentration of 250 µg/ml. The staple strands were purchased from Integrated DNA Technologies (IDT, UK) and resuspended in 1x TE buffer pH 8 (Sigma Aldrich, UK) to a final concentration of 100 µM. The negation strands were purchased from IDT and resuspended in 1x TE buffer pH 8 to a final concentration of 200 µM. For the folding, the ssDNA scaffold (final concentration 10 nM) was mixed with the staple strands (final concentration 75 nM) in 1x TE buffer pH 8 with 12.5 mM of $Mg(Ac)_2$ in 80 µL total volume. To fold the individual tiles, the solution of scaffold and staples was heated to 90°C for 2 min and annealed using a temperature ramp from 90°C to 20°C at 6 sec per 0.1°C in a Mastercycler Nexus PCR Thermal Cycler (Eppendorf). Following the annealing step, the negation strands were added to the solution to achieve a final concentration of 375 nM in 80 µL final total volume. Another temperature ramp was then applied, going from 50°C to 20°C at 2 sec per 0.1°C. The folded structures were purified using Sephacryl S400 (GE Healthcare, UK) size exclusion columns in order to remove the excess staple strands, and the product was eluted in 1x TE pH 8, 12.5 mM $Mg(Ac)_2$. The concentration of the individual tiles was measured using a NanoDrop 2000c Spectrophotometer (Thermo Scientific, UK) to prepare solutions with equal concentration. To fold the higher-order assemblies, equal volumes of the required individual monomers were mixed in PCR tubes and annealed using a temperature ramp from 55°C to 45°C (at 2 min per 0.1°C) followed by a ramp from 45°C to 20°C (at 6 sec per 0.1°C). The folded nanostructures were imaged by AFM to confirm the successful assembly.

3.4.3. Atomic Force Microscopy Imaging

For AFM imaging, 10 µL of purified DNA sample diluted to a final concentration of 0.5 nM in 1x TE pH 8, 12.5 mM $Mg(Ac)_2$ were deposited on a freshly cleaved mica substrate (Agar Scientific, UK) and incubated at room temperature for 15 min. Additional 150–180 µL of 1x TE pH 8, 12.5 mM $Mg(Ac)_2$ buffer was added to the sample to facilitate the imaging. The samples were imaged using a Dimension Fastscan Bio (Bruker, UK) in tapping mode in liquid with Fastscan D Si_3N_4 cantilevers with a Si tip (Bruker, UK). We used the following imaging parameters: scan rate = 2–8 Hz, 256 samples/line, amplitude

setpoint = 150 - 300 mV, drive amplitude = 3000 mV, integral gain = 1, proportional gain = 5. The data were processed using Nanoscope analysis 1.9.

3.4.4. Agarose gel electrophoresis

The quality of the DNA origami nanostructures was further inspected with agarose gel electrophoresis (**Error! Reference source not found.**). For this, 50 mL 0.7% agarose gel w as prepared using 1x TAE buffer containing 12.5 mM $Mg(Ac)_2$. The DNA origami samples were prepared by mixing a 20 µl aliquot at a concentration of 10 ng/µl with 4 µl of 6x Tri Track Loading Dye (Thermo Scientific, UK). M13mp18 scaffold was added as a reference. A GeneRuler 1kb DNA double-stranded ladder (Thermo Scientific) was used as molecular marker and positive control (**Error! Reference source not found.**). The running buffer consisted of 1x TAE and 12.5 mM $Mg(Ac)_2$. The gel was run at a constant voltage of 70 V for 120 min. The gel was then stained for 30 min with Diamond Nucleic Acid Dye (Promega) diluted in 1x TAE buffer. For this, 5 µL 10,000x concentrated Diamond Nucleic Acid Dye was diluted in 1x TAE buffer and the gel incubated at room temperature for 30 min on a rocking platform. The agarose gel imaging was carried out using the GeneSnap software. Quantification of the relative amounts of monomers, various assembly intermediates, and final products for each DNA origami sample was carried out by measuring the corresponding bands' intensity with ImageJ and normalize by the size of the higher-order assemblies to account for the amount of double stranded DNA stained per macromolecule.

3.4.5. Nanopore fabrication and characterization

The nanopores were fabricated starting from 1.2 mm x 0.9 mm quartz capillaries (QF120-90-10; Sutter Instrument, UK) with the SU-P2000 laser puller (World Precision Instruments, UK), using a two-line program: (1) HEAT, 800; FILAMENT, 4, VELOCITY, 30; DELAY, 145' PULL, 95; (2) HEAT, 730, FILAMENT, 3; VELOCITY, 40; DELAY, 135; PULL, 150. The pulling parameters are instrument specific and lead to nanopipettes with a nanopore diameter of approximately 160 nm. The nanopipettes were characterized by measuring their pore resistance in 0.1 M KCl (~40 MΩ) and the nanopore dimensions were confirmed by Scanning Electron Microscopy (SEM) using a Nova NanoSEM at an accelerating voltage of 3–5 kV.

3.4.6. Nanopore translocation measurements

The translocation experiments were carried out by filling the nanopipette with the translocation buffer (100 mM KCl, 0.01% Triton-X, 10 mM Tris, 1 mM EDTA, pH 8.0) containing the DNA origami sample at a concentration of 500 pM. The nanopipette was then immersed in a 100 mM KCl bath with the addition of 50% (w/v) Polyethylene Glycol (PEG) 35 kDa (ultrapure grade, Sigma Aldrich). An Ag/AgCl wire (0.25 mm diameter, GoodFellow UK) was inserted in the nanopipette barrel and acted as the working electrode, while a second Ag/AgCl wire was immersed in the bath and acted as the counter and reference electrodes. The DNA origami nanostructures were driven from inside the nanopipette into the external bath by applying a negative potential to the working electrode placed inside the nanopipette with respect to the reference electrode in the bath. The ion current was recorded with a MultiClamp 700B patch-clamp amplifier (Molecular Devices) in voltage-clamp mode. Data was acquired at a 100 kHz sampling rate with a 20 kHz low-pass filter using the pClamp10 software (Molecular Devices). The ion current traces were further analysed with the MATLAB script Transanlyser, developed by Plesa *et al.* (116). The obtained translocation events were analysed by applying a 7-sigma threshold level from the baseline, and only the events above the threshold were considered as translocation events. The obtained events were further analysed and plotted using Origin 2019b.

3.5. Results & discussion

3.5.1. DNA nanostructures assembly

In this chapter, the discrimination of supramolecular DNA nanostructures with solid-state nanopores is demonstrated by exploiting the unique signature in the translocation signal resulting from the perturbation when the nanostructures pass through the nanopore (Figure 3.1). Here, the translocation signal characteristics such as peak current maxima (maximum peak current amplitude) and dwell time (duration of the event) are used to characterize the translocating nanostructures on individual basis (Figure 3.1B)

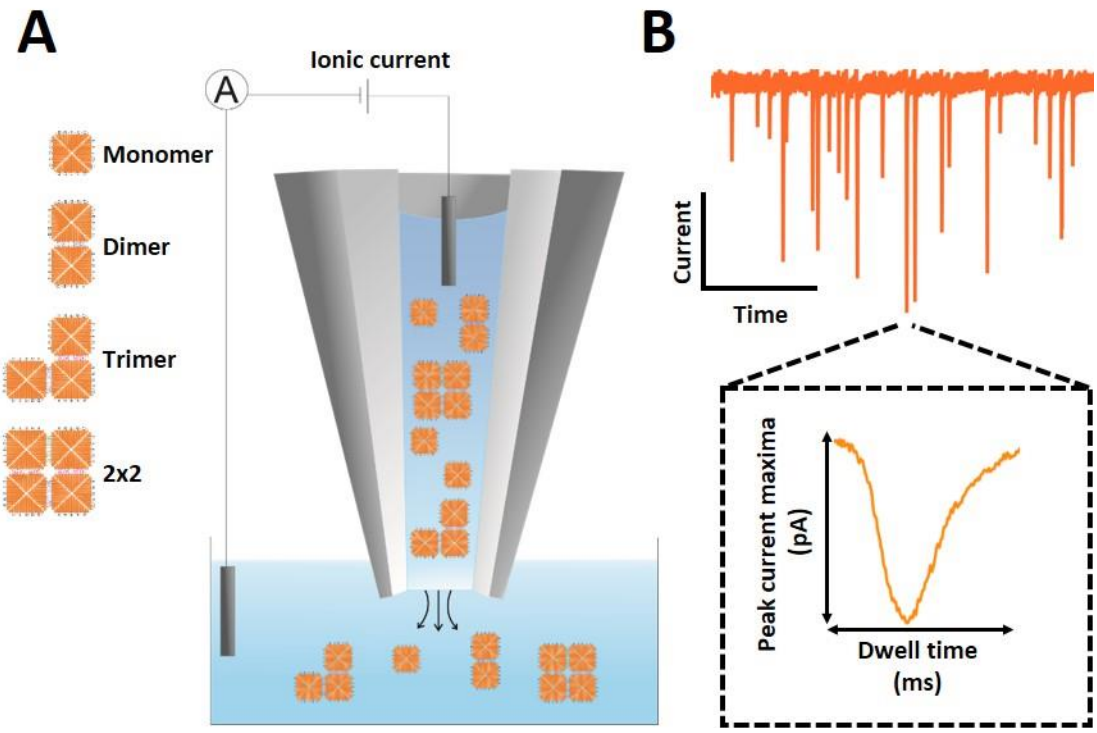

Figure 3.1: Schematic representation of the nanopore setup. **(A)** The DNA origami nanostructures are translocated from inside the nanopore into the outer bath upon the application of a negative potential bias while the ion current is measured. **(B)** Representative ion current trace showing translocation events. A representative event is shown in the inset with the translocation peak characteristics.

For this, four different DNA nanostructures were assembled, starting from a pre-assembled DNA origami (85 nm x 85 nm) used as a building block (referred to hereafter as monomer), followed by a two-monomer assembly (dimer), a three-monomer assembly in an L-shape (trimer), and lastly a 2x2 array of monomers (referred to hereafter as 2x2) (Figure 3.2A). AFM measurements confirmed the correct folding of the DNA nanostructures (Figure 3.2B).

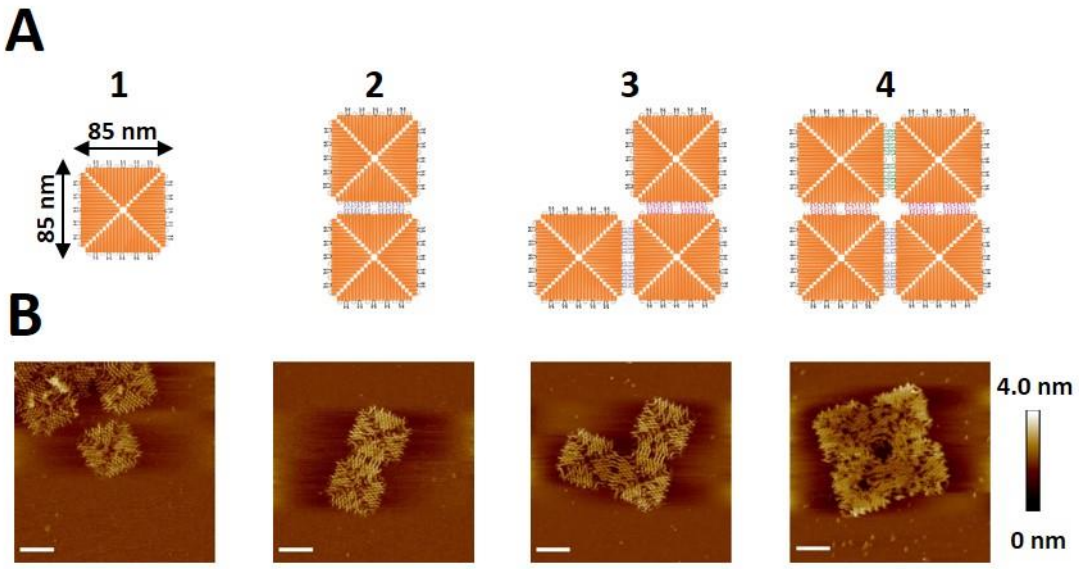

Figure 3.2: Design of the higher-order assembly DNA nanostructures indicating the sets of monomer building-blocks used for their assembly. Schematic representation of the DNA nanostructures, starting with a single monomer building block (1), dimer (2), trimer (3), and 2x2 (4). The sequences for each set of staples are provided in the data repository (142). Edge modification of the monomer nanostructures were made in order to assemble the higher order DNA nanostructures. The tiles design comprise of a single layer of double-stranded DNA helix (~ 2nm thickness). **(B)** AFM micrographs of the DNA nanostructure depicted in panel A (50 nm scale bar).

3.5.2. Nanopore analysis of DNA origami monomer

A pore diameter of 160 nm was chosen to be large enough to accommodate the largest DNA nanostructure (2x2) while retaining a sufficient signal-to-noise ratio for the detection of the monomer. Figure 3.3 shows a representative SEM image of the nanopore, together with current-voltage curves obtained from three different pulled nanopipettes, showing a good overlap between the pore of the nanopipettes.

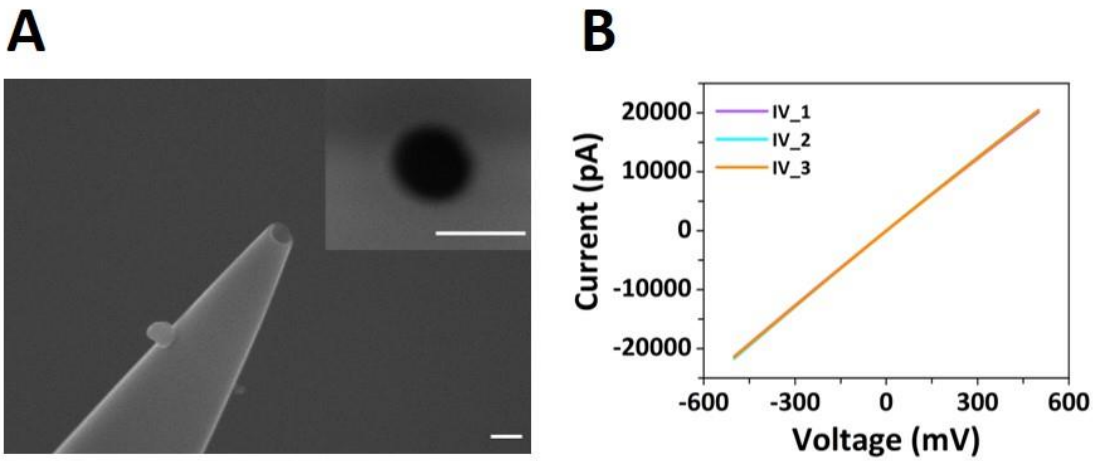

Figure 3.3: Nanopore characterization. **(A)** SEM micrograph of a nanopipette used for translocation experiments, with a top view inset of the pore (200 nm scale bars). The diameter of the pore used in this study was approximately 160 nm. **(B)** Current-voltage curves (IV) of three nanopipettes recorded in 0.1 M KCl.

The detection of the smallest (monomer) and largest (2x2) DNA nanostructures with a fixed pore size was facilitated by adapting the bath conditions where the nanopipette is immersed. It was previously demonstrated the single-molecule-detection sensitivity can be enhanced when polyethylene glycol (PEG) is added to the bath solution to a final concentration of 50% w/v (109,143). The presence of PEG led to translocation peaks that were well-resolved from the ion current baseline (**Error! Reference source not found.**4A). In contrast, the translocation of monomer DNA nanostructures in the absence of PEG resulted in a low signal-noise-ratio, constraining the detection of the monomer nanostructures.

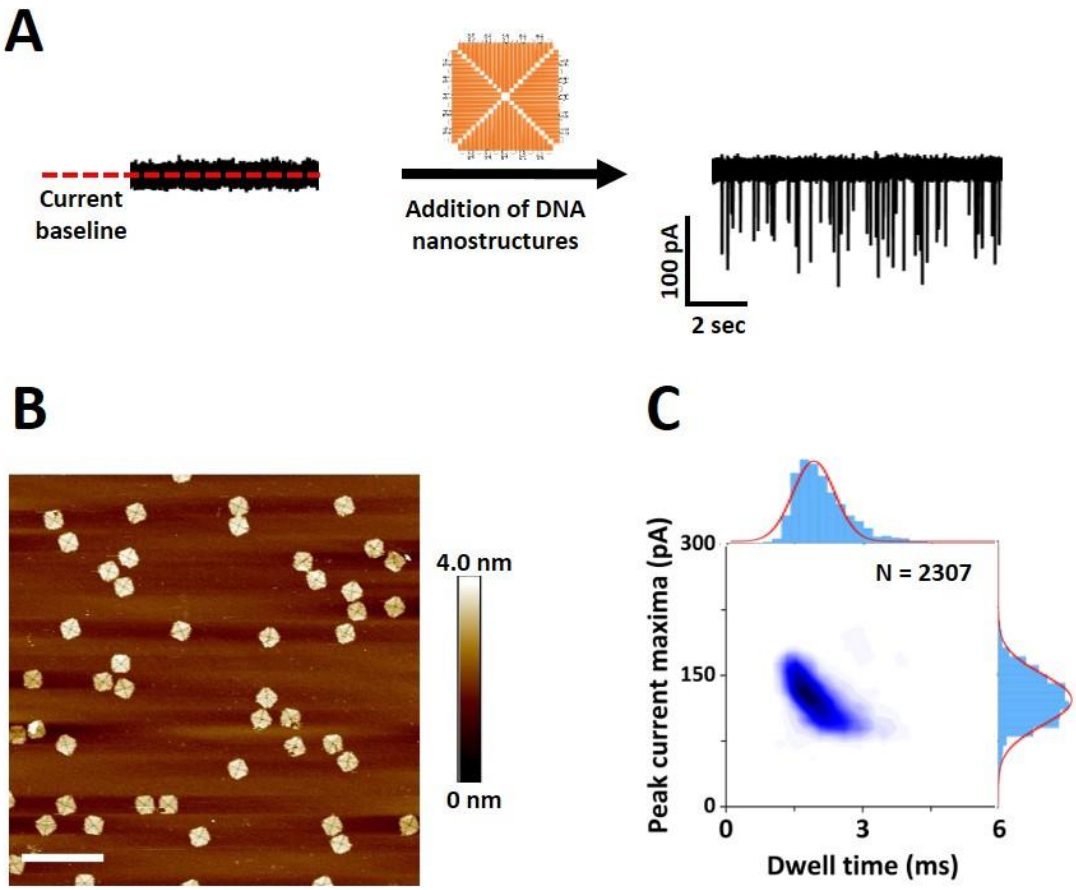

Figure 3.4: Nanopore translocation DNA origami monomer. **(A)** Ion current trace before and after the addition of the DNA origami monomer. **(B)** AFM micrograph of a monomer DNA origami sample (400 nm scale bar). **(C)** Density scatter plot of the monomer DNA origami sample with the peak current amplitude *versus* dwell time and their corresponding marginal histograms. The solid lines in the marginal histograms represent a Gaussian distribution fitted to the data. A total of *N* = 2307 translocation events were analysed, and their corresponding peak current maxima and dwell time values extracted.

Furthermore, the presence of PEG allowed us to detect all DNA nanostructures with a high signal-noise-ratio and to record stable ion current traces with high capture rate (~5 events/sec at -300mV) for several minutes without any evidence of nanopore clogging. This is evidenced in Figure 3.5, depicting a continuous nanopore recording for a duration of 6 min of a 2x2 DNA origami sample.

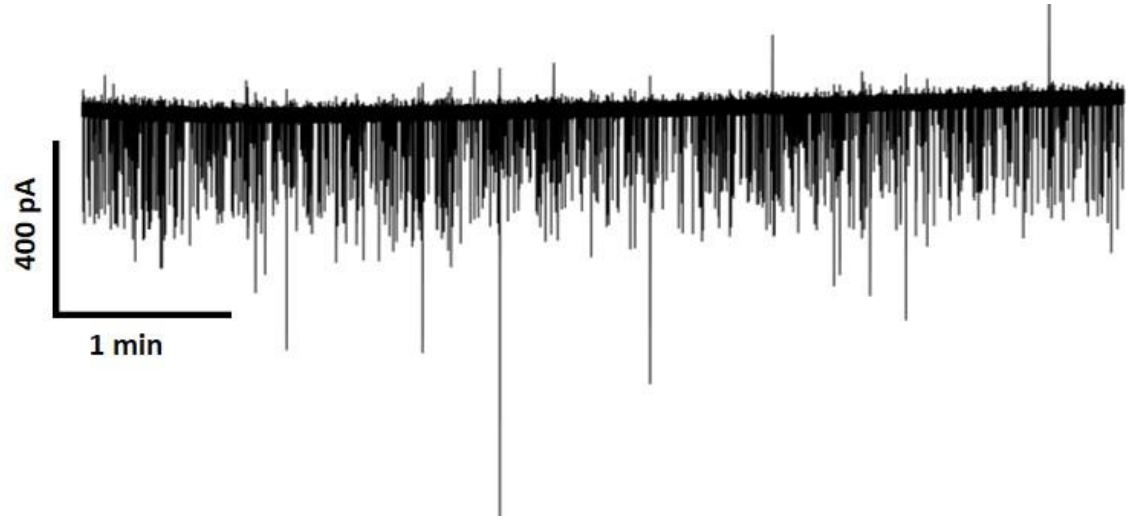

Figure 3.5: Ion Current trace of the 2x2 DNA origami sample recorded for 6 minutes under an applied voltage of -300mV.

Several control experiments were carried out to confirm the translocation of the DNA origami nanostructure. First, the translocation of the monomers was investigated from inside the nanopipette into the outside bath under a constant voltage bias of -300 mV (Figure 3.6B). The translocation of the monomer DNA nanostructures resulted in conductive (current enhancing) translocation signal peaks, where each peak is associated with the passage of one molecule. No peaks were detected under the same conditions if no analyte was added to the nanopipette (Figure 3.6A).

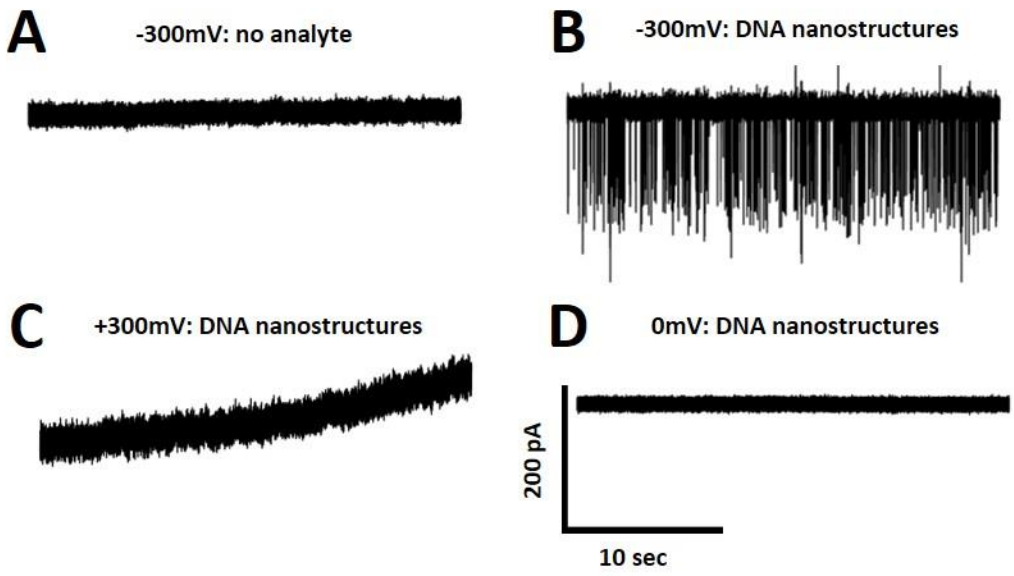

Figure 3.6: Control ion currents traces of monomer DNA nanostructures translocation. **(A)** translocation at -300 mV when no analyte is added inside the nanopipette; **(B)** translocation at -300 mV when monomer DNA origami sample is added inside the nanopipette; **(C)** translocation at +300 mV when monomer DNA origami sample is added inside the nanopipette; **(D)** translocation at 0 mV when monomer DNA origami sample is added inside the nanopipette. The current and timescales are the same for all graphs.

The translocation events of the monomer sample can be characterized using the peak current maxima (maximum amplitude of the peak from the baseline) and dwell time (duration time of an event). The results (*N* = 2307 peaks) are displayed in the density scatter plot of Figure 3.4C, which shows that the translocation peaks fall within a well-defined area. Density scatter plots are commonly used in nanopore experiments to display the characteristic signature of the analyte (108). The histograms showing the peak current maxima and the dwell time distributions, respectively, are also shown in the figure. Both distributions have been fitted with a Gaussian distribution function yielding an average peak amplitude of 123 ± 27 pA and an average dwell time of 2.1 ± 0.6 ms. Upon increasing the applied voltage, an increase in the peak current maxima of the conductive peaks was observed, as well as a decrease of the dwell time (Figure 3.7A-D), suggesting that the DNA nanostructures are electrophoretically driven through the pore. This observation was also confirmed by translocation controls where no potential was applied (Figure 3.6D) or the applied bias was reversed (Figure 3.6C). Furthermore, the effect of DNA nanostructure concentrations and the effect of applied voltage on the translocation event frequency was also probed. With an increasing concentration of

DNA nanostructures, more molecules are expected in the capture region of the nanopore which results in a larger number of translocation events. This observation was confirmed by running translocation measurements at different concentrations (50-500 pM), as shown in Figure 3.7F. Moreover, increasing the applied voltage induces a larger capture region, leading to a greater number of translocation events (Figure 3.7E). Here, a slight increase in the error bars of the event frequency was observed at higher applied voltage. This can potentially be attributed to variations in the translocation of the DNA nanostructures reaching the sensing region over time. Increasing the translocation speed of the nanostructures at higher voltages can also cause a substantial increase in crowding effect at the aperture, which potentially can cause fluctuations in the event frequency. The translocation observations reported in terms of applied voltage and concentration are consistent with established physical models reported in the literature on the study of nucleic acids translocations through solid-state nanopores (144-146).

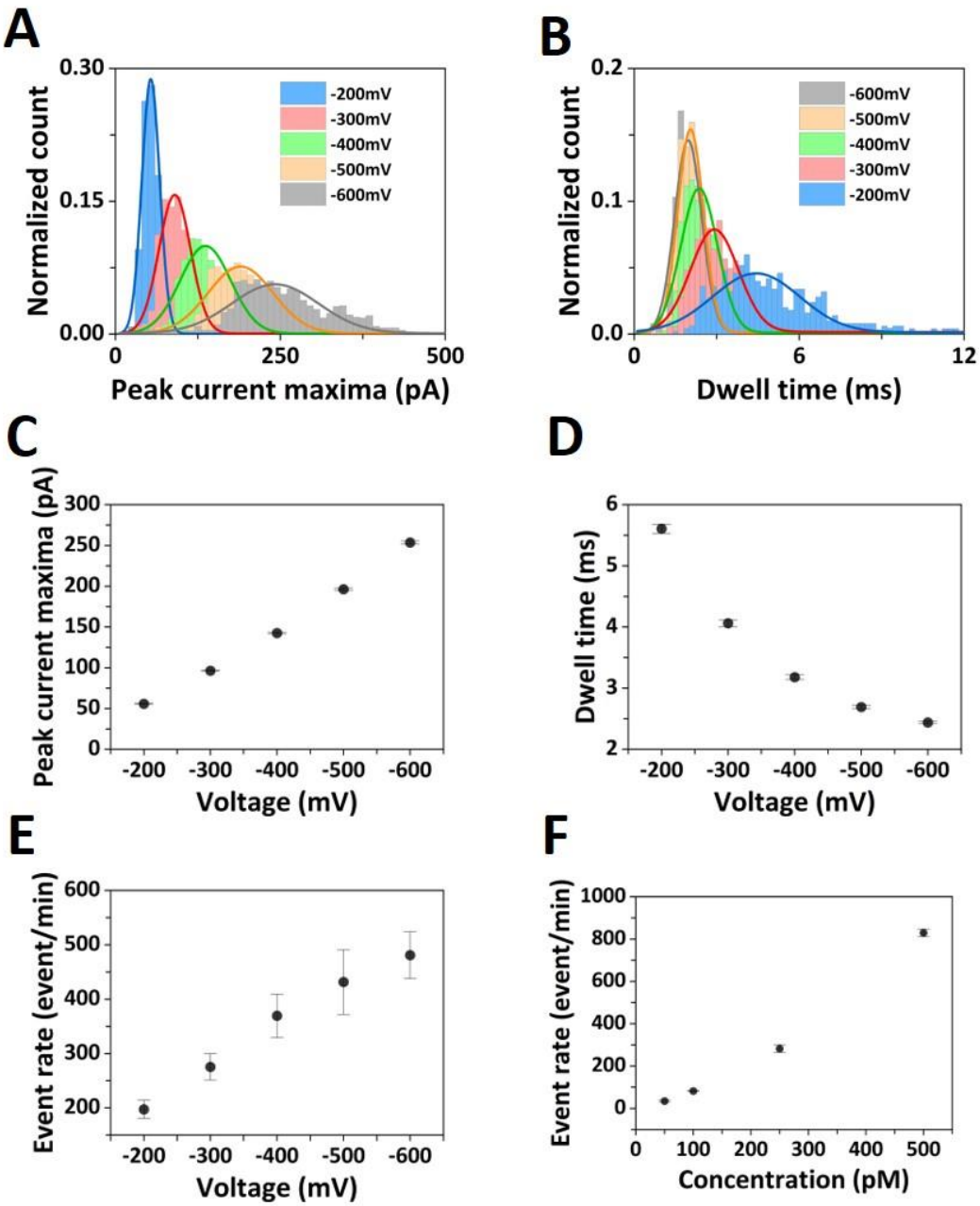

Figure 3.7: Translocation characteristics DNA origami monomer. Histograms of the current peak amplitude **(A)** and the dwell time **(B)** distributions for increasing absolute values of applied voltages *V* = -200 mV, -300 mV, -400 mV, -500 mV, and -600 mV. The solid lines represent Gaussian fits to the distributions. Data was normalized to the total event count recorded for each condition. Average peak current maxima **(C)** and dwell time **(D)** at *V* = -200 mV, -300 mV, -400 mV, -500 mV, and -600 mV. Error bars show the standard deviation from three independent recordings. Event rate of the DNA nanostructures translocation as a function of *V* **(E)** and sample concentration (50 pM, 100 pM, 250 pM, and 500 pM) **(F)**. Error bars show the standard deviation from three independent recordings. Monomer DNA origami sample (250 pM for panel A-E) was used for these translocation experiments, and each translocation condition was repeated independently three times.

3.5.3. Nanopore signal comparison of supramolecular DNA origami assemblies

The higher-order-assembly DNA origami samples were further analyzed using the same translocation conditions as for the monomer analysis. Figure 3.8A depicts the current versus time traces obtained for the monomer and 2x2 samples where a new population of translocation events can be observed for the 2x2 sample.

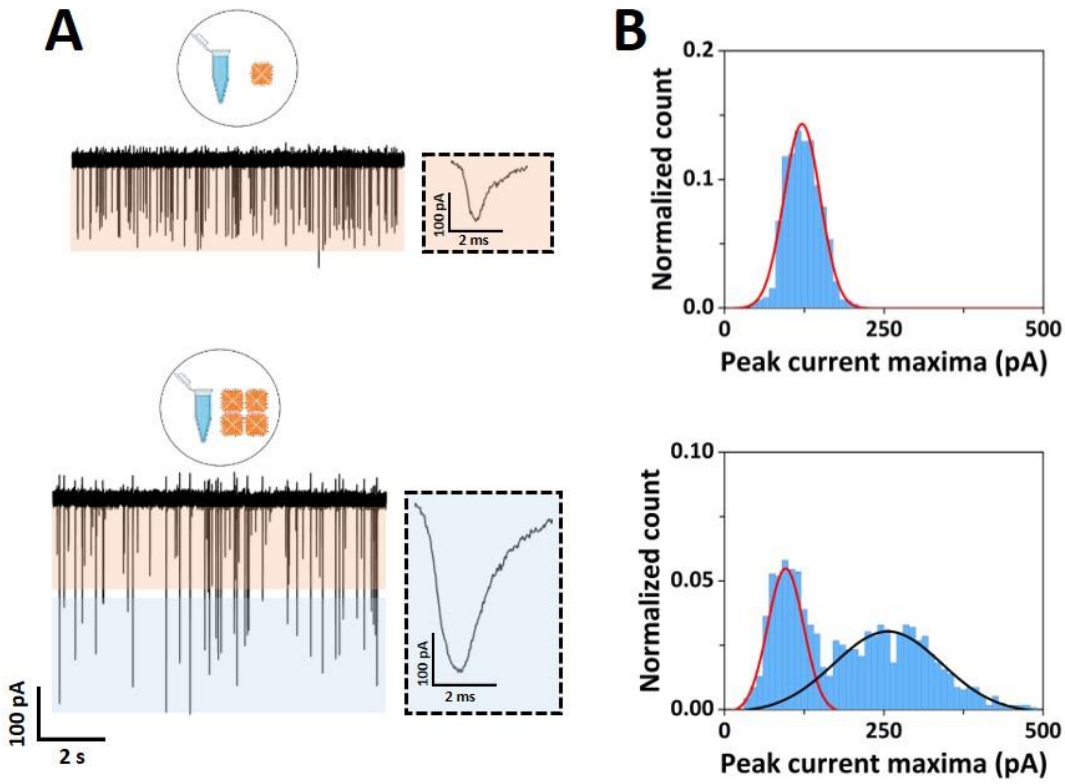

Figure 3.8: Comparison translocation signal monomer and 2x2 supramolecular assembly samples. **(A)** Nanopore translocation current traces of the monomer (left) and the 2x2 (right) samples. The current and time scales for the two traces are identical. The orange shading indicates the current range <150 pA, and the blue shading indicates the current range >150 pA. The insets show a representative translocation event for each sample. The scale bars are the same for both insets. **(B)** Histograms of the current peak amplitude for the monomer sample (left) and the 2x2 sample (right). The solid lines represent Gaussian fits to the data.

While the monomer sample led to translocation events with peak current maxima of less than ~150 pA, events with significantly larger current amplitudes can be seen for the 2x2 sample – the current range within which these new peaks fall is indicated by the blue shading. This observation suggested that our nanopore platform is able to discern the two 'extreme' designs of the higher-order DNA origami assemblies introduced in Figure 3.2A using a fixed nanopore diameter.

The distributions were fitted with a single and a two-peak Gaussian distribution (shown as solid lines in the plot). While the monomer sample yielded an average peak current maximum of ~123 pA , the distribution corresponding to the more well-defined cluster in the 2x2 assembly sample density scatter plot which is reminiscent of the one found for the monomer yielded an average peak current maximum of ~170 pA, and the broader less well-defined distribution an average peak current maximum of ~260 pA. Despite the slight difference in average peak currents, it was hypothesised that the more well-defined cluster of the 2x2 sample corresponds to monomers in the sample which were not successfully assembled into higher-order assemblies. This hypothesis was confirmed by spiking the 2x2 sample with increasing concentrations of the monomer.

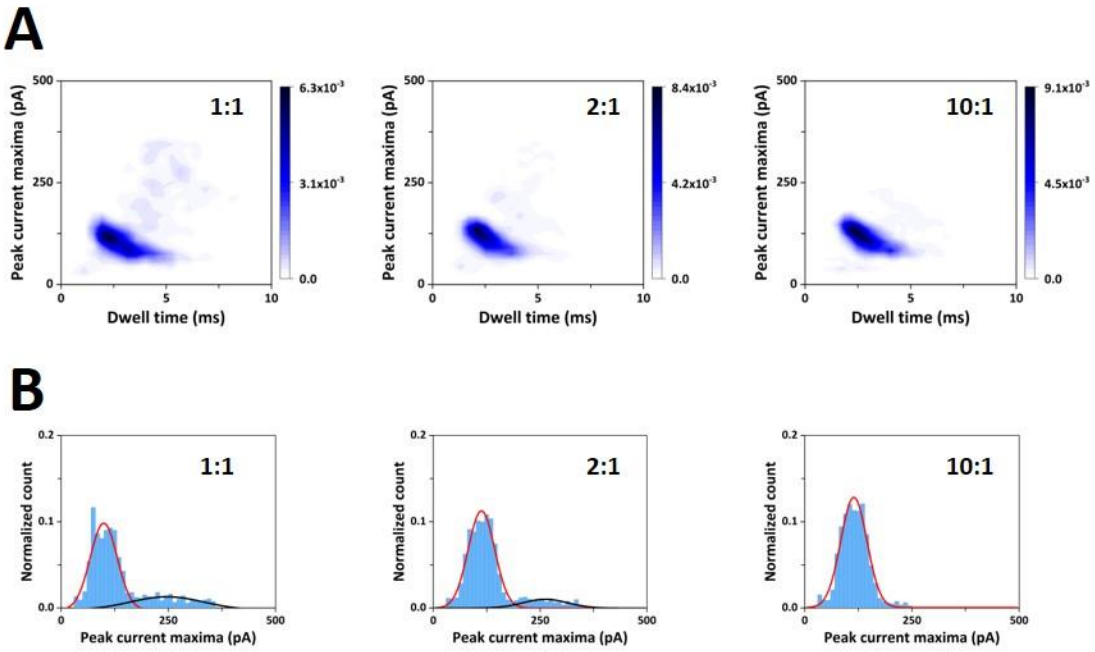

Figure 3.9: Monomer spiking of 2x2 DNA origami samples. **(A)** Density scatter plots of the peak current maxima as a function of dwell time for 2x2 sample spiked with monomer sample. **(B)** Histograms of the current peak maxima distributions for the 2x2 sample spiked with monomer sample with multi-peak Gaussian fits represented by the solid lines. The notation 1:1, 2:1, and 10:1 for the left-to-right graphs in each panel indicates the molar ratio of monomer sample spiked into the 2x2 sample.

As can be seen in Figure 3.9, a shift towards the monomer cluster was observed when increasing the number of monomers spiked into the 2x2 sample. However, it is unlikely, given the relatively broad width of the distribution, that the less well-defined cluster represents only a single assembly state. The range of characteristic translocation peaks

of the 2x2 sample ion current are displayed in Figure 3.10, showing a range of peaks with differences in their conductive peak current amplitude and dwell time.

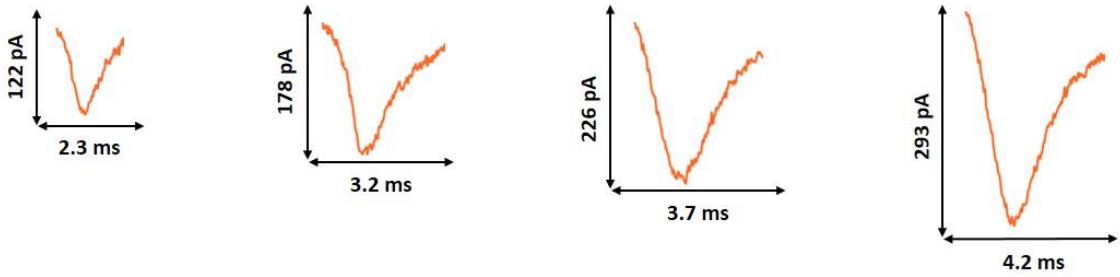

Figure 3.10: Representative translocation peaks characteristic of the heterogeneous 2x2 sample with their corresponding dwell time and peak current maxima values.

This is further supported by both AFM imaging (Figure 3.11) and gel electrophoresis (Figure 3.12) which suggested that the high-order assembly DNA origami samples, contained not only the end-structure folded in the sample, but also intermediates assemblies and unreacted monomers, observation that also applies to the 2x2 DNA origami sample.

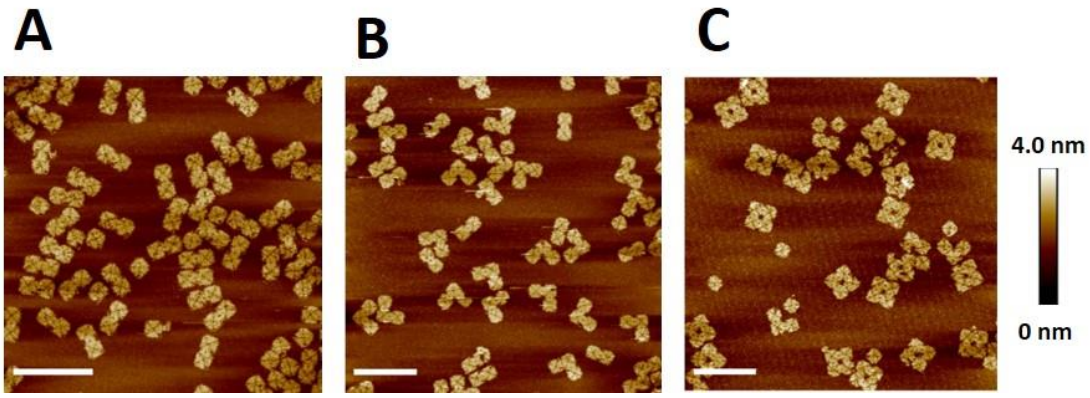

Figure 3.11: AFM micrographs of the higher-order assembly DNA origami samples: dimer **(A)**, trimer **(B)**, and 2x2 **(C)**, using a 2 µm x 2 µm scan size (400 nm scale bars).

As shown in Figure 3.12, the gel electrophoresis analysis also confirmed the presence of multiple DNA nanostructures in the higher-order assembly samples, *i.e.* the dimer sample contains the monomer nanostructures as well. The trimer sample contains monomer and dimer nanostructures. The 2x2 samples contains monomer, dimer, and trimer nanostructures. A dsDNA ladder (1kb) was utilized as a positive control.

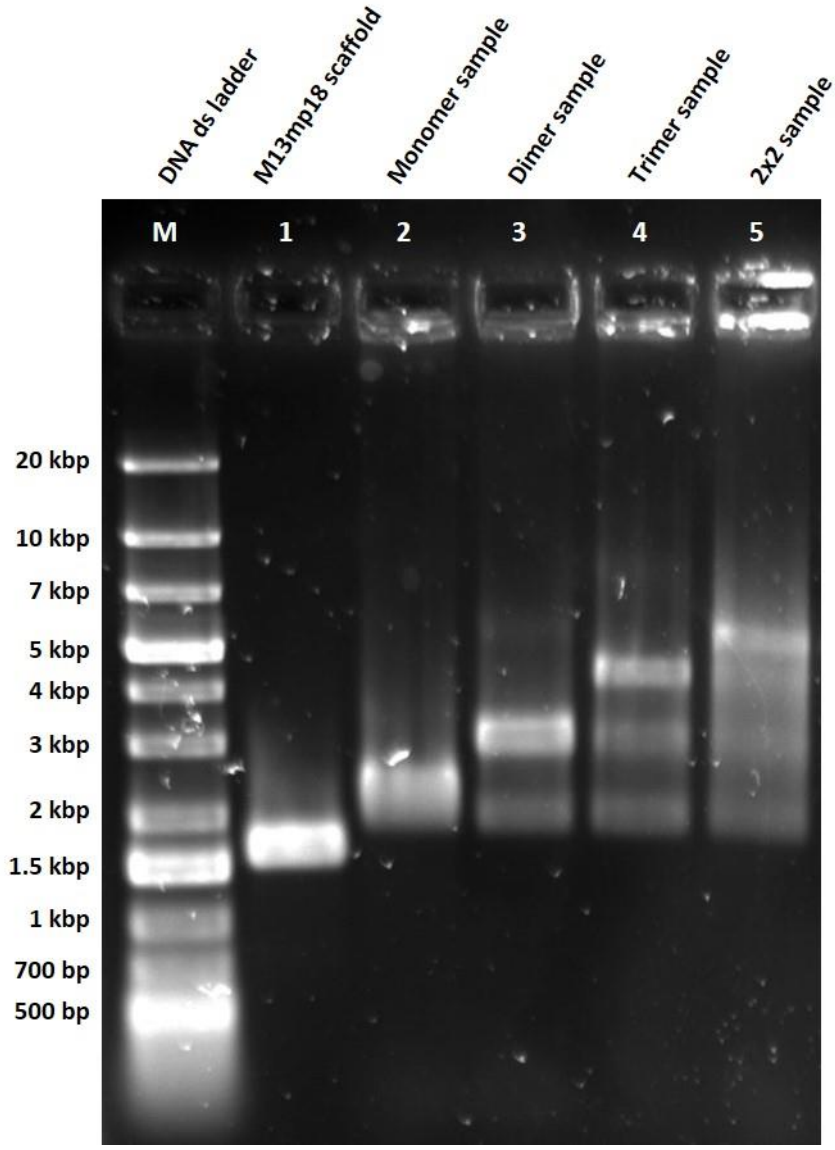

Figure 3.12: Agarose gel electrophoresis of DNA origami samples. Lane M: GeneRuler 1kb dsDNA ladder; Lane 1: M13mp18 circular ssDNA; Lane 2: monomer DNA origami sample; Lane 3: dimer DNA origami sample; Lane 4: trimer DNA origami sample; Lane 5: 2x2 DNA origami sample. Note, Figure 3.15D is a subset of this figure.

In order to deconvolute further the broad less-well defined cluster of translocation events in the 2x2 sample all four DNA origami assembly samples were analyzed, and the respective density scatter plots are shown in Figure 3.13. One of the clusters for the 2x2 sample is very similar to the single population observed in the monomer sample. However, the 2x2 sample shows an additional broader and less well-defined cluster centred at around 4 ms and 250 pA.

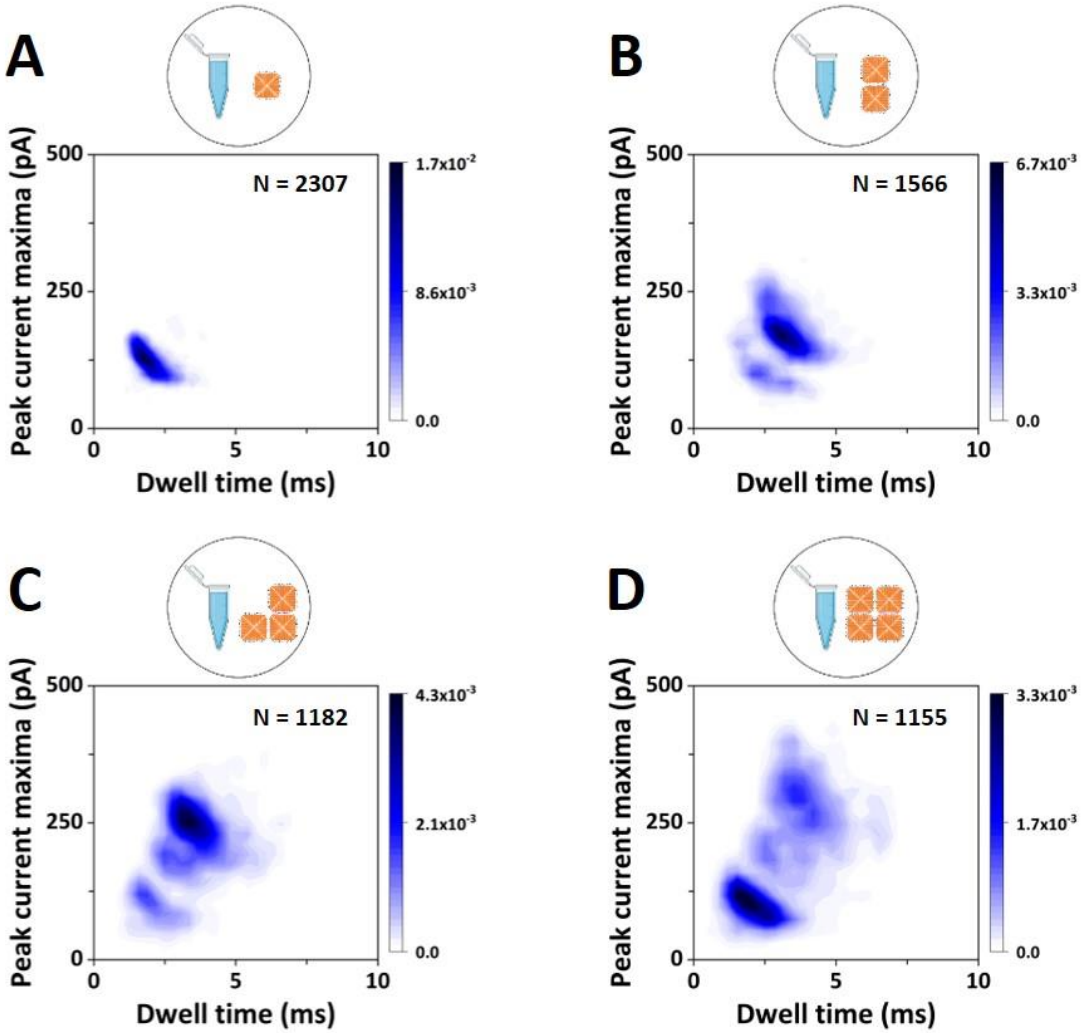

Figure 3.13: Nanopore translocation comparison of all DNA origami samples. Density scatter plots of peak current amplitude as a function of dwell time for the monomer sample **(A)**, dimer sample **(B)**, trimer sample **(C)** and 2x2 sample **(D)**. The number of events analysed, *N*, for each sample is given in each panel.

All four DNA origami assembly samples (monomer, dimer, trimer, 2x2) were analysed individually with the nanopore platform using the same translocation conditions. The density scatter plots allowed the identification of different clusters for each sample, and for all higher-order assembly samples (Figure 3.13B-D) a consistent presence of the monomer cluster was noticed. This is not unexpected – the higher order assembly processes have finite yields and a certain percentage of unassembled monomers are expected to remain. Furthermore, the higher-order assembly is reversible, and while the assembled construct is expected to be energetically favourable, dissociation of higher-order assemblies can occur over time. The translocation peak characteristics of each

DNA origami sample showed differences in terms of their peak current amplitude and dwell time distributions, as shown in the peak current and dwell time distribution plots in Figure 3.14. The dimer sample yielded one additional well-defined cluster of peaks, with slightly higher peak current maxima and dwell time averages, consistent with what is expected for the translocation of assembled dimers. However, the situation is much less clear for the trimer sample – similar to the 2x2 sample – where in addition to the well-defined cluster originating from the monomer peak an additional number of much less-well defined clusters are observed. While the clustering is qualitatively different between the four samples, the density scatter plots cannot provide quantitative details about the assembly intermediates.

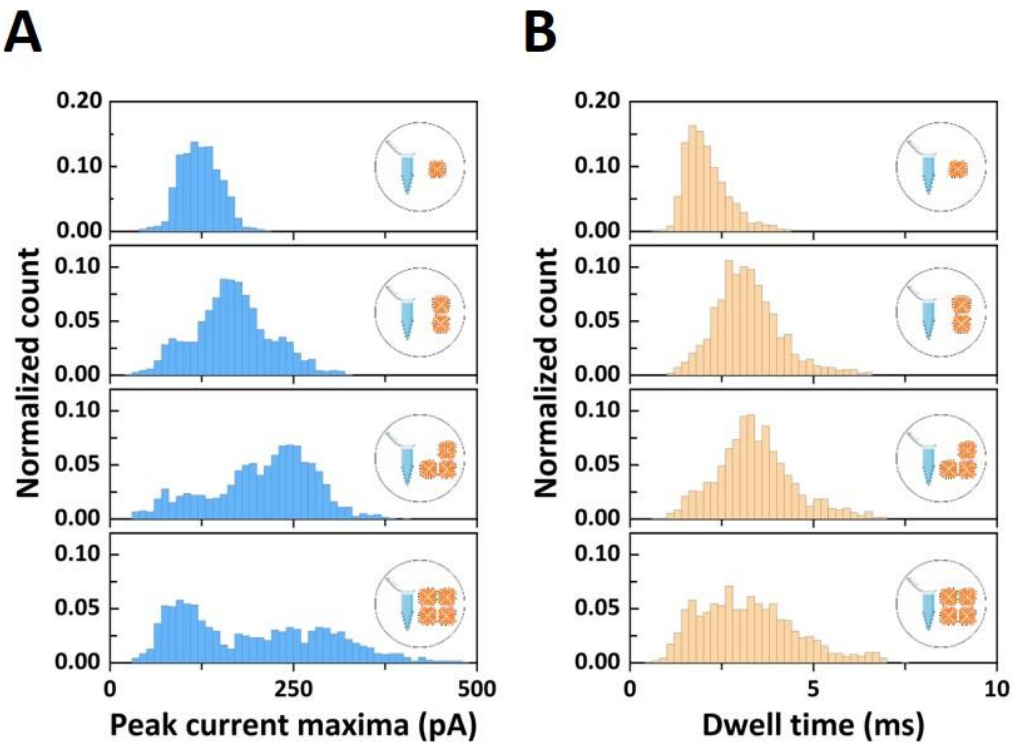

Figure 3.14: Histograms for peak current maxima **(A)** and dwell time **(B)** distributions for each DNA origami sample investigated. From top to bottom: monomer, dimer, trimer, and 2x2 samples. Translocation events were recorded at -300 mV.

3.5.4. DNA origami assembly yield analysis

Finally, in addition to distinguish different assembly intermediates within a mixed sample, the aim was to go beyond the standard analysis of DNA origami nanostructures assembly (AFM and gel electrophoresis) and quantify the percentage of each DNA nanostructures present in the higher-order assembly samples. While the peak current amplitude *versus* dwell time density scatter plots highlighted significant differences between samples, to extract more detail from the translocation information, an additional nanopore translocation discriminant was investigated. The observed translocation peaks are conductive, and therefore imply that an increased amount of charge is passing through the nanopore during the translocation event compared to the baseline while no DNA origami pass through. The Equivalent Charge Surplus (ECS) of each translocation event was defined as the area of the conductive translocation peak (Figure 3.15A) (116).

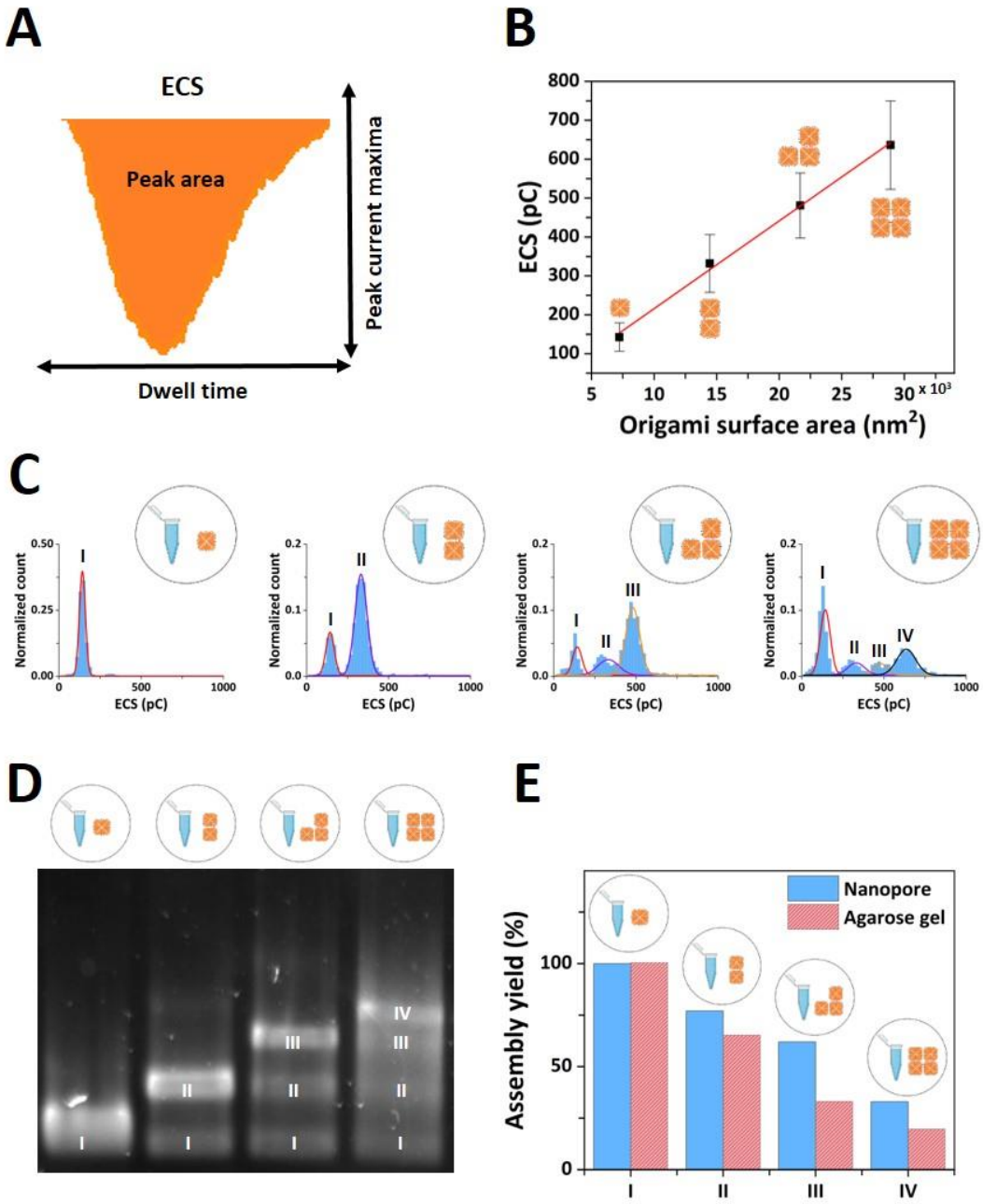

Figure 3.15: Folding yield quantification of DNA nanostructures based on nanopore analysis. **(A)** Schematic representation of Equivalent Charge Surplus (ECS), obtained from calculating the area of the translocation peaks. **(B)** ECS as a function of the DNA origami surface area for the four DNA nanostructure assembled (the red line represents a linear fit to the data). The error bars represent the width of the Gaussian fits displayed in panel C. **(C)** ECS histograms of the DNA origami samples; from left to right: monomer, dimer , trimer, and 2x2 sample. The distributions were fitted with single or multi-peak Gaussian distributions. The notation I-IV marks the peaks corresponding to each of the DNA nanostructures in the respective sample (*e.g.* the dimer sample shows two peaks in the ECS distribution, attributed to the presence of the monomer (I) and dimer DNA origami (II) in the sample). **(D)** Agarose electrophoresis gel of the DNA origami samples; from left to right: monomer samples, dimer sample, trimer sample, and 2x2 sample. The I-IV notation of the gel bands marks the presence of the nanostructure component in the respective sample. **(E)** Bar chart comparison of the assembly yield of each DNA nanostructure (blue bar: nanopore data, red bar: gel electrophoresis data).

The ion current signature discriminants used above (peak current maximum and translocation dwell time) are likely dependent on the shape and orientation of the nanostructure during translocation through the nanopore. In contrast, the overall charge is expected to remain conserved for the same higher-order assembly state of DNA origami, and can be expected to scale linearly with the size of the higher-order assemblies made from identical DNA origami (monomers). This is confirmed in Figure 3.15B, where the average ECS values of the DNA origami designs are plotted versus their surface area. The red line represents a linear fit to the data. Figure 3.15C depicts the ECS distributions for each higher-order DNA origami sample analysed with the nanopore platform. In contrast to the distributions of the peak current maxima (Figure 3.8B), even for the most complex sample (2x2 sample) four clearly discernible peaks can be seen in the distribution, which suggests that each peak corresponds to either the monomer building block, the fully assembled structure, or a particular higher-order assembly intermediate. To allocate the different distribution peaks to a particular structure, the information obtained from less complex assemblies was used in the analysis of the more complex assemblies. Clearly, the monomer sample is expected to contain predominantly monomers and at most a negligible amount of non-specifically assembled higher-order structures. This is reflected in the very prominent peak centred around an ECS of ~150 pC (left-most panel of Figure 3.15C). The solid line represents a Gaussian fit to the distribution, which yielded an average ECS of 143 pC. The barely noticeable contribution to the distribution at around 300 pC may indicate a negligible presence of non-specific assemblies, but the contribution is difficult to quantify and is significantly smaller. Therefore, we allocate the ECS peak centred at 143 pC (labelled I) to the monomer. The ECS distribution of the dimer sample shows two peaks (second panel of Figure 3.15C). In this assembly sample we expect the monomer and of course the dimer to be present. Therefore, we fitted the distribution with a two-peak Gaussian while keeping the first peak fixed at 143 pC, the position obtained from the monomer sample (most-left panel of Figure 3.15C). The fits are represented by solid lines in the figure; the red line represents the fixed monomer peak (I), and the blue line the additional peak (II) which yielded an average ECS of 332 pC, and which we attribute to the presence of the dimer. To confirm that peak II indeed represents the dimer, the dimer sample events were

sliced according to which Gaussian peak of the ECS distribution they belong, and generated the associated peak current maxima *versus* dwell time density scatter plots (Figure 3.16).

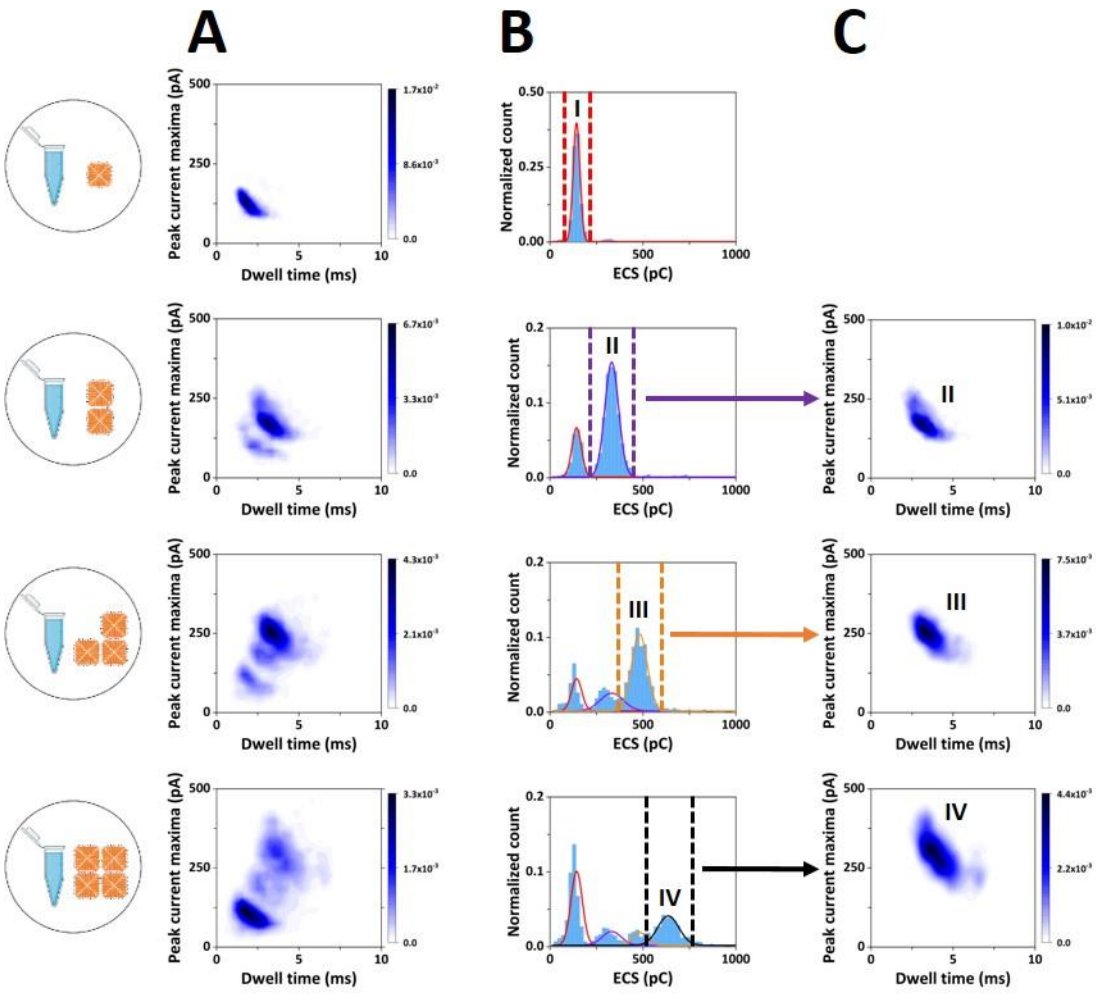

Figure 3.16: Cluster isolation based on ECS. **(A)** Density scatter plots of the current peak maxima as a function of dwell time for (top to bottom): monomer sample, dimer sample, trimer sample, and 2x2 sample. **(B)** ECS histograms for the DNA origami samples presented in panel A. Marked Gaussian fitted peaks correspond to the DNA nanostructures of interest in each sample. **(C)** The corresponding sliced cluster depicted in a density scatter plot using only the translocation events sliced according to the marked Gaussian fitted peaks shown in Panel B. We note that the intensity scales are normalised to the number of translocation events shown, and therefore are different compared to panel A.

As shown in the second row of Figure 3.16, the monomer component in Figure 3.13A is not present in the density scatter plot (panel C of Figure 3.16), supporting the viability of this ECS clustering to mark the different DNA nanostructure components present in the assembly samples. The same approach was then applied for the trimer and the 2x2

sample, resulting in an ECS distribution peak at 481 pC (III) which represents the trimer, and an ECS distribution peak at 636 pC (IV) which represents the 2x2 component. A slight discrepancy was noted between the fixed monomer and dimer peaks in the ECS distributions compared to the observed distribution for both the trimer and 2x2. This may have resulted from small variations in pore size of the nanopipettes used, as each dataset was obtained with different nanopipettes. However, the deviations are small and do not impact on our ability to distinguish different populations. The equivalent data slicing as for the dimer sample was carried out and, like the dimer samples, the fully assembled DNA nanostructures yielded well-defined isolated clusters in the respective density scatter plots (Figure 3.16C). While all current traces were recordings of 3 min, the same analysis was carried out on a shorter trace (1 min) with correspondingly fewer translocation events (Figure 3.17), showing that the results remain consistent for shorter current traces (1min *vs* 3min recorded trace).

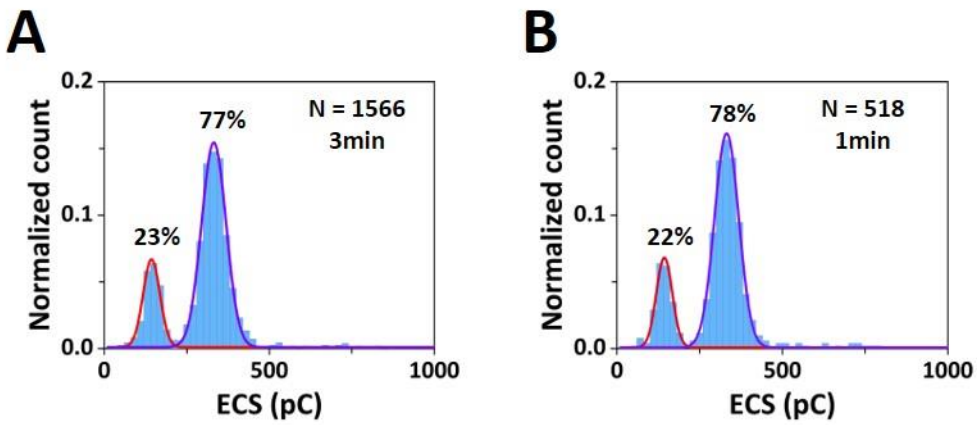

Figure 3.17: ECS histograms for dimer sample based on a 3-minute translocation recording **(A)** and 1-minute translocation recording **(B)**. Solid lines are Gaussian fits to the distributions.

The areas of the Gaussian fits to the ECS distribution peaks allowed to associate individual translocation event to a distinct assembly state (monomer building block, fully assembled DNA nanostructure, or assembly intermediate) and thus to estimate the percentage of each higher-order DNA nanostructure present in the samples and compute an assembly yield for each DNA construct. Figure 3.15E (blue bars) shows the yield for forming the desired end-product for each higher-order assembly sample, *i.e.* the percentage of monomer (I), dimer (II), trimer (III) and 2x2 (IV) in the monomer,

dimer, trimer and 2x2 sample, respectively. As expected from the histogram in Figure 3.15C, the yield for the monomer is 100%, while yields for the higher-order assemblies decrease with the increase in assembly. To further investigate the impact of the intrinsic variability of the nanopipettes for our assembly yield quantification, a number of translocation measurements of the same DNA origami sample was carried out using different but nominally identical nanopipettes. In Figure 3.18 the ECS distribution based on the recordings of five independent nanopipettes is shown and the yield corresponding to the dimer DNA nanostructure for each repeat was quantified, showing a standard deviation in the calculated yield of 2% for 5 independent measurements.

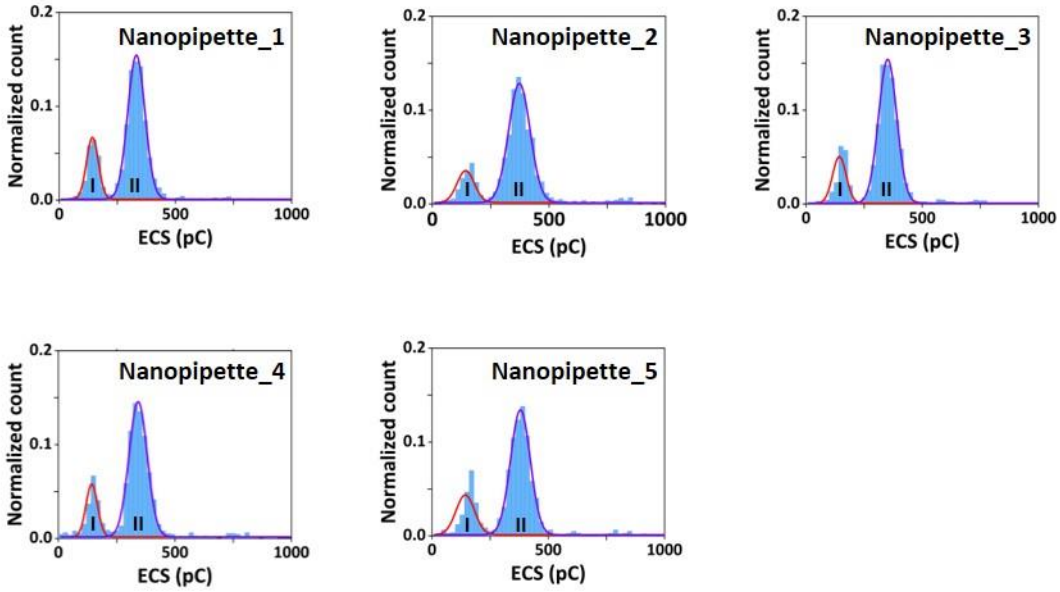

Figure 3.18: ECS histograms for dimer sample based on recordings obtained from five different nanopipettes measurements.

Table 3.1: Percentage of dimer DNA nanostructure yield determined from the ECS distributions based on five different nanopipette measurements of the same sample together with the standard deviation.

Nanopipette repeat	Dimer assembly yield quantification			
	Area ECS peak I	Area ECS peak II	Dimer nanostructure yield	Dimer nanostructure yield ± SD
Nanopipette 1	4.2	14.2	77	
Nanopipette 2	3.2	14.7	82	
Nanopipette 3	3.6	14.0	80	79 ± 2
Nanopipette 4	3.5	14.1	80	
Nanopipette 5	4.3	14.1	77	

To further support the proposed quantification approach based on the ECS discriminant, the analysis of trimer DNA nanostructures with two different assembly configurations was probed. For this purpose, an additional trimer assembly design was built in order to obtain a stacked trimer configuration assembly using the same pre-assembled monomer building blocks. To achieve this, the folding mixture consisted of a monomer set with two edge staples placed on its opposite edges in order to favour a linear assembly of the three pre-assembled monomers. The assembly configuration difference between the L-shape trimer and the stacked trimer is depicted in the AFM micrographs in Figure 3.19A.

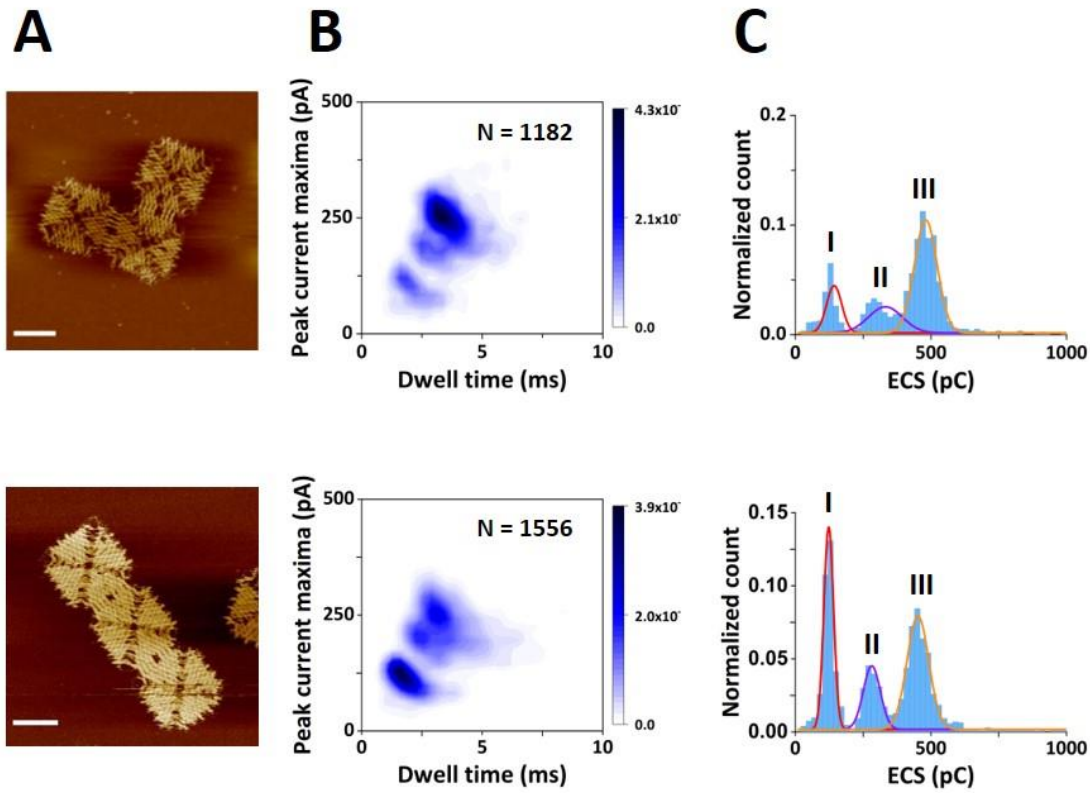

Figure 3.19: Comparison nanopore translocation of two different trimer nanostructure configurations. **(A)** AFM micrographs of trimer DNA nanostructure assembled L-shape (top panel) and stacked (bottom panel) configuration (50 nm scale bar). **(B)** Density scatter plots of peak current maxima as a function of dwell time for the L-shaped trimer DNA sample (top panel) and stacked trimer DNA sample (bottom panel). The number of events analysed, *N*, for each sample is given in each panel. **(C)** ECS histograms of the L-shaped DNA sample (top panel) and stacked DNA origami sample (bottom panel). The distributions were fitted with single or multi-peak Gaussian distributions. The notation I-III marks the peaks corresponding to each of the DNA nanostructures in the respective sample, attributed to the presence of the monomer structures (I), and dimer structures (II), and trimer structures (III) in the sample.

Even though these trimer DNA nanostructures differ in their assembly configuration, they both have similar surface areas and therefore similar ECS distribution peaks is expected in this case. In this line of reasoning, the stacked trimer DNA origami sample was translocated under the same nanopore conditions. Figure 3.19B shows the density scatter plots for the L-shape and stacked trimer DNA origami samples with three clusters identified in both cases which are associated with folding of the trimer nanostructure, its partial folding (dimer), or the presence of unreacted pre-assembled monomers. Moreover, the ECS distribution of the stacked trimer DNA origami samples consistently shows three peaks similar to the analysis of the L-shape trimer DNA origami sample. This

is an agreement with the equivalent nanostructure surface area between the two trimer configurations analysed. Interestingly, the ECS-based quantified yield for the trimer nanostructure present in the two DNA origami samples show particular differences. Whereas the L-shape trimer DNA origami sample resulted in a trimer nanostructure yield of 62%, the stacked trimer DNA origami sample resulted in a trimer yield of 45%. The yield obtained for the monomer nanostructures was approximately double in the case of the stacked trimer sample (35%), in comparison with to L-shape trimer sample (17%). Nevertheless, both trimer samples resulted in similar yields associated with the folding of the dimer nanostructure - 20% for stacked trimer sample and 21% for the L-shape trimer sample, respectively. This potentially suggests that the assembly efficiency for the same amount of building blocks is also influenced but its assembly configuration. Such quantification yield approach can further support the investigation of different assembly designs and serve as feedback in the design optimization of high-order assemblies with high-yield and high-stability characteristics.

3.5.5. Assembly yield comparison with gel electrophoresis

Traditionally, agarose gel electrophoresis is often employed to estimate assembly yields. An electrophoresis gel containing lanes for each higher-order assembly is shown in Figure 3.15D, and the assembly yields were determined from the agarose gel by densitometry and taking into account the size of the structure. The results are shown as red bars in Figure 3.15E and the numerical values are shown in Table 3.2. Overall, the yields obtained with gel electrophoresis show the same trend as the ones obtained from the nanopore measurements. However, there are some notable differences. The agarose gel indicated a larger percentage of monomers in the higher-order assemblies for the trimer and 2x2 sample compared to the nanopore measurements (Table 3.2). Our approach is comparable to gel electrophoresis in terms of costs and ease of use but with the added advantage of single molecule sensitivity and the ability to obtain quantitative results within minutes. Another often employed means of assessing the yield of DNA origami structures is AFM. Our AFM micrographs (Figure 3.11) confirmed the heterogenous character of the higher-order DNA origami samples. AFM is extremely well suited to study small numbers of DNA origami at very high detail so a good understanding of their structures and fine detail of the folding can be obtained. Previous

studies demonstrated the use of AFM imaging to obtain quantification yields of folded DNA nanostructures based on the molecule count from AFM scans in solution (140,147,148). However, their use for quantification of the assembly yield is questionable in this case. AFM scans depend heavily on the mica surface preparation which is required for imaging, and this is likely to lead to an under-representation of smaller DNA constructs owing to the higher sedimentation rate of the larger DNA origami structures onto the mica substrate. This was confirmed here, where we observed an under-representation of monomers in the higher-order assembly samples (trimer and 2x2 samples) compared to the nanopore measurements.

Table 3.2: Percentage of DNA nanostructures determined for each DNA origami sample analyzed. The notation I-IV refers to the DNA origami nanostructures present in the sample analyzed: I - monomer nanostructure, II - dimer nanostructure, III - trimer nanostructure, and IV - 2x2 nanostructures. The dash indicates that the component was not detected and no percentage was computed.

DNA origami sample	Ratio DNA nanostructure nanopore analysis (%)				Ratio DNA nanostructure agarose gel analysis (%)			
	I	II	III	IV	I	II	III	IV
Monomer Sample	100	-	-	-	100	-	-	-
Dimer Sample	23	77	-	-	12	88	-	-
Trimer Sample	17	21	62	-	48	19	33	-
2x2 Sample	44	14	10	33	66	13	3	18

Compared to the standard analysis methods of AFM and agarose gel electrophoresis, the nanopore measurements offer several advantages. Our nanopore method allowed us to obtain a label-free analysis of the DNA origami samples within a few minutes with single molecule resolution at statistically relevant numbers, and no lengthy sample preparations or use of expensive reagents. Another advantage of the nanopore

approach is its single molecule analysis which can potentially detect minute concentrations and reveal the presence of DNA constructs that have formed with very low yields. In Figure 3.7F we demonstrate nanopore detection of DNA origami nanostructures down to the 50 pM concentrations.

In addition to utilising nanopore measurements for the determination of assembly yields of DNA origami, the approach enables a range of other applications. For example, the ability to differentiate between assembly states enables the probing of the association/dissociation of higher-order DNA constructs and shed light on their stability in different assembly configurations. Furthermore, the analysis is real-time and non-destructive, *i.e.* the DNA origami nanostructures could be collected in the bath after translocation and reused. This opens up the possibility for using the nanopore approach in label-free separation or purification, where, depending on the translocation peak characteristics, the DNA nanostructure can be steered (*e.g.* electrophoretically) into a collection or waste tube. Future developments of the nanopore measurement approach will include the parallelisation of measurement using arrays of nanopores to increase throughput. Previous studies demonstrated the fabrication of solid-state nanopore arrays on silicon nitride or graphene membranes (149,150), which are manufactured using inherently scalable approaches. Similarly, Alawami *et al.* have shown the use of multiple glass nanopipettes embedded in a PDMS devices (151). Furthermore, machine learning approaches integrated with nanopore measurements can lead to a real-time classification of the DNA nanostructures. Examples of combining nanopore sensing with machine learning has been demonstrated for different analytes (152-154). As the field of DNA origami is expanding at a fast pace, more intricate structures in terms of design and functionality emerge requiring the integration of additional nanopore features, like machine learning algorithms, to provide accurate and robust identification and quantification of complex supramolecular structures.

3.6. Conclusion

In conclusion, nanopore translocation was explored as a single molecule approach to probe the heterogeneous character of DNA origami assemblies. The large number of events which can be recorded (>1000 events) for each sample within minutes enables statistically relevant studies in a non-destructive and label-free way. The discrimination of various assembly states for higher-order DNA origami assemblies was demonstrated based on their equivalent charge surplus computed from the recorded ion current signals, which allowed the quantification of the assembly yields without any lengthy sample preparations, and importantly enables a range of other applications where rapid single-molecule detection is required. This work complements related approaches of using nanopore translocations characteristics to differentiate between DNA nanostructures with different geometries (58,155,156), further enabling the analysis of higher-order assemblies.

Chapter 4: Nanopore Sensors for Enhanced Detection of Nanoparticle Mixtures

4.1. Overview

In this chapter, the enhanced detection of nanoparticles and nanoparticle mixtures is described, based on a solid-state nanopore approach utilizing a polymer electrolyte bath. First, an introduction to the analysis and characterization of the nanoparticles is given followed by a discussion of the challenges related to the analysis of heterogenous mixtures.

The results section emphasizes the nanopore-based detection strategy for probing a wide range of nanoparticles with distinct chemical composition, capping agents and physical properties. Lastly, the chapter is concluded by offering a perspective of the solid-state nanopore approach to discriminate nanoscale variations and its potential as

a complementary toolbox for the analysis of nanoparticles. The work described in this chapter was adapted for manuscript publication in BioRxiv (157) and submitted for journal publication.

4.2. Aim and challenges

Nanopore sensing has been successfully used to characterize biological molecules with single-entity resolution based on the resistive pulse sensing approach, but it has an untapped potential for the analysis of nanoparticles. Nanopore measurements require the size of the pore to match the size of the analyte, limiting the investigation to homogenous mixtures. Furthermore, they require high ionic concentration electrolytes which precludes the analysis of nanoparticles systems that are unstable at high ionic strength. An adaptable nanopore system is presented here that takes advantage of a polymer electrolyte system to comprise a conductive pulse sensing approach. The proposed nanopore system enables the characterization of heterogenous nanoparticle mixtures and the detection of a variety of nanoparticle samples at low ionic strength. We also demonstrate the wide relevance in materials science of our system by characterizing the degree of branching of "hard" anisotropic Au nanostars and the nucleic acid coverage of "soft" protein spherical nucleic acids (proSNAs). This work will have clear impact in the field of materials science by exploring the potential of nanopore sensing for the label-free analytical characterization of a wide range of nanoparticle systems.

4.3. Introduction

Over the past few decades, the use of nanoparticles has played a significant role in the advancement of medicine, optics, and electronics (120,158,159). The use of nanoparticles not only sparked a strong engagement in the research settings, but they have also become widely incorporated in numerous consumer goods nowadays (160). Understanding the structural-functional relationships of engineered nanoparticles is a continuous undertaking that requires an in-depth exploration of their physicochemical properties. Therefore, the ability to characterize nanoparticles in a high-throughput manner is of utmost importance. However, characterizing nanoparticles in their native

state, specifically in heterogenous mixtures, presents many challenges (111). Dynamic light scattering (DLS) or UV-Vis spectroscopy are ensemble-averaging techniques and, therefore, fall short in fully characterizing heterogenous nanoparticle mixtures (161). Nanoparticle tracking analysis (NTA) is suitable for analysing size distribution of polydisperse nanoparticle suspensions, however it poses limitations in terms of size ranges (~30–1000 nm) and its accuracy dependence on concentration, and assessing particles with different shapes (162). Imaging methods such as transmission electron microscopy (TEM) provide high-resolution characterization of individual nanoparticles but suffer from sampling bias, low throughput, and require careful sample preparation (33).

As discussed in the previous chapter, nanopore sensing is a powerful label-free electrical technique that uses the Coulter principle for single entity analysis (111). This technique has garnered interest thanks to its simplicity and rapid measurements. In nanopore experiments, individual entities are driven through a nanopore under the influence of an electric field, causing a temporary modulation in the recorded ion current by a combination of geometrical exclusion of electrolyte solution, ion concentration polarization, and additional charges brought by the analyte itself (52,163). The magnitude and duration of these modulations reflect the translocation dynamics of the analyte, which are dependent on its physicochemical properties (*e.g.,* size, shape, charge) (131,164,165). Moreover, large numbers of nanoparticles can be driven through the pore, making it an appealing sensing method for high-throughput characterization. Even though nanopores have been employed in numerous sensing applications, it has an untapped potential for the analysis of nanoparticles (166). This is because current nanopore measurements require the size of the pore to match the size of the analyte, limiting the investigation to homogenous mixtures (108,167,168). Furthermore, nanopore measurements require high-ionic-concentration electrolytes which precludes the analysis of nanoparticles systems that are unstable at high ionic strength (85,169). Tuneable resistive pulse sensing (TRPS) is a nanopore technique that has found some applications in nanoparticle characterization, but it is limited to nanoparticles larger than 100 nm in size (67,170).

In this chapter, polymer-electrolyte enhanced nanopore sensing which enables the analysis of heterogenous nanoparticle samples at low ionic strength is presented. The

polymer electrolyte environment generates a large signal enhancement eliminating the need for a nanopore that matches the size of the nanoparticle and therefore allowing the high throughput analysis of heterogenous nanoparticle mixtures, similar to the what has been described in Chapter 3. Then, the characterization of nanoparticles at low ionic strength (10 mM KCl) is demonstrated, enabling the analysis of anisotropic gold nanostars (AuNS) with varying degrees of branching, before reporting the detection and analysis of an emerging class of functional soft nanoparticles, protein spherical nucleic acids (ProSNAs) with distinct oligonucleotides shells. The single-nanoparticle analysis approach described herein will complement the toolbox of existing nanomaterials characterization techniques unleashing the potential of nanopore sensing for the universal analysis of nanoparticles.

4.4. Materials & methods

4.4.1. Chemicals & materials

All reagents used in the translocation experiments were prepared using ultra-pure water (18.2 MΩ.cm) from Millipore system and further filtered through a 0.22 µm syringe. KCl, Triton-X, EDTA, and PEG reagents were purchased from Sigma Aldrich. Gold PEG carboxyl-capped nanospheres (10, 20, 30, 40, and 50 nm diameter), PEG carboxyl-capped nanorods (10 x 40 nm) silver citrate-capped nanospheres (30 nm diameter), and platinum citrate-capped nanospheres (30 nm diameter) were purchased from NanoComposix. The nanoparticle size reported here refers to the diameter of the metallic core particle. The nanoparticles coated with PEG-carboxyl compromise of additional coating layer of approximately 6 nm thickness.

4.4.2. Nanoparticle characterization

The stability of the gold nanoparticles diluted in the KCl translocation buffer was probed by UV-Vis measurements using a NanoDrop ND-1000 spectrophotometer (Thermo Scientific). The size distribution of the standard nanoparticles in solution was determined by Zetasizer NanoZS (Malvern Instruments Ltd.). Unless specified, all the standard nanosphere samples were used as received.

4.4.3. Nanopore fabrication and characterization

The nanopores were fabricated starting from 1.0 mm x 0.5 mm quartz capillaries (QF120-90-10; Sutter Instrument, UK) with the SU-P2000 laser puller (World Precision Instruments, UK), using a two-line program: (1) HEAT, 750; FILAMENT, 4, VELOCITY, 30; DELAY, 145, PULL, 80; (2) HEAT, 600, FILAMENT, 3; VELOCITY, 40; DELAY, 135; PULL, 150. The pulling parameters are instrument specific and lead to glass nanopore with a diameter of approximately 60 nm. Adjustments of the HEAT AND PULL parameters were made to fabricate other pore sizes specified in this study. The pulled glass nanopores were characterized by measuring their pore resistance in 0.1 M KCl and the pore dimensions were confirmed by Scanning Electron Microscopy (SEM) using a Nova NanoSEM at an accelerating voltage of 3–5 kV.

4.4.4. Nanopore translocation measurements

Unless otherwise specified, the translocation experiments were carried out by filling the glass nanopore with the translocation buffer (50 mM KCl, 0.01% Triton-X, 10 mM Tris, 1 mM EDTA, pH 8.0) containing the nanoparticles (25 µg/ml). The glass nanopore was then immersed in a similar buffer with the addition of 50% (w/v) Polyethylene Glycol (PEG) 35 kDa (ultrapure grade, Sigma Aldrich). The notation of the 50% PEG in the text refers to the utilization of 50% (w/v) Polyethylene Glycol (PEG) 35 kDa. An Ag/AgCl wire (0.25 mm diameter, GoodFellow UK) was inserted in the glass nanopore barrel and acted as the working electrode, while a second Ag/AgCl wire was immersed in the bath and acted as the counter and reference electrodes. The nanoparticles were driven from inside the glass nanopore into the external bath by applying a negative potential to the working electrode placed inside the glass nanopore with respect to the reference electrode in the bath. The ion current was recorded with a MultiClamp 700B patch-clamp amplifier (Molecular Devices) in voltage-clamp mode. Data was acquired at a 100 kHz sampling rate with a 20 kHz low-pass filter using the pClamp10 software (Molecular Devices). The ion current traces were further analyzed with the MATLAB script Transalyzer, developed by Plesa *et al.* (171). The obtained translocation events were analyzed by applying a 7-sigma threshold level from the baseline, and only the events above the threshold were considered as translocation events. The obtained events were further analyzed and plotted using Origin 2019b.

4.4.5. Gold nanostars synthesis and characterization

Gold nanostars synthesis and TEM characterization was conducted by Strobbia laboratory at the University of Cincinnati, USA. The samples were used as received.

First, citrate-capped gold nanoparticle (12 nm) seeds were synthesized using the Turkevich method (172). Briefly, 100 mL DI H_2O boiling water and 200 µL of 0.5 M $HAuCl_4$ were dispersed for 10 s. 15 mL of 1% trisodium citrate was added. After the final colour change, the solution was boiled for 15-30 minutes. Then the solution was cooled, filtered through a 0.22 µm nitrocellulose membrane, and stored at 4 °C until further use. The Au nanostars synthesis followed the Vo-Dinh group surfactant-free procedure with a few modifications (173). In brief, under room temperature and fast stirring, 10 mL of DI H_2O, 10 µL 1 M HCl, and 493 µL of 0.5 M $HAuCl_4$ were added to a plastic scintillation vial. Then, 100 µL of Au seeds were added, and 10 sec afterward quickly added $AgNO_3$ of various concentrations (1–3 mM; samples named S5, S10, and S30 relating to the AgNO3 final concentration, 5 µM, 10 µM, and 30 µM, respectively) and 50 µL of 0.1 M AA (ascorbic acid), simultaneously. After the Au nanostar synthesis, 325 µL of thiol stabilizer (HS-PEG-COOH) was added to the Au nanostars, vortexed, then idle for 30 min at room temperature. After 30 minutes, the solution was centrifuged and washed three times with DI H_2O (1500 g, 15 min, 4 °C). Lastly, the samples were redispersed in DI H_2O and stored at 4 °C until used. Au Nanostars with thiol stabilizer were prepared for imaging by dropping 10 µL of 2-fold diluted sample onto a 200-mesh grid. The sample was allowed to dry overnight at room temperature. Then transmission electron microscope (TEM; Hitachi H7650) imaging was performed at 80 kV with an AMT BIOSPR16. To determine the size and concentration were measured via NanoSight NS300 nanoparticle tracking analysis (NTA) system with a 532 nm laser. 20-, 40-, and 80-fold dilutions of the samples were used for the measurements. Extinction spectra of the samples were collected via a Biotek Microplate reader.

4.4.6. ProSNA synthesis and characterization

ProSNA synthesis and characterization was conducted by Samanta laboratory at the University of Austin, USA. The samples were used as received. β-galactosidase SNAs were synthesized by following previously established procedures with some modifications (26,27). Briefly, surface cysteine groups are first modified with Alexa Fluor 647 C_2 maleimide. Following this step, NHS-PEG_4-azides are conjugated to the surface-

accessible lysine residues. Finally, DBCO-terminated DNA is attached to the azide-modified proteins through copper-free click chemistry. A stock solution of β-gal (Sigma) was exchanged into DPBS (Sigma) through centrifuge filtration (15000 rpm, 3 min, 4 °C), three times washing using a centrifuge (Thermo Fisher) using 100 kDa MWCO Amicon filters (Thermo Fisher). The β-gal was then treated with TCEP (4 nM final concentration) to reduce the disulphide bonds and vortexed. Thereafter, the solution was passed through a NAP-5 column to remove the TCEP and the purified β-gal solution was concentrated using a 100 kDa MWCO Amicon filter. The protein concentration was determined via UV-vis spectroscopy using the extinction coefficient at the characteristic protein peak at 280 nm. Then 30-fold molar excess of Alexa Fluor 647 C_2 Maleimide (AF-647, Thermo Fisher, Invitrogen,) was added to the protein and the mixture was shaken overnight (1000 rpm, 4 °C) using a Benchmark MultiTherm Heating and Cooling Shaker (Marshall Scientific). The solution was then rinsed multiple times with 0.1 M $NaHCO_3$ (Thermo Fisher) using a 100 kDa MWCO Amicon filter to remove any unreacted dye. The absorbance of the filtrate was monitored at 650 nm to track the free dye. The washing was stopped when the absorbance at 650 nm was negligible.

Using UV-vis spectroscopy, the concentration of the protein ($c_{\beta-gal}$) and the number of dyes attached per protein (N_{dye}) were calculated using Equations 4.1 and 4.2:

$$c_{\beta-gal} = \frac{A_{280\ nm} - \varepsilon_{280\ nm}^{AF-647} c_{AF-647}}{\varepsilon_{280\ nm}^{\beta-Gal}} \quad \text{(Eq. 4.1)}$$

$$N_{dye} = \frac{c_{AF-647}}{c_{\beta-gal}} \quad \text{(Eq. 4.2)}$$

c_{AF-647} is first determined using Equation 4.1, where $\varepsilon_{650\ nm}^{AF-647}$ = 270,000 M^{-1} cm^{-1}. The value for $\varepsilon_{280\ nm}^{AF-647}$ is 8,100 M^{-1} cm^{-1}.

Thereafter, NHS-PEG_4-azide (Thermo Scientific) was added to the dye-labelled β-gal (β-gal-AF) at 1000-fold molar excess and the reaction was incubated for 1.5 hrs with shaking (1000 rpm, RT). The reaction mixture was then run through a NAP-25 column (Cytiva illustra) and washed 5 times using centrifuge filtration (100 kDa MWCO Amicon filters, 15000 rpm, 4 °C, 3 min per wash) to separate any free azide molecules. The protein concentration of the product (β-gal-AF-azide) was again determined via UV-vis spectroscopy. Then 50-fold molar excess of DBCO-DNA was added to β-gal-AF-azide (samples were prepared with both DBCO-DNA 1 and DBCO-DNA 2; see Table 4.1 for

sequences). The reaction was shaken for 3 days (1000 rpm, RT), following which the reaction mixture was washed several times using PBS and 100 kDa MWCO Amicon filters (15000 rpm, 4 ℃, 6 min per wash) to remove free DNA. The final product (β-gal SNAs) was characterized by UV-vis spectroscopy. First, based on the absorbance at 647 nm, c_{AF-647} was first determined. Then, using Equation 4.2, $c_{\beta-gal}$ was determined. Subsequently, using the absorbance at 260 nm, the number of DNA per protein (N_{DNA}) was determined using Equation 4.3:

$$N_{DNA} = \frac{A_{260\ nm} - \varepsilon_{260\ nm}^{\beta-Gal} c_{\beta-gal}}{\varepsilon_{260\ nm}^{DNA} c_{\beta-gal}} \quad \text{(Eq. 4.3)}$$

Table 4.1: DNA sequences used for ProSNA samples.

Sequence name	Sequence (5'-3')	ε_{260} ($M^{-1}cm^{-1}$)	Expected mass (m/z)	Observed mass (m/z)
DBCO-DNA 1	DBCO TEG-TTTT AAG ACG AAT ATT TAA GAA	240,800	7351	7250
DBCO-DNA 2	DBCO TEG-TTTT AAC GAC TCA TAT TAA CAA	228,600	7247	7162
Thiol-DNA	C6-SS-AAG ACG AAT ATT TAA GAA	200,500	5760	5787

C6-SS: Thiol-Modifier C6 S-S (1-O-Dimethoxytrityl-hexyl-disulfide,1'-[(2-cyanoethyl)-(N,N-diisopropyl)]-phosphoramidite)

DBCO-TEG: 5'-DBCO-TEG Phosphoramidite (10-(6-oxo-6-(dibenzo[b,f]azacyclooct-4-yn-1-yl)-capramido-N-ethyl)-O-triethyleneglycol-1-[(2-cyanoethyl)-(N,N-diisopropyl)]-phosphoramidite)

4.5. Results & discussion

4.5.1. Characterization of spherical nanoparticles

In this study, the discrimination of nanoparticles was probed by means of solid-state nanopores. It has been previously shown that the use solid-state nanopore systems based on polymer nanopore enhances signals when biological macromolecules are analysed (*e.g.*, DNA, see Chapter 3) (60,109). Considering that many of the synthetic nanomaterials are of comparable dimensions, we hypothesized that this nanopore approach can be tailored for the analysis of different nanoparticles and discriminate them on the basis of the recorded ion current. To investigate this hypothesis, PEG-carboxyl gold spherical nanoparticles (AuNPs) were first utilized for the nanopore translocation experiments. One requirement for performing nanopore measurements is the use of electrolyte solution (typically KCl). Prior to nanopore measurements, the stability of the AuNPs was assessed. The AuNPs stability was assessed by diluting the nanoparticles in a 100 mM KCl buffer solution buffered at pH 8.0. The carboxyl acid provides a highly negatively charge surface of the nanoparticle, being the highest at basic pH due to the low isoelectric point, making it favourable for electrophoretically driving the nanoparticles through the nanopore. If the nanoparticles are stable when diluted in the buffer with a particular salt concentration, the measured spectrum of the nanoparticles measured in the salt buffer and pure water is expected to be the same. However, if the particles aggregate, this would be reflected in their spectrum, showing a decrease in the absorbance peak and an increase at longer wavelengths. The UV-Vis measurement after 1 hr incubation in 100 mM KCl of the AuNPs showed no red shift or suppression of the absorbance peak recorded. This was further compared with the same suspension of the AuNPs prepared in water (**Error! Reference source not found.**A). S imilarly, the AuNPs suspension was measured by DLS (**Error! Reference source not found.**B), showing no broadening of the size distribution (hydrodynamic diameter) of the nanoparticle, or the presence of aggregates. All in all, the AuNPs chosen in this study was found to be stable in the electrolyte solution. The ionic strength of the KCl buffer and the incubation period used for the stability assessment exceeded the nanopore measurement conditions (ionic strength and incubation time) and therefore can be regarded as a worst-case scenario.

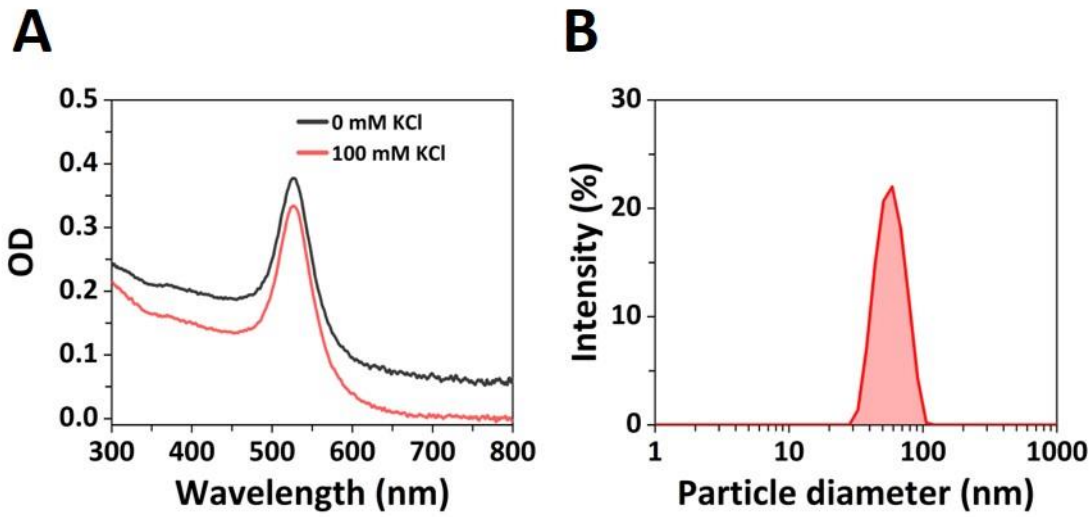

Figure 4.1: Stability assessment AuNP suspended in 100 mM KCl buffer solution. **(A)** UV-Vis spectra of 50 nm PEG carboxyl-capped AuNPs in 100 mM KCl buffer solution measured after 1 hr incubation (red line) compared with a preparation in Milli-Q water (black line). A similar spectrum is observed in both cases indicating that the nanoparticles in 100 mM KCl buffer solution are stable for >1 hr. **(B)** Dynamic light scattering (DLS) measured size distribution (hydrodynamic diameter) of nominally 50 nm diameter PEG carboxyl-capped AuNPs measured in 100 mM KCl after 1 hr incubation.

4.5.2. Enhanced detection of spherical nanoparticles

In this work, a polymer electrolyte nanopore system (57) was used to enable the detection of heterogenous nanoparticle mixtures with a fixed nanopore size (diameter) (109). Glass nanopores with a diameter of 60 nm were fabricated by mean of laser-pulling nanopipettes. A representative SEM image of the nanopore and current-voltage of nanopores from different pulls recorded in 0.1M KCl are depicted in Figure 4.2.

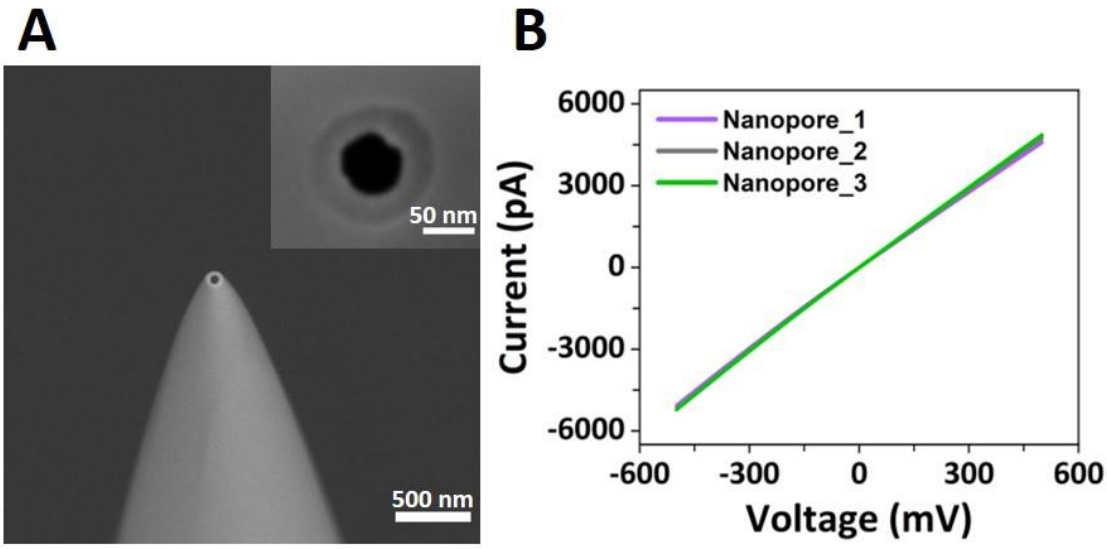

Figure 4.2: Representative nanopore characterization. **(A)** Scanning electron micrograph of a representative glass nanopores used in this study. Inset: top view of the nanopore tip showing that it has a ~60 nm internal diameter. Note: The micrograph foreshortens depth resulting in an exaggerated angle of the pipette wall **(B)** Current-voltage curves (I-V) of three glass nanopores recorded in 100 mM KCl. All three pipettes were pulled with an identical program which gave ~60 nm pores, such as the one shown in panel A.

The translocation of uniform 20 nm gold spherical nanoparticles (AuNPs) sample was probed utilizing a glass nanopore-based system with a tailored pore size diameter. The TEM image in Figure 4.3 depicts the uniform spherical nanoparticles, confirming their diameter size.

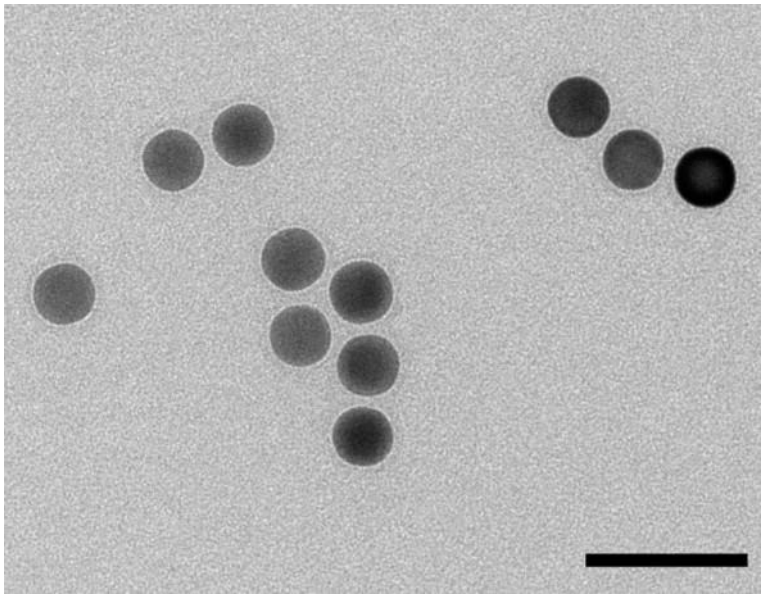

Figure 4.3: TEM image of 20 nm diameter gold spherical nanoparticles. Scale bar TEM graph: 50 nm.

The translocation of 20 nm gold spherical nanoparticles (AuNPs) samples was investigated under an applied voltage of -500 mV. As depicted in Figure 4.4, the nanopore setup consisted of a nanopipette filled with and immersed in an electrolyte (KCl) solution where the application of a potential between a pair of Ag/AgCl electrodes, inside the glass pore and external bath respectively, drive the translocation of the analyte towards the external bath. As shown in Figure 4.4A, no translocation events were observed for the 20 nm AuNPs using standard electrolyte buffer conditions (*i.e.* 50mM KCl solution) due to the large pore with respect to the diameter of the AuNPs. However, the addition of 50% w/v PEG (polymer electrolyte) to the outer bath resulted in conductive (current-enhancing) translocation events well-resolved from the ion current baseline (Figure 4.4B). These events are characterised by a specific conductive peak maxima amplitude (ΔI_c) and dwell time (as shown in Figure 4.4B inset), where each peak is generated by individual nanoparticles translocating from inside the pore to the outer bath. The enhanced detection approach by adapting the external bath conditions of the nanopore setup proved to be easy-to-implement and reproducible, leading to the recording of several hundreds of events in several minutes. Compared to other methods for increasing detection of molecules (174), our method solely relies on adjusting the external bath conditions, therefore excluding potential interferences related to the nanoparticle samples investigated. Utilizing a concentration of 50% 35K PEG in the external electrolyte bath was adopted and kept constant throughout all the nanopore measurements, as it was previously demonstrated to provide the highest SNR (signal-to-noise ratio) (57,109).

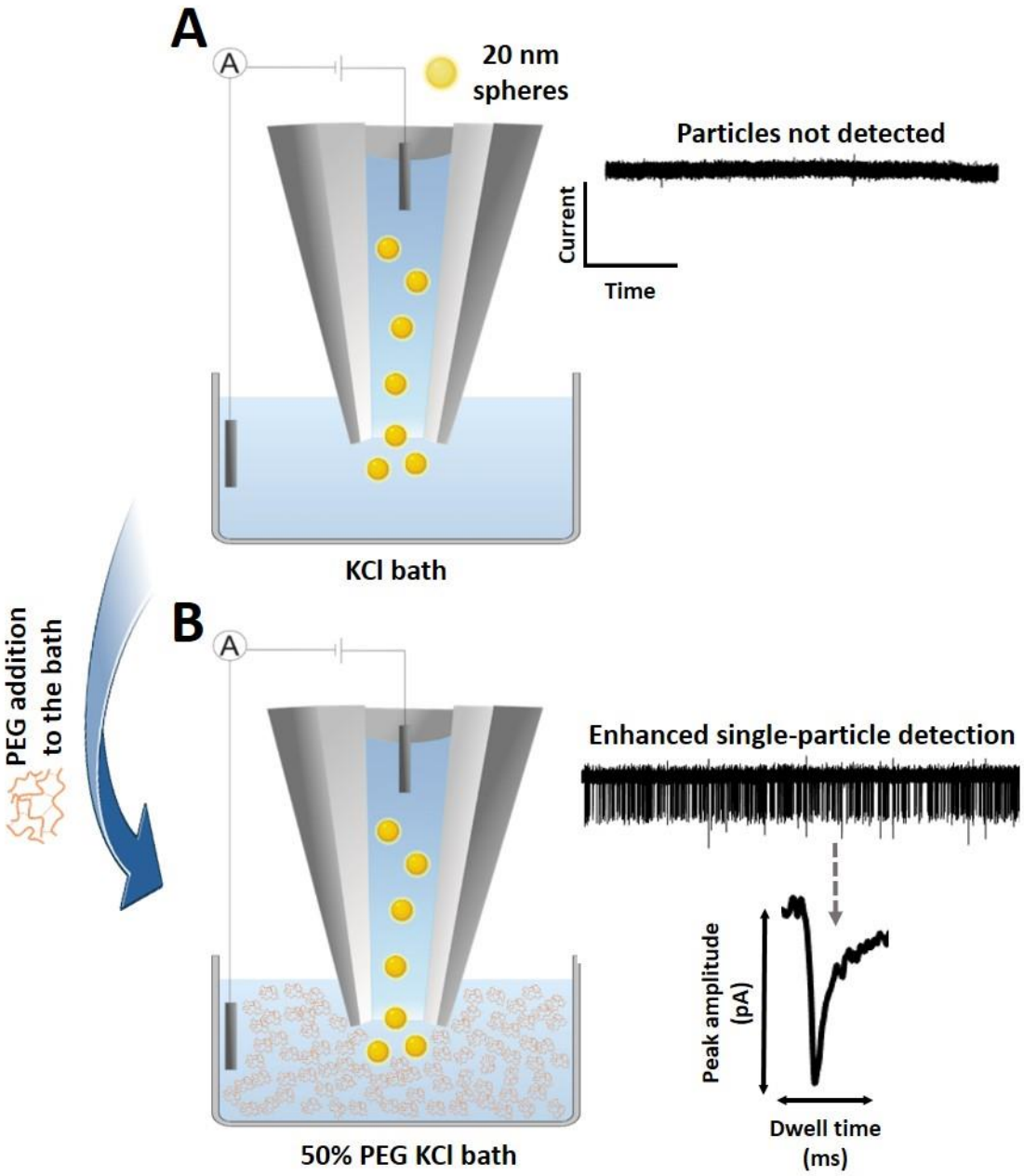

Figure 4.4: Enhanced nanoparticle detection in polymer electrolyte bath. **(A)** Schematic illustration depicting 20 nm AuNPs translocating across the nanopore towards the outer bath into the outside and the recorded ion current trace at -500 mV for 20 nm AuNPs utilizing a 50 mM KCl external electrolyte bath and a 60 nm diameter pore. No translocation events were observed under these conditions. **(B)** Representative translocation setup depicting the use of 50% (w/v) PEG (polymer electrolyte) in 50 mM KCl in the external electrolyte bath with the corresponding recorded ion current trace at -500 mV, showing conductive translocation events for 20 nm AuNPs. A representative translocation event is shown in the inset with the translocation peak amplitude and dwell time characteristics.

The translocation characteristics of the 20 nm AuNPs was first studied. Control experiments were conducted to confirm that the recorded peaks from ion current traces are associated with the translocation of AuNPs. No events were observed in absence of nanoparticles in solution (Figure 4.5A) or under the application of a positive voltage (Figure 4.5C). Furthermore, no translocation events were observed under no-bias conditions (Figure 4.5D).

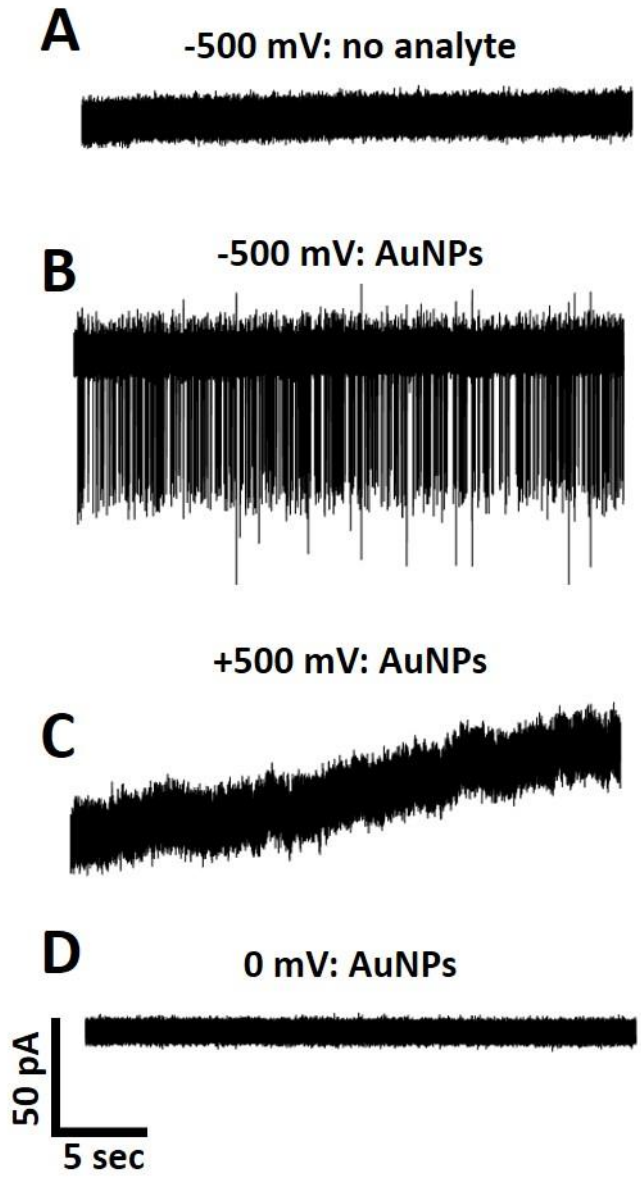

Figure 4.5: Ion current traces recorded with a 60 nm diameter glass nanopore in a bath solution containing 50% PEG in 50 mM KCl. The glass nanopore was biased at **(A)** -500 mV when no analyte was added inside the glass nanopore; **(B)** -500 mV when 20 nm diameter PEG carboxyl-capped AuNPs were added inside the nanopipette; **(C)** +500 mV when 20 nm diameter AuNPs were added inside the glass nanopore; **(D)** 0 mV when 20 nm diameter AuNPs were added inside the glass nanopore. The current and timescales are the same for all graphs. A concentration of 25 µg/mL was used for the recordings with 20 nm diameter AuNPs.

Furthermore, in Figure 4.6, a plot of the power spectral density depicts the noise profile for measurements with and without the addition of PEG to the external bath, showing similar noise characteristics.

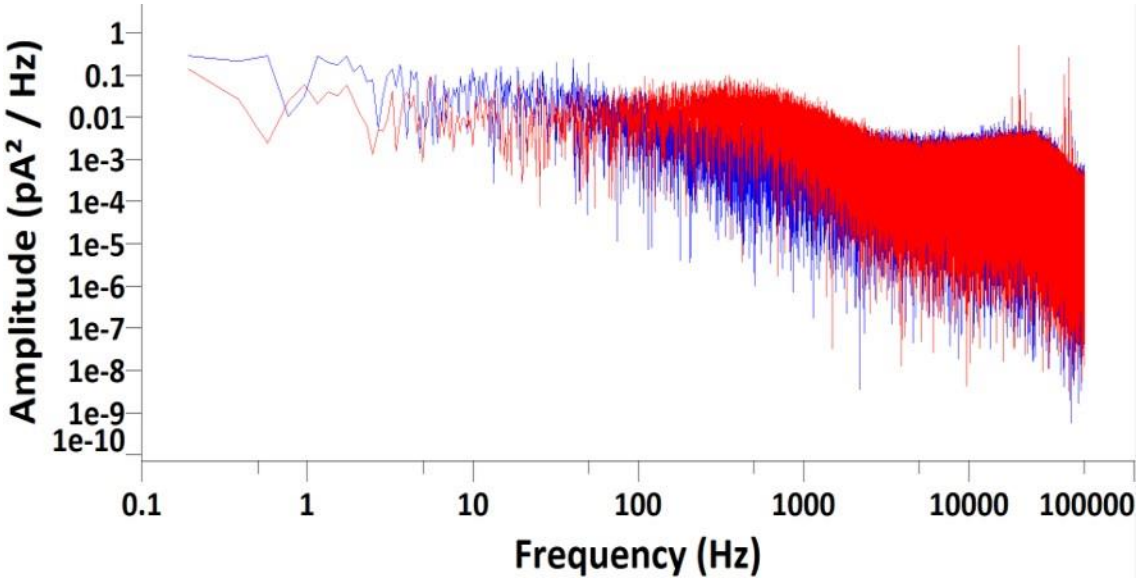

Figure 4.6: Power spectrum density plot of 60 nm diameter pore biased at -500 mV with 50 mM KCl (blue trace) and 50% PEG and 50 mM KCl (red trace) external bath solution.

Apart from the control experiments shown above, statistical histograms of the amplitude and dwell time events at different voltages events are displayed for translocation of 20 nm AuNPs. The translocation events were normalized to the event count for each recording. Increasing the magnitude of the applied voltage led to an increase in amplitude of the conductive peak current and a decrease in the dwell time, suggesting that the electrophoretic force plays a major contribution in driving the negatively charged AuNPs through the pore (Figure 4.7A-D). Statistical histograms of the amplitude and dwell time events at different voltages events are displayed in Figure 4.7A and Figure 4.7C. The voltage dependence suggested that the recorded current signals are the result of particle translocations through the nanopore, rather that binding or accumulation of particles at the orifice. Similarly, a linear increase in the frequency of the translocation events was observed with increasing voltage and increasing nanoparticle concentrations (Figure 4.7E-F).

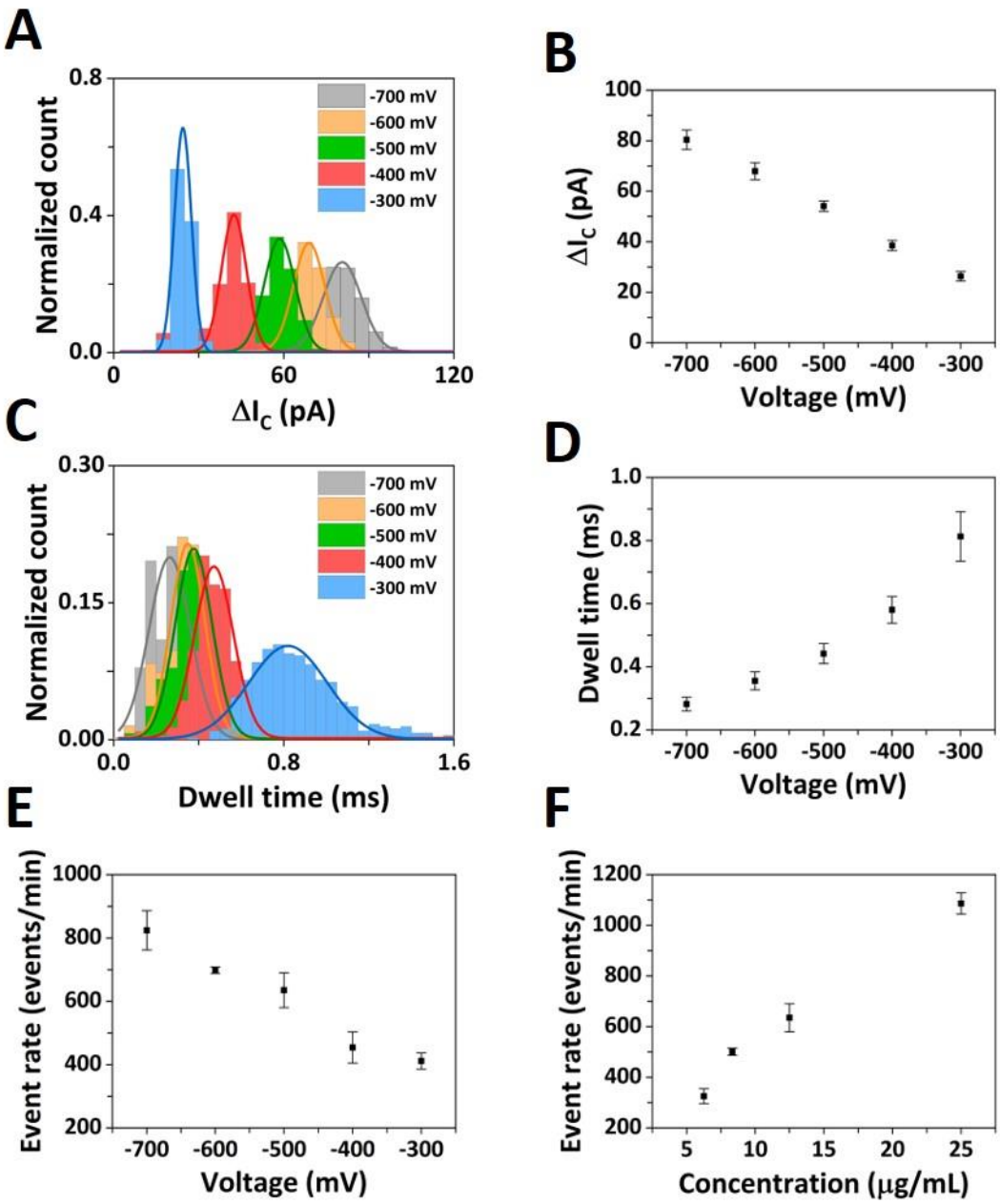

Figure 4.7: Translocation event characteristics of 20 nm diameter PEG carboxyl-capped AuNPs translocating through a ~60 nm diameter pore with 50% PEG in 50 mM KCl external bath. Histograms of the conductive peak current **(A)** and dwell time **(C)** distributions for applied voltages V = 300 mV, -400 mV, -500 mV, -600 mV, and -700 mV. The solid lines represent Gaussian fits to the distributions. Average conductive peak current **(B)** and dwell time **(D)** at V = -300 mV, -400 mV, -500 mV, -600 mV, and -700 mV. Error bars show the standard deviation from three independent recordings with different pulled glass nanopores. The conductive current peaks were larger with increasingly negative voltages, while the dwell times shortened. **(E)** Event rate of the 20 nm diameter AuNPs translocation as a function of voltage. **(F)** Event rate of the 20 nm diameter AuNPs translocation as function of the sample concentration 6, 8, 12, and 25 μg/mL which correspond to concentrations of 1.4×10^9, 1.1×10^{10}, 7.1×10^{10}, and 3.1×10^{10} particles/mL (calculated assuming all particles have the same average diameter). Error bars show the standard deviation from three independent recordings with different pulled glass nanopores.

To better interpret the enhanced detection effect described here, pores with similar diameter (60 nm) were utilized to translocate different AuNPs samples (50 nm, 20 nm, and a mixture of 50 and 20 nm AuNPs) both in KCl and 50% PEG and KCl, by switching external bath where the glass pore is immersed into. These results are depicted in Figure 4.8, where a dramatic increase in the SNR of the translocation peaks can be observed between the no PEG case and when PEG is added to external electrolyte bath.

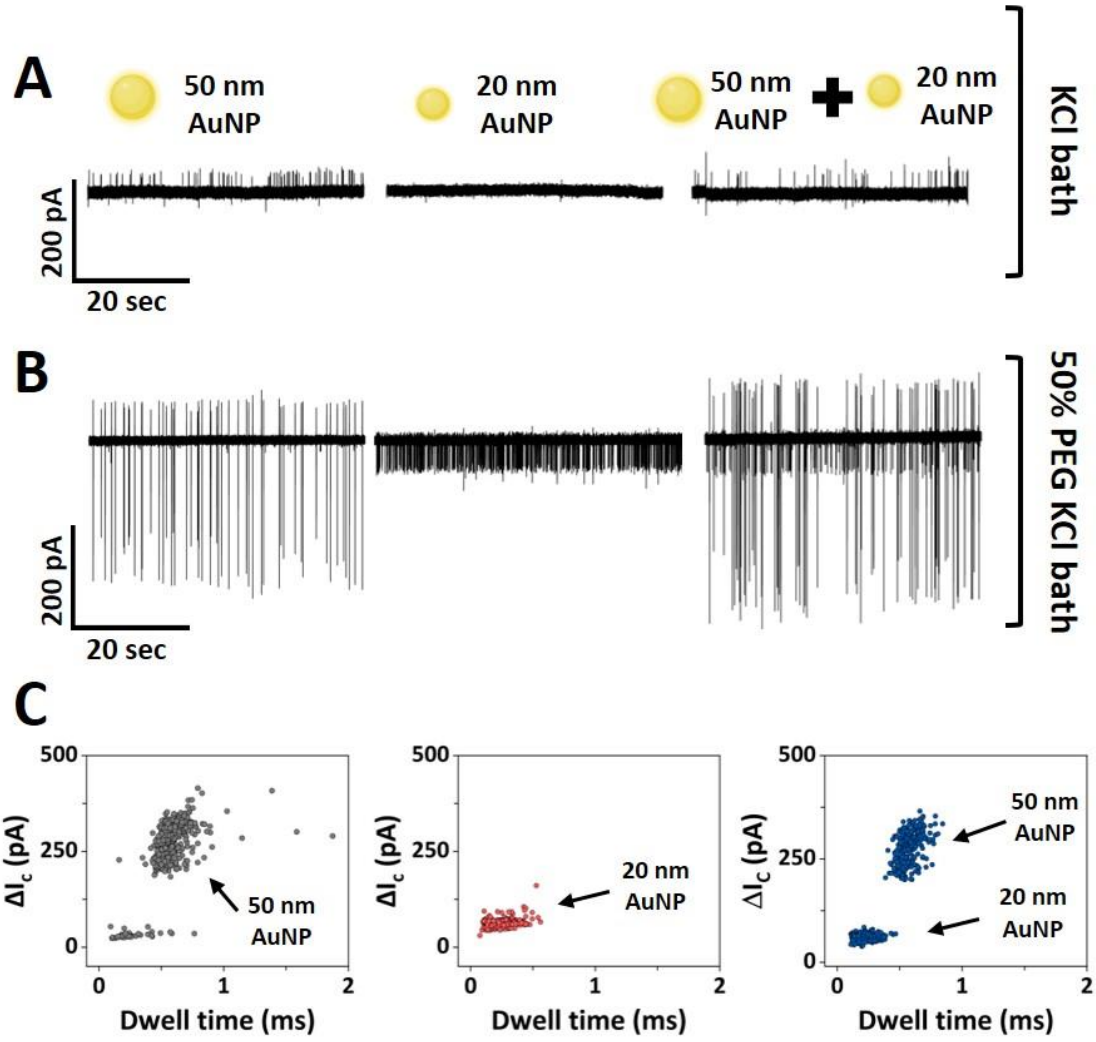

Figure 4.8: Ion current traces of nanoparticle translocations through a ~60 nm diameter pore in which the external electrolyte bath was either **(A)** 50 mM KCl or **(B)** 50 mM KCl + 50% PEG. The inside of the nanopore contained PEG carboxyl-capped AuNPs of 50 nm diameter (left), 20 nm diameter (middle), or a mixture of a 50 nm and 20 nm diameter (right). Single glass nanopores (~60 nm diameter) was used for each nanoparticle mixture in the two conditions. In the absence of PEG in the bath solution 20 nm AuNPs translocation peaks are not resolved from the current baseline. The current and time scales are the same for all the ion current traces in panels A and B. In all cases, the glass nanopore contained 50 mM KCl without PEG. **(C)** Scatter plots of the conductive peak current (ΔI_C) versus dwell time of the translocation events extracted from the ion current traces in panel (B). Ion current traces were recorded at -500 mV. The concentration of the individual AuNPs (50 nm and 20 nm AuNPs) was 25 µg/mL, whereas the 50 nm and 20 nm AuNP mixture was recorded at mixture ratio of 10:1 50-to-20 nm AuNPs

Interestingly, for larger diameter AuNPs (50 nm) that closely match the diameter of the pore, a change from resistive peaks (current reducing signals) to biphasic signal (resistive and conductive peaks) was observed when PEG was used in the externa bath. This is exemplified in Figure 4.8A-B where in both cases, 50 nm AuNPs and 50 nm AuNPs artificially mixed with 20 nm AuNPs, a strong biphasic signal can be observed. The ion current traces in Figure 4.8B show a clear discrimination regarding the current amplitude of the conductive signals recorded for the two sets of AuNPs (50 and 20 nm diameter) with similar pore diameter, that also resulted in distinct populations in the events scatter plots (Figure 4.8C). The average conductive peak amplitude was 61.1 ± 1 pA for the 20 nm AuNPs and 225 ± 1 pA for the 50 nm AuNPs. In order to demonstrate the reproducibility of the enhanced effect observed in 50% PEG and KCl conditions, the translocation of 50 nm AuNPs was carried with three different nanopores having a 60 nm nominal pore diameter. As displayed in the ion current traces and the individual translocation peaks in Figure 4.9, a similar enhanced effect was observed in the case of all three different pulled glass nanopores with similar pore diameter (60 nm). The large amplitude difference denotes the strong signal enhancement generated by the polymer electrolyte that allowed the analysis of a range of different AuNPs with a fixed nanopore size (60 nm in diameter), as further exemplified in the following sections.

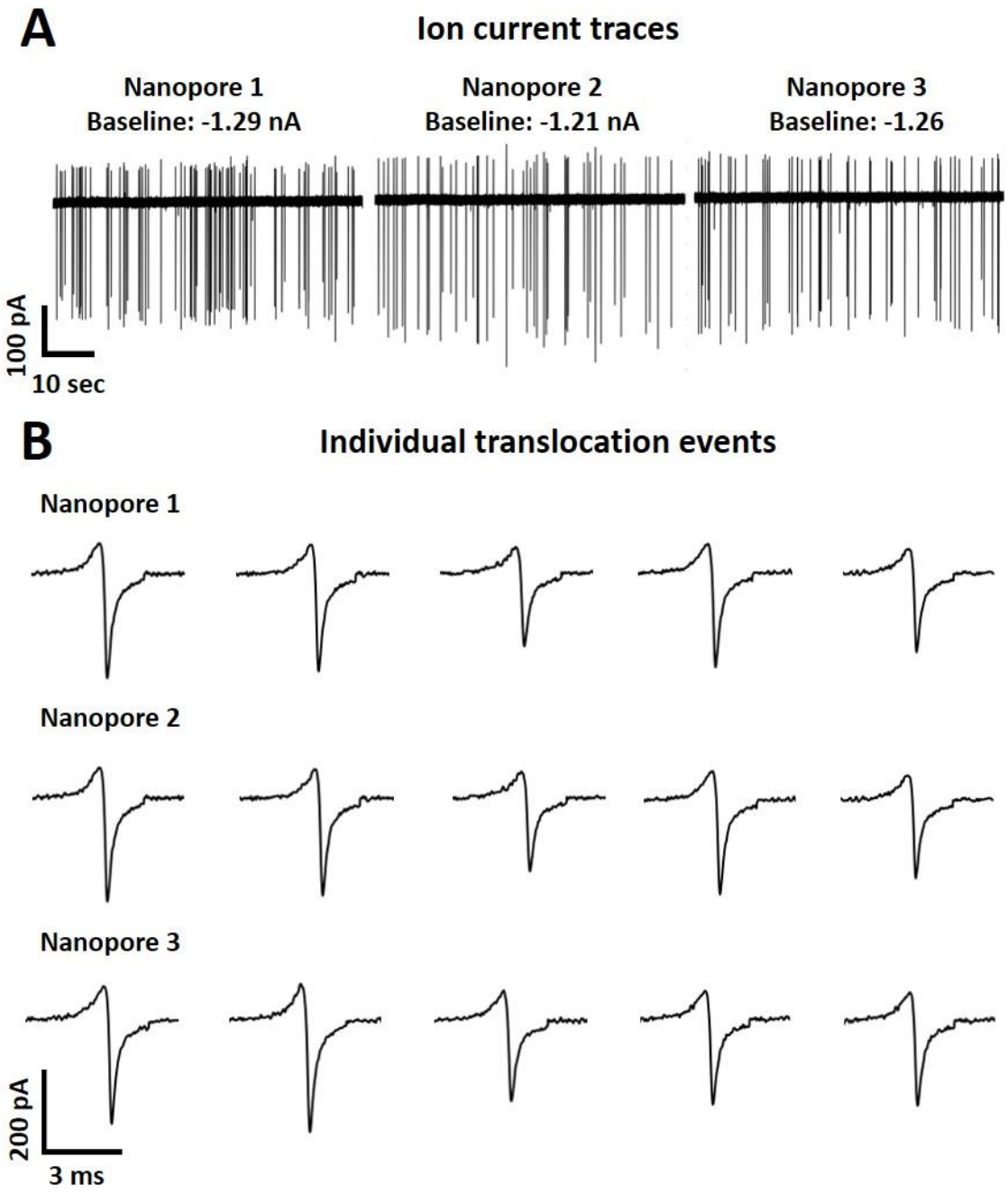

Figure 4.9: Enhanced translocation signal reproducibility of 50 nm AuNPs. **(A)** Ion current traces obtained with three different glass nanopores. All the ion current traces were adjusted to the same current and time scale. **(B)** Consecutive translocation events extracted from ion current traces recorded in (A) with three different glass nanopores. All the individual translocation events have the same current and time scales. Nanopore recordings were carried out using 60 nm diameter pore sizes and 50 nm diameter AuNPs translocated in 50% PEG and 50mM KCl and biased at -500 mV. A reproducible effect of the enhanced translocation signal can be observed.

4.5.3. Enhanced detection of nanoparticle mixtures

Following the detection of two sets of the AuNPs (50 and 20 nm) analysed with the electrolyte nanopore platform, this analysis was further extended to a range of uniform AuNPs suspensions with different diameters, ranging from 10 nm to 50 nm. Similarly, a fixed pore size (60 nm diameter) was utilized for each set of AuNPs. The corresponding ion current traces recorded for each set of AuNPS are shown in Figure 4.10, showing clear differences in terms of the amplitude magnitude of the each AuNPs set analysed.

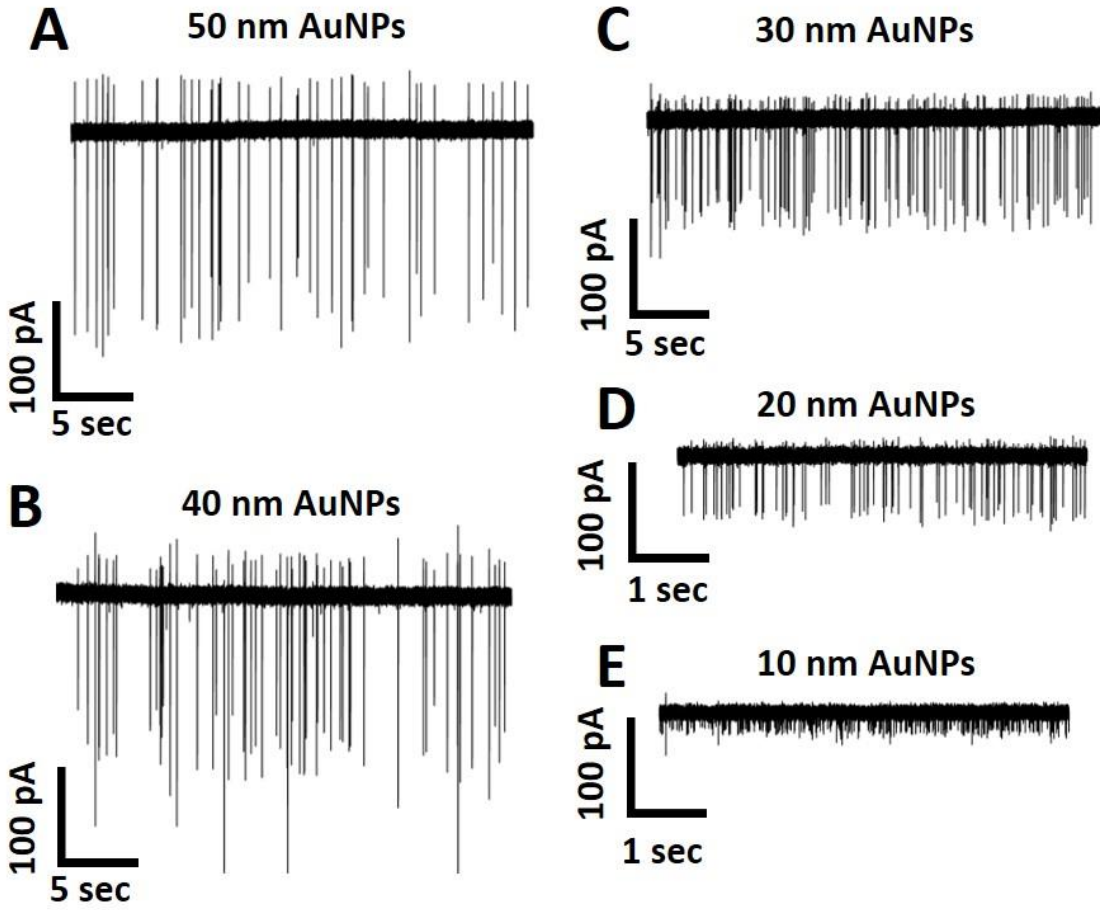

Figure 4.10: Ion current traces for PEG-carboxyl capped AuNP samples translocated through 60 nm diameter nanopores into an electrolyte bath of 50% PEG in 50 mM KCl. The pipettes were biased at -500 mV and filled with 50 mM KCl containing **(A)** 50 nm diameter AuNPs; **(B)** 40 nm diameter AuNPs; **(C)** 30 nm diameter AuNPs; **(D)** 20 nm diameter AuNPs; **(E)** 10 nm diameter AuNPs; or **(F)** or a mixture containing: 10, 20, 30, 40, and 50 nm AuNPs. All the ion current traces have the same current scale; however, parts D and E have a shorter timescale to allow showing the higher translocation frequency. Optimization of the event rate has not been a focus in this study. The nanoparticles concentrations in panels (A)-(E) were 25 µg/mL.

The individual signals obtained for each set of AuNPs was analysed. Whereas the conductive peak represents the dominant feature in the ion current signatures, a distinct change in the translocation signature was observed when different nanoparticle to pore size ratios were employed. Namely, when the size of the nanoparticle closely matched the size of the pore, an additional resistive peak was observed. This behaviour is evidenced in Table 4.2 and Figure 4.11A, where a biphasic (resistive and conductive peak) signal transitions to a conductive signal when the size of the AuNP decreases with respect to the size of the pore.

Table 4.2: Average conductive (ΔI_C) and resistive (ΔI_R) peak current values with the standard error (SE) obtained for PEG-carboxyl capped AuNP samples translocating through ~60 nm diameter nanopores into an electrolyte bath containing 50% PEG and 50 mM KCl. The pipette was biased at -500 mV, and filled with a solution containing 50 mM KCl and 25 µg/mL of nanoparticles. Note: we were unable to measure resistive peaks for the 10 and 20 nm diameter particles under these conditions. Each value shows the results based on a single nanopore recording with number of translocated events displayed in the table.

Pore diameter (nm)	NP diameter (nm)	NP diameter / pore diameter	Translocated events	$\Delta I_C \pm SE$ (pA)	$\Delta I_R \pm SE$ (pA)
60	50	0.83	286	225 ± 1	71 ± 1
	40	0.67	469	160 ± 2	37 ± 1
	30	0.50	937	98 ± 1	24 ± 1
	20	0.33	1132	61 ± 1	-
	10	0.17	1715	21 ± 1	-

The translocation signal distributions of each set of AuNPs were fitted to Gaussian curves which enabled the identification of 5 distinct populations, one for each nanoparticle set (Figure 4.11B). The average conductive peak current increased with the ratio of nanoparticle to pore diameter (d_{NP}/d_{pore}), as shown in Figure 4.11C.

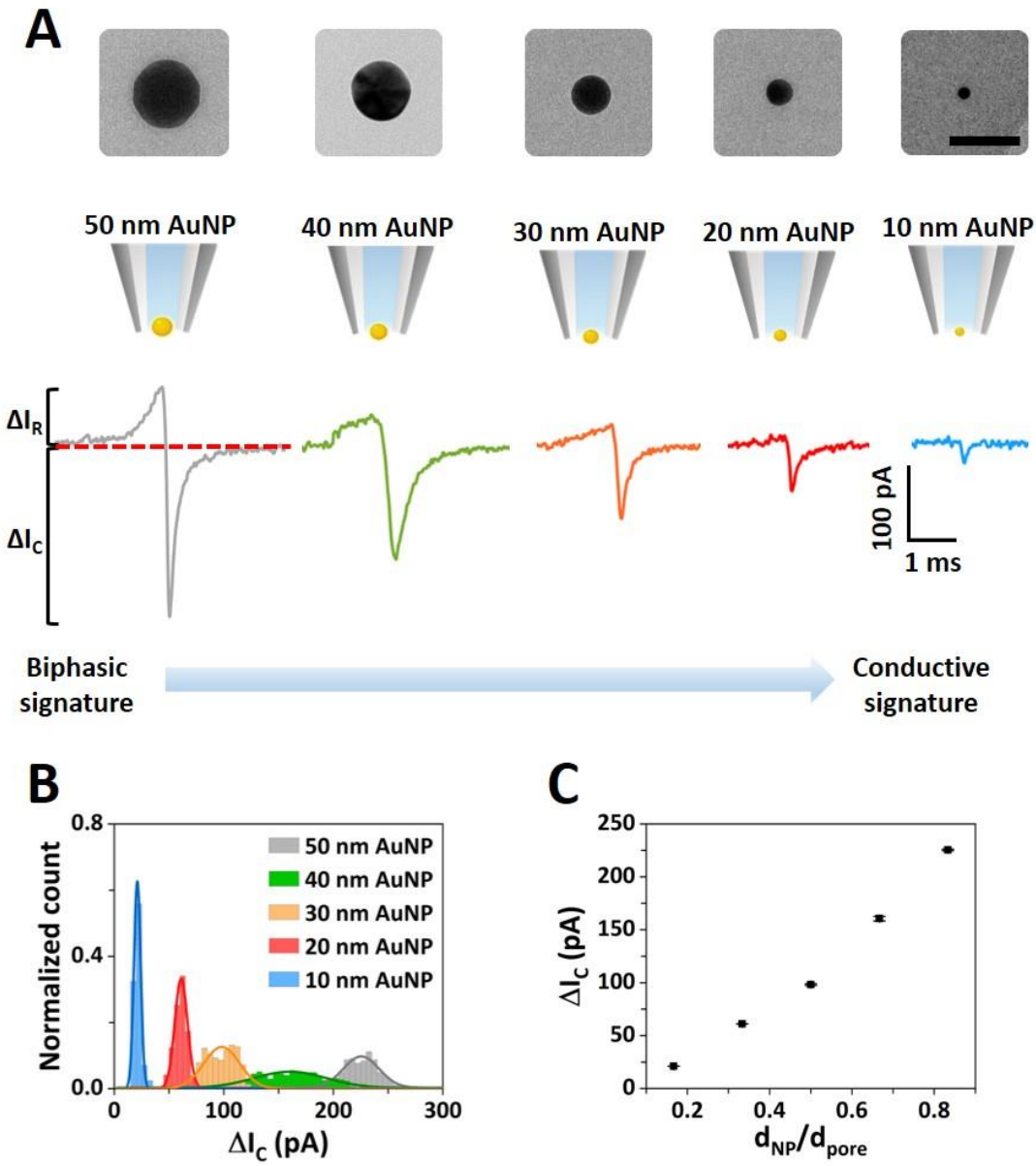

Figure 4.11: Nanopore detection of gold nanoparticle mixtures. **(A)** Top panel: TEM images of the standard AuNPs, left-to-right: 50, 40, 30, 20, and 10 nm diameter (50 nm scale bar). Bottom panel: schematic representation of the AuNP translocating through a 60nm fixed pore size with representative individual translocation peaks for each AuNP, denoting a transition from biphasic to conductive signature when the ratio of nanoparticle to pore size decreases. **(B)** Event histogram of the conductive peak current for the 5 different AuNPs (50, 40, 30, 20, and 10 nm) translocated with a fixed pore size (60 nm). The solid lines represent Gaussian fits to each translocation data set. The distribution of the 40nm sample is wider because of a 15% coefficient of variation of the nanoparticle size compared to 5% for the other samples. **(C)** Average conductive peak current as a function d_{Np}/d_{pore}. The error bars represent the standard error of the Gaussian fits displayed in panel B.

Conventionally, nanoparticle analysis with nanopores leads to resistive (current-decreasing) translocation signals because of the ion flow hindrance by the presence of

the nanoparticle within the nanopore region resulting in a volume-exclusion of ions (175). However, several studies have shown the occurrence of conductive peaks when translocation of charged analytes was carried out in low ionic strength buffers, due to the introduction of new ions brought by the ion cloud of the charged particles which temporarily increases the pore conductivity (176-178). The formation of biphasic signals (resistive and conductive peaks) has been reported as well. In this case, it has been proposed that this signal stems from two main competing effects: the geometric volume exclusion of ions by the particle generating a resistive pulse, and the local increase in pore conductivity due to the screening of the particle traversing the pore (179). Nevertheless, the magnitude of the resistive and conductive peaks can be influenced by several factors, including the electrolyte concentration, nanoparticle to pore size ratio, and the nanoparticle surface charge (177). Sensale *et al.,* identified the surface charge of the particle as the main factor that influences the characteristics of the translocation signal through the glass nanopores (180). The authors suggested that this phenomenon occurs due to an ion accumulation/depletion associated with the surface charge of the particle translocating through the pore, overriding the volume-exclusion effect. Similarly, in the studies conducted by Menestrina *et al*. and Chen *et al*., biphasic signals were reported both experimentally and in simulations when charged particles are translocated through in low-salt buffer conditions (below 200 mM KCl) (181,182). The authors reported resistive peaks followed by a conductive component and explained the effect considering the charge carried by the analyte that causes a temporary ion enrichment at the aperture when low-salt conditions are used. Although, similar behaviour has been reported in this study, the magnitude of the conductive peak proves to be much larger in case of PEG electrolyte bath. Similar to what has been reported before, the presence of PEG in the external bath induces an ion depletion at the region of the tip at negative applied bias, as shown in the voltammogram in Figure 4.11. This has been suggested to be the effect of cation transport hindrance due to the PEG binding of cations in the external bath (57,109). Under such conditions, the counter-ion cloud carried by the charged particle contributes to the temporal increased in the local ion concentration at the tip region during translocation events, explaining the presence of the conductive (current enhancing) signals.

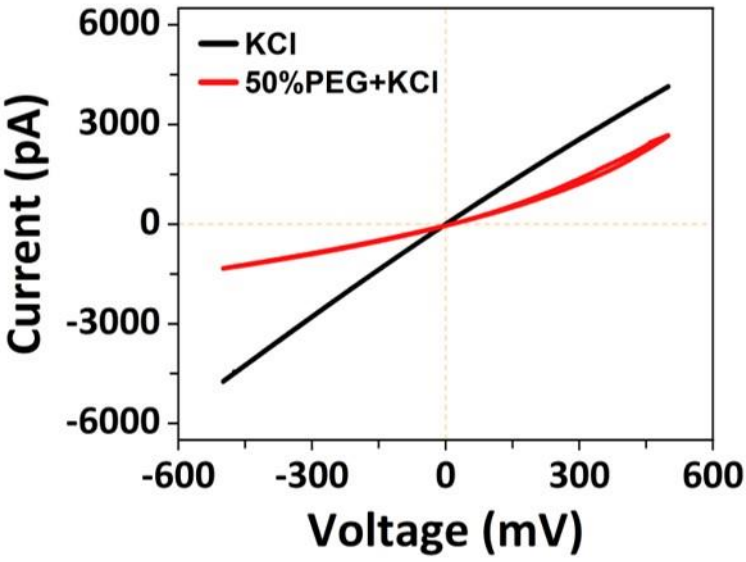

Figure 4.12: Voltammograms of a nanopipette in the presence of 50% PEG (red line) and absence (black line) in the 50 mM KCl external bath. The slightly higher conductivity at negative bias in the KCl only bath is due to the negatively charged glass wall of the nanopipette, which makes it permselective to cations, as previously described for glass nanopores (183). In the presence of PEG in the external electrolyte bath the ion current response at the negative bias is ~ 4 times lower than the conditions without PEG in the external bath. The conductivity of the external electrolyte bath was ~7 less conductive with the addition of PEG (0.09 S/m), compared with the condition in the absence of PEG (0.6 S/m).

Furthermore, in a recently reported mechanistic study from our group on the role of PEG on the translocation signal enhancement it was suggested that an interface is formed at the nanopore tip between the inner and outer solution (KCl only and the polymer electrolyte bath) (110). Here, it has been proposed that the interface at the aperture is deformed by translocating particles from inside the pore into the outer bath and this deformation induces an ionic rearrangement that plays a role in the ion enrichment at the aperture, in addition to the screening effect of the charged particle. Although, the conductive component proves to be the dominant feature here, the experimental results presented here suggest that when the dimensions of the particle and the pore diameter closely match, the geometry volume-exclusion effect contributes to the ion current signal modulation as well (Figure 4.9A). Sensale *et al.,* also suggested a potential ion cloud distortion around the charged translocating particle due to the applied electric field, leading to a tail of the counter-ions, where the translocating particle first results in a resistive peak due to the volume-exclusion effect, and the exiting of the particle through the pore follow with a local increase in the ion due to the

tail of counter-ions under the applied electric field inside the pore (180). This explanation can potentially give insight into the order of peak formation (resistive followed by a conductive) in the biphasic signals recorded.

Considering that the conductive peak component represents the main feature in all the translocation signals recorded, the current amplitude of the conductive peak was used as the main discriminant between the different nanoparticles analysed with our nanopore approach. To further evidence that the transition from conductive to biphasic signal is dependent on the d_{Np}/d_{pore}, pores with different diameter (large and small) were tested as well, while fixing the size of the AuNPs. Figure 4.13A portrays the effect of this ratio change when a larger pore (150 nm diameter) was used for the translocation of the 50 nm diameter AuNPs, leading to the loss of the resistive component. Alternatively, pores with smaller diameter (30 nm) were used to show that even for the 20 nm diameter AuNPs, that previously gave a conductive signal only (Figure 11A), a transition to the biphasic signal is obtained (Figure 4.13B). These combined results where first the pore diameter size was fixed and different AuNPs were analysed and vice versa, support our observations with the regards to the effect of d_{Np}/d_{pore} on the translocation signal recorded with the polymer electrolyte nanopores.

Having conducted experiments to elucidate the enhanced translocation signal recorded, numerical simulations can be further explored to develop models that can explain the shape of the enhanced translocation signals observed. Biphasic signals such as those reported here, with a decrease and increase in the current, are believed to be due to competing effects of geometric exclusion of ions (resistive contribution) and ion concentration polarization. Poisson-Nerst-Planck and Navier-Stokes equations have bene previously implemented for simulating the shape of biphasic signals and ion concentration modulation when particles translocate through a cylindrical pore (182).

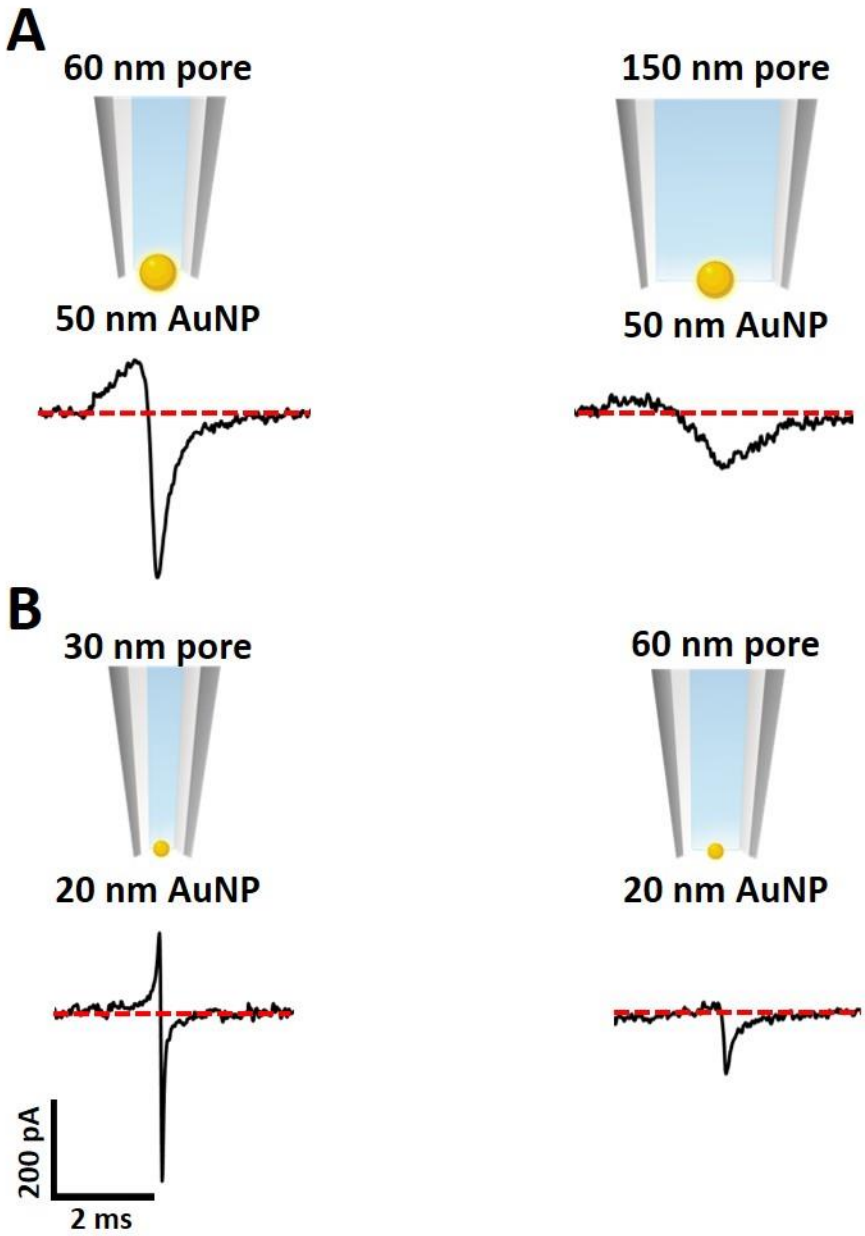

Figure 4.13: Nanoparticle-pore ratio effect. **(A)** Representative individual translocation peaks for 50 nm AuNPs translocating through a 60 nm pore (left) and 150 nm pore size (right), showing the transition from biphasic to conductive shape when the pore size increases with respect to the size of the particle. **(B)** Representative individual translocation peaks for the 20 nm AuNP translocated through a 30 nm pore (left) and 60 nm pore size (right), showing the transition from biphasic to conductive peak shape when the pore size is increased with respect to the size of the particle. The current and time scales are the same for all the translocation peaks. Translocation carried in 50% PEG and 50 mM KCl, under a -500 mV applied voltage.

To further support the capability of our nanopore approach to discriminate heterogeneous nanoparticles mixtures, a mixture containing all AuNPs (50, 40, 30, 20, and 10 nm) in one solution was translocated under similar conditions. The representative ion current trace illustrated in Figure 14.A shows a good resemblance to

the current signals recorded for the individual AuNPs sets in Figure 4.8. The Gaussian distributions obtained for the individual AuNPs sets (Figure 4.11B) were fixed to the conductive peak current distributions obtained for the AuNPs mixture, showing a good data overlap for each peak (Figure 14.B). As depicted in the ion current traces and the individual consecutive depicted in Figure 4.14A and Figure 4.14C, a clear difference between the amplitude and shape (conductive and biphasic) of the translocation signals can be observed, attributed to the different AuNPs translocating through the pore.

In contrast to previous nanopore strategies employing chemical modifications (184) or arrayed nanopores (103), the nanopore system described here supports rapid detection of heterogenous nanoparticles mixture and clear discrimination of their diameter size within one measurement utilizing a fixed pore diameter size. Whereas previous studies demonstrated the discrimination of nanoparticle mixtures utilizing a single nanopore, they were predominantly applied for the analysis of binary mixtures with relatively large difference in their size (175,185). Here, the discrimination of nanoparticles with 10 nm size difference in the low nanometre (10-50 nm diameter) range was explored. Although, a large number of events were recorded in one measurement (N=2474), the normalized conductive peak current distributions in Figure 14.B show a large discrepancy between the ratio of small diameter AuNPs (10-30 nm) and the larger diameter AuNPs (40 and 50 nm) with respect to the pore diameter (60 nm). Further adjustments of the concentration of each set of AuNPs mixed in one solution can lead to more well-defined distributions. Although, the Gaussian distributed peaks plotted for the AuNPs mixture in Figure 4.14B resulted in relatively flat distributions centred at 160 pA and 225 pA (attributed to the 40 and 50 nm translocation), the biphasic signal component recorded for these particles further facilitates their additional fingerprinting in the mixture. The additional resistive component of the translocation signal recorded stands as a potential feature that can allow the detection of a particular analyte present low concentration, relative to the other components present in the mixture. This scenario is often met in the case of biological samples or other synthesized particle mixtures, where the analyte of interest is present in low concentrations, that fall below the limit of detection of the ensemble technique employed in the analysis. A single-entity measurement approach similar to the one showed here can support such detection. Furthermore, the advantage of recording ion current traces for mixtures over

several minutes is advantageous in maximizing the detection output for low-concentrated analytes that have a low event rate.

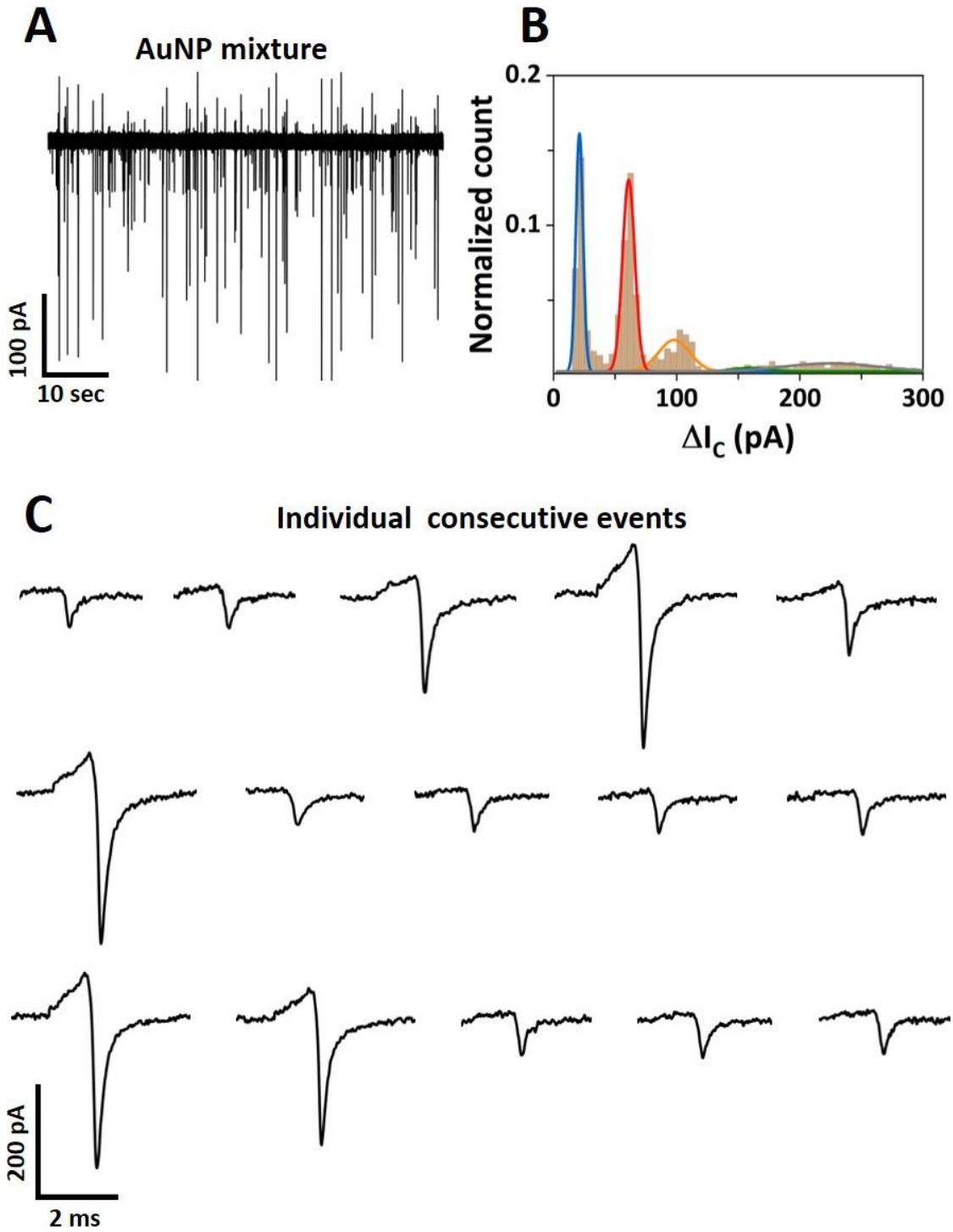

Figure 4.14: AuNPs mixture analysis. **(A)** Ion current of AuNPs mixture containing 10, 20, 30, 40, and 50 nm AuNPs in one solution translocated trough a 60 nm diameter nanopore biased at -500 mV using 50% PEG and 50 mM KCl. **(B)** Event histogram of the conductive peak current for AuNPs mixture shown in (A). The solid lines represent multi-peak Gaussian fits to the translocation data. **(C)** Consecutive individual translocation signals based on the AuNPs mixture recorded in (A).

4.5.4. Translocation of rod-like nanoparticles

Apart from the spherical nanoparticles described in the section above, anisotropic particles with different aspect-ratio were investigated by employing the same electrolyte polymer nanopore system. Metallic rod-shaped nanoparticles present unique properties. Due to their anisotropic shape, their optical, electronic, and catalytic properties can be tuned, making them appealing for various applications such as biomedical imaging, nanophotonics, drug delivery, and biosensing (186). Here, PEG-carboxyl coated gold nanorods (AuNRs) were probed under similar translocation conditions as reported for the AuNPs. Figure 4.15 shows the characterization of the AuNRs utilized in this study. In comparison with the gold nanospheres, the AuNRs have different optical properties. A characteristic absorbance peak at 800 nm and 990 nm was observed for the AuNRs investigated here (Figure 4.15A), due to their anisotropic shape. The TEM measurements of the AuNRs confirmed their anisotropic character showing particles with a broken symmetry, namely having an elongated rod-like shape (Figure 4.15B). The size measurements based on the TEM indicated an approximate ratio of 1:4 between the diameter (~10 nm) and the length (~40 nm) of the rod-shaped particles, as shown in Figure 4.15C. A wider size distribution of their length was observed, compared with their diameter, as presented in the normally distributed histogram for the particle size data obtained in Figure 4.15C. This observation can explain the presence of two optical absorbance peaks recorded in Figure 4.15A at longer wavelengths.

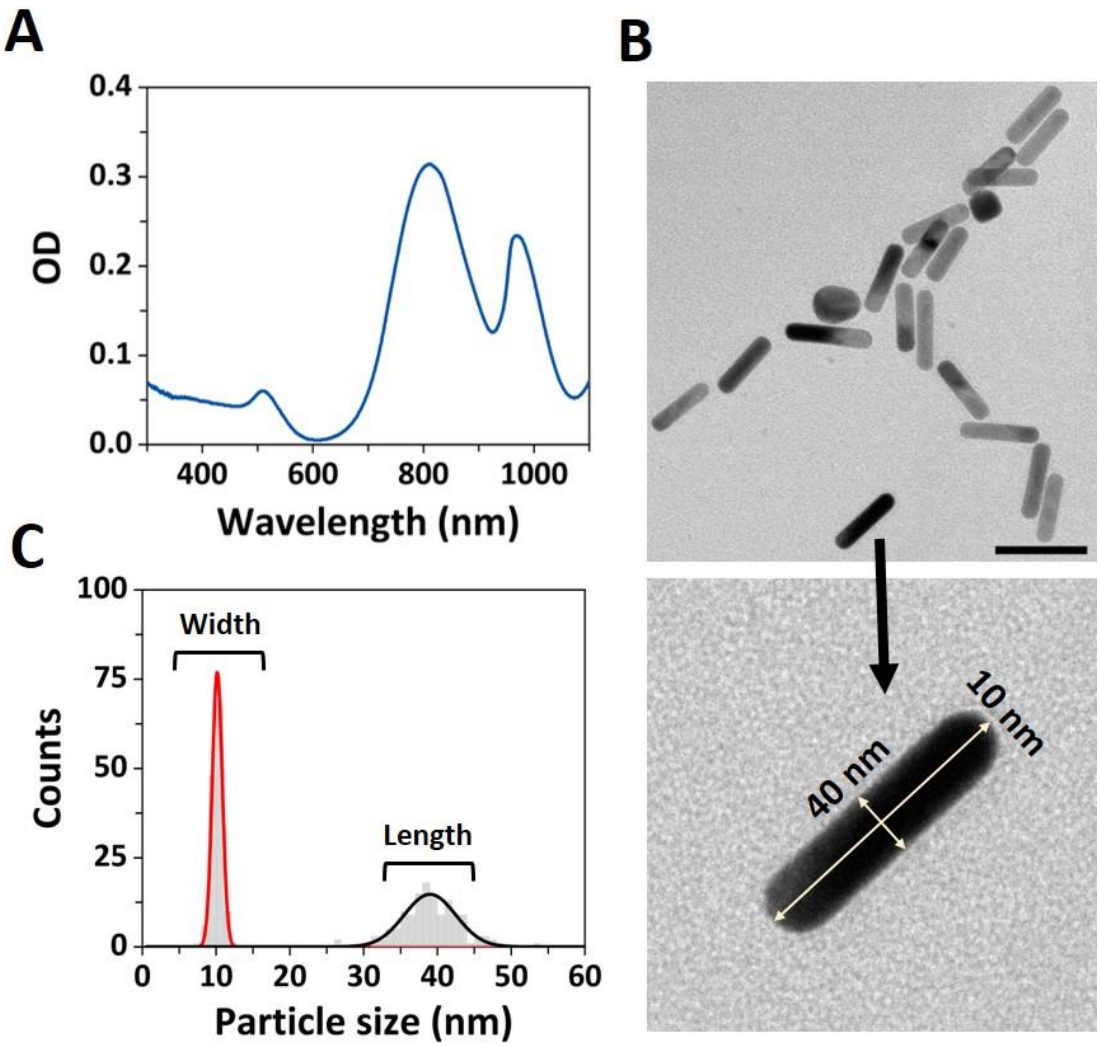

Figure 4.15: Characterization of gold rod-like particles. **(A)** UV-Vis spectra of PEG carboxyl-capped AuNRs depicting the corresponding optical absorbance peaks. **(B)** TEM image of the gold nanorods sample and a close-up view of the individual rod-like particle with its diameter and length dimensions. TEM graph scale bar: 50 nm. **(C)** Histogram displaying the size distribution of the nanorods particle measured from TEM images, with average diameter and length of 10 ± 1 nm (±1σ) and 39 ± 4 nm (±1σ), respectively (based on n=135 data points).

The translocation of nanorods through solid-state nanopores is influenced by a variety of factors, including the size, shape, and charge of the nanorod. The translocation of the 10 x 40 nm AuNRs was carried out using the same pore diameter as before (60 nm pore). The AuNRs' volume of ~3.1 x 10^3 nm^3 is situated between the volume of the 10 nm and 20 nm spherical nanoparticles. The translocation of the AuNRs through the 60 nm pore resulted in conductive translocation peaks, with a peak current distribution centred at 40 pA (Figure 4.16A). This value falls in between the values obtained for the 10 nm and

20 nm average conductive peak currents, 21 pA and 61 pA, respectively. Given the anisotropic shape of these AuNRs, different orientations can be expected during their translocation through the nanopore. The shape and orientation can exert an influence on the magnitude and shape of the translocation signals during nanopore measurements. Interestingly in this case, the majority of the translocation events showed similar peak amplitudes and dwell times when AuNRs were translocated through a 60 nm diameter pore. The amplitude of the translocation events with one conductive current distribution peak suggested a consistent orientation during their translocation. If the long axis of the nanorod is parallel to the electric field inside the nanopore, then a smaller blockage of the pore is expected due to the smaller diameter of the rod particle, with respect to the pore diameter size. On the other hand, assuming the long axis of the nanorod is perpendicular to the electric field inside the pore, then the larger cross-section area will likely generate larger current amplitudes. Here, it is hypothesized that a parallel orientation is likely to occur during the AuNR translocation through the glass nanopore. The long conical shape of the glass nanopores potentially favours the alignment of the nanorods' long axis with the electric field inside and therefore led to consistent (similar current amplitude and dwell time) translocation peaks recorded (Figure 4.16C and Figure 4.17A). In order to induce a stronger interaction of the nanorods with the pore, a smaller pore diameter (30 nm) was used to translocate the same sample of AuNRs. Under these confinement conditions the AuNRs translocation resulted in a larger magnitude of the conductive peak current, with a conductive peak current distribution centred at 60 pA (Figure 4.16D). Apart from this, a change in the translocation signal from conductive to biphasic was observed for the majority of the evens (Figure 4.17B).

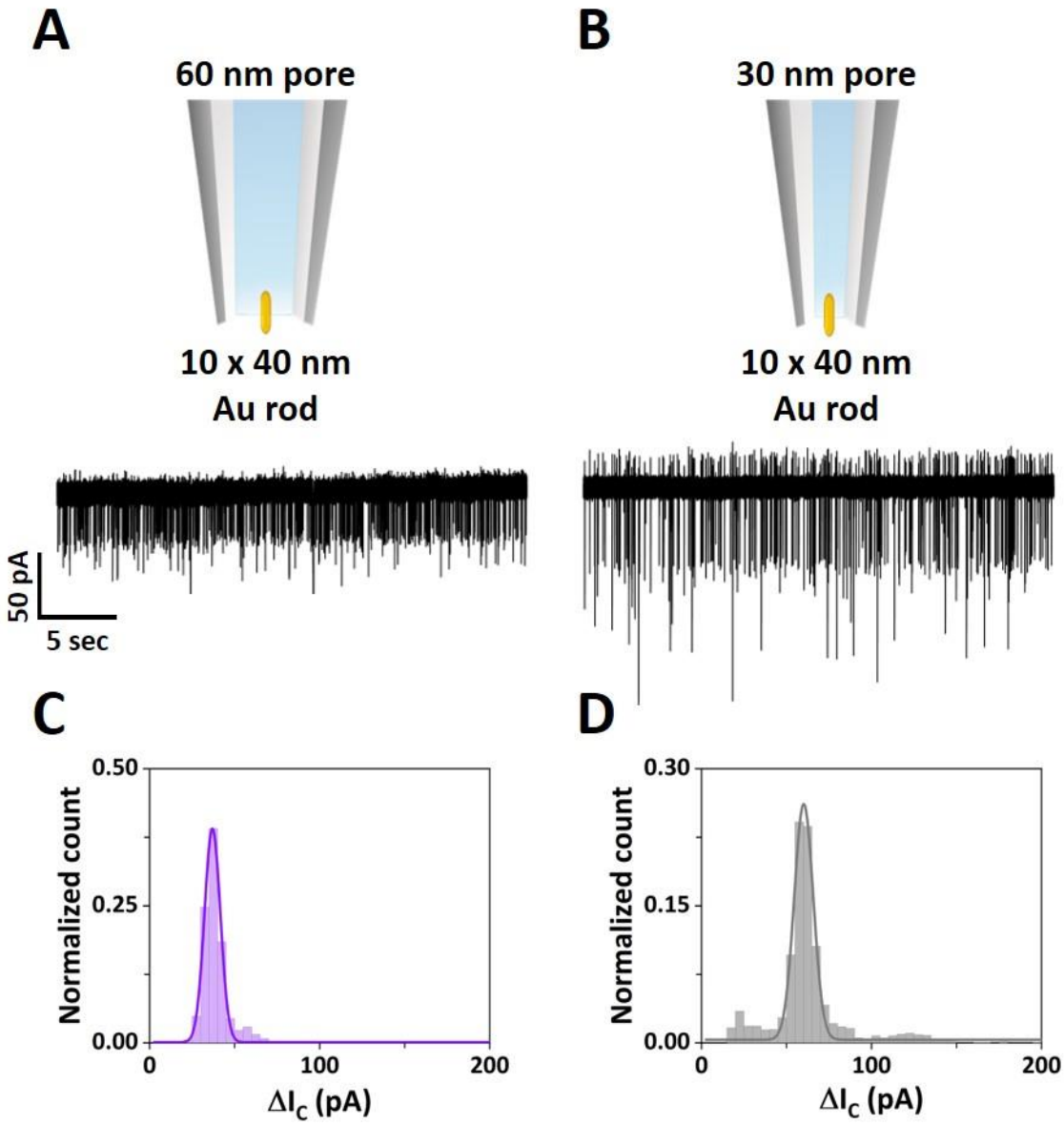

Figure 4.16: Ion current of AuNRs translocated through a 60 nm diameter pore **(A)** and 30 nm diameter pore **(B)**. The pore was biased at -500 mV utilizing 50% PEG in 50 mM KCl external bath. Corresponding event histograms of the conductive peak current of the AuNRs recorded with a 60 nm diameter pore **(C)** and 30 nm diameter pore **(D)**. The solid lines represent Gaussian fits to the translocation data.

The translocation of the AuNRs through the 30 nm diameter nanopore generates translocation events with long dwell time (> 1 ms). As shown in Figure 4.17A-B, a clear difference can be noticed between the translocation of AuNRs through a large (60 nm diameter) and small pore (30 nm diameter). Considering the average dimension of the AuNRs (~10 x 40 nm) and the smaller pore diameter (~30 nm), translocation through the long-axis is predominantly expected to occur in this case. Whereas a wider spread was

observed for the AuNRs translocating through the smaller pore, it is worth mentioning that these events represent only a small fraction from the total number of events recorded (~10 %). This can be potentially assigned the translocation of nanorods with larger lengths that leads to a longer retention time at the aperture and a higher probability for collisions and/or adsorption between the particle and the walls of pore to occur before the particle is expelled in the external bath from inside the pore. Apart from this, a difference in the shape of the translocation signals was observed for the long dwell time events. Although, the amplitude and duration of translocation events are the main discriminants employed in nanopore analysis for single particles, previous reports suggested the translocation peak shape as a potential feature related to the shape of the analyte. Events with multiple current states have been reported for nanoparticles with ligand attachment (104), interactions with the pore (65), or translocations through different orientations (187). As displayed in Figure 4.17C, these long translocation events deviate from the triangular shape reported for spherical particles, with the presence of multiple levels and/or shoulder peaks. The shape of these events suggests that translocating particles experience a stronger interaction with the walls of the pore and/or rotational tumbling effects.

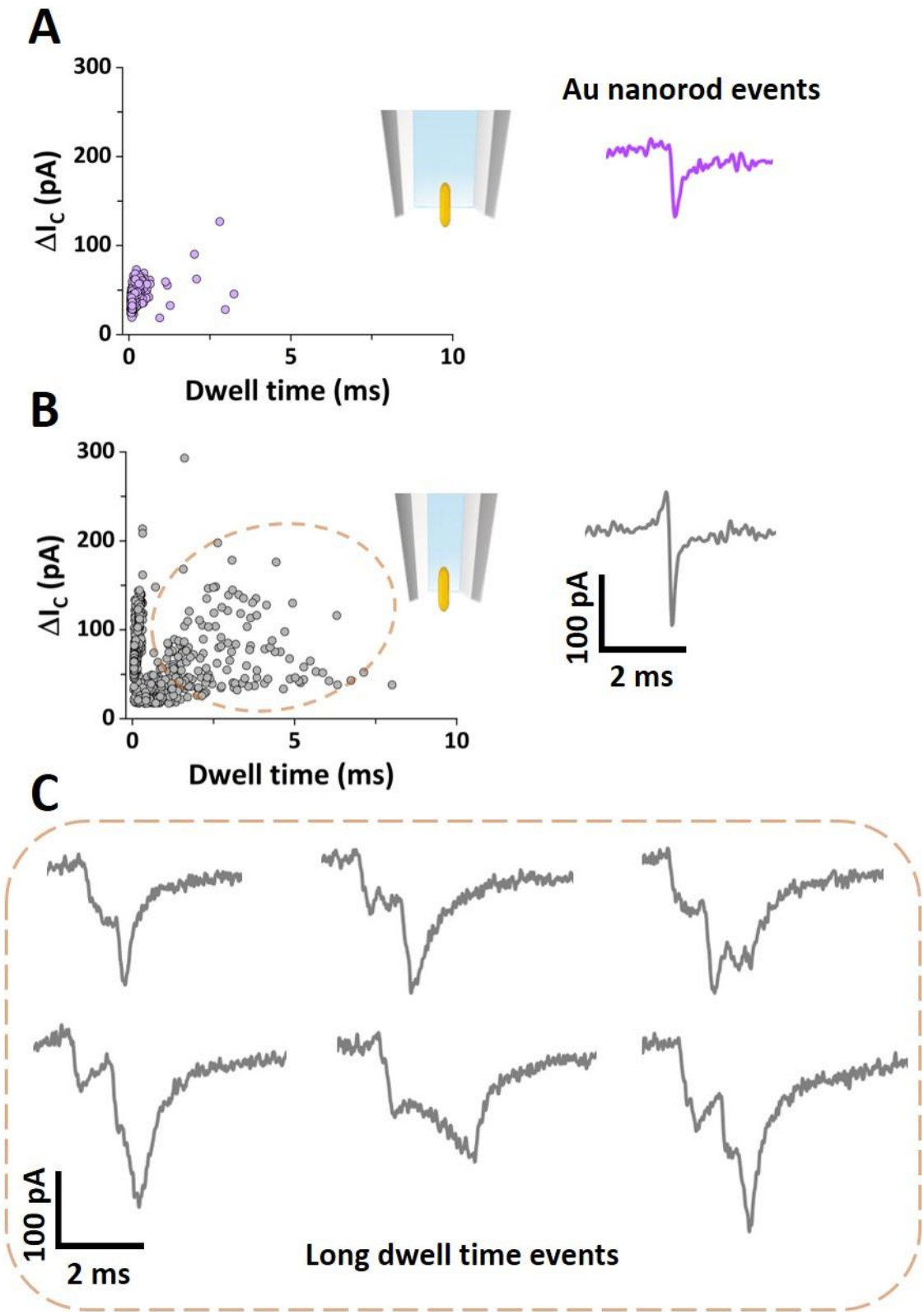

Figure 4.17: Scatter plots of the conductive peak current (ΔI_C) versus dwell time of the translocation events of AuNRs translocated through a **(A)** 60 nm diameter pore and **(B)** 30 nm diameter pore, biased at – 500 mV. Representative individual translocation signals are shown for each translocation condition. **(C)** Long dwell time translocation events obtained for the AuNRs translocating through a 30 nm diameter pore, as highlighted in the scatter plot in panel (B). All the individual translocation events have the same current and time scales.

Previous studies have reported similar peak shapes for the translocation of nanorods through glass nanopores (187-189). In study carried out by Zhang *et al*., the presence of multiple peaks within a single translocation pulse were reported for the nanopore analysis of nanorods (187). Their experimental and simulated data suggested that, in contrast with spherical nanoparticles, nanorods particles can experience rotational tumbling as they translocate through the pore, giving rise to multiple sub-peaks within a single translocation pulse for an individual nanorod particle. The reported peak shapes following the translocation of the nanorods presented multiple levels or a dominant peak feature and one or several shoulder sub-peaks, similar to the individual event shapes described here. Similarly, in the study conducted by Liu *et al*., the nanorods translocation thorough solid-state nanopores resulted in different behaviours, with wider distributions of the dwell time being related to the different lengths of the nanorods (188). To further confirm that the presence of the wider distributions is the result of the anisotropic shape of the nanorods, the translocation of the nanorods was compared with a set of 10 nm diameter spherical particles (similar diameter to the rod particles) utilizing the smaller pore (30 nm). These differences are exemplified in the scatter plots in Figure 4.18, where a clear difference can be observed in the events distribution. The increase in dwell time events was not observed for the spherical nanoparticles under similar nanopore conditions.

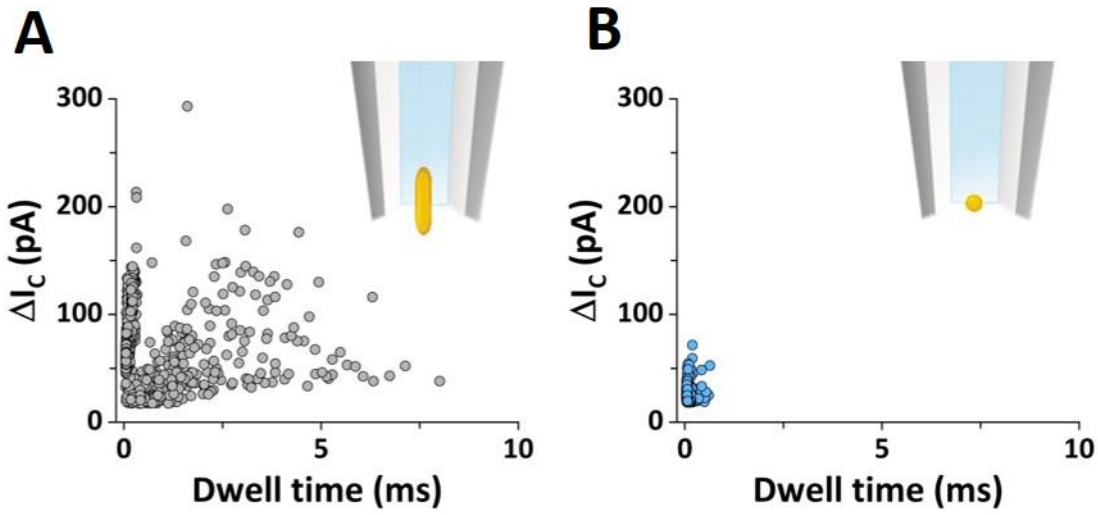

Figure 4.18: Scatter plots with conductive peak current and dwell time for the translocation of 10 x 40 nm gold nanorods **(A)** and 10 nm nanospheres **(B).** A 30 nm diameter nanopore was used in 50% PEG 50 mM KCl, biased at -500 mV.

The influence of the voltage for the translocation of the AuNRs through the different size of the pores was also investigated. The applied voltage can often play a critical role in the translocation of particles by affecting the particle's mobility and conformation. As shown in the dwell time box plots in Figure 4.19, the data points show a larger spread and positive skewness at lower voltages (-300 mV), as opposed to the high voltage extreme (-900 mV). Furthermore, this trend is more evident for the translocation data sets using the smaller pore diameter (30 nm).

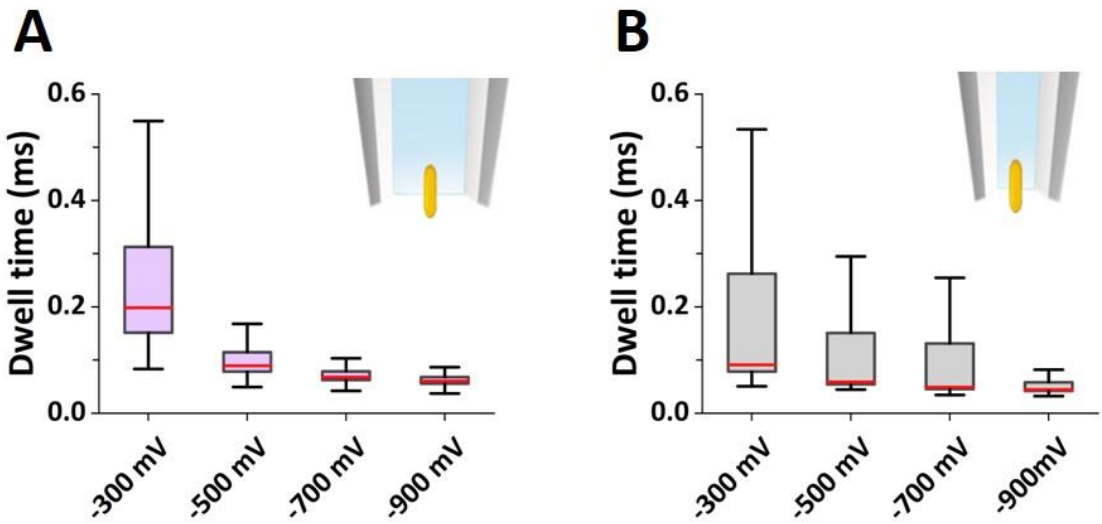

Figure 4.19: Box-and-whisker plots showing the dwell time distribution of the AuNRs events recorded at different voltages through **(A)** a 60 nm diameter pore and (B) and 30 nm diameter pore. The line within the box is the median of the data. Lower and upper bounds of the boxes represent the first and the third interquartile values of the data sets and the whisker represent the outliers.

The lower voltage condition (weaker electric field) favours a longer retention time of the nanorods during their translocation, which leads to longer steric interactions with the nanopore. This effect is also reflected in the event peak shape difference obtained for the voltage extremes. In Figure 4.20, representative long dwell time individual events are depicted shedding light on the peak shape. Namely, at lower voltage multiple levels within a single translocation event were observed, typically presented as a "stair-case" shape. Opposite to this, the high voltage (-900 mV) events resulted in translocation signals presenting split-peak shape and shorter dwell time due to the stronger electric fields.

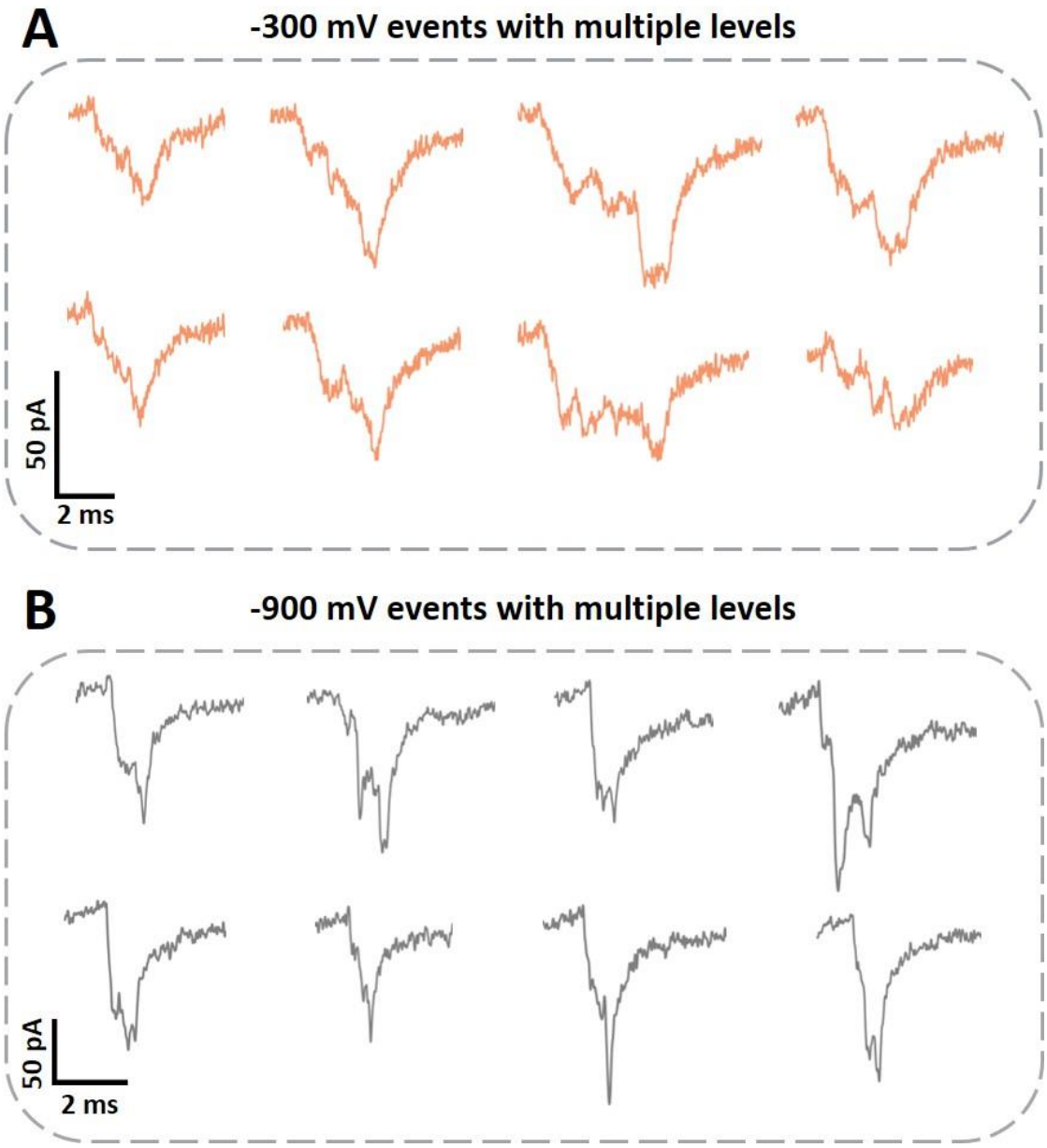

Figure 4.20: Individual translocation events with multiple levels extracted from recording of 10 x 40 nm gold nanorods through a 30 nm diameter pore in 50% PEG and 50 mM KCl, biased at -300 mV (A) and -900 mV (B). All the individual translocation events have the same current and time scales.

Based on these AuNRs nanopore measurements, it is evident the confinement of the AuNRs translocation leads to a stronger interaction between the particles and the pore with the detection of multiple sub-peaks, due to the increased SNR and dwell time. As previously suggested in literature, the particular shape of these peaks can be further used to extract information about the size/shape of the particle. Rod-like nanoparticles displayed different translocation behaviour under nanopore confinement. Based on the signals recorded, it was inferred that diverse forms of spatial confirmation can occur

during the translocation of these anisotropic structures. Variations in the orientation of nanorods offers an intriguing additional insight to monitor for nanoparticle translocation through nanopores. The results presented in this section show the possibility of analysing particle with high aspect ratios and how the recorded current responds to it. In this study the AuNRs translocation was limited to the use of AuNRs sample with only one nominal aspect ratio. Exploring the translocation of AuNRs with different aspect ratios of their diameter and length can give valuable insight into the study of peak shape, such as the number and/or the magnitude of the subpeaks presented within a single translocation event. One final point worthy of discussion is the influence of the nanorod concentration. Although, not investigated here, the particle concentration of the rods inside the pore can potentially have impact on the orientation as well. At high concentrations, the presence of large numbers of particles can potentially hinder the rotation of the nanorod with high aspect ratios and potentially favour one orientation.

4.5.5. Nanopore analysis at low ionic strength

The polymer electrolyte system also enables the analysis of nanoparticles at very low ionic strength (10 mM). Generally, nanopore measurements are carried out in high-salt conditions (> 100 mM KCl), due to improved SNR. However, this excludes the analysis of less stable nanoparticles. Depending on nature of the material and the surface functionalization, the particle stability when suspended in salt buffers can vary. One example is the stability of the commonly used citrate-capped nanoparticles that is limited when these are diluted in buffers with high ionic strength, typically higher than 20 mM KCl (190). To demonstrate that our electrolyte polymer approach can accommodate such measurements, three sets of spherical metallic particles with a nominal diameter of 30 nm, but of different material: PEG carboxyl-capped gold nanospheres (AuNPs), citrate capped platinum nanospheres (PtNPs), and citrate capped silver nanospheres (AgNPs) were analysed. The UV-Vis and DLS characterization of these nanoparticles is displayed in Figure 4.121. Here the particles were diluted in a translocation electrolyte solution containing 10 mM KCl, which is regarded as a suitable range even for the citrate capped particles (platinum and silver particles in this study) for the span of the measurement time.

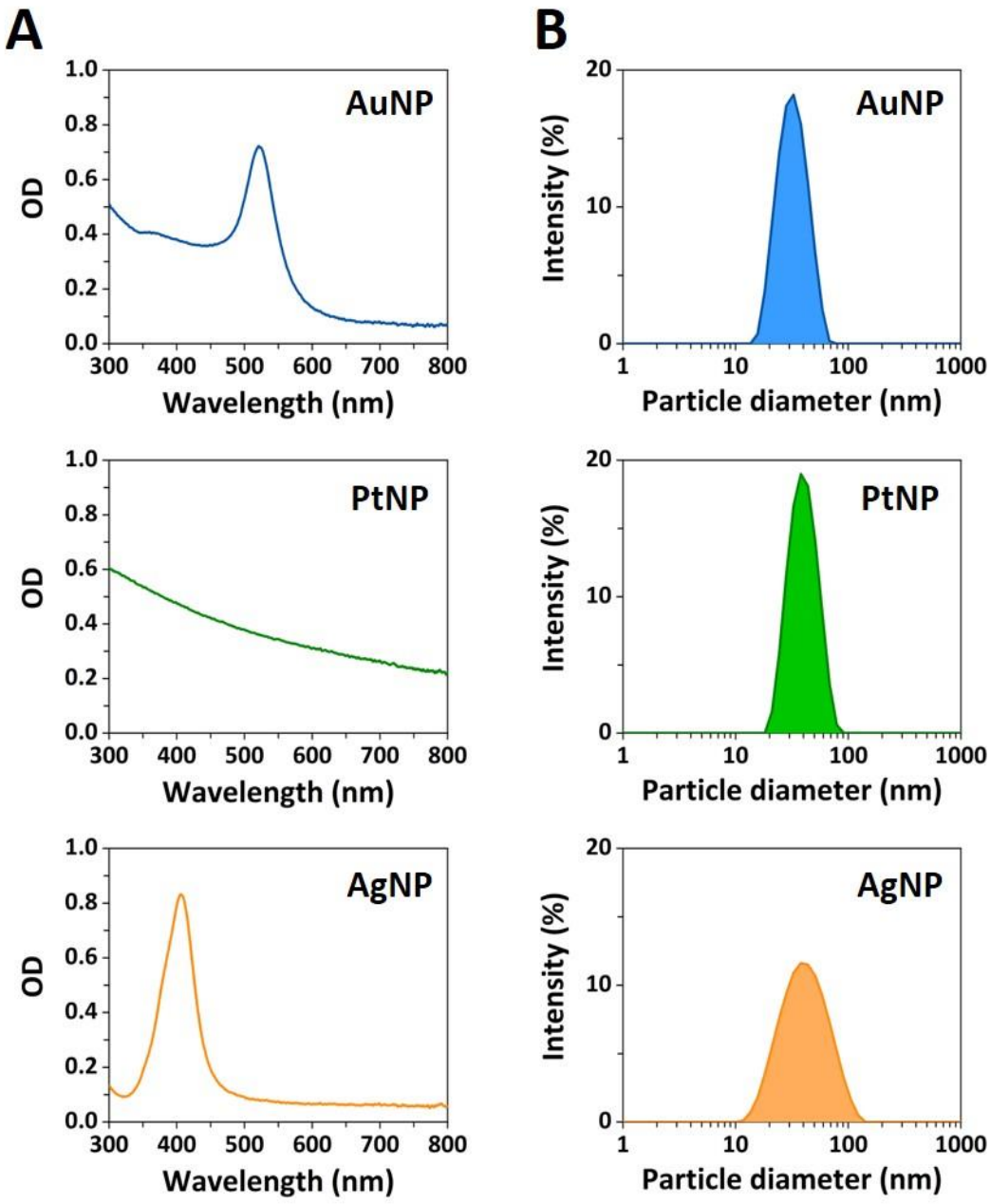

Figure 4.21: Characterization of the homogeneous metallic nanosphere samples. **(A)** UV-Vis spectra of nominally 30 nm diameter nanospheres in 10 mM KCl: PEG carboxyl-capped AuNPs (top panel), citrate- capped PtNPs (middle panel), citrate-capped AgNPs (bottom panel). **(B)** Dynamic light scattering (DLS) measured size distribution (hydrodynamic diameter) of nominally 30 nm diameter nanospheres in 10 mM KCl: PEG carboxyl-capped AuNPs (top panel), citrate-capped PtNPs (middle panel), citrate-capped AgNPs (bottom panel).

Figure 4.21A shows the characteristic UV-Vis absorbance of these particles. A strong plasmon resonance optical absorbance at 520 nm was recorded for the AuNPs (top panel) and 420 nm for the AgNPs (bottom panel). No plasmon resonance was observed for the PtNPs (middle panel). No red shift or suppression of the absorbance peak was

recorded after 1hr incubation. Similarly, the size distribution measured by DLS indicate homogenous mixtures, without the presence of aggregates formation, as depicted in Figure 4.21B for the three sets of metallic nanospheres diluted in 10 mM KCl buffer solution.

The translocation of gold, platinum, and silver nanoparticles diluted in 10 mM KCl was probed, demonstrating that polymer electrolyte nanopores can reliably detect nanoparticles with high-capture rates and high signal-to-noise ratios (SNR). These results are evident in Figure 4.22A, where the translocation of three sets of the 30 nm metallic nanospheres is shown utilizing a 60 nm nanopore biased at -500 mV in 50% PEG and 10 mM KCl conditions. The data also shows a good agreement between the average conductive peak current recorded for each set of nanoparticles with nominally the same size (30 nm diameter), as depicted in Figure 4.22 and Table 4.3. The Gaussian fits of the peak current distribution in Figure 4.20A resulted in average conductive peak current of 40 ± 1 pA for the AuNPs, 40 ± 1 pA for the PtNPs, and 38 ± 1 for the AgNPs, respectively.

Table 4.3: Average conductive (ΔI_C) peak current values with the standard error (SE) obtained for 30 nm nominal diameter NPs translocated through ~60 nm diameter nanopores into an electrolyte bath containing 50% PEG and 10 mM KCl. The nanopipette was biased at -500 mV, and filled with a solution containing 10 mM KCl and 25 µg/mL of nanoparticles. Each value shows the results based on a single nanopore recording with the number of translocated events displayed in the table.

Pore diameter (nm)	NP diameter (nm)	NP material	NP capping	Translocated events	ΔI_C ± SE (pA)
60	30	Gold	PEG-Carboxyl	2477	40 ± 1
		Platinum	Citrate	1898	40 ± 1
		Silver	Citrate	890	38 ± 1

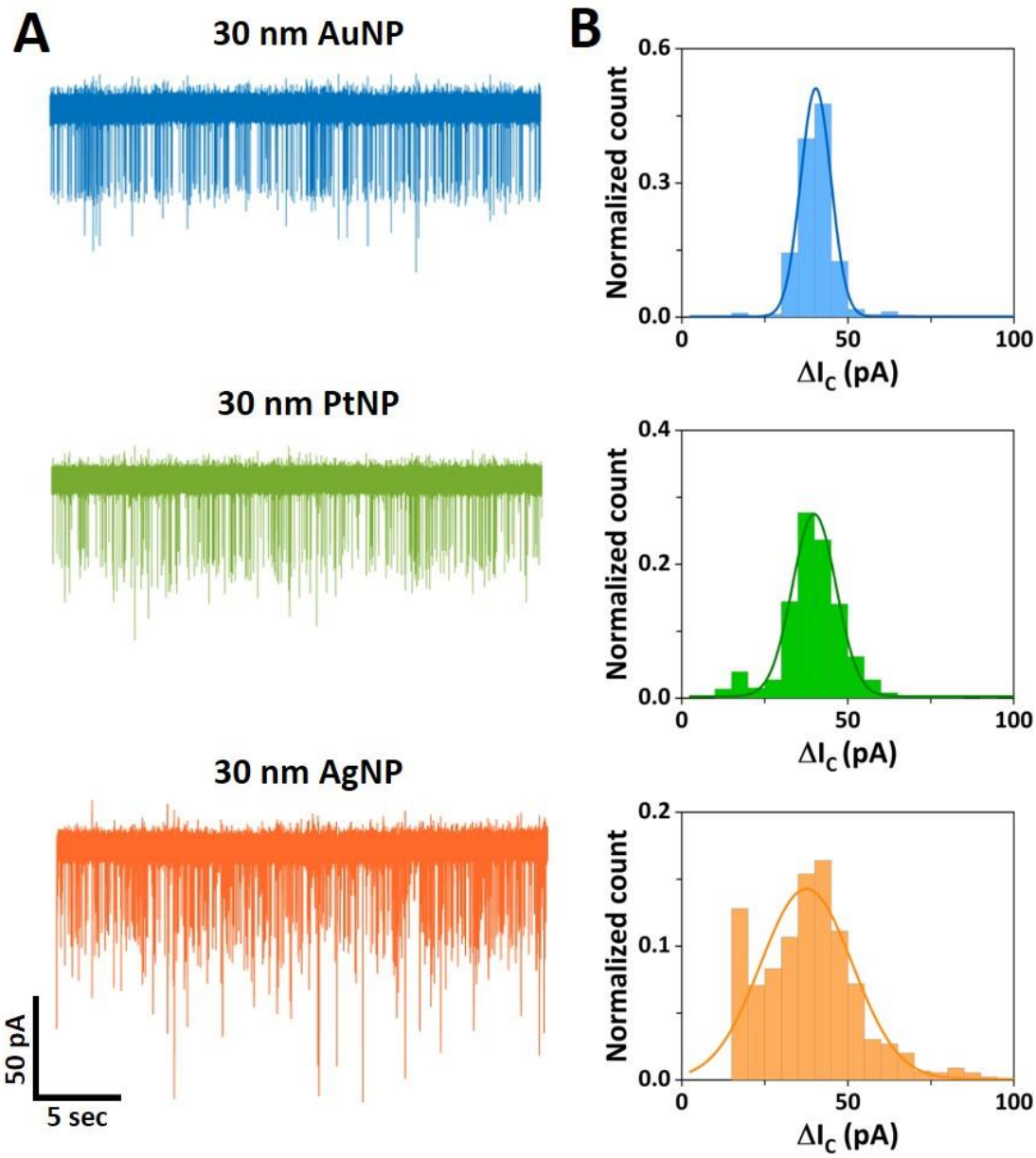

Figure 4.22: Nanopore sensing of metallic nanospheres. Representative ion current traces **(A)** and histograms of the conductive peak current distribution (**B)** for: 30 nm diameter PEG carboxyl-capped gold nanospheres (top panels), 30 nm diameter citrate-capped platinum nanospheres (middle panels), and 30 nm diameter citrate-capped silver nanospheres (bottom panels). The solid lines represent Gaussian fits to each translocation data set. Nanopore recordings were carried out in 50% PEG in 10 mM KCl utilizing a 60 nm diameter fixed pore size biased at -500 mV. The current and time scales are the same for all the ion current traces.

4.5.6. Nanopore analysis of gold nanospheres and nanostars

Inspired by the results above, nanopore measurements were expanded to tackle complex anisotropic nanoparticles. The unique properties (*i.e.* electronic and catalytic) of anisotropic nanomaterials have gained popularity for various applications. One class

of such anisotropic nanomaterials are gold nanostars (AuNS). These branched nanoparticles are emerging as prominent plasmonic particles for application in surface-enhanced Raman scattering (SERS) and offer several advantages over spherical nanoparticles (173,191,192). The localized surface plasmon in AuNS is tuneable by controlling the shape of the structure during the synthesis (193). However, current characterization and quality control for these anisotropic nanostructures is not a trivial task. The method of choice in this case mainly resumes to performing TEM imaging. TEM can be used to identify anisotropy at the single particle level; however, it only measures a small subset of particles, it cannot be performed during synthesis, and it requires in most cases to remove particles from liquid medium. These issues make increasing the complexity for real quality control of such nanoparticles. In contrast, measuring the extinction spectrum and the motion of particles permits to measure the sample as an ensemble, but it lacks information at the single-particle level and cannot detect heterogeneity and diverging particles. Nanoparticle tracking systems can be used to investigate particles at the single particle level, but they do not offer information such as anisotropy or particle shape, as it assumes a spherical model. The effective characterization of AuNS at the single-particle level remains a challenge that needs to be overcome for effective translation of these nanoparticles to clinical settings, where shape and heterogeneity of the particles has to be highly controlled.

First, a nanoparticle solution composed of AuNS was compared with the translocation of gold spherical nanoparticles. As shown in the TEM images in Figure 4.23A-B, their nominal hydrodynamic radius was broadly similar (60 nm for AuNS *vs* 50 nm for AuNP), but the ion current signals generated two clearly distinct populations indicating the potential of this nanopore approach for the quantitative analysis of anisotropic nanoparticles (scatter plots Figure 4.23C). Under these nanopore conditions, the gold spherical nanoparticles show a confined cluster in terms of peak current amplitude and translocation time, as depicted in the top panel of Figure 4.21C. However, opposite to the translocation events obtained for the gold nanospheres, the events recorded for the AuNS sample show a wider spread in terms of the peak current and dwell time (middle panel Figure 4.21C). Similarly, when these two sets of particles (spherical and star-shaped) were translocated as a mixture, two distinct clusters were observed that match their individual sets (bottom panel Figure 4.21C). These results suggested that the

nanopore measurements can support the single-particle analysis of anisotropic nanostructures and support their differentiation from spherical nanoparticles.

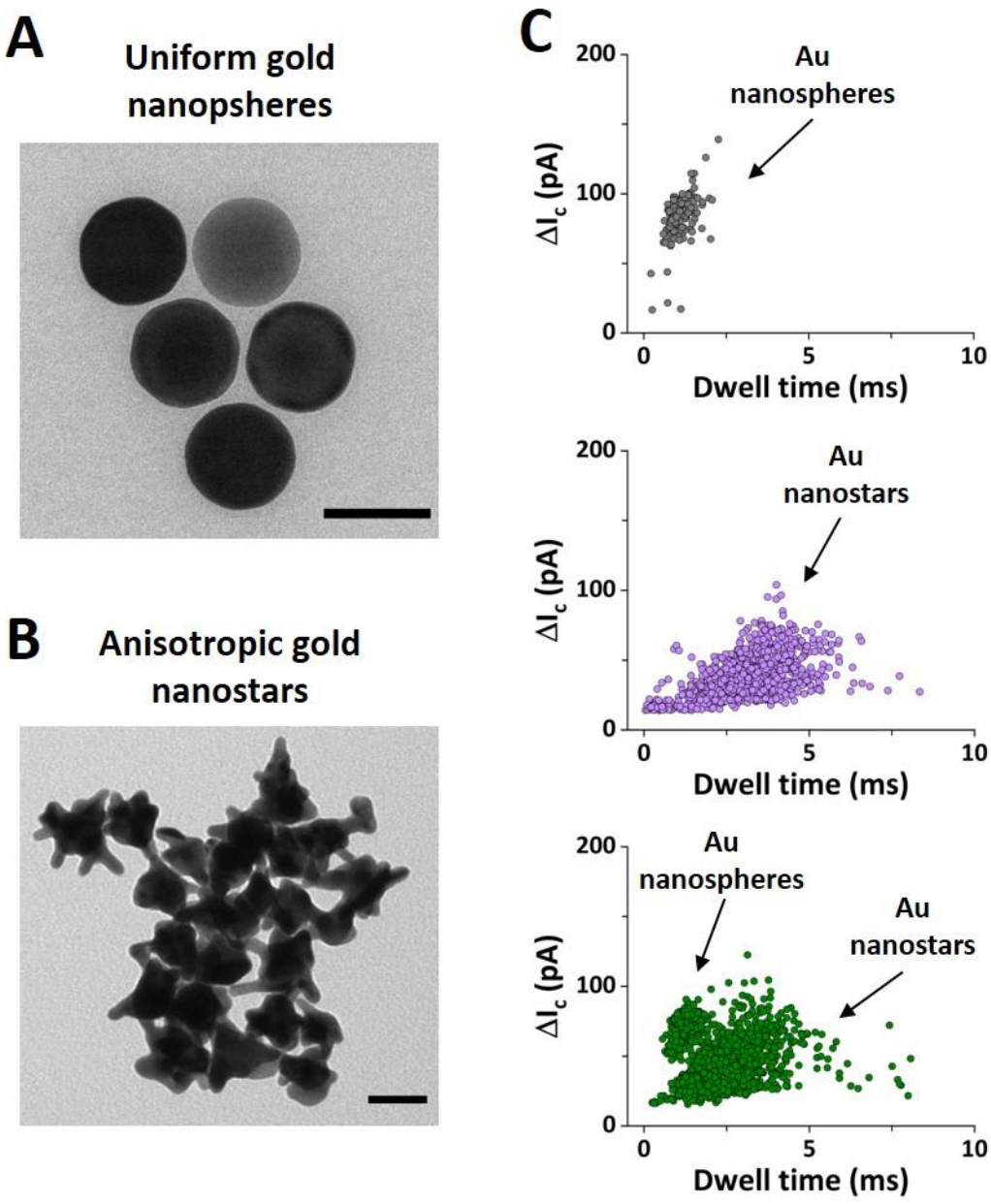

Figure 4.23: TEM images of homogenous gold nanospheres **(A)** and heterogenous gold nanostars **(B)**. Scale bar TEM graphs: 50 nm. **(C)** Scatter plots with conductive peak current (ΔI_C) versus dwell time of the translocation events are depicted for the individual sets (top panel: gold nanospheres; middle panel: gold nanostars), and a mixture (bottom panel: gold nanospheres and gold nanostars) in similar nanopore conditions (50% PEG in 10 mM KCl using an 80 nm diameter fixed pore biased at -500 mV).

Figure 4.24 depicts the analysis of the nanosphere and nanostar particles analysed under similar nanopore conditions. The conductive peak current obtained for the nanospheres resulted in an average value larger than the that of the nanostars sample

(87 ± 1 pA *vs* 31 ± 1 pA), as shown in Figure 4.24B. As for the dwell time, depicted in Figure 4.24C, the nanospheres resulted in an approximately three times faster translocation with an average dwell time centred at 1 ms, compared to the nanostars' dwell time centred at 3 ms.

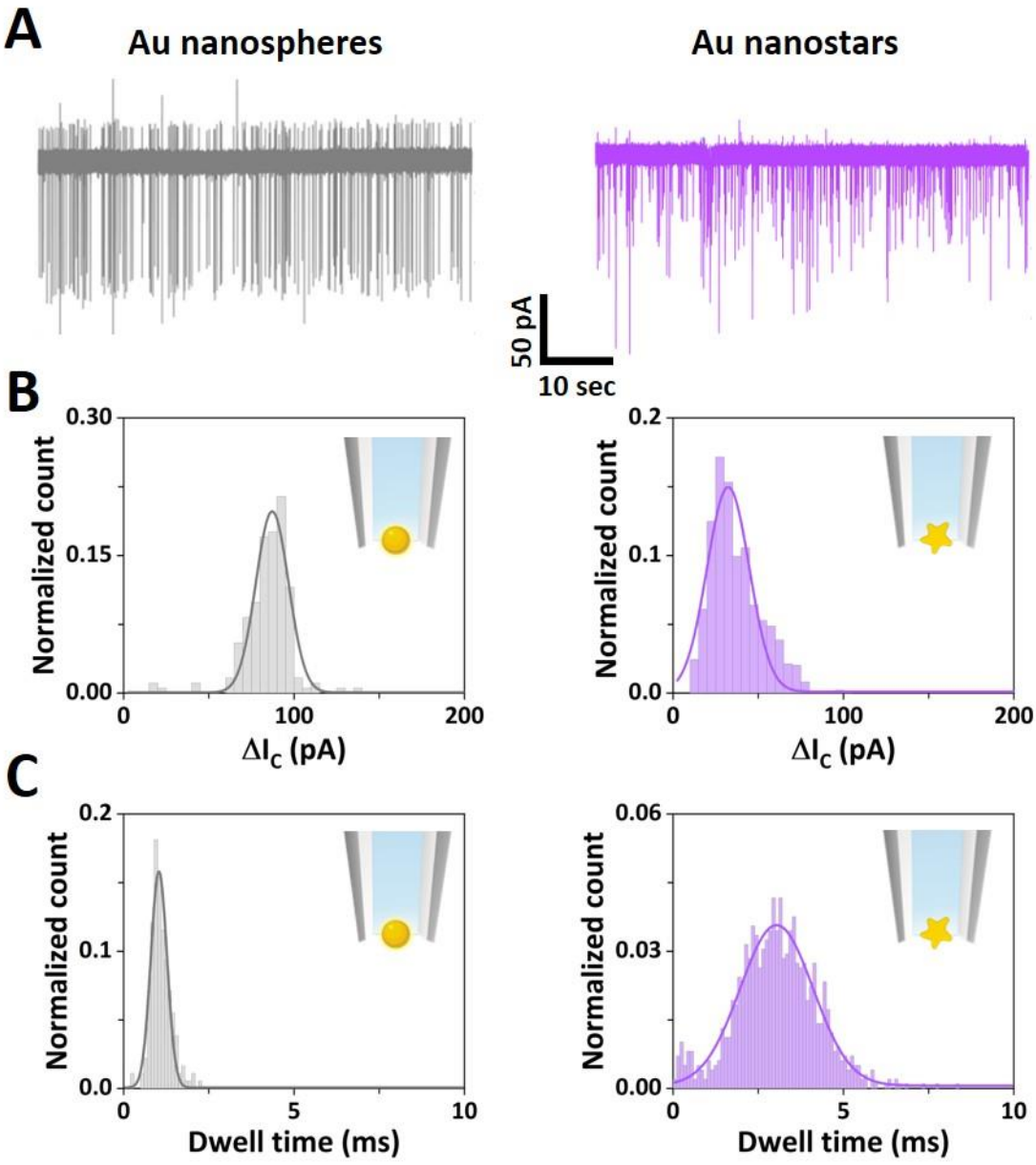

Figure 4.24: Nanopore translocation comparison of spherical gold nanoparticles and nanostars. **(A)** Representative ion current traces obtained for the spherical (left panel) and nanostar (right panel) nanoparticles translocated through an approximately 80 nm diameter pore in 50% PEG and 10 mM KCl conditions, biased at -500 mV. The current and time scales are the same for all the ion current traces. Event histograms of the conductive peak current **(B)** and dwell time **(C)** distributions of the nanospheres (right panels) and nanostars samples (left panels). The solid lines represent Gaussian fits to the distributions.

These differences were attributed to the irregular shape of the star-shaped nanoparticles and their heterogenous character, as depicted in the TEM images (Figure 4.23A-B).

4.5.7. Nanopore analysis of gold nanostars with different branching degree

Furthermore, different suspensions of AuNS samples with low and high degree of branching were probed, following their different synthesis stages, here named S5, S10, and S30, according to their branching degree, as shown in TEM images in Figure 4.25.

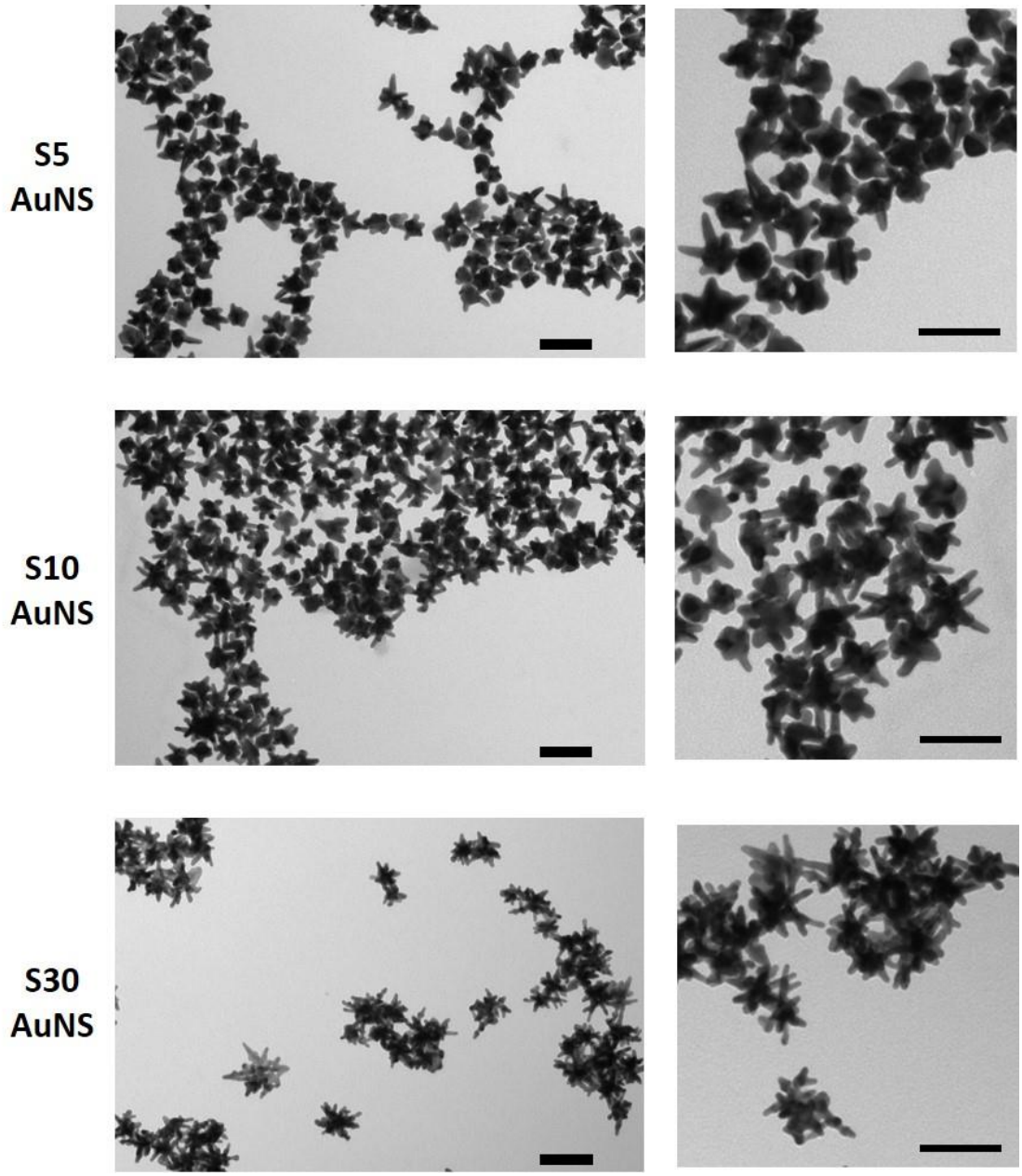

Figure 4.25: TEM images of the synthesized gold nanostars: S5 (top panel), S10 (middle panel), S30 (bottom panel). Scale bar graphs: 100 nm.

As described in the material and methods section of this chapter, the branching degree difference is the main result of varying the concentration of the $AgNO_3$ (5, 10, and 30 µM) in the synthesis process, hence the notation S5, S10, and S30 AuNS. The AuNS samples all exhibit a large amount of anisotropy which gives rise to their unique optical properties, as shown in Figure 4.26B. A shift to higher wavelength was observed with increasing density of the nanostar branches: 659 nm for S5 AuNS, 696 nm for S10 AuNS, and 888 nm for S30 AuNS. The mean size (hydrodynamic diameter) determined: 63.4 ± 0.3 for S5 sample, 65.4 ± 0.3 for S10 sample, and 70.7.4 ± 0.3 for S30 sample (Figure 4.26C). The multiple AuNS morphologies are responsible for the skewed and broad hydrodynamic size distribution.

Similarly to the analysis approach described above, nanopores with a fixed size (80 nm diameter) were used to accommodate the translocation of the three different sets of AuNS samples. The nanopore analysis of the AuNS samples is shown in Figure 2.27A. With increasing branching density, a broadening of the distributions was observed, both in terms of peak current amplitude and dwell time, as shown in the scatter plots in Figure 4.27B and box plots in Figure 4.28. Although, the average size differences between the AuNS samples are relatively small (Figure 4.26C), the heterogenous character of these sample changes with increasing branching density. As presented in the TEM images (Figure 4.26A), the S5 AuNS nanostructure retain a more symmetric shape with sparse short spikes present. Whereas, in the case of S10, and even more evident in the case of S30 AuNS samples, the nanostructures synthesized present multiple spike-like extensions, contributing to their anisotropic morphology.

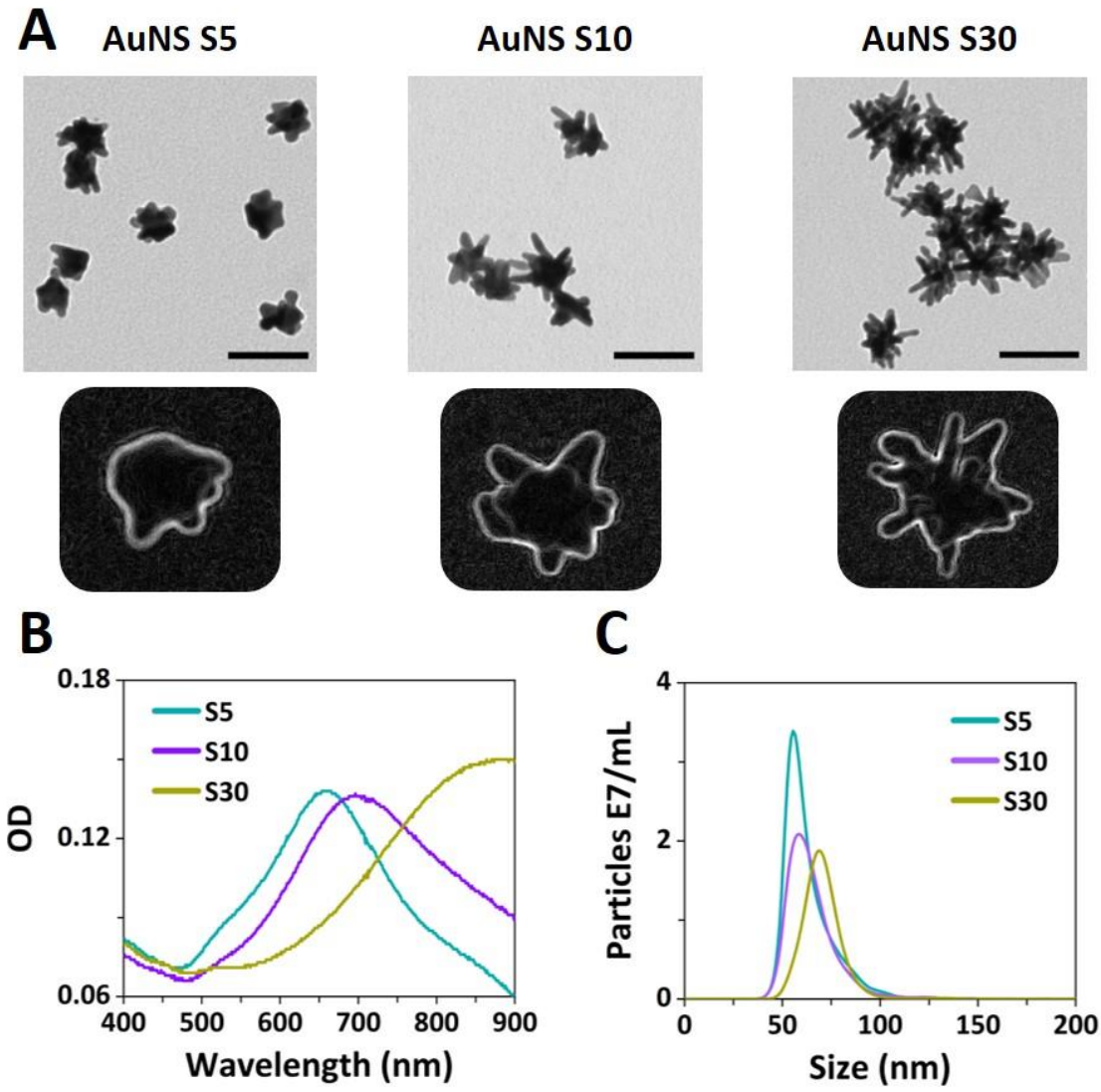

Figure 4.26: Characterization of the synthesized gold nanospheres samples. **(A)** Representative TEM images of the S5, S10, and S30 synthesized AuNS samples (100 nm scale bar) and close-up view of individual nanoparticles outlining the morphological difference between the samples. **(B)** UV-Vis spectra of the synthesized gold nanostar samples: S5 (blue line: λ_{max} = 658 nm), S10 (green line: λ_{max} = 696 nm), and S30 (black line: λ_{max} = 888 nm). **(C)** Nanoparticle tracking analysis spectra of the gold nanostar samples: S5 (blue line), S10 (green line), and S30 (black line). The mean size (hydrodynamic diameter) determined was: 63.4 ± 0.3 for S5 sample, 65.4 ± 0.3 for S10 sample, and 70.7.4 ± 0.3 for S30 sample.

Nevertheless, as it can be observed from the TEM images (Figure 4.25), the branching density is not consistent throughout the S5, S10, and S30 AuNS samples and some particles show morphological resemblance with the S5 AuNS particles. There are many subtle avenues of influence with regard to the growth conditions that can exert a dramatic effect on the morphology and the yield of the synthesized anisotropic nanostructures. This represents a limitation of the overall synthesis procedure of the

AuNS samples and the optimization process for morphology and yield of the synthesized nanostructures was not a focus in this study. To evidence the progression in terms of nanopore detection from synthesis of AuNS (S5) to the high-density branched AuNS (S30), 95% confidence interval (CI) was computed using the S5 translocation events as an input. Then, the S5 CI was applied to the translocation events obtained for S10 AuNS and S30 AuNS samples. Based on this CI fitting an increase in the percentage (from the total number of events) of the events falling outside the S5 CI was outlined, namely 12% for the S10 and 35% for the S30 AuNS (Figure 4.27B). To my knowledge, this is the first study demonstrating nanopore translocation of anisotropic synthesized star-shaped colloids with different morphologies. Based on the nanopore measurements, their translocation can be conducted in a high-throughput manner with several hundreds of events recorded in low ionic strength conditions without clogging of the pore. Opposite to the uniform standard AuNPs that fall within a narrow interval, the translocation of AuNS displayed a large spread in terms of peak current and dwell time. As expected, the non-uniform shape of these nanostructures are subjected to different orientations traversing the nanopore. Hence, a large variation in both dwell time and peak current amplitude is expected in the case of this heterogenous nanoparticle samples (Figure 4.28).

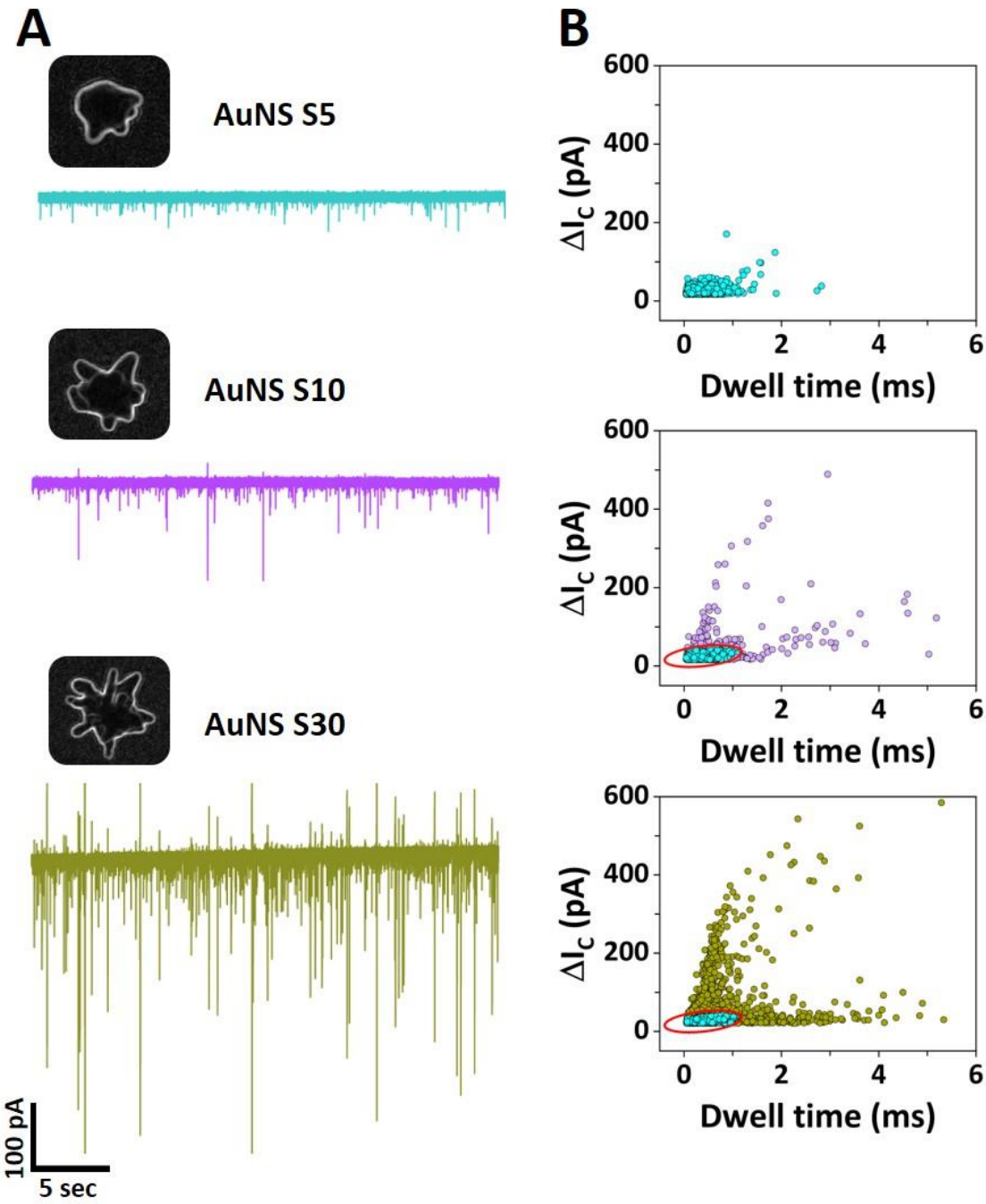

Figure 4.27: Nanopore analysis of gold nanostars with different branching degree. **(A)** Representative ion current traces obtained for S5, S10, and S30 gold nanostars in 50% PEG in 10 mM KCl conditions using a fixed pore size (80 nm diameter) biased at -700 mV. **(B)** Scatter plots of conductive peak currents as a function of dwell time for the S5 AuNS sample (top panel), S10 AuNS sample (middle panel), and S30 AuNS sample (bottom panel). The red ellipse in the S10 and S30 scatter plot data indicates the 95% confidence interval of the S5 translocation events. 12% of the events fall outside the S5 CI for the S10 sample and 35% of the events fall outside the S5 CI.

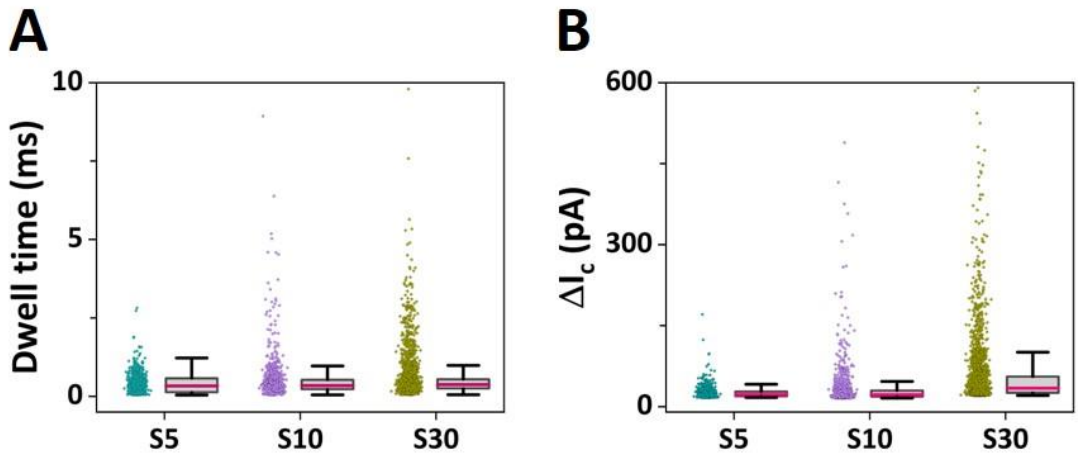

Figure 4.28: Box-and-whisker plots showing the conductive peak current **(A)** and the dwell time **(B)** for the S5, S10, and S30 AuNS samples (median, interquartile range 25-75%, and whiskers range 5-95%). Translocation of the S5, S10, and S30 was carried out in 50% PEG in 10 mM KCl conditions using a fixed pore size (80 nm diameter) biased at -700 mV.

Similar to the analysis described for the nanorods, the peak shape of the translocation events falling outside the CI of the S5 was further explored. Assuming that the majority of the events falling outside of the S5 CI present a change in their size and/or morphology, the peak shapes of these individual events were further examined for the S30 AuNS sample. This sample was chosen as it exhibited the highest degree of anisotropy and showed the largest difference compared to the S5 AuNS sample. As shown in Figure 4.29, apart from the change in peak current amplitude and/or dwell time for event clusters falling outside the S5 CI, a change in the peak shape was confirmed as well. Interestingly, two predominant type of translocation signals were observed in the case of S30 AuNS sample, apart the events falling within the S5 CI. At large conductive peak current amplitudes (> 50 pA), the translocation events mainly showed the presence of a resistive component, similar to the case of spherical nanoparticles matching the size of the pore diameter. These are believed to be large nanostructures that have an increased diameter due to the presence of the dense branches, but potentially still retaining a relatively symmetric shape, hence the presence of one peak feature (type ii events - top panel Figure 4.29). On the other hand, the long dwell time events that fall outside the S5 CI (> 1 ms), showed translocation signals with multiple levels. It is believed that these events are attributed to the presence of nanostar particles with high morphological anisotropy that, due to the presence of long spikes,

translocate in different orientations through the pore. The shape of the translocation signals (type iii - middle panel Figure 4.29) show resemblance to the rod-like nanoparticles presented in the section above, where the multi-level peaks are believed to result due rotational tumbling and interaction with pore walls. Even though, our nanopore characterization of these AuNS mixtures is mainly providing a qualitative comparison in relation to the branching density of these nanostructure, we foresee a more in-depth analysis in conjunction with more complex data analytics routines. The ability of the nanopore approach to analyse the gold nanostar samples and show clear differences from their isotropic analogous emphasizes the great utility of this single-entity tool for nanoparticles characterization. Furthermore, potential yield analysis of the synthesis products can be examined with this nanopore platform.

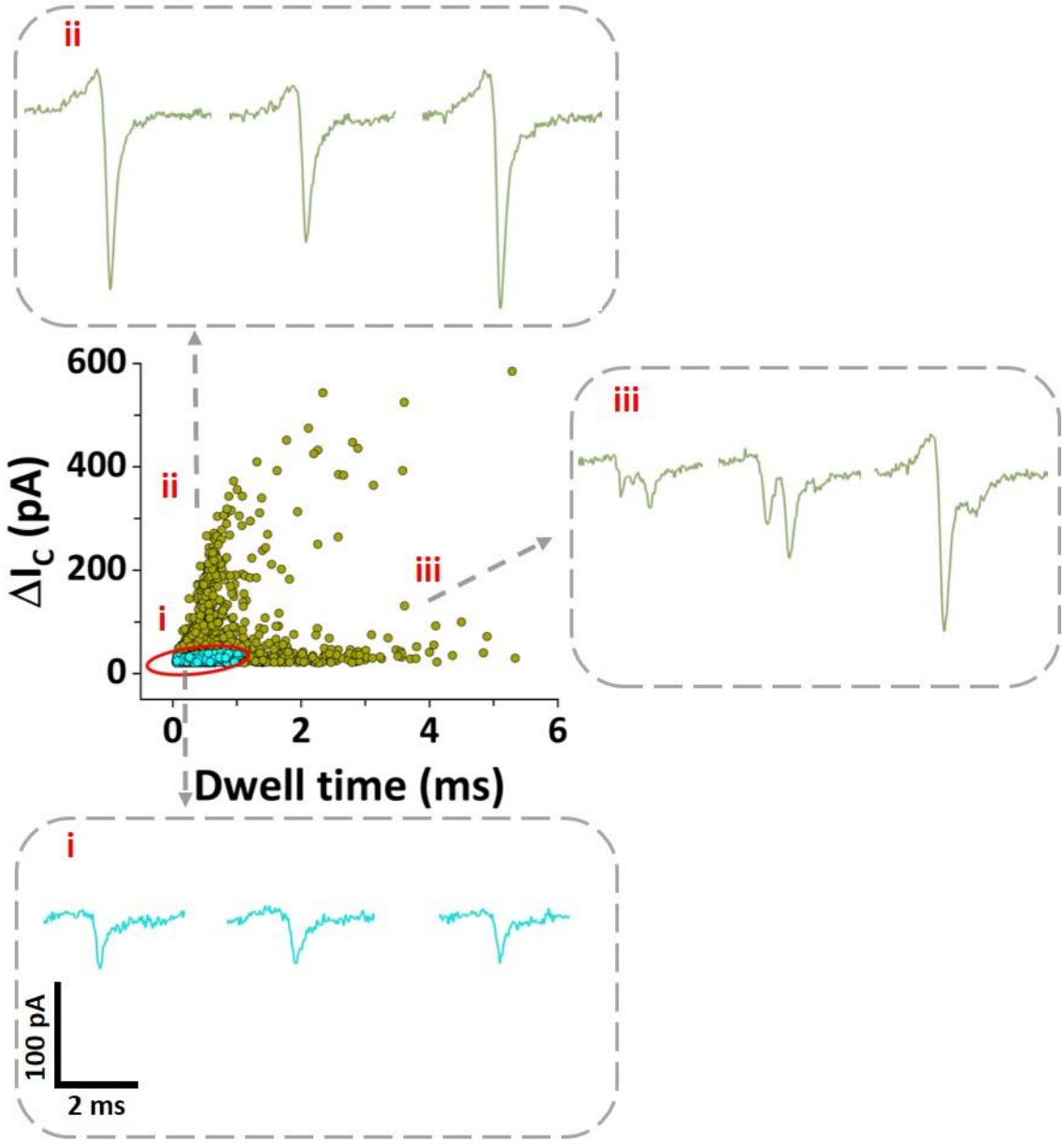

Figure 4.29: Scatter plots of conductive peak current as a function of dwell time for the S30 AuNS sample. Individual translocation signals pooled from the different event clusters are marked by the arrows and the panel notations (i - refers to type i events; ii – refers to type ii events; iii – refers to type iii events). The red ellipse in the S10 and S30 scatter plot data indicates the 95% confidence interval of the S5 translocation events.

4.5.8. Detection of soft functionalized nanoparticles

Having demonstrated that this strategy is suitable for investigating a variety of colloidal particles regardless of their size and shape, the applicability of the polymer electrolyte nanopore system was expanded to the detection of a "soft" class of functionalized nanoparticles. One relevant example here is the analysis of proteins and protein spherical nucleic acids (ProSNAs). ProSNAs are an emerging class of "soft" nanoparticles

with wide-spread applications in bottom-up materials assembly, intracellular sensing, and CRISPR-based gene editing (26,27,194). ProSNAs are based on the spherical nucleic acid (SNA) architecture and consist of a protein core functionalized with a dense shell of DNA strands (Figure 4.30) (26). Compared to its analogous native protein, ProSNAs, *i.e*. the protein functionalized with ssDNA (single-stranded DNA), show an increase in cellular uptake, with the oligonucleotide density playing a critical role in the cellular uptake efficiency (194). Hence, a rational investigation of the DNA-mediated functionalization of these hybrid nanostructures can support the development of new architectures. The ProSNAs platform brings flexibility in allowing the independent tuning of the protein core and the DNA shell (26). Here, a well-established and characterized ProSNA with ssDNA (22 nucleotides long) construct based on a large protein β-galactosidase (464 kDA) was utilized, based on previously reported in ProSNAs studies (26,195).

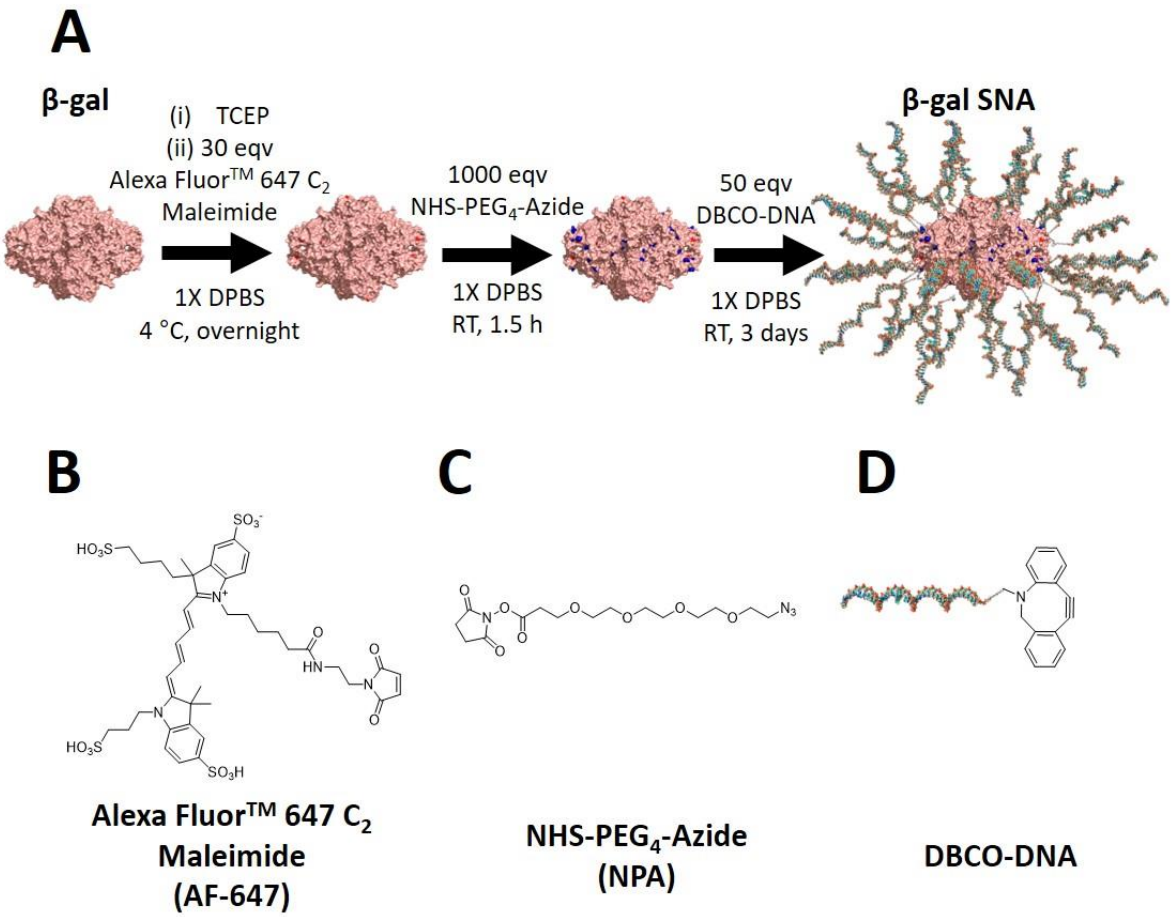

Figure 4.30: **(A)** Schematic depicting the synthesis steps of β-gal SNAs. Structures of **(B)** AF-647, **(C)** NHS-PEG4-azide, and **(D)** DBCO-DNA.

Figure 4.30 shows the synthesis steps of obtaining β-gal SNAs. Based on the calculations described in Section 4.4.6 Materials and Methods, it was determined that the final β-gal SNAs employing DBCO-DNA 1 had an average of ~2 dyes and ~42 DNA strands on the protein surface whereas those using DBCO-DNA 2 had ~5 dyes and ~22 DNA strands on the protein surface. Figure 4.31 shows UV-Vis spectra of β-gal derivates. The absorbance spectrum of native β-gal shows a peak at 280 nm, however, once β-gal is modified with AF-647 (β-gal-AF), an additional absorbance peak is observed at 647 nm corresponding to AF-647. β-gal SNAs show absorbance peaks at both 260 nm (corresponding to DNA) and 647 nm (corresponding to the AF-647). The number of dyes and DNA strands per protein calculated using the absorbance spectra below indicated that on an average, ~2 dyes and ~42 DNA strands on the protein surface for DBCO-DNA 1 and ~5 dyes and ~22 DNA strands on the protein surface for DBCO-DNA 2. Representative data is shown for β-gal SNA_{22} with DBCO-DNA 2 (Figure 4.31).

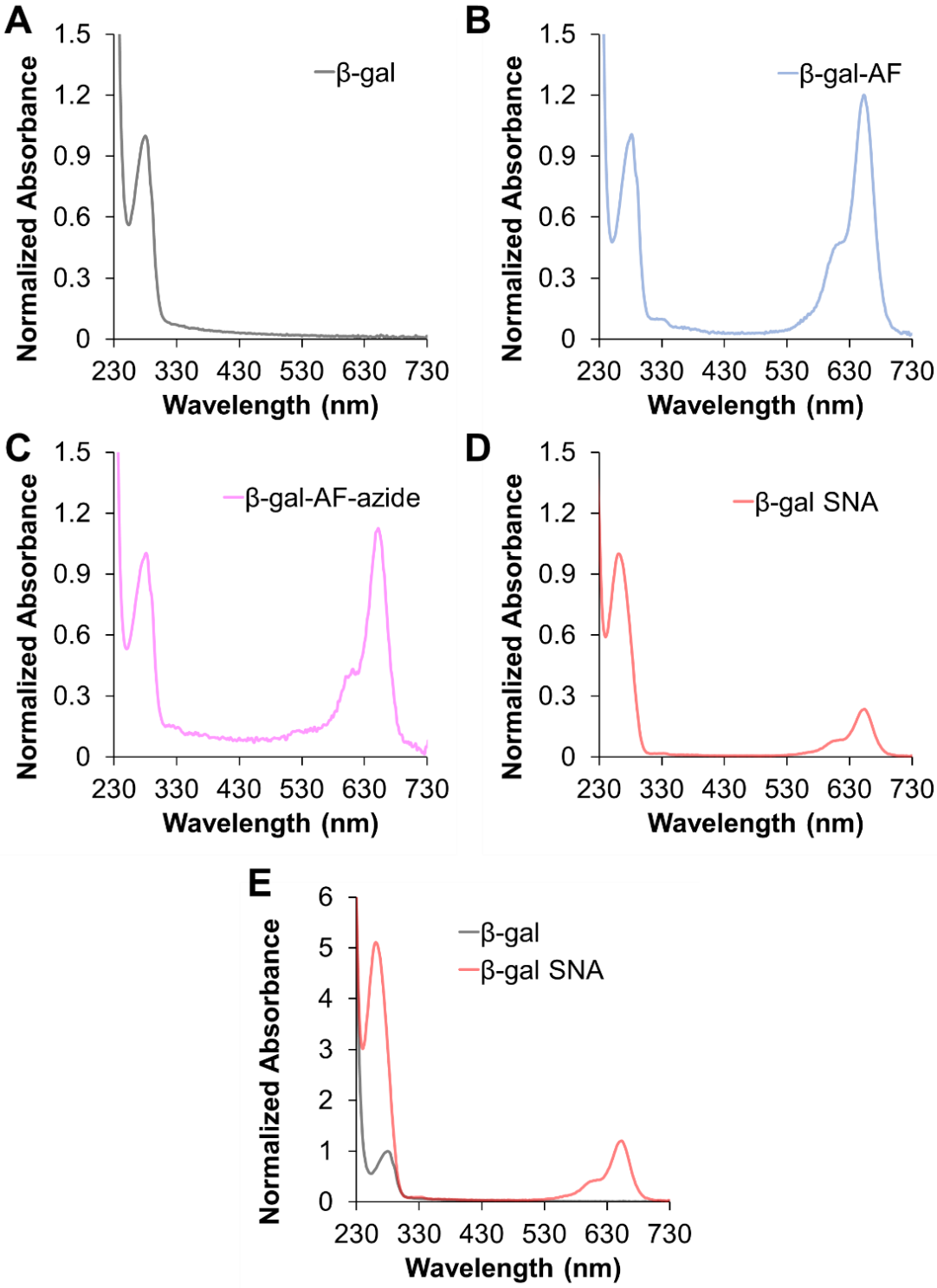

Figure 4.31: Representative UV-Vis spectra of **(A)** native β-gal, **(B)** β-gal-AF, **(C)** β-gal-AF-azide, and **(D)** β-gal SNA_{22}. **(E)** Absorbance of identical concentrations of β-gal and β-gal in Mili-Q water. In all graphs, the absorbance is normalized to the absorbance at 280 nm (corresponding to the characteristic protein absorbance) is normalized to a value of 1.

Given that β-galactosidase (β-gal) has an estimated isoelectric point of 5.5, the protein core is overall negatively charged under physiological conditions (195). Furthermore, the addition of the DNA provides a high density of negative charges through their phosphate backbone (195). In this sense, the nanopore translocation was carried out at near-physiological salt concentration, utilizing 100 mM KCl electrolyte buffer for the ProSNA dilution and 50% PEG 100 mM KCl in the external bath. The large globular β-gal protein with an estimated hydrodynamic radius around 10 - 15 nm (196), makes it an ideal candidate for probing its translocation with solid-state nanopores. For this, a pore diameter of approximately 30 nm was utilized for probing the translocation of native and DNA-functionalized protein constructs. Here, the discrimination of the native β-gal protein and β-gal SNAs with functionalized ssDNAs was investigated using our polymer electrolyte nanopore system. This approach enabled the direct detection of β-gal protein and β-gal SNAs and their subsequent comparison without additional functionalization steps of the nanopore, as previously reported for proteins detection (99,197,198). As depicted in Figure 4.32A, the polymer electrolyte enhanced sensing approach enabled the detection of the native β-gal protein and β-gal SNAs with two different DNA loadings: 22 ssDNAs (β-gal SNA_{22}) and 42 ssDNAs (β-gal SNA_{42}), respectively. The average conductive peak current obtained for the native β-gal protein was centred at 32 pA, whilst a substantial increase was observed for the β-gal SNA samples with a peak centred at 94 pA for the β-gal SNA_{22} (Figure 4.32 and Table 4.4). The large discrepancy in the recorded amplitude of the conductive peak current between the native β-gal protein and β-gal SNAs can be attributed to the increase surface area of the protein core due to the presence of the functionalized ssDNA strands and its increase in the hydrodynamic size. The 22 nucleotide long ssDNA strands lead to an approximate extension of 13 nm in length, assuming an approximately 0.6 nm for the nucleotide length (199). Similarly, a slight increase in the translocation duration was observed between the native β-gal protein and β-gal SNAs (Table 4.4). Importantly, apart from the clear discrimination between the native protein and the DNA-functionalized analogous (Figure 4.32), we were also able to differentiate the β-gal SNAs with two different DNA loadings based on their conductive peak current amplituds (SNA_{22}- centred at 94 pA and SNA_{42}- centred at 171 pA). Remarkably, even at low DNA loading (SNA_{22}), comprising only of several sparsely attached ssDNA to the protein

surface, we were able to provide a clear discrimination from the bare protein serving as scaffold for attachment. In similar fashion, we showed the ability to differentiate between the two different ssDNA loadings, with an increase in the peak current and dwell time with the increasing density of the ssDNAs attached to the protein. These results are in line with the approximately two-fold increase in the DNA shell density of the functionalized protein. The increase in the density of the functionalized ssDNA can change the effective size of the particle and lead to an increase in the hydrodynamic radius. Interestingly, the increase in the density of the functionalized ssDNA strands (~ two-fold increase) also resulted in a change in the shape of the translocation signal, as evidenced in Figure 4.33, namely the presence of small resistive conductive. The increase in the density of the ssDNA strands not only increases the surface area of the translocating particle, but it can potentially also increase its rigidity, as opposed to the less dense β-gal SNA_{22} construct.

Table 4.4: Average conductive peak current (ΔI_C) and dwell time values with their standard error (SE) obtained for the ProSNA samples translocated through a 30 nm nanopore diameter biased at -700 mV. The nanopore was filled with 100 mM KCl and 5 nM β-gal derivatives, whereas the external bath contained 50% PEG and 100 mM KCl.

ProSNA sample	Translocated events	ΔI_C ± SE (pA)	Dwell time ± SE (ms)
β-gal NT	262	32 ± 1	0.10 ± 0.01
β-gal SNA_{22}	2042	94 ± 1	0.11 ± 0.01
β-gal SNA_{42}	1224	171 ± 1	0.13 ± 0.01

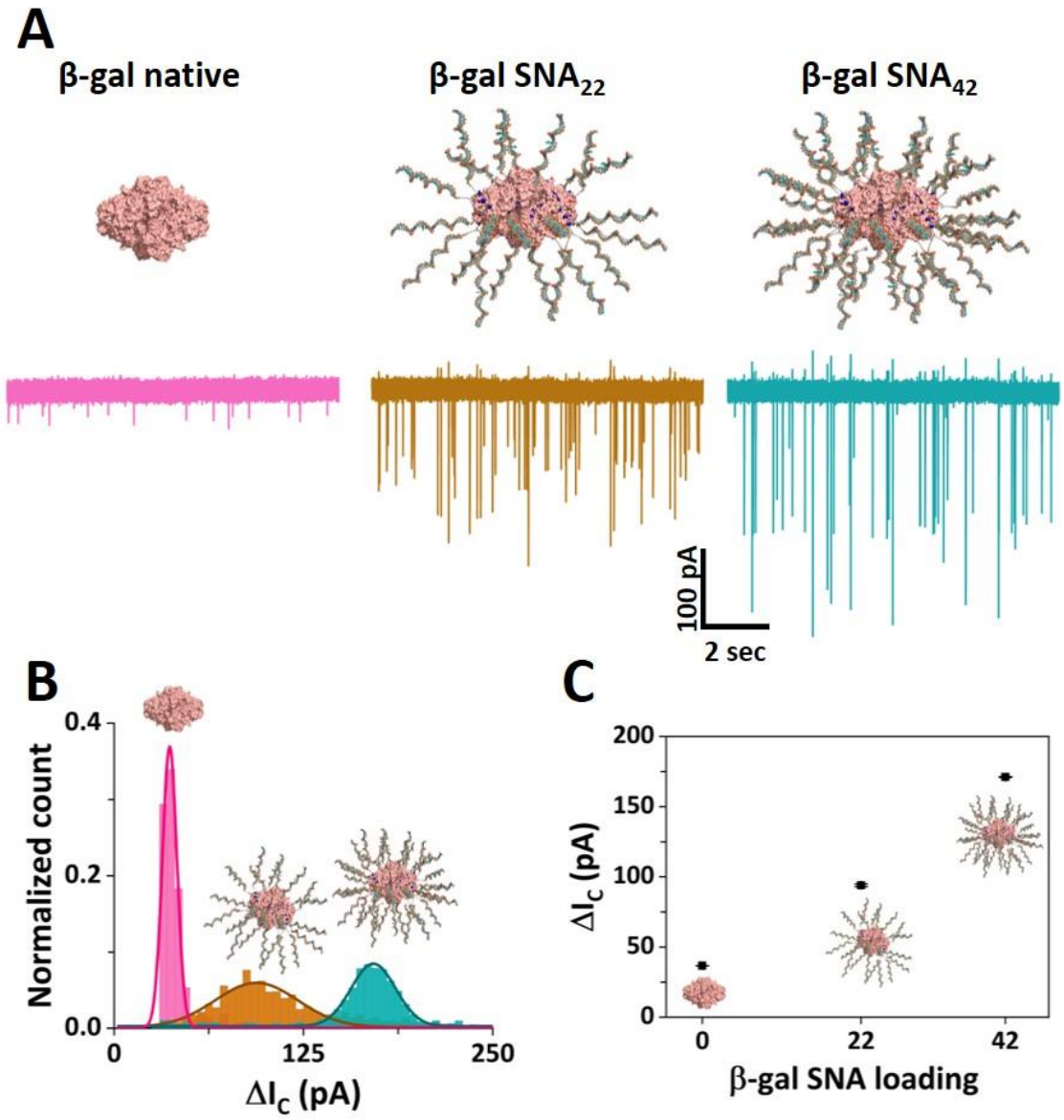

Figure 4.32: Nanopore sensing of protein spherical nucleic acids. **(A)** Nanopore translocation ion current traces obtained for the native β-gal (left), β-gal SNA_{22} (middle), and β-gal SNA_{42} (right). The current and time scales are the same for all the ion current traces. **(B)** Histograms of the conductive peak current for native β-gal (pink bars), β-gal SNA_{22} (brown bars), and β-gal SNA_{42} (teal bars). **(C)** Average conductive peak current as a function of the oligonucleotide loading. The error bars represent the standard error. Nanopore measurements were carried in 50% PEG and 100 mM KCl using a 30 nm diameter pore size biased at -700 mV.

This rapid yet easy-to-implement nanopore sensing allowed to probe small variations in the density of the soft DNA shell on the surface of the protein. Taken together, these results show that the polymer-electrolyte nanopore system can enable the characterization of soft nanomaterials and allow for the discrimination of nanoparticles based on their functionalization state. These measurements provide a basis to

investigate functionalization strategies with biomolecules (*i.e.,* different densities/moieties) for hybrid materials at the nanoscale level with implications in cellular imaging, sensing, or drug delivery (200,201).

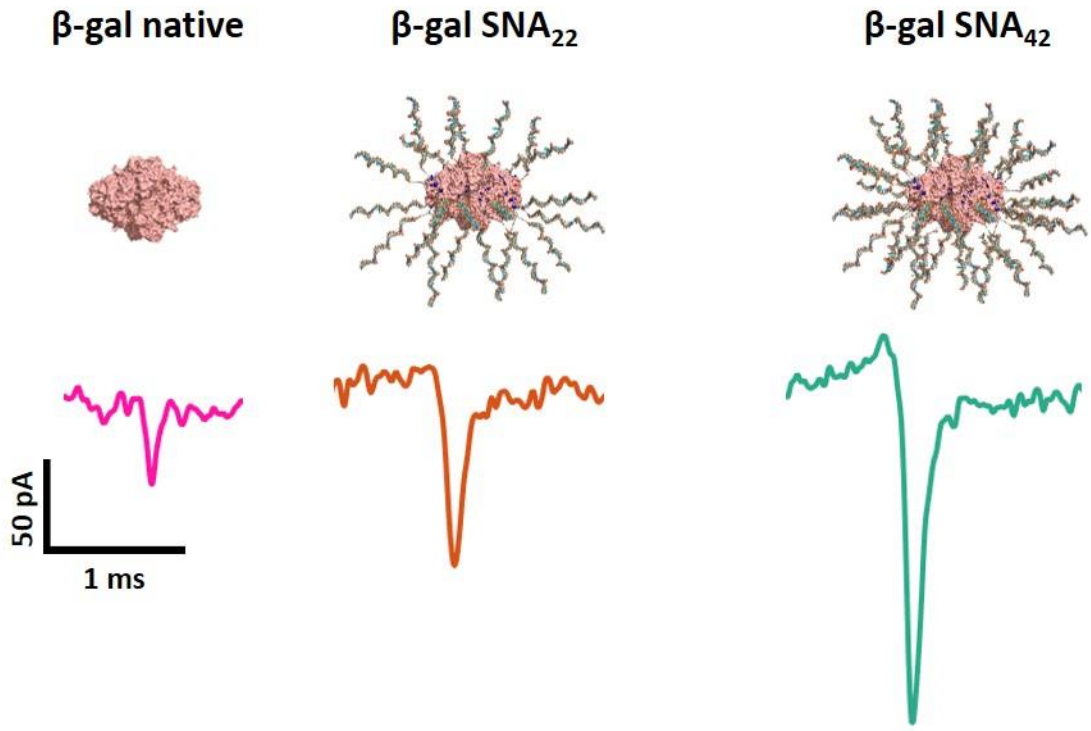

Figure 4.33: Representative individual translocation events recorded for ProSNA samples: β-gal native protein, β-gal SNA_{22}, and β-gal SNA_{42}. A 30 nm pore diameter biased at -700 mV was used and the pipette filled with 100 mM KCl and 5 nM β-gal derivatives into a bath containing 50% PEG in 100 mM KCl. The current and time scales are the same for all the translocation peaks.

This nanopore approach is envisioned to be applied to other classes of soft nanoparticles as well. Under the same nanopore conditions the β-gal SNA with higher DNA loading, not only resulted in a higher average conductive peak current, but also showed the presence of resistive component within the translocation signal, as shown in Figure 4.33. This signature can potentially be exploited beyond the fingerprinting of particles whose hydrodynamic radius matches the pore diameter size. One interesting aspect that could be explored here is the rigidity of the translocating particles. Nanopore studies targeting the translocation of soft nanomaterials and probing their dynamic deformation, particularly biological carriers such as viruses, exosomes, liposomes, are limited. The current techniques in the analysis of such classes of nanoparticles relies on confocal microscopy, electron microscopy, and AFM (202). However, apart from AFM, these techniques cannot be applied for studying the dynamics of deformation. AFM offers

high-resolution imaging and the ability to conduct mechanical deformation of whole particles, but it poses limitation in terms of the analysis throughput. Alternatively, nanopores can be explored to carry out such study, by tailoring pore sizes that can induce deformation of different soft particles as their traverse the aperture. In the study carried out by Holden *et al*., microgel deformation was investigated by translocation through a glass nanopores with diameter sizes smaller than the size of the microgels (203). By combination of applied pressure to the glass nanopore and applied voltage, the microgels were driven through the nanopore and their current signals were recorded. In the case of smaller pores, the microgel deformation led to an increasing interaction with the pore and occupation of the pore's sensing zone, leading to longer dwell times and large current amplitudes during their translocation. The conformational flexibility of many biological soft particles facilitate their translocation through smaller pores. However, in the case of rigid particles, translocations occurs only when the particle size is smaller than the pore. In this sense, rigid nanoparticles can also be used as a reference analyte to measure stiffness of soft particles. A similar approach has been proposed in the study conducted by Lee *et al*., where the stiffness of nanosized liposomes measured by means of solid-state nanopores was inferred by comparing to the translocation behaviour of rigid polystyrene beads (204). Such experiments utilizing our nanopores platform can facilitate numerous studies where controlling the stiffness of the particle is important (*e.g*., drug delivery vesicles).

4.6. Conclusion

In this chapter, the development and implementation of a nanopore system enhanced by a polymer electrolyte enabling the characterization of nanoparticles was demonstrated. The enhanced detection and direct comparison of a range of spherical nanoparticles with different diameters was demonstrated utilizing tailored pores with fixed diameter size, facilitating the nanoparticle discrimination on individual basis and in a mixture. The ability of this nanopore approach to fingerprint nanoparticle was further expanded to demonstrate the wide applicability of the method to characterize metallic nanospheres of varied sizes, nanorods, plasmonic nanostars with various degrees of branching, and protein-based spherical nucleic acids with different

oligonucleotide loadings. Discrimination of the various type of particles was inferred by exploring nanopore discriminants such as dwell time, peak current amplitude, and shape of the translocation signal. This universal nanopore system represents as viable method that can complement the characterization of nanomaterials at the single-entity level in a rapid and non-destructive way to support the exploration of newly synthesized nanomaterials.

Chapter 5: Conclusions & future outlook

5.1. Overview

In this chapter a summary of the main research achievements of this thesis and future perspectives are described. Two future directions are emphasized for this work, namely the integration of solid-state nanopores with portable and compact amplifiers readers and the possibility to carry out multimodal measurements.

5.2. Summary of key achievements

The overall objective of thesis was to develop a single-entity approach for characterizing the physicochemical properties of heterogenous engineered nanomaterials by means of solid-state nanopores. In this sense, the detection and characterization of several emerging nanomaterials has been explored by utilizing a polymer electrolyte nanopore-based approach facilitating enhanced label-free and rapid measurements at the single particle level in various mixtures. Nanomaterials characteristics such as size, shape, assembly state, and functionalization layer were investigated. The approach did not require the chemical modification of the nanopore or extensive sample preparation. It provided a large number of translocation events within minutes, enabling the analytical characterization of the samples.

In Chapter 3, the application of a polymer electrolyte nanopore system provided valuable insight into the heterogeneous nature of supramolecular DNA origami assemblies. The use of a fixed size of the nanopore diameter enabled the direct comparison of four DNA nanostructures with different assembly degree, starting from a pre-folded square tile and supramolecular high-order assemblies such as dimer, trimer, and 2x2 assembly. The label-free nature of the method proposed facilitated the fingerprinting of the four different assembly states based on their nanopore translocation signal characteristics (peak current amplitude, dwell time, and ECS).

Furthermore, quantification of their assembly yield was obtained from each folding mixture based on their ECS nanopore discrimination parameter. Whereas the assembly yield comparison with agarose gel electrophoresis showed comparable results, the nanopore-based approach proposed here benefited of rapid and simple-to-implement quantification of supramolecular DNA nanostructures in solution with low-volume and low-concentration requirements. This approach not only aids in the rapid detection and characterization of intricate DNA nanostructures, but also opens doors to investigate various nanomaterial designs to enable the analysis and manipulation of large DNA assemblies in real time.

In Chapter 4, the versatility of the proposed polymer electrolyte nanopore systems to inspect a wider range of functional nanoparticles was demonstrated. The utilization of tailored pores with fixed diameter sizes enabled the detection of low nanometer sized spherical nanoparticles (10 – 50 nm diameter), and their size-based comparison and discrimination both in homogenous and heterogeneous nanoparticle mixtures. The enhanced detection with larger event count of colloidal suspensions was demonstrated in low ionic strength conditions, favoring colloidal stability depending on the capping agent used in their synthesis. Furthermore, the adaptability of this nanopore approach was showcased by successfully fingerprinting metallic nanospheres, nanorods, plasmonic nanostars with varying degree of branching, and protein-based spherical nuclei acids with different oligonucleotide loadings. Discrimination among these classes of nanoparticles was obtained by exploiting nanopore discriminants, including peak current amplitude, dwell time, shape and subpeaks of the translocation signals. This universal polymer electrolyte nanopore-based technique stands as a complementary toolbox that support the characterization of newly synthesized nanomaterials and potentially integrate such nanoscale probes with on-line synthesis setups for continuous monitoring of synthesis products.

5.3. Future outlook

Several directions can be further explored with regard to the nanopore-based approach described in this thesis for nanomaterial detection and characterization. These directions can be classified in two parts: (1) integration of the nanopores with portable

devices and/or microfluidic setups; (2) combining nanopore with other single-entity measurements.

5.3.1. Nanopore integration modalities

The combination of solid-state nanopores measurements with lab-on-chip devices offers a great potential for nanomaterials characterization and opens us a wide range of applications. Such integrated approaches leverage the unique single-entity measurement capabilities of nanopores and the ability of microfluidic setups to enable precise control and manipulation of solutions with low volumes, facilitating nanomaterials sample handling/delivery. Particularly, the geometry of nanopipettes and the small tip size and needle-like shape allows for integration in spatially confined setups. One example in this direction is the work carried by Gong *et al.*, where an integrated nanopipette-microfluidic device was developed for in-flow detection of DNA molecules (205). Varongchayakul *et al*. reported a microfluidic-nanopore device that supports on-chip sample preparation, purification and single-molecule nanopore measurements (206). In terms of nanomaterial synthesis, such integrated architectures can be used to monitor growth, assembly, and functionalization of nanoparticles and potentially contribute to the optimization of the synthesized batch. The ability to obtain real-time readouts can accelerate the characterization processes and provide quick feedback for optimizing experimental parameters or making informed decisions concerning the nanomaterial synthesis or quality monitoring. Time-sensitive applications would also greatly benefit or such integrated nanopore measurements.

Furthermore, the ability of performing nanopore measurements using compact and nanopore readers is desirable. This would eliminate the need for fixed laboratory setups, providing flexibility to carry out measurements in various settings, remote locations, or on-site analysis. The portability aspect also translates into faster nanopore analysis of nanomaterialas directly at the point of interest. Figure 5.1A depicts a commercial nanopore reader (Elements SRL) with compact dimensions (101 x 44 x 18 mm and 140 g) capable of providing low-noise nanopore measurements. Here, miniaturized 3D-printed flow-cells were prototyped for accommodating the integration of nanopipettes (Figure 5.1B) and silicon nitride pore (Figure 5.1C) on PCB chip that is compatible with the nanopore reader. Whilst the integrated flow-cells are simple in their design for accommodating small volumes exchange, more intricate architectures can be designed

for coupling with microfluidic systems. Furthermore, adaptations can be made to support pressure-assisted nanopipette translocations. An example in this regard is the study carried out by German *et al*. where applied pressure within nanopipettes was used to draw individual particles into the pore (168).

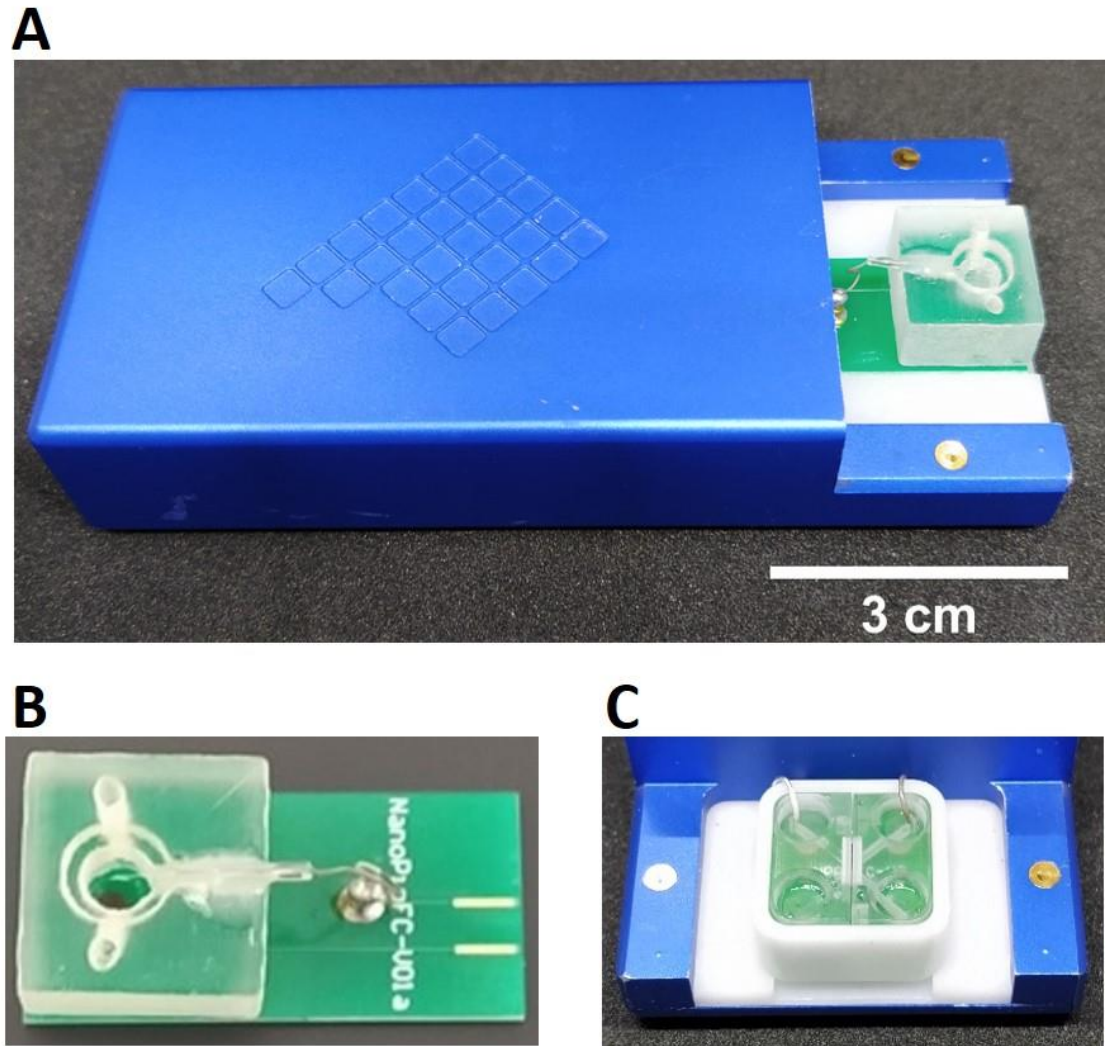

Figure 5.1: Compact and portable nanopore reader. **(A)** Picture of a commercial compact USB-powered nanopore reader (Elements SRL) and prototyped flow-cells mobilized onto PCB chips to accommodate the integration of glass nanopipettes **(B)** and silicon nitride membrane nanopore **(C)**.

5.3.2. Multi-modal measurements

The small footprint of nanopores and the possibility to integrate them with miniaturized devices can stimulate the combination of these measurements with other modes of analysis. One example of dual-measurement concept explored here is the combination of nanopore-based translocation and nanoimpact electrochemistry (NIE). While the nanopore-based measurements can provide information about the physical

characteristics of individual particles, NIE can provide insight into the electrochemical and reactivity properties of individual particles in solution. NIE relies on the collision of nanoparticles to the surface of microelectrode in aqueous conditions due to Brownian motion (207). Upon a collision event on the surface of the electrode, electroactive nanoparticles can induce an electrochemical reaction, such as direction oxidation and reduction on the surface of the biased electrode (207). Figure 5.2A shows dual-probe platform consisting of nanopore and a platinum microelectrode probe to obtain a multimode characterisation of nanoparticles through ionic current measurements (nanopore translocation) and nanoimpact events measuring faradaic currents upon the nanoparticle collision with the electrode surface. Here, a 30 nm diameter citrate-capped silver nanospheres diluted in an electrolyte solution (20 mM KCl) were measured using the dual-probe setup using the portable nanopore reader described in Figure 5.1. Figure 5.2B-C shows the current-time traces recorded for both reverse translocation of the AgNPs and the current spikes obtained due to the oxidation events on the surface of the electrode. The combination of these techniques can favor simultaneous detection and classification of nanoparticles based on their physical and electrochemical characteristics. One potential application would be the identification of specific nanoparticle type in a mixture, or nanoparticles with different functionalization chemistries (*i.e.* electroactive versus insulating particles).

Apart from this, the interface of nanopore-based measurements with nonelectrical readouts can be explored. One such combination is carrying our nanopore measurements and surface-enhanced Raman scattering (SERS) measurements (208). SERS relies on optical detection of unlabeled analytes by detection of the Raman scattering in the presence of a nearby analyte (208). Depending on the nature of the nanomaterials analyzed different strategies can be adopted. In the context of anisotropic nanoparticle described in chapter 5, simultaneous ionic current readout and single particle SERS measurement could be explored. Apart from these, integration of SERS nanostructures to enhance the optical signal, such as patterned gold nanostructures on the silicon nitride membrane (209) or by direct coating of glass nanopipettes (108) can be used for characterizing a wider range of nanomaterials. However, one challenging that needs to be accounted for is the time required for

recording a Raman spectrum, considering the fast duration of a single analyte translocation event.

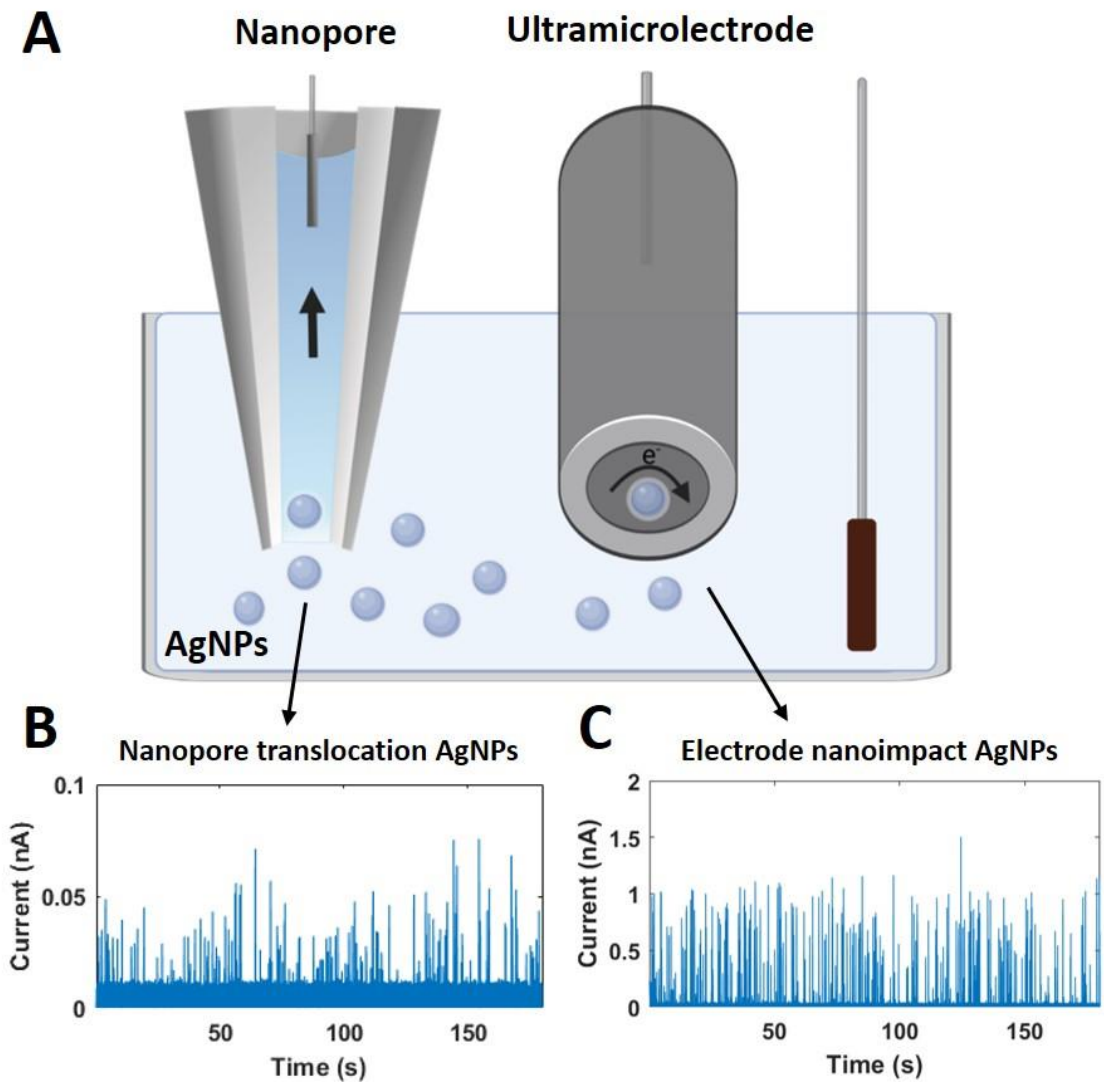

Figure 5.2: Multi-modal nanoparticles analysis example. **(A)** Schematic representation of dual-probe setup consisting of nanopore (50 nm pore diameter) for reverse translocations (from bath inside the nanopipette) of 30 nm diameter citrate-capped AgNPs and a disk-shaped platinum ultramicroelectrode (10 µm diameter) for AgNPs oxidation by nanoimpact electrochemistry. Corresponding ion current trace obtained for nanopore translocation and faradic current traces with oxidative spikes following the AgNPs collisions with the ultramicroelectrode **(B)**. The nanopore and ultramicroelectride were biased at +700 mV and AgNPs were diluted in 20 mM KCl electrolyte solution.

Bibliography

1. Heath, J. R. 1999. Nanoscale Materials. *Accounts of Chemical Research*. 32(5):388-388, doi: 10.1021/ar990059e.
2. Abid, N.*, et al.* 2022. Synthesis of nanomaterials using various top-down and bottom-up approaches, influencing factors, advantages, and disadvantages: A review. *Advances in Colloid and Interface Science*. 300:102597
3. Bagher, A. M. 2016. Quantum dots applications. *Sensors & Transducers*. 198(3):37
4. Pearce, A. K., T. R. Wilks, M. C. Arno, and R. K. O'Reilly. 2021. Synthesis and applications of anisotropic nanoparticles with precisely defined dimensions. *Nature Reviews Chemistry*. 5(1):21-45
5. Mathur, D., and I. L. Medintz. 2019. The growing development of DNA nanostructures for potential healthcare-related applications. *Advanced Healthcare Materials*. 8(9):1801546
6. Ryu, Y., C. Am Hong, Y. Song, J. Beak, B. Am Seo, J.-j. Lee, and H.-S. Kim. 2020. Modular protein–DNA hybrid nanostructures as a drug delivery platform. *Nanoscale*. 12(8):4975-4981
7. Burrows, N. D.*, et al.* 2016. Anisotropic nanoparticles and anisotropic surface chemistry. *The journal of physical chemistry letters*. 7(4):632-641
8. Kooij, E. S., W. Ahmed, C. Hellenthal, H. J. W. Zandvliet, and B. Poelsema. 2012. From nanorods to nanostars: Tuning the optical properties of gold nanoparticles. *Colloids and Surfaces A: Physicochemical and Engineering Aspects*. 413:231-238
9. Huang, X., I. H. El-Sayed, W. Qian, and M. A. El-Sayed. 2006. Cancer cell imaging and photothermal therapy in the near-infrared region by using gold nanorods. *Journal of the American Chemical Society*. 128(6):2115-2120
10. Yuan, H., A. M. Fales, C. G. Khoury, J. Liu, and T. Vo-Dinh. 2013. Spectral characterization and intracellular detection of Surface-Enhanced Raman Scattering (SERS)-encoded plasmonic gold nanostars. *Journal of Raman spectroscopy*. 44(2):234-239
11. Xu, R., D. Wang, J. Zhang, and Y. Li. 2006. Shape-dependent catalytic activity of silver nanoparticles for the oxidation of styrene. *Chemistry–An Asian Journal*. 1(6):888-893
12. Mock, J. J., M. Barbic, D. R. Smith, D. A. Schultz, and S. Schultz. 2002. Shape effects in plasmon resonance of individual colloidal silver nanoparticles. *The Journal of Chemical Physics*. 116(15):6755-6759
13. Tian, F., F. Bonnier, A. Casey, A. E. Shanahan, and H. J. Byrne. 2014. Surface enhanced Raman scattering with gold nanoparticles: effect of particle shape. *Analytical Methods*. 6(22):9116-9123
14. Seeman, N. C. 1982. Nucleic acid junctions and lattices. *Journal of theoretical biology*. 99(2):237-247
15. Seeman, N. C. 2010. Nanomaterials based on DNA. *Annual review of biochemistry*. 79:65-87
16. Rothemund, P. W. K. 2006. Folding DNA to create nanoscale shapes and patterns. *Nature*. 440(7082):297-302, doi: 10.1038/nature04586.

17. Chandrasekaran, A. R., N. Anderson, M. Kizer, K. Halvorsen, and X. Wang. 2016. Beyond the Fold: Emerging Biological Applications of DNA Origami. *ChemBioChem*. 17(12):1081-1089, doi: https://doi.org/10.1002/cbic.201600038.
18. Zhang, Q.*, et al.* 2014. DNA origami as an in vivo drug delivery vehicle for cancer therapy. *ACS nano*. 8(7):6633-6643
19. Walsh, A. S., H. Yin, C. M. Erben, M. J. A. Wood, and A. J. Turberfield. 2011. DNA cage delivery to mammalian cells. *ACS nano*. 5(7):5427-5432
20. Liu, F.*, et al.* 2021. A tetrahedral DNA nanorobot with conformational change in response to molecular trigger. *Nanoscale*. 13(37):15552-15559
21. Kuzuya, A., and M. Komiyama. 2009. Design and construction of a box-shaped 3D-DNA origami. *Chemical Communications*.(28):4182-4184
22. Tikhomirov, G., P. Petersen, and L. Qian. 2017. Fractal assembly of micrometre-scale DNA origami arrays with arbitrary patterns. *Nature*. 552(7683):67-71, doi: 10.1038/nature24655.
23. Wang, X., H. Jun, and M. Bathe. 2022. Programming 2D Supramolecular Assemblies with Wireframe DNA Origami. *Journal of the American Chemical Society*. 144(10):4403-4409, doi: 10.1021/jacs.1c11332.
24. Zhan, P., T. Wen, Z. g. Wang, Y. He, J. Shi, T. Wang, X. Liu, G. Lu, and B. Ding. 2018. DNA origami directed assembly of gold bowtie nanoantennas for single-molecule surface-enhanced Raman scattering. *Angewandte Chemie International Edition*. 57(11):2846-2850
25. Tanwar, S., K. K. Haldar, and T. Sen. 2017. DNA origami directed Au nanostar dimers for single-molecule surface-enhanced Raman scattering. *Journal of the American Chemical Society*. 139(48):17639-17648
26. Ebrahimi, S. B., D. Samanta, C. D. Kusmierz, and C. A. Mirkin. 2022. Protein transfection via spherical nucleic acids. *Nature Protocols*. 17(2):327-357, doi: 10.1038/s41596-021-00642-x.
27. Samanta, D., S. B. Ebrahimi, C. D. Kusmierz, H. F. Cheng, and C. A. Mirkin. 2020. Protein Spherical Nucleic Acids for Live-Cell Chemical Analysis. *Journal of the American Chemical Society*. 142(31):13350-13355, doi: 10.1021/jacs.0c06866.
28. Brodin, J. D., A. J. Sprangers, J. R. McMillan, and C. A. Mirkin. 2015. DNA-Mediated Cellular Delivery of Functional Enzymes. *Journal of the American Chemical Society*. 137(47):14838-14841, doi: 10.1021/jacs.5b09711.
29. Yang, X.-Z., S. Dou, Y.-C. Wang, H.-Y. Long, M.-H. Xiong, C.-Q. Mao, Y.-D. Yao, and J. Wang. 2012. Single-Step Assembly of Cationic Lipid–Polymer Hybrid Nanoparticles for Systemic Delivery of siRNA. *ACS Nano*. 6(6):4955-4965, doi: 10.1021/nn300500u.
30. Melnikova, I. 2007. RNA-based therapies. *Nature Reviews. Drug Discovery*. 6(11):863
31. Yi Xue, H., P. Guo, W.-C. Wen, and H. Lun Wong. 2015. Lipid-based nanocarriers for RNA delivery. *Current pharmaceutical design*. 21(22):3140-3147
32. Richman, E. K., and J. E. Hutchison. 2009. The Nanomaterial Characterization Bottleneck. *ACS Nano*. 3(9):2441-2446, doi: 10.1021/nn901112p.
33. Modena, M. M., B. Rühle, T. P. Burg, and S. Wuttke. 2019. Nanoparticle Characterization: What to Measure? *Advanced Materials*. 31(32):1901556, doi: https://doi.org/10.1002/adma.201901556.

34. Albanese, A., P. S. Tang, and W. C. W. Chan. 2012. The effect of nanoparticle size, shape, and surface chemistry on biological systems. *Annual review of biomedical engineering*. 14:1-16
35. Sosa, I. O., C. Noguez, and R. G. Barrera. 2003. Optical Properties of Metal Nanoparticles with Arbitrary Shapes. *The Journal of Physical Chemistry B*. 107(26):6269-6275, doi: 10.1021/jp0274076.
36. Powers, K. W., S. C. Brown, V. B. Krishna, S. C. Wasdo, B. M. Moudgil, and S. M. Roberts. 2006. Research strategies for safety evaluation of nanomaterials. Part VI. Characterization of nanoscale particles for toxicological evaluation. *Toxicological Sciences*. 90(2):296-303
37. Kuchibhatla, S. V. N. T., A. S. Karakoti, and S. Seal. 2005. Colloidal stability by surface modification. *Jom*. 57(12):52-56
38. Behrens, S. H., D. I. Christl, R. Emmerzael, P. Schurtenberger, and M. Borkovec. 2000. Charging and Aggregation Properties of Carboxyl Latex Particles: Experiments versus DLVO Theory. *Langmuir*. 16(6):2566-2575, doi: 10.1021/la991154z.
39. Clogston, J. D., and A. K. Patri. 2011. Zeta potential measurement. *Characterization of nanoparticles intended for drug delivery*.63-70
40. Snee, P. T. 2018. The Role of Colloidal Stability and Charge in Functionalization of Aqueous Quantum Dots. *Accounts of Chemical Research*. 51(11):2949-2956, doi: 10.1021/acs.accounts.8b00405.
41. Lin, P.-C., S. Lin, P. C. Wang, and R. Sridhar. 2014. Techniques for physicochemical characterization of nanomaterials. *Biotechnology advances*. 32(4):711-726
42. Gooding, J. J., and K. Gaus. 2016. Single-molecule sensors: challenges and opportunities for quantitative analysis. *Angewandte Chemie International Edition*. 55(38):11354-11366
43. Sapsford, K. E., K. M. Tyner, B. J. Dair, J. R. Deschamps, and I. L. Medintz. 2011. Analyzing Nanomaterial Bioconjugates: A Review of Current and Emerging Purification and Characterization Techniques. *Analytical Chemistry*. 83(12):4453-4488, doi: 10.1021/ac200853a.
44. Stetefeld, J., S. A. McKenna, and T. R. Patel. 2016. Dynamic light scattering: a practical guide and applications in biomedical sciences. *Biophysical reviews*. 8:409-427
45. Uskoković, V. 2012. Dynamic light scattering based microelectrophoresis: main prospects and limitations. *Journal of dispersion science and technology*. 33(12):1762-1786
46. Brydson, R., A. Brown, C. Hodges, P. Abellan, and N. Hondow. 2015. Microscopy of nanoparticulate dispersions. *Journal of microscopy*. 260(3):238-247
47. Hondow, N., R. Brydson, P. Wang, M. D. Holton, M. R. Brown, P. Rees, H. D. Summers, and A. Brown. 2012. Quantitative characterization of nanoparticle agglomeration within biological media. *Journal of Nanoparticle Research*. 14:1-15
48. Ilett, M., R. Brydson, A. Brown, and N. Hondow. 2019. Cryo-analytical STEM of frozen, aqueous dispersions of nanoparticles. *Micron*. 120:35-42
49. Ilett, M.*, et al.* 2022. Evaluation of correlated studies using liquid cell and cryo-transmission electron microscopy: Hydration of calcium sulphate and the phase transformation pathways of bassanite to gypsum. *Journal of Microscopy*.

50. Lopez-Sanz, S., F. J. G. Bernardo, R. C. R. Martín-Doimeadios, and A. Rios. 2019. Analytical metrology for nanomaterials: Present achievements and future challenges. *Analytica Chimica Acta*. 1059:1-15
51. Xue, L., H. Yamazaki, R. Ren, M. Wanunu, A. P. Ivanov, and J. B. Edel. 2020. Solid-state nanopore sensors. *Nature Reviews Materials*. 5(12):931-951, doi: 10.1038/s41578-020-0229-6.
52. Miles, B. N., A. P. Ivanov, K. A. Wilson, F. Doğan, D. Japrung, and J. B. Edel. 2013. Single molecule sensing with solid-state nanopores: novel materials, methods, and applications. *Chemical Society Reviews*. 42(1):15-28
53. Lee, K., K. B. Park, H. J. Kim, J. S. Yu, H. Chae, H. M. Kim, and K. B. Kim. 2018. Recent progress in solid-state nanopores. *Advanced materials*. 30(42):1704680
54. Baker, L. A. 2018. Perspective and prospectus on single-entity electrochemistry. *Journal of the American Chemical Society*. 140(46):15549-15559
55. Shi, W., A. K. Friedman, and L. A. Baker. 2017. Nanopore Sensing. *Analytical Chemistry*. 89(1):157-188, doi: 10.1021/acs.analchem.6b04260.
56. Li, M.-Y., Y.-L. Ying, J. Yu, S.-C. Liu, Y.-Q. Wang, S. Li, and Y.-T. Long. 2021. Revisiting the origin of nanopore current blockage for volume difference sensing at the atomic level. *Jacs Au*. 1(7):967-976
57. Chau, C., F. Marcuccio, D. Soulias, M. A. Edwards, A. Tuplin, S. E. Radford, E. Hewitt, and P. Actis. 2022. Probing RNA Conformations Using a Polymer–Electrolyte Solid-State Nanopore. *ACS Nano*. 16(12):20075-20085, doi: 10.1021/acsnano.2c08312.
58. Alibakhshi, M. A., J. R. Halman, J. Wilson, A. Aksimentiev, K. A. Afonin, and M. Wanunu. 2017. Picomolar Fingerprinting of Nucleic Acid Nanoparticles Using Solid-State Nanopores. *ACS Nano*. 11(10):9701-9710, doi: 10.1021/acsnano.7b04923.
59. Raveendran, M., A. J. Lee, R. Sharma, C. Wälti, and P. Actis. 2020. Rational design of DNA nanostructures for single molecule biosensing. *Nature Communications*. 11(1):4384, doi: 10.1038/s41467-020-18132-1.
60. Confederat, S., I. Sandei, G. Mohanan, C. Wälti, and P. Actis. 2022. Nanopore fingerprinting of supramolecular DNA nanostructures. *Biophysical Journal*. 121(24):4882-4891, doi: https://doi.org/10.1016/j.bpj.2022.08.020.
61. Li, W., N. A. W. Bell, S. Hernández-Ainsa, V. V. Thacker, A. M. Thackray, R. Bujdoso, and U. F. Keyser. 2013. Single protein molecule detection by glass nanopores. *ACS nano*. 7(5):4129-4134
62. Thakur, A. K., and L. Movileanu. 2019. Single-molecule protein detection in a biofluid using a quantitative nanopore sensor. *ACS sensors*. 4(9):2320-2326
63. Raveendran, M., A. R. Leach, T. Hopes, J. L. Aspden, and P. Actis. 2020. Ribosome Fingerprinting with a Solid-State Nanopore. *ACS Sensors*. 5(11):3533-3539, doi: 10.1021/acssensors.0c01642.
64. Arima, A.*, et al.* 2018. Selective detections of single-viruses using solid-state nanopores. *Scientific reports*. 8(1):16305
65. Wu, H., Y. Chen, Q. Zhou, R. Wang, B. Xia, D. Ma, K. Luo, and Q. Liu. 2016. Translocation of Rigid Rod-Shaped Virus through Various Solid-State Nanopores. *Analytical Chemistry*. 88(4):2502-2510, doi: 10.1021/acs.analchem.5b04905.

66. Bacri, L., A. G. Oukhaled, B. Schiedt, G. Patriarche, E. Bourhis, J. Gierak, J. Pelta, and L. Auvray. 2011. Dynamics of Colloids in Single Solid-State Nanopores. *The Journal of Physical Chemistry B*. 115(12):2890-2898, doi: 10.1021/jp200326w.
67. Maugi, R., P. Hauer, J. Bowen, E. Ashman, E. Hunsicker, and M. Platt. 2020. A methodology for characterising nanoparticle size and shape using nanopores. *Nanoscale*. 12(1):262-270, doi: 10.1039/C9NR09100A.
68. Si, W., J. Sha, Q. Sun, Z. He, L. Wu, C. Chen, S. Yu, and Y. Chen. 2020. Shape characterization and discrimination of single nanoparticles using solid-state nanopores. *Analyst*. 145(5):1657-1666
69. Fried, J. P., J. L. Swett, B. P. Nadappuram, J. A. Mol, J. B. Edel, A. P. Ivanov, and J. R. Yates. 2021. In situ solid-state nanopore fabrication. *Chemical Society Reviews*. 50(8):4974-4992
70. Wu, Y., and J. J. Gooding. 2022. The application of single molecule nanopore sensing for quantitative analysis. *Chemical Society Reviews*.
71. Ying, Y.-L., C. Cao, and Y.-T. Long. 2014. Single molecule analysis by biological nanopore sensors. *Analyst*. 139(16):3826-3835
72. Song, L., M. R. Hobaugh, C. Shustak, S. Cheley, H. Bayley, and J. E. Gouaux. 1996. Structure of staphylococcal α-hemolysin, a heptameric transmembrane pore. *Science*. 274(5294):1859-1865
73. Jain, M., H. E. Olsen, B. Paten, and M. Akeson. 2016. The Oxford Nanopore MinION: delivery of nanopore sequencing to the genomics community. *Genome biology*. 17:1-11
74. Lo, C. J., T. Aref, and A. Bezryadin. 2006. Fabrication of symmetric sub-5 nm nanopores using focused ion and electron beams. *Nanotechnology*. 17(13):3264
75. Kwok, H., K. Briggs, and V. Tabard-Cossa. 2014. Nanopore fabrication by controlled dielectric breakdown. *PloS one*. 9(3):e92880
76. Tahvildari, R., E. Beamish, V. Tabard-Cossa, and M. Godin. 2015. Integrating nanopore sensors within microfluidic channel arrays using controlled breakdown. *Lab on a Chip*. 15(6):1407-1411
77. Yanagi, I., H. Hamamura, R. Akahori, and K.-i. Takeda. 2018. Two-step breakdown of a SiN membrane for nanopore fabrication: Formation of thin portion and penetration. *Scientific reports*. 8(1):10129
78. Perry, D., D. Momotenko, R. A. Lazenby, M. Kang, and P. R. Unwin. 2016. Characterization of Nanopipettes. *Analytical Chemistry*. 88(10):5523-5530, doi: 10.1021/acs.analchem.6b01095.
79. Karhanek, M., J. T. Kemp, N. Pourmand, R. W. Davis, and C. D. Webb. 2005. Single DNA molecule detection using nanopipettes and nanoparticles. *Nano letters*. 5(2):403-407
80. Yu, R. J., Y. L. Ying, R. Gao, and Y. T. Long. 2019. Confined nanopipette sensing: from single molecules, single nanoparticles, to single cells. *Angewandte Chemie International Edition*. 58(12):3706-3714
81. Kececi, K., A. Dinler, and D. Kaya. 2022. Nanopipette Applications as Sensors, Electrodes, and Probes: A Study on Recent Developments. *Journal of The Electrochemical Society*. 169(2):027502
82. Hall, A. R., A. Scott, D. Rotem, K. K. Mehta, H. Bayley, and C. Dekker. 2010. Hybrid pore formation by directed insertion of α-haemolysin into solid-state nanopores. *Nature nanotechnology*. 5(12):874-877

83. Engst, C. R., M. Ablay, G. Divitini, C. Ducati, T. Liedl, and U. F. Keyser. 2012. DNA Origami Nanopores. *Nano Letters*. 12(1):512-517, doi: 10.1021/nl204098n.
84. Hurley, J. 1970. Sizing particles with a Coulter counter. *Biophysical journal*. 10(1):74-79
85. Smeets, R. M. M., U. F. Keyser, D. Krapf, M.-Y. Wu, N. H. Dekker, and C. Dekker. 2006. Salt Dependence of Ion Transport and DNA Translocation through Solid-State Nanopores. *Nano Letters*. 6(1):89-95, doi: 10.1021/nl052107w.
86. Varongchayakul, N., J. Song, A. Meller, and M. W. Grinstaff. 2018. Single-molecule protein sensing in a nanopore: a tutorial. *Chemical Society Reviews*. 47(23):8512-8524
87. Tang, W., J. P. Fried, R. D. Tilley, and J. J. Gooding. 2022. Understanding and modelling the magnitude of the change in current of nanopore sensors. *Chemical Society Reviews*.
88. Wang, V., N. Ermann, and U. F. Keyser. 2019. Current Enhancement in Solid-State Nanopores Depends on Three-Dimensional DNA Structure. *Nano Letters*. 19(8):5661-5666, doi: 10.1021/acs.nanolett.9b02219.
89. Chang, H., F. Kosari, G. Andreadakis, M. A. Alam, G. Vasmatzis, and R. Bashir. 2004. DNA-Mediated Fluctuations in Ionic Current through Silicon Oxide Nanopore Channels. *Nano Letters*. 4(8):1551-1556, doi: 10.1021/nl049267c.
90. Melnikov, D. V., Z. K. Hulings, and M. E. Gracheva. 2017. Electro-osmotic flow through nanopores in thin and ultrathin membranes. *Physical Review E*. 95(6):063105
91. Lan, W.-J., M. A. Edwards, L. Luo, R. T. Perera, X. Wu, C. R. Martin, and H. S. White. 2016. Voltage-Rectified Current and Fluid Flow in Conical Nanopores. *Accounts of Chemical Research*. 49(11):2605-2613, doi: 10.1021/acs.accounts.6b00395.
92. Yao, Y., C. Wen, N. H. Pham, and S.-L. Zhang. 2020. On Induced Surface Charge in Solid-State Nanopores. *Langmuir*. 36(30):8874-8882, doi: 10.1021/acs.langmuir.0c01189.
93. Chen, P., J. Gu, E. Brandin, Y.-R. Kim, Q. Wang, and D. Branton. 2004. Probing single DNA molecule transport using fabricated nanopores. *Nano letters*. 4(11):2293-2298
94. Li, J., and D. S. Talaga. 2010. The distribution of DNA translocation times in solid-state nanopores. *Journal of Physics: Condensed Matter*. 22(45):454129
95. Albrecht, T. 2019. Single-molecule analysis with solid-state nanopores. *Annual Review of Analytical Chemistry*. 12:371-387
96. Eggenberger, O. M., C. Ying, and M. Mayer. 2019. Surface coatings for solid-state nanopores. *Nanoscale*. 11(42):19636-19657
97. Hu, R.*, et al.* 2016. Intrinsic and membrane-facilitated α-synuclein oligomerization revealed by label-free detection through solid-state nanopores. *Scientific reports*. 6(1):1-11
98. Yusko, E. C., J. M. Johnson, S. Majd, P. Prangkio, R. C. Rollings, J. Li, J. Yang, and M. Mayer. 2011. Controlling protein translocation through nanopores with bio-inspired fluid walls. *Nature nanotechnology*. 6(4):253-260
99. Schmid, S., P. Stömmer, H. Dietz, and C. Dekker. 2021. Nanopore electro-osmotic trap for the label-free study of single proteins and their conformations. *Nature Nanotechnology*. 16(11):1244-1250

100. Choi, J., C. C. Lee, and S. Park. 2019. Scalable fabrication of sub-10 nm polymer nanopores for DNA analysis. *Microsystems & Nanoengineering*. 5(1):12
101. Cadinu, P., G. Campolo, S. Pud, W. Yang, J. B. Edel, C. Dekker, and A. P. Ivanov. 2018. Double Barrel Nanopores as a New Tool for Controlling Single-Molecule Transport. *Nano Letters*. 18(4):2738-2745, doi: 10.1021/acs.nanolett.8b00860.
102. Cadinu, P., M. Kang, B. P. Nadappuram, A. P. Ivanov, and J. B. Edel. 2020. Individually Addressable Multi-nanopores for Single-Molecule Targeted Operations. *Nano Letters*. 20(3):2012-2019, doi: 10.1021/acs.nanolett.9b05307.
103. Wen, C., S. Zeng, Z. Zhang, and S.-L. Zhang. 2018. Group Behavior of Nanoparticles Translocating Multiple Nanopores. *Analytical Chemistry*. 90(22):13483-13490, doi: 10.1021/acs.analchem.8b03408.
104. Ren, R., M. Sun, P. Goel, S. Cai, N. A. Kotov, H. Kuang, C. Xu, A. P. Ivanov, and J. B. Edel. 2021. Single-Molecule Binding Assay Using Nanopores and Dimeric NP Conjugates. *Advanced Materials*. 33(38):2103067
105. Wang, X.*, et al.* 2023. Nanopore Detection Using Supercharged Polypeptide Molecular Carriers. *Journal of the American Chemical Society*. 145(11):6371-6382, doi: 10.1021/jacs.2c13465.
106. Zhu, J., R. Tivony, F. Bošković, J. Pereira-Dias, S. E. Sandler, S. Baker, and U. F. Keyser. 2023. Multiplexed Nanopore-Based Nucleic Acid Sensing and Bacterial Identification Using DNA Dumbbell Nanoswitches. *Journal of the American Chemical Society*. doi: 10.1021/jacs.3c01649.
107. Weckman, N. E., N. Ermann, R. Gutierrez, K. Chen, J. Graham, R. Tivony, A. Heron, and U. F. Keyser. 2019. Multiplexed DNA Identification Using Site Specific dCas9 Barcodes and Nanopore Sensing. *ACS Sensors*. 4(8):2065-2072, doi: 10.1021/acssensors.9b00686.
108. Ren, R., M. Sun, P. Goel, S. Cai, N. A. Kotov, H. Kuang, C. Xu, A. P. Ivanov, and J. B. Edel. 2021. Single-Molecule Binding Assay Using Nanopores and Dimeric NP Conjugates. *Advanced Materials*. 33(38):2103067, doi: https://doi.org/10.1002/adma.202103067.
109. Chau, C. C., S. E. Radford, E. W. Hewitt, and P. Actis. 2020. Macromolecular Crowding Enhances the Detection of DNA and Proteins by a Solid-State Nanopore. *Nano Letters*. 20(7):5553-5561, doi: 10.1021/acs.nanolett.0c02246.
110. Marcuccio, F., D. Soulias, C. C. C. Chau, S. E. Radford, E. Hewitt, P. Actis, and M. A. Edwards. 2023. Mechanistic Study of the Conductance and Enhanced Single-Molecule Detection in a Polymer–Electrolyte Nanopore. *ACS Nanoscience Au*. doi: 10.1021/acsnanoscienceau.2c00050.
111. Xu, X., D. Valavanis, P. Ciocci, S. Confederat, F. Marcuccio, J.-F. Lemineur, P. Actis, F. Kanoufi, and P. R. Unwin. 2023. The New Era of High-Throughput Nanoelectrochemistry. *Analytical Chemistry*. 95(1):319-356, doi: 10.1021/acs.analchem.2c05105.
112. Samuel, C.*, et al.* 2023. Next-Generation Nanopore Sensors for Enhanced Detection of Nanoparticles. *bioRxiv*.2023.2003.2031.534385, doi: 10.1101/2023.03.31.534385.
113. INSTRUMENT, S. 2022. 2023. https://www.sutter.com/MICROPIPETTE/p-2000.html

114. Shigyou, K.*, et al.* 2020. Geometrical Characterization of Glass Nanopipettes with Sub-10 nm Pore Diameter by Transmission Electron Microscopy. *Analytical Chemistry*. 92(23):15388-15393, doi: 10.1021/acs.analchem.0c02884.
115. Wanunu, M. 2012. Nanopores: A journey towards DNA sequencing. *Physics of life reviews*. 9(2):125-158
116. Plesa, C., and C. Dekker. 2015. Data analysis methods for solid-state nanopores. *Nanotechnology*. 26:084003, doi: 10.1088/0957-4484/26/8/084003.
117. Seeman, N. C., and H. F. Sleiman. 2017. DNA nanotechnology. *Nature Reviews Materials*. 3(1):17068, doi: 10.1038/natrevmats.2017.68.
118. Dey, S.*, et al.* 2021. DNA origami. *Nature Reviews Methods Primers*. 1(1):13, doi: 10.1038/s43586-020-00009-8.
119. Engelhardt, F. A. S.*, et al.* 2019. Custom-Size, Functional, and Durable DNA Origami with Design-Specific Scaffolds. *ACS Nano*. 13(5):5015-5027, doi: 10.1021/acsnano.9b01025.
120. Zhang, Y., Q. Li, X. Liu, C. Fan, H. Liu, and L. Wang. 2020. Prescribing DNA Origami Patterns via Scaffold Decoration. *Small*. 16(16):e2000793, doi: 10.1002/smll.202000793.
121. Gu, H., J. Chao, S.-J. Xiao, and N. C. Seeman. 2009. Dynamic patterning programmed by DNA tiles captured on a DNA origami substrate. *Nature Nanotechnology*. 4(4):245-248, doi: 10.1038/nnano.2009.5.
122. Huang, Y., M.-K. Nguyen, A. K. Natarajan, V. H. Nguyen, and A. Kuzyk. 2018. A DNA Origami-Based Chiral Plasmonic Sensing Device. *ACS Applied Materials & Interfaces*. 10(51):44221-44225, doi: 10.1021/acsami.8b19153.
123. Arroyo-Currás, N.*, et al.* 2020. An electrochemical biosensor exploiting binding-induced changes in electron transfer of electrode-attached DNA origami to detect hundred nanometer-scale targets. *Nanoscale*. 12(26):13907-13911, doi: 10.1039/D0NR00952K.
124. Selnihhin, D., S. M. Sparvath, S. Preus, V. Birkedal, and E. S. Andersen. 2018. Multifluorophore DNA Origami Beacon as a Biosensing Platform. *ACS Nano*. 12(6):5699-5708, doi: 10.1021/acsnano.8b01510.
125. Zhang, Q.*, et al.* 2014. DNA Origami as an In Vivo Drug Delivery Vehicle for Cancer Therapy. *ACS Nano*. 8(7):6633-6643, doi: 10.1021/nn502058j.
126. Ge, Z.*, et al.* 2020. DNA Origami-Enabled Engineering of Ligand-Drug Conjugates for Targeted Drug Delivery. *Small*. 16(16):e1904857, doi: 10.1002/smll.201904857.
127. Lee, A. J., M. Endo, J. K. Hobbs, and C. Wälti. 2018. Direct Single-Molecule Observation of Mode and Geometry of RecA-Mediated Homology Search. *ACS Nano*. 12(1):272-278, doi: 10.1021/acsnano.7b06208.
128. Lee, A. J., M. Endo, J. K. Hobbs, A. G. Davies, and C. Walti. 2021. Micro-homology intermediates: RecA's transient sampling revealed at the single molecule level. *Nucleic Acids Res*. 49(3):1426-1435, doi: 10.1093/nar/gkaa1258.
129. Platnich, C. M., F. J. Rizzuto, G. Cosa, and H. F. Sleiman. 2020. Single-molecule methods in structural DNA nanotechnology. *Chemical Society Reviews*. 49(13):4220-4233, doi: 10.1039/C9CS00776H.
130. Alfaro, J. A.*, et al.* 2021. The emerging landscape of single-molecule protein sequencing technologies. *Nature Methods*. 18(6):604-617, doi: 10.1038/s41592-021-01143-1.

131. Houghtaling, J., C. Ying, O. M. Eggenberger, A. Fennouri, S. Nandivada, M. Acharjee, J. Li, A. R. Hall, and M. Mayer. 2019. Estimation of Shape, Volume, and Dipole Moment of Individual Proteins Freely Transiting a Synthetic Nanopore. *ACS Nano*. 13(5):5231-5242, doi: 10.1021/acsnano.8b09555.
132. Karmi, A., H. Dachlika, G. P. Sakala, D. Rotem, M. Reches, and D. Porath. 2021. Detection of Au Nanoparticles Using Peptide-Modified Si3N4 Nanopores. *ACS Applied Nano Materials*. 4(2):1000-1008, doi: 10.1021/acsanm.0c02126.
133. Arima, A.*, et al.* 2018. Identifying Single Viruses Using Biorecognition Solid-State Nanopores. *Journal of the American Chemical Society*. 140(48):16834-16841, doi: 10.1021/jacs.8b10854.
134. Yu, R.-J., S.-M. Lu, S.-W. Xu, Y.-J. Li, Q. Xu, Y.-L. Ying, and Y.-T. Long. 2019. Single molecule sensing of amyloid-β aggregation by confined glass nanopores. *Chemical Science*. 10(46):10728-10732, doi: 10.1039/C9SC03260F.
135. Plesa, C., N. van Loo, P. Ketterer, H. Dietz, and C. Dekker. 2015. Velocity of DNA during Translocation through a Solid-State Nanopore. *Nano Letters*. 15(1):732-737, doi: 10.1021/nl504375c.
136. Plesa, C., A. N. Ananth, V. Linko, C. Gülcher, A. J. Katan, H. Dietz, and C. Dekker. 2014. Ionic Permeability and Mechanical Properties of DNA Origami Nanoplates on Solid-State Nanopores. *ACS Nano*. 8(1):35-43, doi: 10.1021/nn405045x.
137. Raveendran, M., A. J. Lee, C. Wälti, and P. Actis. 2018. Analysis of 2D DNA Origami with Nanopipettes. *ChemElectroChem*. 5(20):3014-3020, doi: https://doi.org/10.1002/celc.201800732.
138. Beamish, E., V. Tabard-Cossa, and M. Godin. 2019. Programmable DNA Nanoswitch Sensing with Solid-State Nanopores. *ACS Sensors*. 4(9):2458-2464, doi: 10.1021/acssensors.9b01053.
139. Chen, K., J. Zhu, F. Bošković, and U. F. Keyser. 2020. Nanopore-Based DNA Hard Drives for Rewritable and Secure Data Storage. *Nano Letters*. 20(5):3754-3760, doi: 10.1021/acs.nanolett.0c00755.
140. Tikhomirov, G., P. Petersen, and L. Qian. 2017. Programmable disorder in random DNA tilings. *Nature Nanotechnology*. 12(3):251-259, doi: 10.1038/nnano.2016.256.
141. Douglas, S. M., A. H. Marblestone, S. Teerapittayanon, A. Vazquez, G. M. Church, and W. M. Shih. 2009. Rapid prototyping of 3D DNA-origami shapes with caDNAno. *Nucleic Acids Research*. 37(15):5001-5006, doi: 10.1093/nar/gkp436.
142. Confederat, S. 2022. Data repository: Nanopore Fingerprinting of Supramolecular DNA Origami Nanostructures. *Research Data Leeds Repository*
143. Chau, C. C., F. Marcuccio, D. Soulias, M. A. Edwards, S. E. Radford, E. W. Hewitt, and P. Actis. 2021. Cooperative electrolyte-PEG interactions drive the signal amplification in a solid-state nanopore. *bioRxiv*.2021.2011.2001.466478, doi: 10.1101/2021.11.01.466478.
144. Wanunu, M., J. Sutin, B. McNally, A. Chow, and A. Meller. 2008. DNA Translocation Governed by Interactions with Solid-State Nanopores. *Biophysical journal*. 95:4716-4725, doi: 10.1529/biophysj.108.140475.
145. Li, J., and D. Talaga. 2010. The distribution of DNA translocation times in solid-state nanopores. *Journal of physics. Condensed matter : an Institute of Physics journal*. 22:454129, doi: 10.1088/0953-8984/22/45/454129.

146. Zhu, L., Z. Zhang, and Q. Liu. 2020. Deformation-Mediated Translocation of DNA Origami Nanoplates through a Narrow Solid-State Nanopore. *Anal Chem*. 92(19):13238-13245, doi: 10.1021/acs.analchem.0c02396.
147. Zenk, J., C. Tuntivate, and R. Schulman. 2016. Kinetics and Thermodynamics of Watson–Crick Base Pairing Driven DNA Origami Dimerization. *Journal of the American Chemical Society*. 138(10):3346-3354, doi: 10.1021/jacs.5b10502.
148. Dunn, K. E., F. Dannenberg, T. E. Ouldridge, M. Kwiatkowska, A. J. Turberfield, and J. Bath. 2015. Guiding the folding pathway of DNA origami. *Nature*. 525(7567):82-86, doi: 10.1038/nature14860.
149. Kim, M. J., M. Wanunu, D. C. Bell, and A. Meller. 2006. Rapid Fabrication of Uniformly Sized Nanopores and Nanopore Arrays for Parallel DNA Analysis. *Advanced Materials*. 18(23):3149-3153, doi: https://doi.org/10.1002/adma.200601191.
150. Verschueren, D. V., W. Yang, and C. Dekker. 2018. Lithography-based fabrication of nanopore arrays in freestanding SiN and graphene membranes. *Nanotechnology*. 29(14):145302, doi: 10.1088/1361-6528/aaabce.
151. Alawami, M. F., F. Bošković, J. Zhu, K. Chen, S. E. Sandler, and U. F. Keyser. 2022. Lifetime of glass nanopores in a PDMS chip for single-molecule sensing. *iScience*. 25(5):104191, doi: https://doi.org/10.1016/j.isci.2022.104191.
152. Meyer, N., J. M. Janot, M. A.-O. Lepoitevin, M. A.-O. Smietana, J. A.-O. Vasseur, J. A.-O. Torrent, and S. Balme. Machine Learning to Improve the Sensing of Biomolecules by Conical Track-Etched Nanopore. LID - 10.3390/bios10100140 [doi] LID - 140. (2079-6374 (Electronic))
153. Taniguchi, M., H. Takei, K. Tomiyasu, O. Sakamoto, and N. Naono. 2022. Sensing the Performance of Artificially Intelligent Nanopores Developed by Integrating Solid-State Nanopores with Machine Learning Methods. *The Journal of Physical Chemistry C*. doi: 10.1021/acs.jpcc.2c02674.
154. Taniguchi, M.*, et al.* 2021. Combining machine learning and nanopore construction creates an artificial intelligence nanopore for coronavirus detection. *Nature Communications*. 12(1):3726, doi: 10.1038/s41467-021-24001-2.
155. Xie, Z.-P., S.-m. Liu, and Y.-M. Zhai. 2022. Study on the Self-assembly and Signal Amplification Ability of Nucleic Acid Nanostructure with the Nanopipette. *Journal of Electroanalytical Chemistry*. 914:116307, doi: 10.1016/j.jelechem.2022.116307.
156. Yang, J., N. Zhao, Y. Liang, Z. Lu, and C. Zhang. 2021. Structure-flexible DNA origami translocation through a solid-state nanopore. *RSC Advances*. 11(38):23471-23476, doi: 10.1039/D1RA04267J.
157. Samuel, C.*, et al.* 2023. Nanopore Sensors for Enhanced Detection of Nanoparticles. *bioRxiv*.2023.2003.2031.534385, doi: 10.1101/2023.03.31.534385.
158. Zhang, H. 2020. Molecularly Imprinted Nanoparticles for Biomedical Applications. *Advanced Materials*. 32(3):1806328, doi: https://doi.org/10.1002/adma.201806328.
159. Tan, H. W., J. An, C. K. Chua, and T. Tran. 2019. Metallic Nanoparticle Inks for 3D Printing of Electronics. *Advanced Electronic Materials*. 5(5):1800831, doi: https://doi.org/10.1002/aelm.201800831.

160. Stark, W. J., P. R. Stoessel, W. Wohlleben, and A. Hafner. 2015. Industrial applications of nanoparticles. *Chemical Society Reviews*. 44(16):5793-5805, doi: 10.1039/C4CS00362D.
161. Tomaszewska, E., K. Soliwoda, K. Kadziola, B. Tkacz-Szczesna, G. Celichowski, M. Cichomski, W. Szmaja, and J. Grobelny. 2013. Detection limits of DLS and UV-Vis spectroscopy in characterization of polydisperse nanoparticles colloids. *Journal of Nanomaterials*. 2013:60-60
162. Filipe, V., A. Hawe, and W. Jiskoot. 2010. Critical evaluation of Nanoparticle Tracking Analysis (NTA) by NanoSight for the measurement of nanoparticles and protein aggregates. *Pharmaceutical research*. 27:796-810
163. Lu, S.-M., Y.-Y. Peng, Y.-L. Ying, and Y.-T. Long. 2020. Electrochemical sensing at a confined space. *Analytical chemistry*. 92(8):5621-5644
164. Waduge, P., R. Hu, P. Bandarkar, H. Yamazaki, B. Cressiot, Q. Zhao, P. C. Whitford, and M. Wanunu. 2017. Nanopore-based measurements of protein size, fluctuations, and conformational changes. *ACS nano*. 11(6):5706-5716
165. Arjmandi, N., W. Van Roy, L. Lagae, and G. Borghs. 2012. Measuring the Electric Charge and Zeta Potential of Nanometer-Sized Objects Using Pyramidal-Shaped Nanopores. *Analytical Chemistry*. 84(20):8490-8496, doi: 10.1021/ac300705z.
166. Lee, K., K.-B. Park, H.-J. Kim, J.-S. Yu, H. Chae, H.-M. Kim, and K.-B. Kim. 2018. Recent Progress in Solid-State Nanopores. *Advanced Materials*. 30(42):1704680, doi: https://doi.org/10.1002/adma.201704680.
167. Yang, W., B. Radha, A. Choudhary, Y. You, G. Mettela, A. K. Geim, A. Aksimentiev, A. Keerthi, and C. Dekker. 2021. Translocation of DNA through Ultrathin Nanoslits. *Advanced Materials*. 33(11):2007682, doi: https://doi.org/10.1002/adma.202007682.
168. German, S. R., L. Luo, H. S. White, and T. L. Mega. 2013. Controlling Nanoparticle Dynamics in Conical Nanopores. *The Journal of Physical Chemistry C*. 117(1):703-711, doi: 10.1021/jp310513v.
169. Kowalczyk, S. W., D. B. Wells, A. Aksimentiev, and C. Dekker. 2012. Slowing down DNA Translocation through a Nanopore in Lithium Chloride. *Nano Letters*. 12(2):1038-1044, doi: 10.1021/nl204273h.
170. Platt, M., G. R. Willmott, and G. U. Lee. 2012. Resistive Pulse Sensing of Analyte-Induced Multicomponent Rod Aggregation Using Tunable Pores. *Small*. 8(15):2436-2444, doi: https://doi.org/10.1002/smll.201200058.
171. Plesa, C., and C. Dekker. 2015. Data analysis methods for solid-state nanopores. *Nanotechnology*. 26(8):084003
172. Turkevich, J., P. C. Stevenson, and J. Hillier. 1951. A study of the nucleation and growth processes in the synthesis of colloidal gold. *Discussions of the Faraday Society*. 11:55-75
173. Yuan, H., C. G. Khoury, H. Hwang, C. M. Wilson, G. A. Grant, and T. Vo-Dinh. 2012. Gold nanostars: surfactant-free synthesis, 3D modelling, and two-photon photoluminescence imaging. *Nanotechnology*. 23(7):075102
174. Yao, F., X. Peng, Z. Su, L. Tian, Y. Guo, and X.-f. Kang. 2020. Crowding-induced DNA translocation through a protein nanopore. *Analytical chemistry*. 92(5):3827-3833

175. Lan, W.-J., D. A. Holden, B. Zhang, and H. S. White. 2011. Nanoparticle Transport in Conical-Shaped Nanopores. *Analytical Chemistry*. 83(10):3840-3847, doi: 10.1021/ac200312n.
176. Wu, H., H. Liu, S. Tan, J. Yu, W. Zhao, L. Wang, and Q. Liu. 2014. The estimation of field-dependent conductance change of nanopore by field-induced charge in the translocations of AuNPs-DNA conjugates. *The Journal of Physical Chemistry C*. 118(46):26825-26835
177. Lastra, L. S., Y. M. N. D. Y. Bandara, M. Nguyen, N. Farajpour, and K. J. Freedman. 2022. On the origins of conductive pulse sensing inside a nanopore. *Nature Communications*. 13(1):2186, doi: 10.1038/s41467-022-29758-8.
178. Chen, K., N. A. W. Bell, J. Kong, Y. Tian, and U. F. Keyser. 2017. Direction-and salt-dependent ionic current signatures for DNA sensing with asymmetric nanopores. *Biophysical journal*. 112(4):674-682
179. Weatherall, E., and G. R. Willmott. 2015. Conductive and biphasic pulses in tunable resistive pulse sensing. *The Journal of Physical Chemistry B*. 119(16):5328-5335
180. Sensale, S., Z. Peng, and H.-C. Chang. 2019. Biphasic signals during nanopore translocation of DNA and nanoparticles due to strong ion cloud deformation. *Nanoscale*. 11(47):22772-22779, doi: 10.1039/C9NR05223B.
181. Menestrina, J., C. Yang, M. Schiel, I. Vlassiouk, and Z. S. Siwy. 2014. Charged Particles Modulate Local Ionic Concentrations and Cause Formation of Positive Peaks in Resistive-Pulse-Based Detection. *The Journal of Physical Chemistry C*. 118(5):2391-2398, doi: 10.1021/jp412135v.
182. Chen, K., L. Shan, S. He, G. Hu, Y. Meng, and Y. Tian. 2015. Biphasic Resistive Pulses and Ion Concentration Modulation during Particle Translocation through Cylindrical Nanopores. *The Journal of Physical Chemistry C*. 119(15):8329-8335, doi: 10.1021/acs.jpcc.5b00047.
183. Momotenko, D., F. Cortés-Salazar, J. Josserand, S. Liu, Y. Shao, and H. H. Girault. 2011. Ion current rectification and rectification inversion in conical nanopores: a perm-selective view. *Physical Chemistry Chemical Physics*. 13(12):5430-5440, doi: 10.1039/C0CP02595J.
184. Prabhu, A. S., T. Z. N. Jubery, K. J. Freedman, R. Mulero, P. Dutta, and M. J. Kim. 2010. Chemically modified solid state nanopores for high throughput nanoparticle separation. *Journal of Physics: Condensed Matter*. 22(45):454107, doi: 10.1088/0953-8984/22/45/454107.
185. Terejánszky, P., I. Makra, P. Fürjes, and R. E. Gyurcsányi. 2014. Calibration-Less Sizing and Quantitation of Polymeric Nanoparticles and Viruses with Quartz Nanopipets. *Analytical Chemistry*. 86(10):4688-4697, doi: 10.1021/ac500184z.
186. Huang, X., S. Neretina, and M. A. El-Sayed. 2009. Gold nanorods: from synthesis and properties to biological and biomedical applications. *Advanced materials*. 21(48):4880-4910
187. Zhang, Y., M. A. Edwards, S. R. German, and H. S. White. 2016. Multipass Resistive-Pulse Observations of the Rotational Tumbling of Individual Nanorods. *The Journal of Physical Chemistry C*. 120(37):20781-20788, doi: 10.1021/acs.jpcc.6b02018.

188. Liu, L., J. Kong, X. Xie, H. Wu, X. Ye, Z. Zhao, L. Wang, and Q. Liu. 2014. Gold nanorod translocation through a solid-state nanopore. *Chinese Science Bulletin*. 59:598-605
189. Xi, G., Y. Ye, L. Wang, W. Zhuang, X. Yan, Y. Wang, L. Zhang, and L. Wu. 2020. Spatial conformation measurement of gold nanorods translocated through a solid-state nanopore. *Materials Express*. 10(10):1732-1739
190. Wei, X., A. Popov, and R. Hernandez. 2022. Electric Potential of Citrate-Capped Gold Nanoparticles Is Affected by Poly(allylamine hydrochloride) and Salt Concentration. *ACS Applied Materials & Interfaces*. 14(10):12538-12550, doi: 10.1021/acsami.1c24526.
191. Strobbia, P., V. Cupil-Garcia, B. M. Crawford, A. M. Fales, T. J. Pfefer, Y. Liu, M. Maiwald, B. Sumpf, and T. Vo-Dinh. 2021. Accurate in vivo tumor detection using plasmonic-enhanced shifted-excitation Raman difference spectroscopy (SERDS). *Theranostics*. 11(9):4090
192. Indrasekara, A. S. D. S., S. Meyers, S. Shubeita, L. C. Feldman, T. Gustafsson, and L. Fabris. 2014. Gold nanostar substrates for SERS-based chemical sensing in the femtomolar regime. *Nanoscale*. 6(15):8891-8899
193. Barbosa, S., A. Agrawal, L. Rodríguez-Lorenzo, I. Pastoriza-Santos, R. A. Alvarez-Puebla, A. Kornowski, H. Weller, and L. M. Liz-Marzán. 2010. Tuning Size and Sensing Properties in Colloidal Gold Nanostars. *Langmuir*. 26(18):14943-14950, doi: 10.1021/la102559e.
194. Samanta, D., S. B. Ebrahimi, and C. A. Mirkin. 2020. Nucleic-Acid Structures as Intracellular Probes for Live Cells. *Advanced Materials*. 32(13):1901743, doi: https://doi.org/10.1002/adma.201901743.
195. Giljohann, D. A., D. S. Seferos, P. C. Patel, J. E. Millstone, N. L. Rosi, and C. A. Mirkin. 2007. Oligonucleotide loading determines cellular uptake of DNA-modified gold nanoparticles. *Nano letters*. 7(12):3818-3821
196. Matthews, B. W. 2005. The structure of E. coli β-galactosidase. *Comptes rendus biologies*. 328(6):549-556
197. Sexton, L. T., H. Mukaibo, P. Katira, H. Hess, S. A. Sherrill, L. P. Horne, and C. R. Martin. 2010. An Adsorption-Based Model for Pulse Duration in Resistive-Pulse Protein Sensing. *Journal of the American Chemical Society*. 132(19):6755-6763, doi: 10.1021/ja100693x.
198. Ding, S., C. Gao, and L.-Q. Gu. 2009. Capturing Single Molecules of Immunoglobulin and Ricin with an Aptamer-Encoded Glass Nanopore. *Analytical Chemistry*. 81(16):6649-6655, doi: 10.1021/ac9006705.
199. Chi, Q., G. Wang, and J. Jiang. 2013. The persistence length and length per base of single-stranded DNA obtained from fluorescence correlation spectroscopy measurements using mean field theory. *Physica A: Statistical Mechanics and its Applications*. 392(5):1072-1079
200. Huang, X.*, et al.* 2021. DNA scaffolds enable efficient and tunable functionalization of biomaterials for immune cell modulation. *Nature Nanotechnology*. 16(2):214-223, doi: 10.1038/s41565-020-00813-z.
201. He, L., J. Mu, O. Gang, and X. Chen. 2021. Rationally programming nanomaterials with DNA for biomedical applications. *Advanced Science*. 8(8):2003775

202. Ruozi, B., D. Belletti, A. Tombesi, G. Tosi, L. Bondioli, F. Forni, and M. A. Vandelli. 2011. AFM, ESEM, TEM, and CLSM in liposomal characterization: a comparative study. *International journal of nanomedicine*.557-563
203. Holden, D. A., G. Hendrickson, L. A. Lyon, and H. S. White. 2011. Resistive pulse analysis of microgel deformation during nanopore translocation. *The journal of physical chemistry C*. 115(7):2999-3004
204. Lee, J. S., J. Saharia, Y. M. N. D. Y. Bandara, B. I. Karawdeniya, G. Goyal, A. Darvish, Q. Wang, M. J. Kim, and M. J. Kim. 2019. Stiffness measurement of nanosized liposomes using solid-state nanopore sensor with automated recapturing platform. *Electrophoresis*. 40(9):1337-1344
205. Gong, X., A. V. Patil, A. P. Ivanov, Q. Kong, T. Gibb, F. Dogan, A. J. deMello, and J. B. Edel. 2014. Label-Free In-Flow Detection of Single DNA Molecules using Glass Nanopipettes. *Analytical Chemistry*. 86(1):835-841, doi: 10.1021/ac403391q.
206. Varongchayakul, N., J. S. Hersey, A. Squires, A. Meller, and M. W. Grinstaff. 2018. A solid-state hard microfluidic–nanopore biosensor with multilayer fluidics and on-chip bioassay/purification chamber. *Advanced functional materials*. 28(50):1804182
207. Stevenson, K. J., and K. Tschulik. 2017. A materials driven approach for understanding single entity nano impact electrochemistry. *Current Opinion in Electrochemistry*. 6(1):38-45
208. Spitzberg, J. D., A. Zrehen, X. F. van Kooten, and A. Meller. 2019. Plasmonic-nanopore biosensors for superior single-molecule detection. *Advanced materials*. 31(23):1900422
209. Verschueren, D. V., S. Pud, X. Shi, L. De Angelis, L. Kuipers, and C. Dekker. 2019. Label-Free Optical Detection of DNA Translocations through Plasmonic Nanopores. *ACS Nano*. 13(1):61-70, doi: 10.1021/acsnano.8b06758.